Effect of Endwall Fluid Injection on Vortex Formation in a First Stage Nozzle Guide Vane Passage

Prethive Dhilip Dhilipkumar

Thesis submitted to the faculty of the Virginia Polytechnic Institute and State University in partial fulfillment of the requirements for the degree of

Master of Science

In

Mechanical Engineering

Srinath V. Ekkad, Chair

Scott T. Huxtable

Kevin T. Lowe

08/11/2016
Blacksburg, Virginia

Keywords: Computational Fluid Dynamics, Gas Turbines, Passage Vortex, Endwall Flow, Fluid Injection

Effect of Endwall Fluid Injection on Vortex Formation in a First Stage Nozzle Guide Vane Passage

Prethive Dhilip Dhilipkumar

ABSTRACT

The growing need for increased performance from gas turbines has fueled the drive to raise turbine inlet temperatures. This results in high thermal stresses especially along the first stage nozzle guide vane cascade as the hot combustion products exiting modern day gas turbine combustors generally reach temperatures that could endanger the structural stability of these vanes and greatly reduce the vane life. The highest heat transfer coefficients in the vane passage occurs near the endwall, particularly in the leading edge-endwall junction where vortical flows cause the flow of hotter fluid in the mainstream to mix with relatively lower temperature boundary layer fluid. This work documents the computational investigation of air injection at the end wall through a cylindrical hole placed upstream of the nozzle guide vane leading edge-end wall junction. The effect of the secondary jet on the formation of the leading edge horseshoe vortex and the consequent formation of the passage vortex has been studied. For the computations, the Reynolds averaged Navier–Stokes (RANS) equations were solved with the commercial software ANSYS Fluent using the SST k-ω model. Total pressure loss coefficient and kinetic energy loss Coefficient contour plots at the exit of the cascade to estimate the effect of the endwall fluid injection on loss profiles at the vane cascade exit. Swirling strength contours were plotted at several axial chord locations in order to track the path of the passage vortex in and downstream of the vane cascade. Two different hole-positions (located at 1 hole diameter and 2 hole diameters from the leading edge) along a plane parallel to the incident flow were considered in order to study the effect of the hole position with respect to the vane leading edge-endwall junction. Three different streamwise hole inclination angles with respect to the mainstream flow direction were studied to identify the best angle for the injection of fluid through the endwall. This angle was combined with five different compound angles (0°, 30°, 45°, 60° and 90°) in order to study the effect of varying the compound angle on the leading edge vortex and the passage vortex. Each of the above studies were conducted at two different injected fluid-to-mainstream mass flow ratios (0.5% and 1%) in order to study the effect of varying injected flow rate on the formation of the leading edge vortex and

the vane passage vortex. From the results it was observed that suitable selection of the secondary injection mass flow rate, injection angle and hole-position caused an absence of the leading edge horseshoe vortex and delayed migration of the passage vortex across the guide vane passage. Heat Transfer studies were also conducted to observe the absence/weakening of the leading edge vortex and the delayed pitch-wise movement of the passage vortex.

Effect of Endwall Fluid Injection on Vortex Formation in a First Stage Nozzle Guide Vane Passage

Prethive Dhilip Dhilipkumar

GENERAL ABSTRACT

Gas turbines are a kind of Internal Combustion engine that convert chemical energy to mechanical energy by way of burning an air-fuel mixture to cause turbine blades to spin and produce power. A typical gas turbine consists of a compressor which compresses the air intake into the combustion chamber, the combustion chamber in which energy is released from fuel by the combustion of the air-fuel mixture, and a turbine coupled to the compressor that is made to spin by the high pressure high temperature exhaust from the combustor. In order to increase the amount of power produced per unit (by weight or volume) of fuel consumed and increase the performance of the engine, the turbine inlet temperature i.e. the temperature of the hot gas products leaving the gas turbine combustor is increased by changing the fuel flow rate into the combustors and the amount of compression of the air entering the combustor. Consequently, the first component of the turbine, the nozzle guide vane faces high thermal loading which could structurally endanger vane life. The existence of complex secondary flows (leading edge vortex, passage vortex, corner vortices) near the junction of vane's leading edge and the turbine endwall to which the vane is connected to causes increased heat transfer at this point as opposed to other points on the vane surface. The aim of this work is to study through computational simulations how injecting high momentum fluid (air) near the leading edge junction to observe any changes to the secondary flow near the endwall. The angle at which this fluid is injected and the rate of injection of this fluid are, among others, the parameters varied in this study. The flow near the leading edge and through the vane passage is visualized and the pressures at the inlet and outlet of the test domain measured at each step to compute parameters which decide how further studies are designed. The ultimate aim of this project is to identify if injecting fluid through the endwall would prove useful in reducing the vortical flows near the endwall (thereby reducing the thermal load on the endwall).

ACKNOWLEDGEMENTS

I would like to thank my advisor Dr. Srinath Ekkad for his firm guidance and unbridled enthusiasm which have often reassured me in moments of doubt and uncertainty during my Master's thesis work. This work couldn't possibly have taken shape without his help.

I would like to express my gratitude to Dr. Scott Huxtable for letting me walk into his office at any time for a chat and lending a sympathetic ear whenever I needed one.

I would like to extend my thanks to Dr. Todd Lowe for teaching me about propulsion in my first ever course at Virginia Tech, and for willing to serve on my committee.

I would like to thank my lab mates both past and present, Kartikeya, Kris, David, Samruddhi, Prashanth, Bharath, Shubham, Sandeep, Suhyeon and Siddhartha for giving me great company in the lab.

I'd especially like to thank Sridharan and Jaideep for guiding me through every step of the way during my Master's thesis and for bearing the brunt of all my silly questions.

My friends have been a constant source of support these past two years and I couldn't thank them enough for it. Kaushik, Karthik, Shankar, Rahul, Anand and Balaji, here's to all the great times we've had in Blacksburg.

My parents have always been my pillars of strength. Their constant support and motivation have kept me sane all the way through grad school and helped me weather many a storm. Thanks Amma and Appa, for always being there for me!

TABLE OF CONTENTS

LIST OF FIGURES

LIST OF TABLES

NOMENCLATURE

D_h Hydraulic diameter [m]

D Hole diameter [m]

HTC Heat transfer coefficient [W/m2K] $= \frac{q''}{(T_{endwall} - T_{freestream})}$

p Pressure [Pa]

η Kinetic Energy loss coefficient $= \frac{(\dot{m}_{inlet} + \dot{m}_{hole\ inlet}) * \left[1 - \left(\frac{P_{outlet}}{P_{0,outlet}}\right)^{\frac{(\gamma-1)}{\gamma}}\right]}{\dot{m}_{inlet} * \left[1 - \left(\frac{P_{outlet}}{P_{0,inlet}}\right)^{\frac{(\gamma-1)}{\gamma}}\right] + \dot{m}_{hole\ inlet} * \left[1 - \left(\frac{P_{outlet}}{P_{0,hole\ inlet}}\right)^{\frac{(\gamma-1)}{\gamma}}\right]}$

M Mach number

MFR Mass Flow Ratio % $= \frac{\dot{m}_{hole\ inlet}}{\dot{m}_{inlet}} * 100$

ω Total pressure loss coefficient $= \frac{(P_{0,inlet} - P_{0,outlet})}{(P_{0,outlet} - P_{S,outlet})}$

T Temperature [K]

u Total fluid velocity [m/s]

X Streamwise length [m]

Y Pitchwise length [m]

Z Spanwise length [m]

C Axial chord [m]

S Vane span [m]

P Vane cascade pitch [m]

X_h Distance of hole from vane leading edge [m]

Subscripts

inlet Measured at inlet of computational domain

hole inlet Measured at inlet plane of hole

endwall Area averaged value at endwall

outlet	Measured at outlet of vane cascade

CHAPTER 1: INTRODUCTION

The continually increasing global energy demand has led to a drive to increase the power output of gas turbine engines, and higher turbine inlet temperatures are a direct consequence of this. In present-day gas turbines, the turbine inlet temperatures are higher than the maximum temperature that the first stage nozzle guide vane can withstand, thus causing increased thermal loads. The upper limit of the permissible turbine inlet temperature depends on the material strength of the gas turbine components. The leading edge end wall junction region of the first stage nozzle guide vane is of particular interest due to the complex flow field in the region. This occurs due to the interaction between the boundary layer and strong pressure gradients which results in the formation of leading edge horseshoe vortices. The leading edge horseshoe vortices form due to the separation of the inlet boundary layer at the saddle point of separation and subsequent rolling up of the boundary layer due to the radial total pressure gradient. These vortices split into pressure side and the suction side vortices at the leading edge. In vane cascades the pressure-side vortices migrate towards the suction side of adjacent vanes due to the crossflow resulting from the pitch-wise pressure gradient and form the passage vortex. The passage vortex is detrimental due to the fact that it causes the flow in the approaching endwall boundary layer to separate from the endwall and get swept towards the suction side, thus leaving a large section of the endwall to get exposed to large thermal gradients. This poses a problem from the film-cooling perspective as greater the portion of the endwall exposed to high heat transfer from the mainstream to the endwall, greater the mass flow of coolant required to cool the vane and endwall and ensure structural stability. The vane-endwall region poses a particular challenge due to the complex nature of the flow in this region that impedes attempts to cool the endwall through traditional cooling methods as the secondary flow structures, in addition to causing aerodynamic losses, also result in the relatively low momentum cooling fluid injected through the endwall being lifted off the surface, thus exposing the endwall to high temperatures and increased rates of convective heat transfer. According to Langston [1], secondary flows account for a third of all aerodynamic losses in turbine cascades. This study is driven by a desire to reduce the endwall aerodynamic losses cause by the secondary flow in a first stage nozzle guide vane passage. The endwall region in a turbine cascade is subjected to high thermal loading (high fluid temperatures, high temperature gradients) owing to the formation of secondary flows, primarily the leading edge horseshoe vortex upstream of the vane leading edge and a passage vortex within the vane passage. When the flow upstream of the

vane leading edge endwall junction within the incoming endwall boundary layer approaches the vane stagnation point, it decelerates and there occurs a corresponding rise in the local static pressure. As the mainstream flow velocity is much higher than the velocity in the endwall boundary layer, there is a greater deceleration in the mainstream flow as opposed to the flow in the near-wall boundary layer region. This causes a larger static pressure rise in the mainstream region above the boundary layer as opposed to the endwall boundary layer. The resulting span-wise pressure gradient causes the boundary layer flow to separate from the endwall and causes a vortex roll up by turning the flow towards the endwall, which is known as the leading edge horseshoe vortex. Eckerle and Langston [2] reported that this horseshoe vortex is typically confined to a region less than one boundary-layer thickness from the endwall. The point at which the approaching endwall boundary layer flow meets the near-wall reverse flow resulting from the vortex roll up is known as the saddle point. The location of the center of the horseshoe vortex and this saddle point depend on the diameter of the leading edge and the thickness of the oncoming endwall boundary layer([3], [4]). This leading edge horseshoe vortex splits into two legs near the saddle point, i.e. the pressure and suction-side legs of the horseshoe vortex, that are convected downstream by the mainstream flow into adjacent passages of the blade cascade on either side of the vane. Each of these legs has a sense of rotation that is opposite to that of the other leg. The pressure side-leg travels across the passage along the pressure side endwall separation line to the suction side of the adjacent blade owing to the pitchwise pressure gradient in the blade cascade. According to Denton[5] who discussed loss mechanisms in turbomachines, this cross passage migration of boundary layer fluid to the suction side is hastened by the increased blade loading. Meanwhile, the suction side leg travels from the stagnation region, around the blade leading edge to the suction side of the blade along the suction side separation line and further downstream close to the suction side. Downstream of the endwall separation/liftoff lines, a new thin boundary layer develops[6]. Flow from this boundary layer is continuously swept towards the suction side blade surface due to the pitchwise pressure gradient and the secondary flow near the endwall. Hence this endwall continues to remain very thin overall, and relatively thicker closer to the suction side. The pressure side leg of the horseshoe vortex encounters the suction side leg near the blade suction surface after which they combine to form a counter-rotating vortex pair which grows in size as it ingests more endwall boundary layer fluid. This passage vortex continues to travel downstream along the edge of the suction side/endwall junction and lifts off the endwall surface owing to the spanwise

pressure gradient near the suction surface of the blade. After it passes the trailing edge of the cascade, the passage vortex mixes out with the mainstream flow. In actual gas turbine operating conditions, the vortex roll up would cause high temperature fluid above the endwall to convect toward the endwall thus resulting in high local convective heat transfer coefficient values. A number of flow models have been previously proposed to depict the complex secondary flow structures in the endwall boundary layer region. Langston et al [7] studied the flowfield in turbine cascade passage and presented a model that described the three dimensional nature of flow in the endwall boundary layer region including the separation of boundary layer fluid as it approached the airfoil leading edge and the formation of a new relatively thin endwall boundary layer beyond the separation line of the incoming endwall boundary layer. They reported the vortical roll-up of the endwall boundary layer that resulted in the formation of the leading edge horseshoe vortex and the consequent formation of the passage vortex from the pressure side leg of the leading edge horseshoe vortex. As the passage vortex is guided by the cross passage pressure gradient across the passage to the suction side of the adjacent vane. The suction side-leg, with a sense of rotation opposite that of the passage vortex, travels downstream close to the suction surface until it meets the passage vortex becomes a counter rotating vortex within the larger passage vortex. The growth of the passage vortex as it propagated through the cascade passage was attributed to the entrainment of fluid from the mainstream, the newly formed thin endwall boundary layer and the suction side surface boundary layer. Sharma and Butler [10] provided a similar description of the flow structure in the endwall region, albeit with one primary difference. In their model, the suction side leg of the horseshoe vortex lifts off the endwall and orbits around the passage vortex instead of being surrounded by the passage vortex itself, as proposed by Langston et al [7].

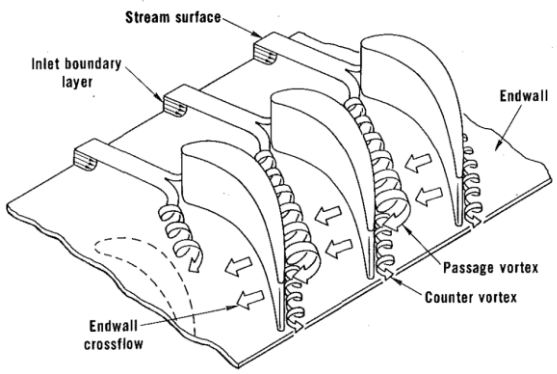

a) Three dimensional boundary layer separation in a turbine cascade as proposed by Langston[8]

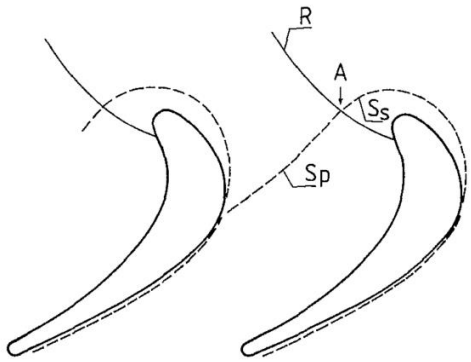

b) Schematic of endwall three dimensional separation lines (Sieverding [9]) based on work by Langston et al [7]

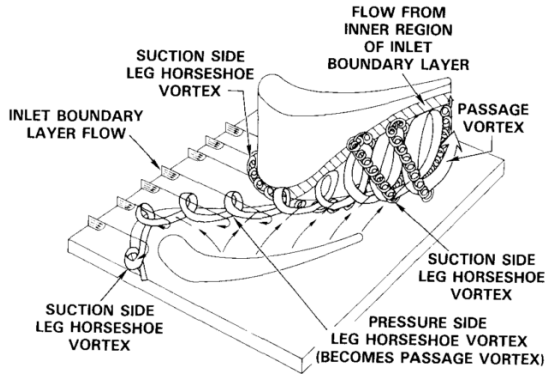

c) Cascade endwall flow structure as explained by Sharma et al [10]

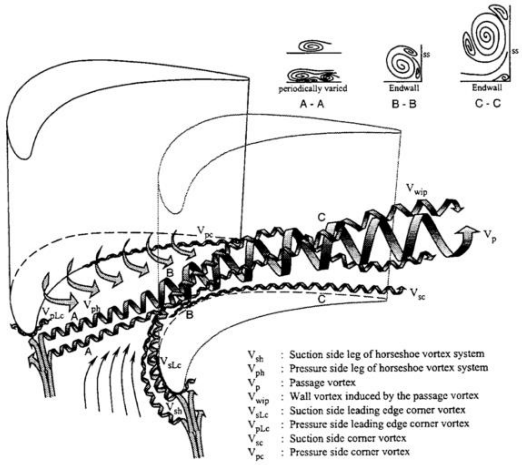

d) Interpretation of vortex flow pattern by Wang et al [11]

Figure 1: Endwall flow models proposed by (a) Langston (b) Sieverding (c) Sharma et al and (d) Wang et al

Sieverding et al [12] a similar vortex set-up with the suction side vortex wrapping itself around the pressure side vortex leg during their colored smoke visualization studies in a turbine blade cascade. Wang et al [11] also proposed a model similar to the one suggested by Sharma and Butler [10]. In addition, they also noticed corner vortices at the leading edge, and on the pressure and suction sides. Lastly, they noticed another small vortex induced by the passage vortex originating at the merging point of the pressure and suction side-legs of the horseshoe vortex. Goldstein and Spores [13] proposed a model in which the suction side leg of the horseshoe vortex lifts off the endwall at the separation layer and continues downstream adjacent to the passage

vortex. Like Wang et al [11] they too noticed the presence of the smaller corner vortices at the pressure and suction sides in addition to the main legs of the horseshoe vortex. Praisner et al [14] conducted experimental studies in a water channel to investigate the flowfield at the leading edge junction of a bluff body and noticed the presence of a smaller secondary vortex upstream of the larger primary (horseshoe) vortex and another tertiary vortex upstream of the secondary vortex. The secondary vortex, while not apparent in the time-mean streamline data, was characterized by a region of negative vorticity between the primary and the tertiary vortices. Kang et al [15] performed an experimental study to determine the effects of Reynolds number of the incoming flowfield on the leading edge vortex flowfield. They observed that the leading edge flow separation occurred further upstream for higher Reynolds numbers. They also observed that the roll up of the leading edge vortex was more pronounced for lower Reynolds numbers. Various control methods have been proposed to control secondary flow structures like the leading edge horseshoe vortex and the passage vortex. Some of them are a) Addition of a fence of the endwall ([16],[17],[18]) , b) Vortex Generators- The generation of a vortex rotating opposite to that of the passage/horseshoe vortex ([19], [20]) c) Contoured endwalls([21], [22]) d) Contouring of the leading edge of the blade that include the addition of leading edge fillets[23] and e) Endwall flow injection[24]. N. Sundaram et al [25] performed measurements in the endwall region upstream of a vane leading edge in order to study the flowfield upstream of the leading edge in the presence of the injection of coolant from the endwall through a combination of a 45° interface slot and 30° trenched holes, 17D and 4D upstream of the vane leading edge respectively. They found that the addition of a trench to the film cooling holes helped destroy a second vortex formed due to the coolant ejection, between the un-trenched holes and the vane leading edge. It was observed that the presence of the slot did not influence the flow approaching the vane stagnation region. In addition, they did not report changes to the leading edge horseshoe vortex in comparison to the baseline case without any coolant injection. Vortex was formed at X/C=-0.06. Levchenya et al [26] performed a RANS-based numerical simulation on a computational model that resembled the experimental configuration used by Praisner et al [14] . The computational results, which corroborated the findings of Praisner et al [14], showed the existence of a multiple-vortex system (i.e. the horseshoe vortex, the secondary vortex and the tertiary vortex in addition to the corner vortex) ahead of the leading edge of the bluff body. Hermanson and Thole [4] computationally studied the effect of inlet boundary layer thickness on leading-edge horseshoe vortex and other secondary flow

formation in the endwall region of a first stage stator vane. They concluded that a thicker boundary layer causes the leading edge horseshoe vortex to occupy a greater region of the endwall and the core of the horseshoe vortex is located farther away from the leading edge than a thinner boundary layer. Takeishi et al [27] experimentally and numerically investigated the interaction between a film cooling jet injected from the endwall upstream of a symmetric airfoil on the formation of a leading edge horseshoe vortex. They reported that the injection of insufficient amount of coolant reinforced the horseshoe vortex while the injection of a sufficient amount of coolant could weaken the downwash responsible for the formation of the horseshoe vortex by giving counter momentum, thus diminishing the size of the leading edge horseshoe vortex and pushing it closer to the leading edge. According to Oda et al [28] The location of the center of the horseshoe vortex is determined by the relative strengths of the oncoming boundary layer flow and the reverse flow caused by the vortex roll-up. They concluded that since sufficient injection of coolant weakens the downwash responsible for the horseshoe vortex, the oncoming boundary layer flow forces the center of the vortex closer to the blade leading edge. Thrift et al [24] experimentally investigated the interaction of fluid injected through a slot located in the endwall region upstream of a vane leading edge with the endwall boundary layer flow. They performed experiments for a range of flow injection angles (30^0, 45^0, 65^0, and 90^0) and two mass flux ratios (0.5% and 1%). For the higher MFR, they reported the presence of a time averaged vortex for the 90^0 and 65^0 slots that was larger than the vortex formed in the baseline case, while no presence of the vortex structure was detected in the 45^0 and 30^0 slot cases resulting from the stronger shear layers in the endwall region and a stronger upwash in the corner region. For the case with the lower MFR, a horseshoe vortex was noticed for all slot injection angles as the weaker injection was unable to counteract the strong turning of flow toward the endwall. Kost et al [29] conducted measurements of the flowfield in the near endwall region of a turbine cascade to study the effect of fluid injection (MFR: 1.3%) an upstream slot placed 0.2 axial chord lengths upstream of blade leading edge and observed that the ejection through the slot intensified the leading edge horseshoe vortex. There have been numerous studies on the control strategies to limit/ suppress the leading edge horseshoe vortex and to delay the migration of the passage vortex across the blade cascade. Some of these are the axisymmetric and non-axisymmetric endwall profiling/contouring, blade leading edge modifications (bulbs, fillets etc.,), endwall fences, vortex generators, and endwall injection. Previous flowfield studies on fluid injection through holes in blade cascade endwalls have generally accompanied film cooling studies

and the study of endwall fluid injection with the prime motive of controlling leading edge horseshoe vortices and passage vortices are few in number. The aim of the present study is to employ endwall fluid injection through a hole placed along a plane parallel to the incident flow immediately upstream of the vane leading edge in the vicinity of the saddle point and vane stagnation region. The effects of the of the endwall fluid injection on the flowfield at the leading edge and the vane passage are to be studied.

CHAPTER 2: COMPUTATIONAL METHODOLOGY

This section contains a summary of the computational domain, the grid used for computation, and details of the CFD solver, the turbulence model and the boundary conditions used for solving.

2.1 Computational Domain and Grid Generation

Figure 2 depicts the computational domain of the baseline case that was used for numerical simulations. The domain was intended to be representative of the vane cascade used for experimental heat transfer studies by Ravi et al [30], which consisted of GE E^3 vanes scaled up four times, axial chord, pitch, span, pitch and absolute flow angle 0.1349 m, 0.1778m, 0.1524 m and 73.1°. The present computational domain consists of one vane with half the vane passage on either side of the vane. The computational domain was aligned with the vane span in the Z-direction, the vane pitch in the Y direction and the vane axial chord in the X- direction. A symmetry boundary condition was used at the midspan plane to save on computation time. Translational periodicity was applied to the top and bottom planes of the domain in the pitchwise direction. A velocity inlet boundary condition was applied 0.75C upstream of the blade leading edge and a pressure outlet boundary condition was placed 1C downstream of the vane passage. A second velocity inlet boundary condition was also applied at the hole inlet in those cases with secondary fluid injection through a hole placed in the endwall. All the other surfaces were designated as no slip walls. All the holes had a diameter of 5mm and were inclined at either 30°, 90° or 150° to the endwall surface in the streamwise direction. The hole openings were placed at either 1d or 2d away from the leading edge along a plane parallel to the incident flow. A series of hole geometries which combined the 30° inclination angle to the streamwise with compound angles (30°,45°, 60° and 90°) in the Y-Z plane were also investigated. All the hole geometries that have been investigated are depicted in figure 3. The different planes that were used for studying the flowfield at the leading edge and through the vane passage have been highlighted in Figure 8. A hybrid mesh comprising tetrahedrons, pyramids and prism elements created using the ANSYS meshing software. The computational grid used for the numerical study is presented in figure **4**. The sizing functions in ANSYS meshing were made use of in order to refine the mesh close to the vane leading edge and trailing edge. The non-dimensional wall distance of y^+~1 was maintained on all physical surfaces in accordance with the near-wall requirement of the SST k-ω turbulence model. The number of prism layers used in the endwall region was 18 layers while those used near the vane surface and hole wall were 18 and 19 layers respectively. The growth rate used in all three

regions was 1.2, thus corresponding to a first cell height of 0.0125mm near the endwall, 0.0075mm near the vane surface, and 0.005mm near the hole wall.

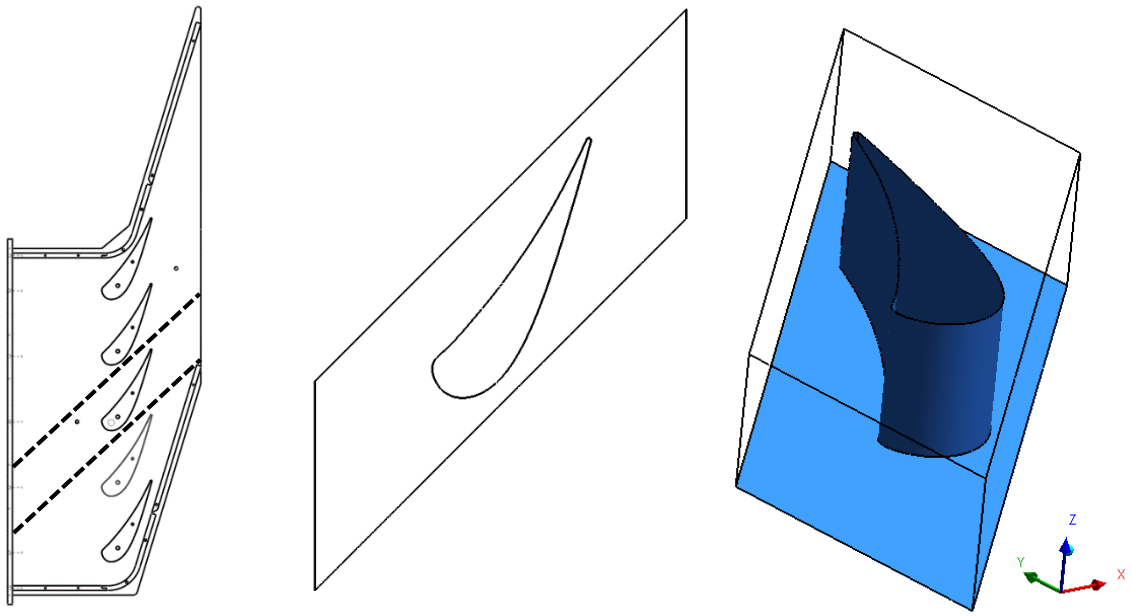

(a) (b) (c)

Figure 5: (a) Schematic of vane cascade used by Ravi et al [30] (b) 2D cut-section of computational domain (c) 3D view of computational domain

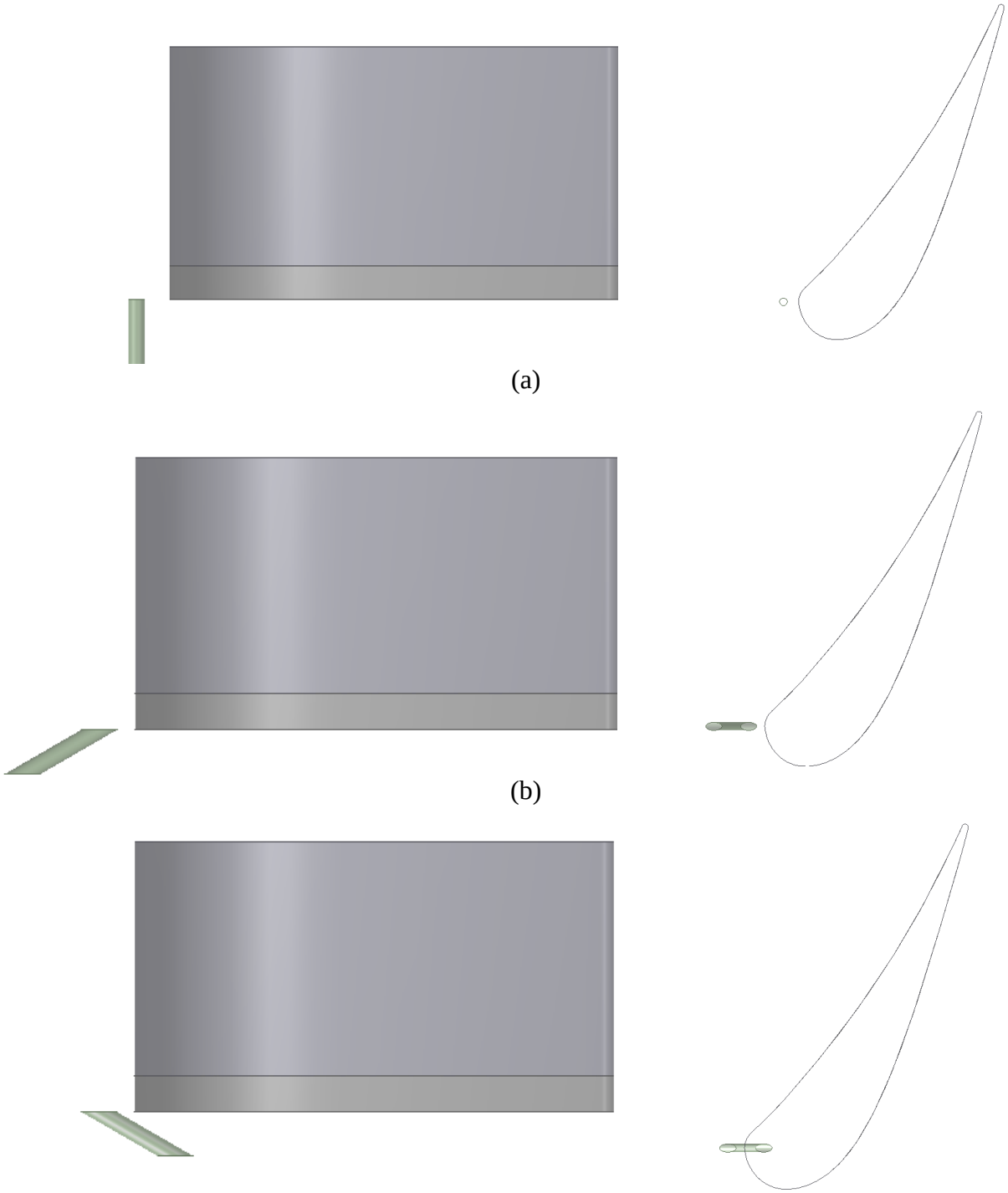

Figure 6: Top and side views of hole configurations at X=2D for (a) α=90° (b)α=30° (c)α=150

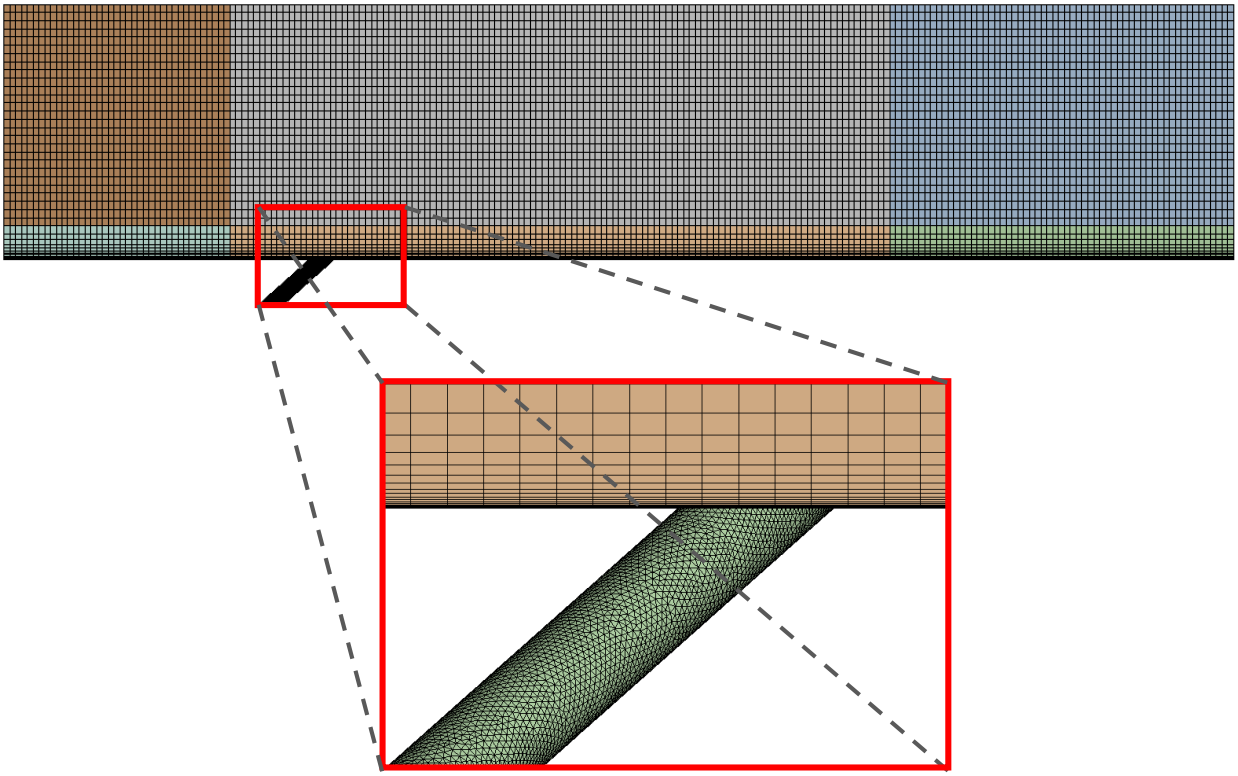

Figure 7: Numerical grid with endwall inflation layers highlighted

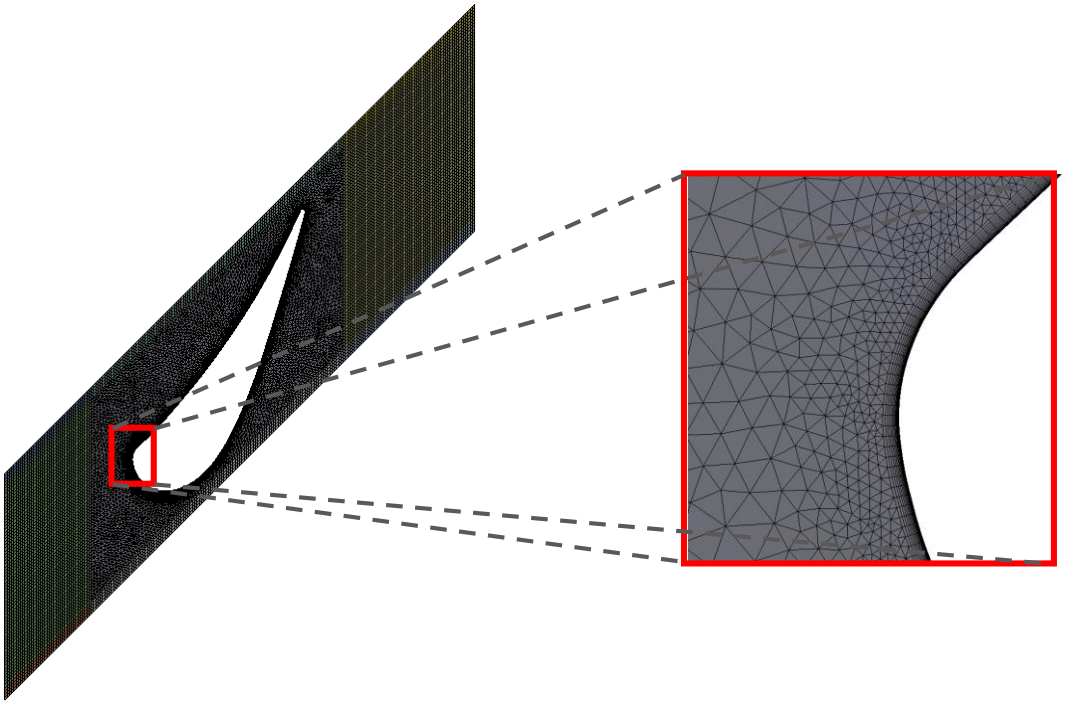

Figure 8: Numerical grid with vane inflation layers highlighted

2.2 Solver and Turbulence Model

The Steady state Reynolds Averaged Navier Stokes (RANS) equations for the mass and momentum conservation of an incompressible fluid were numerically solved using the ANSYS *Fluent* 15.0 solver. The numerical method used to solve the RANS equations in Fluent is a second order accurate Finite Volume discretization scheme. The SIMPLE method was used for pressure-velocity coupling. Previous studies using RANS-based models have been shown to accurately predict the secondary flow structures near endwalls in turbine vane cascades. The Shear Stress Model (SST) is a combination of the k-ω and k-ε models, with the k-ω model being used in the near wall region and the k-ε model farther away from the wall surface. The merits the SST model in handling adverse pressure gradients have been previously demonstrated. Also many studies ([26],[31],[32],[33] have shown that the SST model accurately predicts the flow field and heat transfer in the leading edge region, and the passage in a turbine vane cascade, which is essential for this study. Therefore we have used the SST k-ω model with automatic wall function treatment to model the turbulent flowfield.

2.3 Grid Independence Study and Convergence Criteria

A grid independence study was performed on the baseline case (i.e. without secondary injection) to establish the independence of the obtained numerical results of the mesh size used. The three different mesh sizes considered were 3.74 million, 6.98 million and 8.86 million. The parameter used to establish the grid independence was the total pressure loss coefficient, ω. The results of this study are shown in Table 1. The percentage difference in the Ω value between the coarsest and the finest mesh sizes was 5.2% while the same between the finest and the next finest mesh was 0.9%. Thus the grid with 6.98 million mesh elements was chosen as the mesh size for all the computations in this study. For cases involving change of geometry such as the change in hole location or orientation, appropriate mesh controls were made use of to approximately keep the mesh size constant. The computational solution was said to have converged if the residuals for the continuity, momentum and turbulent transport equations reached values lower that 10^{-5} and if the residual for the energy equation reached values below 10^{-8} (In select cases in which the energy equation was solved, in order to study the heat transfer from endwall). In addition to monitoring the residuals, the velocity and the temperature of the mainstream flow close to the endwall (in

cases where the energy equation was solved) were monitored at a number of locations in order to ensure a steady converged solution.

Table 1: Grid Independence Study

Elements(millions)	Total Pressure Loss Dynamic
3.74	0.078930492
6.98	0.082288401
8.86	0.083084893

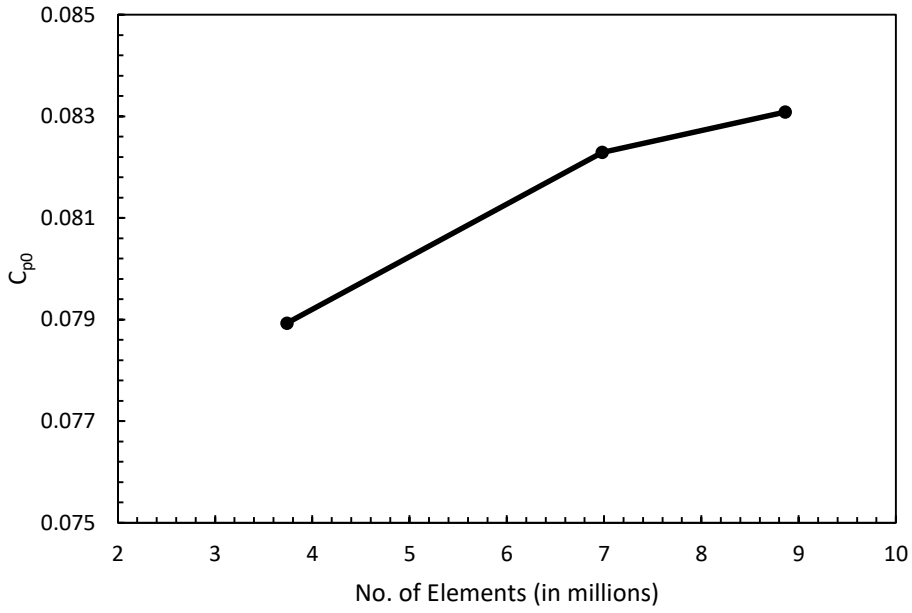

Figure 9: Total Pressure Loss Coefficient values for different mesh sizes

2.4 Boundary Conditions

The working fluid (air) was assumed to be incompressible with constant fluid properties. The flow was assumed to be steady, three-dimensional and turbulent. Uniform velocity of 12.1516 m/s (M=0.035) was specified at the inlet. The inlet velocity was calculated based on the inlet conditions used by Ravi et al[30]. At the hole inlet, a velocity inlet corresponding to the appropriate mass flow ratio was placed. The turbulence intensity value was retained at the default value of 5% for both the and the length scale used was 0.1 times that of the hydraulic diameter used at the inlet

(4*A/P). A pressure boundary condition was specified at the outlet with the pressure equal to the atmospheric pressure (Gauge pressure=0). A no-slip wall condition was specified at all the physical surfaces in the domain. A symmetry boundary condition was specified at the vane midspan while a periodic boundary condition was used on the other two surfaces. In certain cases where the heat transfer from the endwall was studied too, the endwall and the vane surface were held at the constant temperature of 300K while the mainstream inlet at 12.1516 m/s was at a temperature of 325K. All the other aforementioned boundary conditions remained the same.

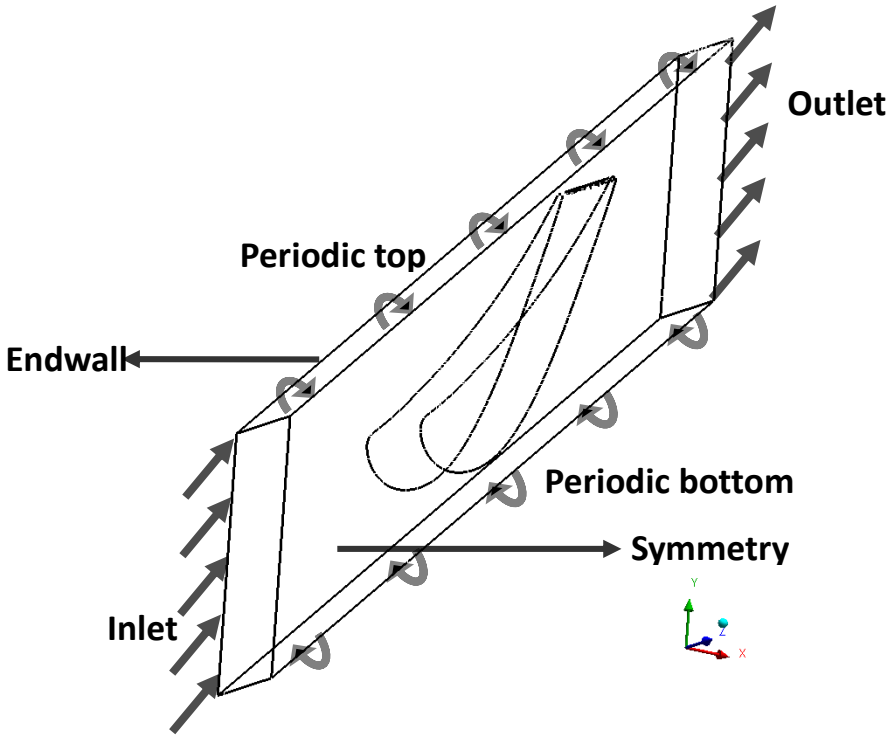

Figure 10: Schematic of boundary conditions applied on computational domain

CHAPTER 3: RESULTS AND DISCUSSION

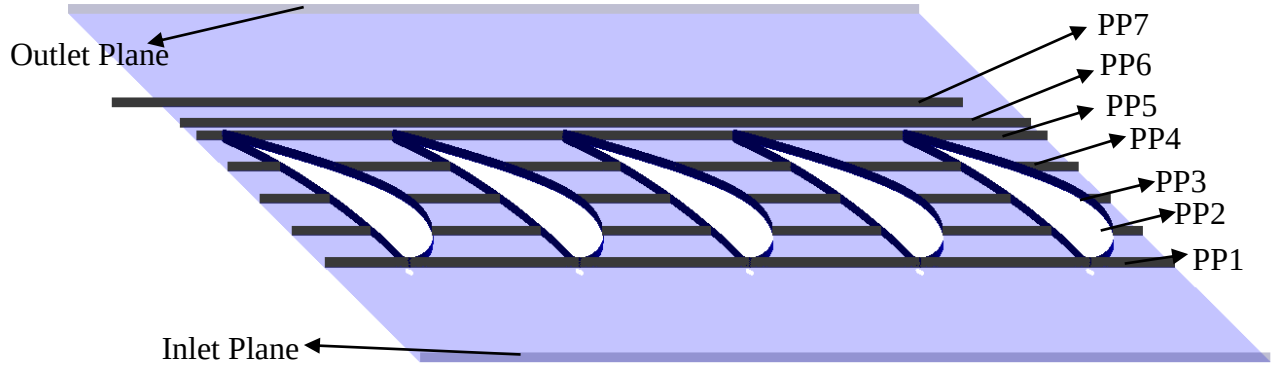

Figure 11: Depiction of planes PP1-PP7 at different axial locations, inlet plane, and outlet plane

The study was conducted in three parts in order to identify the ideal parameters at which all further cases were to be studied. First the flow through the baseline case with no endwall fluid injection was studied following which studies were conducted to identify two mass flow ratios to conduct further optimization studies. Following this, three different hole inclination angles with respect to the endwall (α) i.e. 30°, 90°, and 150° were studied in order to identify an inclination angle with which the aerodynamic losses would be minimized. After identifying a suitable hole inclination angle, the compound angle of the hole is varied to further minimize the aerodynamic losses by way of weakening/destroying the leading edge horseshoe vortex and delaying the of the adjacent blade. Progress of the pressure side leg of the horseshoe vortex i.e. the passage vortex to the suction side Planes perpendicular to the inlet flow direction, named PP1-PP7 (as shown in figure 12) located at the leading edge of the vane cascade, 25%, 50%, 75%, 100%, 110% and 125% of the axial chord distance of the vane from the leading edge through the vane passage and downstream of the vane passage in order to track the motion of the passage vortex and measure the total and static pressures for calculating the total pressure loss coefficient and the kinetic energy loss coefficient. For all studies, the leading edge vortex structure is visualized by plotting velocity streamlines and velocity vectors at the leading edge plane LE, which is parallel to the inlet flow and is incident upon the vane at the stagnation line. Total pressure contours are plotted on the plane to witness the momentum of the fluid jet of the fluid being injected through the hole upstream of the leading edge. The total pressure loss coefficient, ω was calculated at the exit plane of the

domain by using the following formula by following the same method as that used by Blot et al [34] and Denton[5] by normalizing the total pressure loss with the outlet dynamic pressure. The kinetic energy loss coefficient, η which in essence takes into account the loss of kinetic energy/momentum through the vane cascade due to the mixing of the injected fluid with the mainstream was calculated at the exit plane of the computational domain. Contours of the total pressure loss coefficient were plotted at the exit plane, which is located at the outlet of the domain, 1C downstream of the vane passage. Pitchwise averaged values of both the total pressure loss coefficient and the kinetic energy loss coefficient were found in order to study the span-wise variation of losses for the various cases studied. Mass averaged values of the same were studied in order to estimate the difference in losses between the baseline and the case being considered. In addition to the above parameters, the vane surface Mach number was plotted at the midspan region for each case to check how much the injected fluid alters the vane aerodynamics when compared to the baseline. The aim is to reduce secondary flow losses while not impacting the overall aerodynamics of the blade midspan too drastically.

3.1 Baseline Case

3.1.1 Leading edge vortex

Figure 9 shows the flow pattern in the near-wall region upstream of the vane leading edge. The region which extends upto 15% of the axial chord upstream of the leading edge and 4% of the blade span away from the endwall contains the leading edge vortical structures that occur due to the roll-up of the inlet boundary layer i.e. the primary horseshoe vortex HV with a clockwise sense of rotation, the smaller secondary vortex SV with an opposite sense of rotation as that of the primary vortex and the tertiary vortex TV with the same sense of rotation as that of the primary horseshoe vortex. There is also a small corner vortex at the junction region of the leading edge and the endwall.

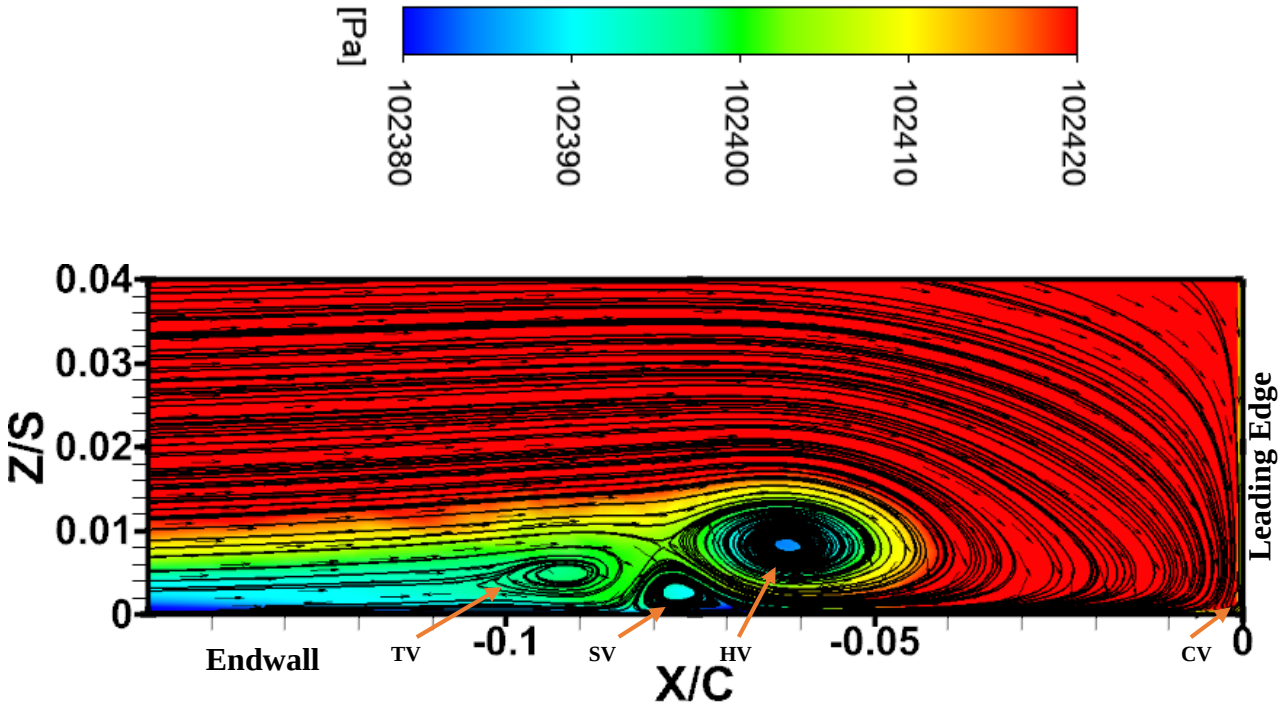

Figure 13: Leading edge velocity streamlines and vectors overlaid with total pressure (absolute) contours for the baseline case

These clearly match with the flow description presented by Praisner et al [14] which has been shown in figure 14. The saddle point of rotation which results from the confluence of two flows with opposing sense of direction, which are namely the near wall boundary layer fluid whose direction of flow has been reversed by the horseshoe vortex, and the mainstream flow that is approaching the leading edge region.

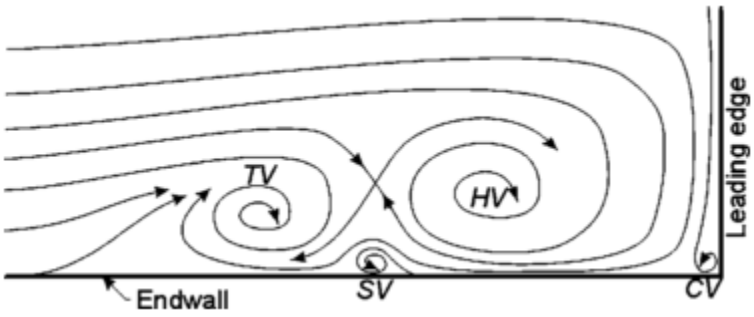

Figure 15: Schematic representation of the time-mean symmetry- plane streamline topology in a turbulent endwall flow[14]

3.1.2 Passage vortex

Figure 16 shows swirling strength plots for the baseline case with no endwall fluid injection. As explained by Sangston et al [35] and Chakraborty et al[36], swirling strength is a method of vortex identification, which quantifies the rate of rotation of local fluid elements. As opposed to vorticity which takes into account the rotation as well as shear of the fluid elements, this method doesn't take into account regions which possess an appreciable amount of vorticity but no spiraling movement of the fluid flow (i.e. shear layers as opposed to vortical structures). This method has previously been explained in detail by Zhou et al [37].

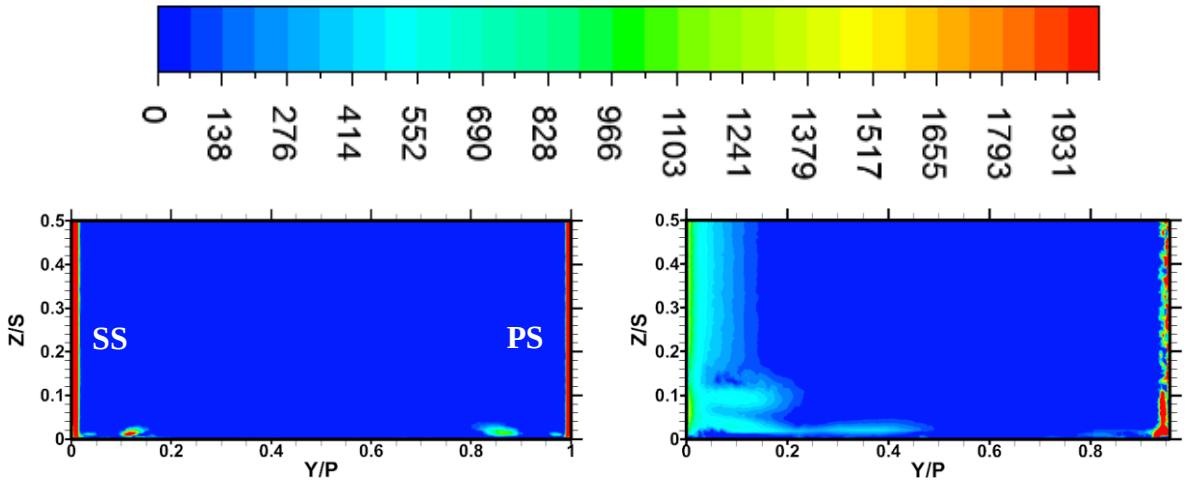

(a) PP1 **(c) PP5**

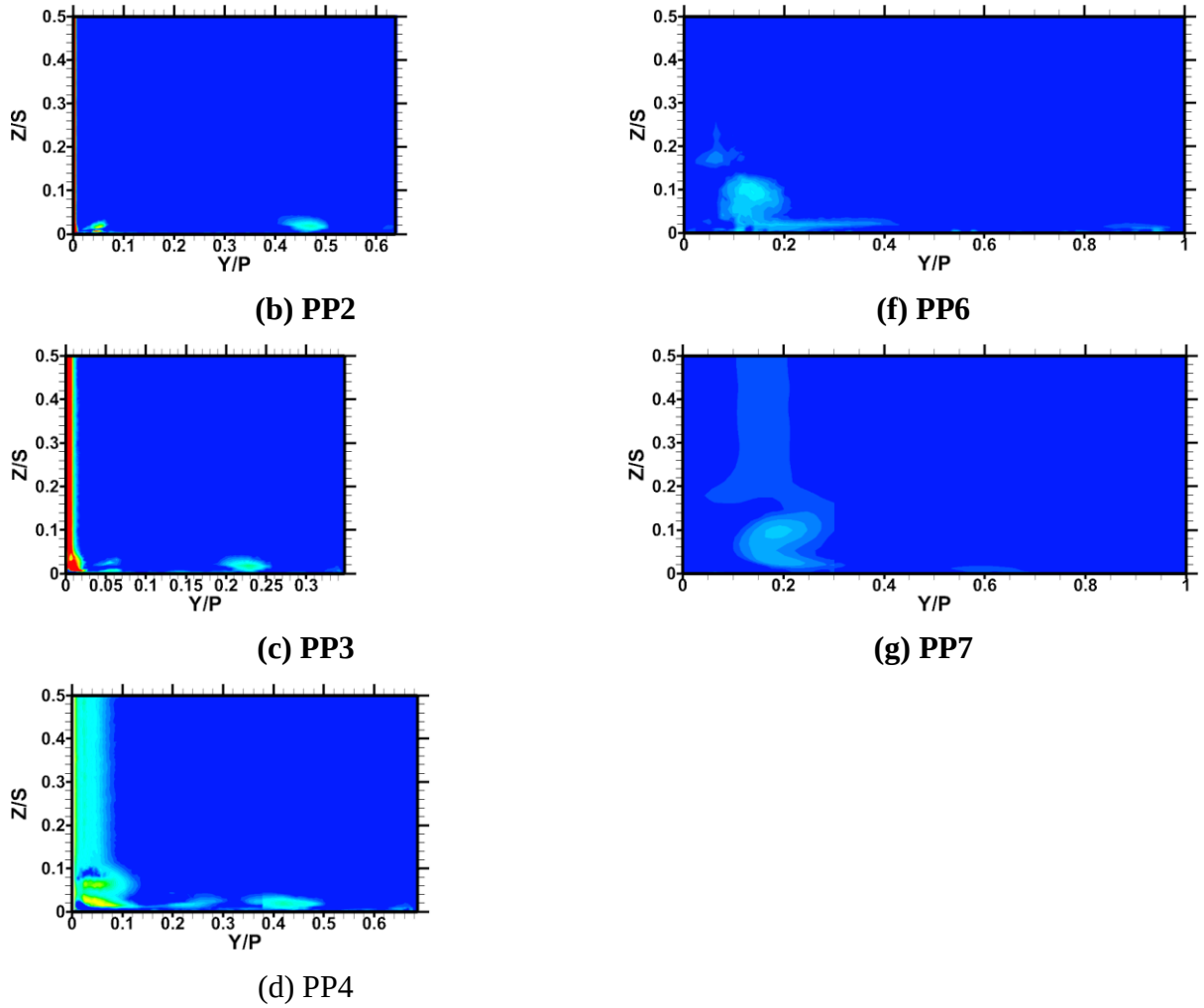

Figure 17: Swirling strength (s^{-1}) contours located at planes PP1-PP7 in the vane passage

The leading edge vortex as shown in Figure 18 is drawn by the stream-wise gradient into the vane passage. The leading edge vortex structure splits into the suction side vortex and the pressure side vortex One can clearly notice the movement of the pressure side section of the leading edge vortex from the pressure side of one blade bounding the vane passage to the suction side (these have been denoted by the acronyms PS and SS in the contour plot at the location PP1) of the adjacent blade bounding the vane passage. The vortex appears to be restricted to 5% of the total vane span. Meanwhile the suction side vortex, initially about 10% of the cascade pitch away from the suction side is convected much close to the suction side surface. Through the passage, as it ingests low energy fluid from the boundary layer region, it seems to grow in size (as can be seen from the plane PP4) and appears to rise from the endwall surface owing to the upwash close to the

suction side surface. The passage vortex can be seen to have completed the cross-over to the suction side vane at the exit of the vane cascade, as can be seen in the trailing edge plane PP5, wherein it encounters the suction side vortex that has begun to rise up from the endwall close to the suction side and appears to combine with it to form one region of swirling flow. This region of spiraling fluid appears to slightly mix out with the mainstream flow at 25% of the axial chord distance downstream of the vane cascade. This can be conjectured from the fact that the region of vortical movement of fluid appears to lack a defined boundary the further it moves beyond the exit plane of the vane cascade, as can be seen in planes PP6 and PP7 which are at located at 10% and 25% of the vane axial chord distance downstream of the vane cascade.

3.1.3 Exit plane loss coefficients

The exit plane EP coincides with the outlet of the computational domain, which is situated at 1C downstream of the vane cascade. This plane is used to visualize the total pressure loss coefficient contours and the kinetic energy loss coefficient contours. These are useful in identifying regions of high loss at the cascade exit. The total pressure loss coefficient values do not take into account the energy difference between the injected secondary flow and the

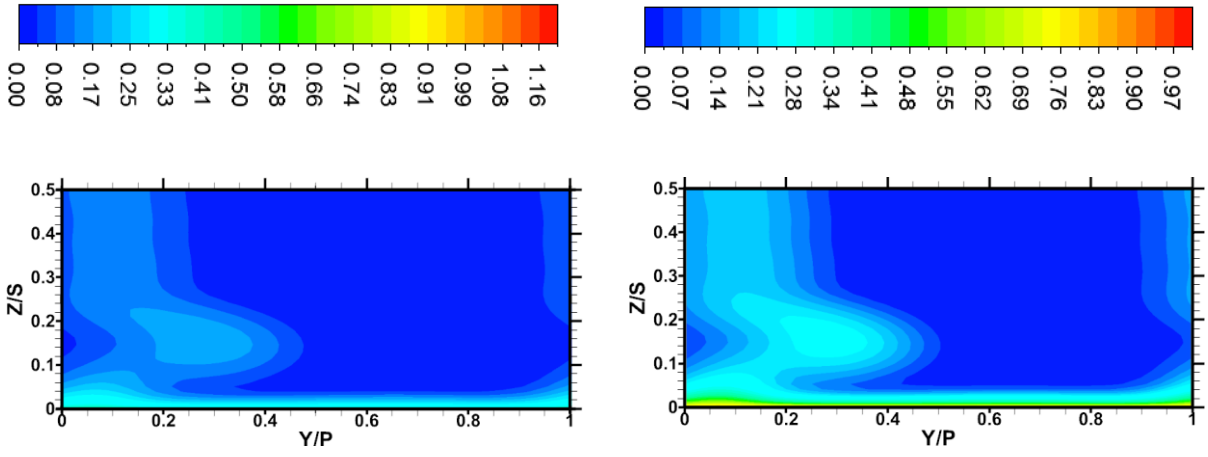

(a) Total pressure loss coefficient **(b) Kinetic energy loss coefficient**

Figure 19: Exit Plane Loss Contours for total pressure loss coefficient and kinetic energy loss coefficient

mainstream flow. This difference becomes more prominent as the mass flow ratio between the

injected flow and the mainstream flow increases (especially at blowing ratios greater than 1). The kinetic energy loss coefficient is an extension of the total pressure loss coefficient, but accounts for the energy of the coolant flow. This coefficient has been used by Raffel et al [38] in investigating the aerodynamic losses due to coolant ejection.

Figure 20 provides a graphic description of the total pressure loss coefficient and the kinetic energy loss coefficient plots for the baseline case. As can be seen from the plots in figure 21 and the pitch-wise averaged plots in figure 22, the losses reach a maximum value around 20% of the vane span in the mainstream region above the boundary layer region. In the near-endwall boundary layer region, the losses increase rapidly to reach a maximum value at the endwall. This is due to the velocity profile in the boundary layer region which leads to a corresponding total pressure profile, which reaches a minimum value in the total pressure at the endwall. This in turn causes the total pressure difference between the mass averaged total pressure at the outlet and the local total pressure to reach a maximum value at the endwall.

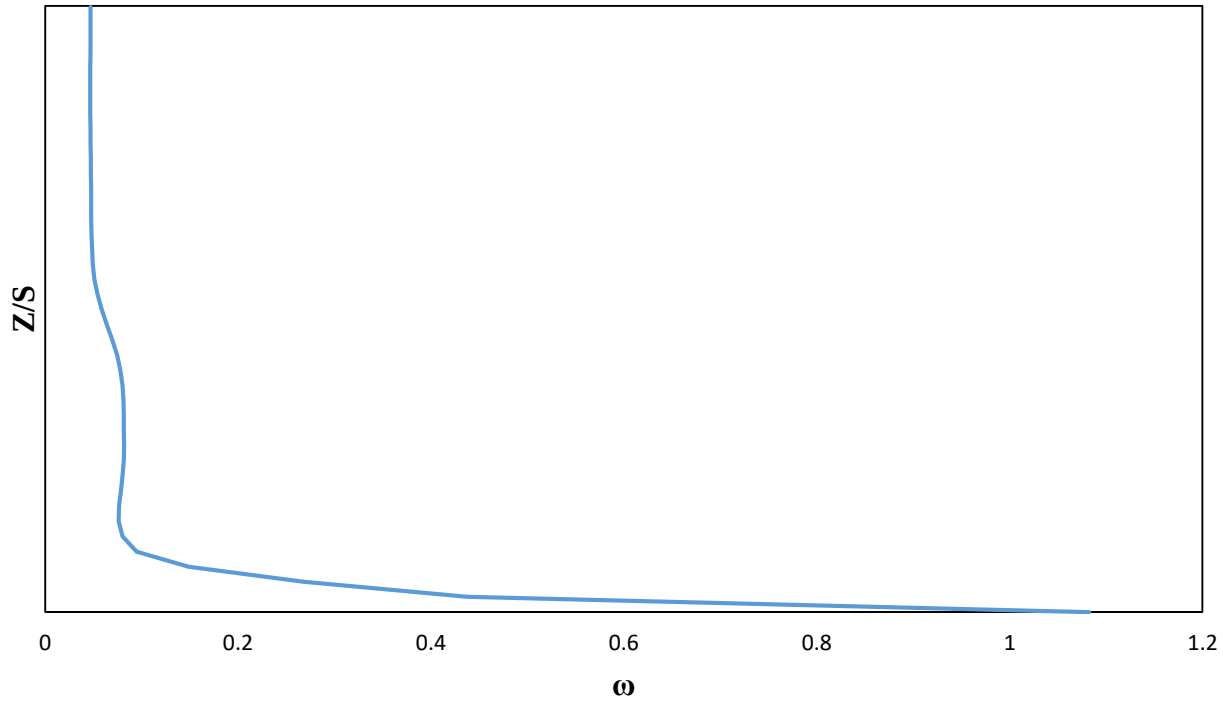

Figure 23: Pitchwise averaged total pressure loss coefficient for the baseline case

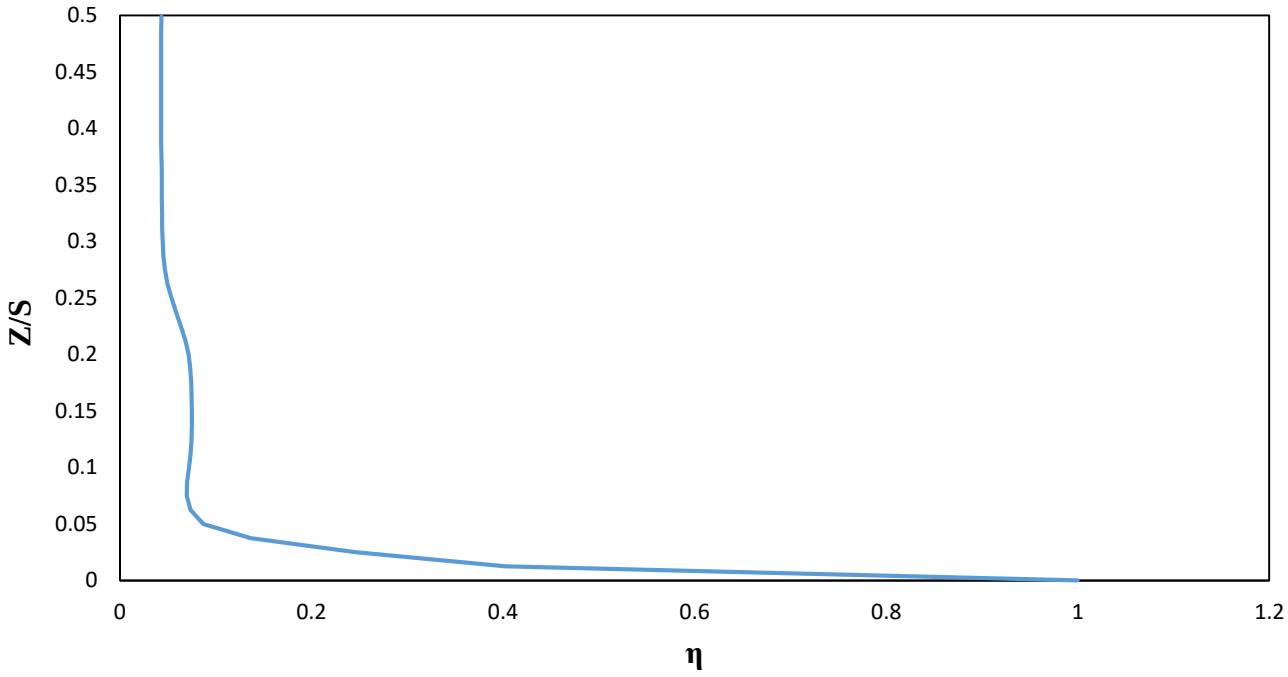

Figure 24: Pitchwise averaged kinetic energy loss coefficient for the baseline case

Table 2: Mass averaged value of total pressure loss coefficient and kinetic energy loss coefficient values

ω	η
0.0823	0.0760

Table 3 provides the mass averaged values of the total pressure and the kinetic energy loss coefficients. This provides us with a numerical value of the loss coefficients which we can use to compare cases against the baseline case, to look at enhancement or worsening of the secondary flow characteristics.

3.1.4 Vane surface Mach number profile

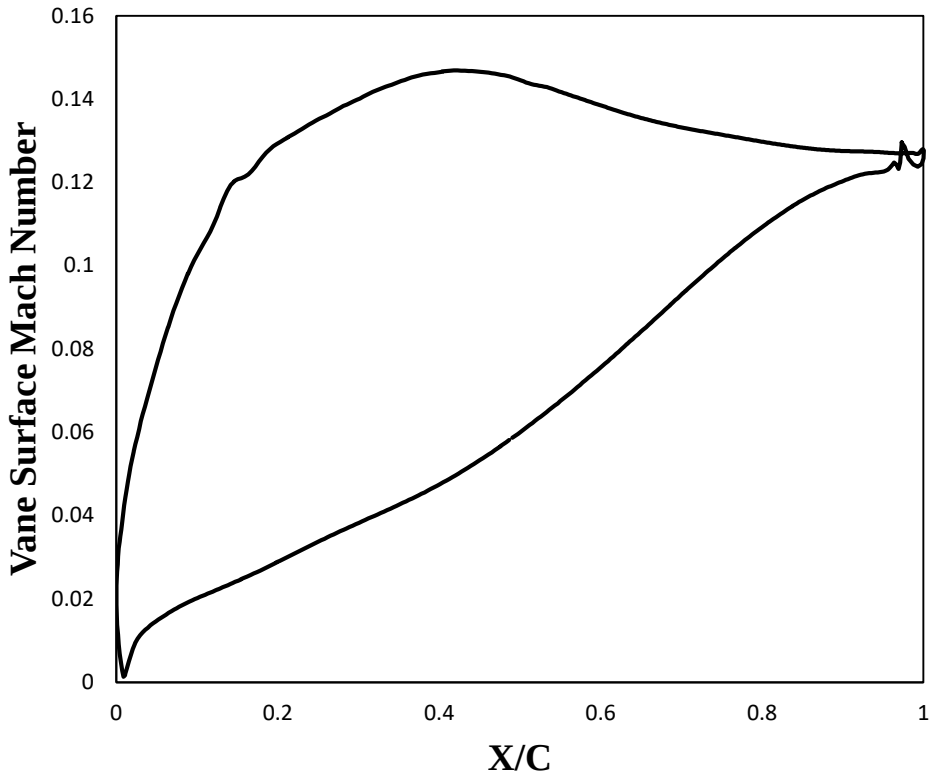

Figure 25: Midspan vane surface Mach number profile for the baseline case

Figure 26 shows the streamwise variation of the vane surface Mach number. The vane surface Mach number is essentially a plot of the ideal surface Mach number one would have without any losses resulting from wall friction and no-slip conditions. The quantity is calculated using isentropic flow relations. This plot has been used to determine by how much the vane surface Mach number profile has been altered by the addition of the fluid injected through the endwall. Thus by describing the vane surface Mach number profile and the loss coefficient plots, we have successfully established a baseline to compare which establish a baseline to compare all further cases against, in order to look at improvements/ diminishments.

3.2 MFR Study

In order to identify suitable mass flow ratios for further studies involving endwall injection, the cases described in the test matrices in tables 4 and 5 were considered. These two angles were mainly chosen in accordance with the ultimate aim of optimizing the hole-inclination angle. The hole exit and inlet are along a plane parallel to the endwall and the exit areas along the plane are the same for the 30° and the 150° hole inclination angles, while it is different for the 90° case. This area is of importance as the difference causes the hole inlet velocity to be different for the 90° case as opposed to the 30° and 150° cases. Thus for the same MFR values we get different blowing ratios for different hole inclination angles. Thus it was decided to perform an MFR study for both the 30° as well as the 90° case to find common ground in selecting MFR values to use for subsequent tests(i.e. that of optimizing hole inclination and hole compound angles).

Table 6: Test Matrix for MFR study of 30 degree hole

x/d	α	β	MFR
2	30	0	0.1
2	30	0	0.25
2	30	0	0.5
2	30	0	0.75
2	30	0	1

Table 7: Test Matrix for MFR study of 90 degree hole

x/d	α (deg)	β (deg)	MFR (%)
2	90	N/A	0.1
2	90	N/A	0.25
2	90	N/A	0.5
2	90	N/A	0.75
2	90	N/A	1

3.2.1 Leading Edge Vortex

The leading edge vortex was visualized by using velocity streamlines overlaid with total pressure contour plots in order to study the interaction of the leading edge vortex system with the injected fluid. Figure 27 shows the comparison of a number of cases with different MFRs for the 30° hole located at a distance of 2D from the leading edge along a plane parallel to the inlet flow direction.

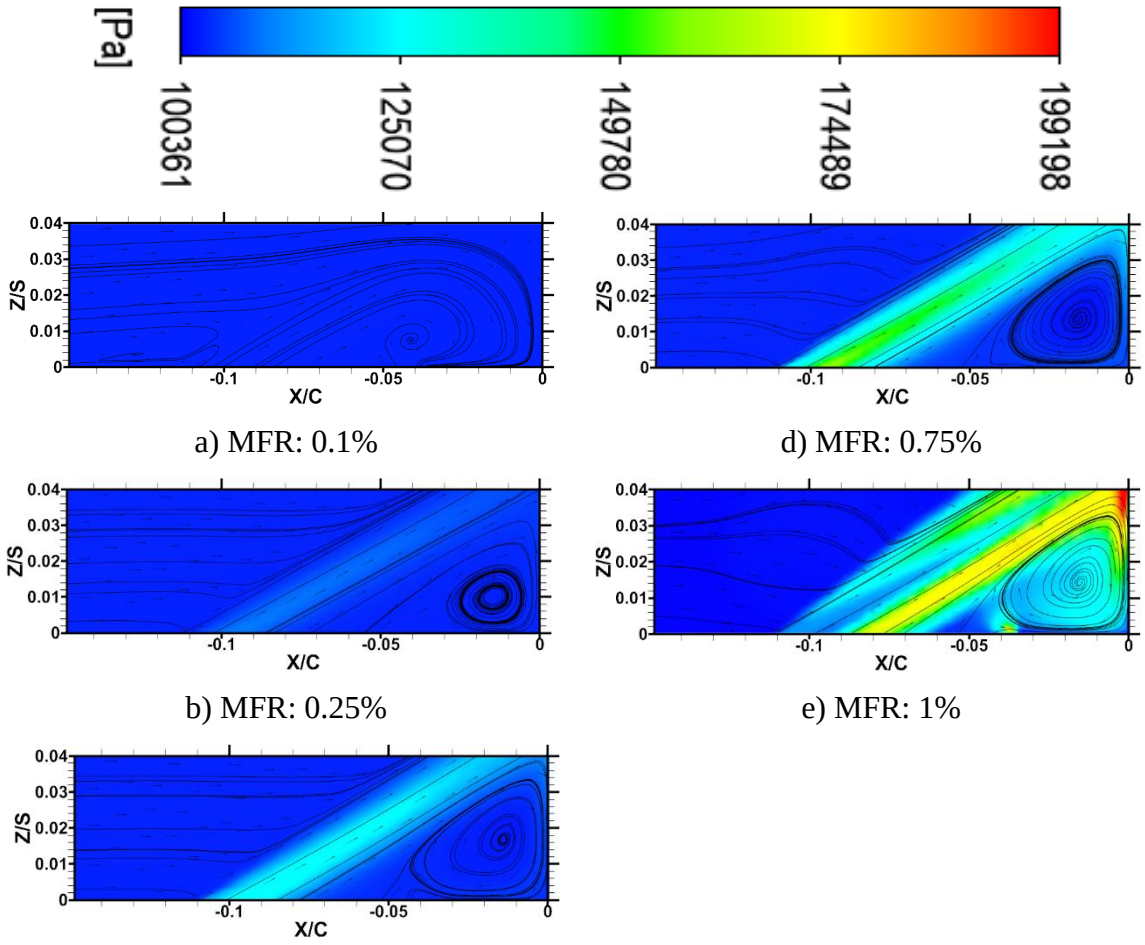

a) MFR: 0.1%

d) MFR: 0.75%

b) MFR: 0.25%

e) MFR: 1%

c) MFR: 0.5%

Figure 27: Leading edge velocity streamlines and vectors overlaid with total pressure contours at different MFRs α=30°, X=2D

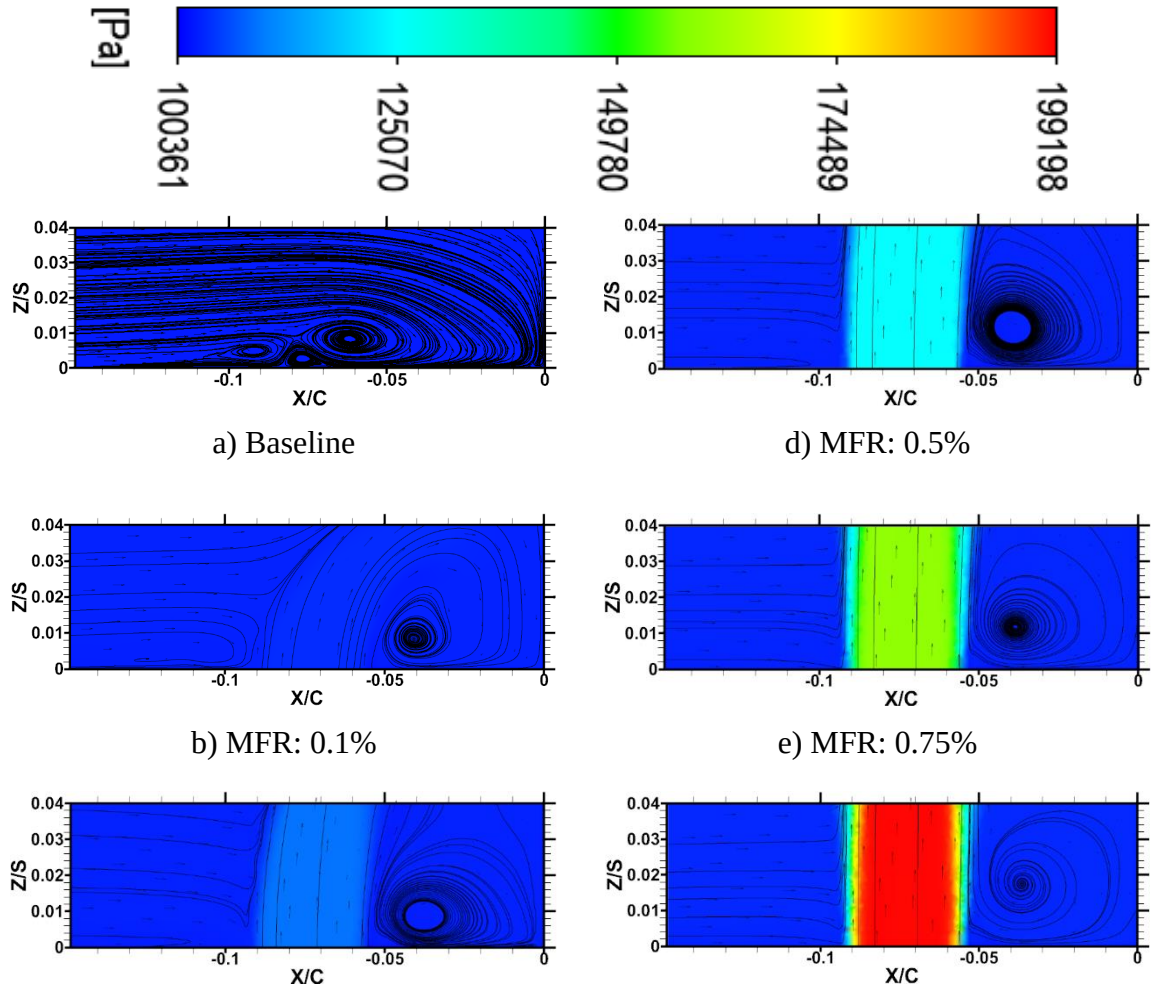

a) Baseline

d) MFR: 0.5%

b) MFR: 0.1%

e) MFR: 0.75%

c) MFR: 0.25%

f) MFR: 1%

Figure 28: Leading edge velocity streamlines and vectors overlaid with total pressure contours at different MFRs α=90°, X=2D

From the figure it can be seen that for the case with MFR=0.1%, there is not much of an effect on the leading edge vortex structure except for the fact that the weaker secondary vortex has been dissipated while fragments of the tertiary vortex remain. For the cases with MFR=0.25%-1%, the leading edge horseshoe vortex system has been dissipated by the injection of the secondary jet; however, a second vortex has been created in the region downstream of the hole because the high momentum jet blocks the mainstream flow and causes a low pressure region closer to the endwall junction thus creating a total pressure difference which drives the injected fluid back down to the surface thus causing a second vortex downstream of the film cooled hole. This effect has been observed by Sundaram et al [25] in studying the effect of trenched holes on film cooling flowfields. A similar effect was also observed in cases with 90° (Figure 28). As the MFR is increased from

0.25 to 1%, this effect is even more pronounced and the greater pressure differential between the stagnation region at the location of impingement of the jet, thus causing more injected fluid roll down to the surface thus causing greater velocity of the induced vortex. This can be seen

Thus from the leading edge flowfield study, it was possible to eliminate the 0.1% MFR case from further studies based on the fact that it did not aid the cause of eliminating the leading edge vortex structure. However, further investigation was required to draw conclusions regarding the selection of suitable MFRs.

3.2.2 Passage Vortex

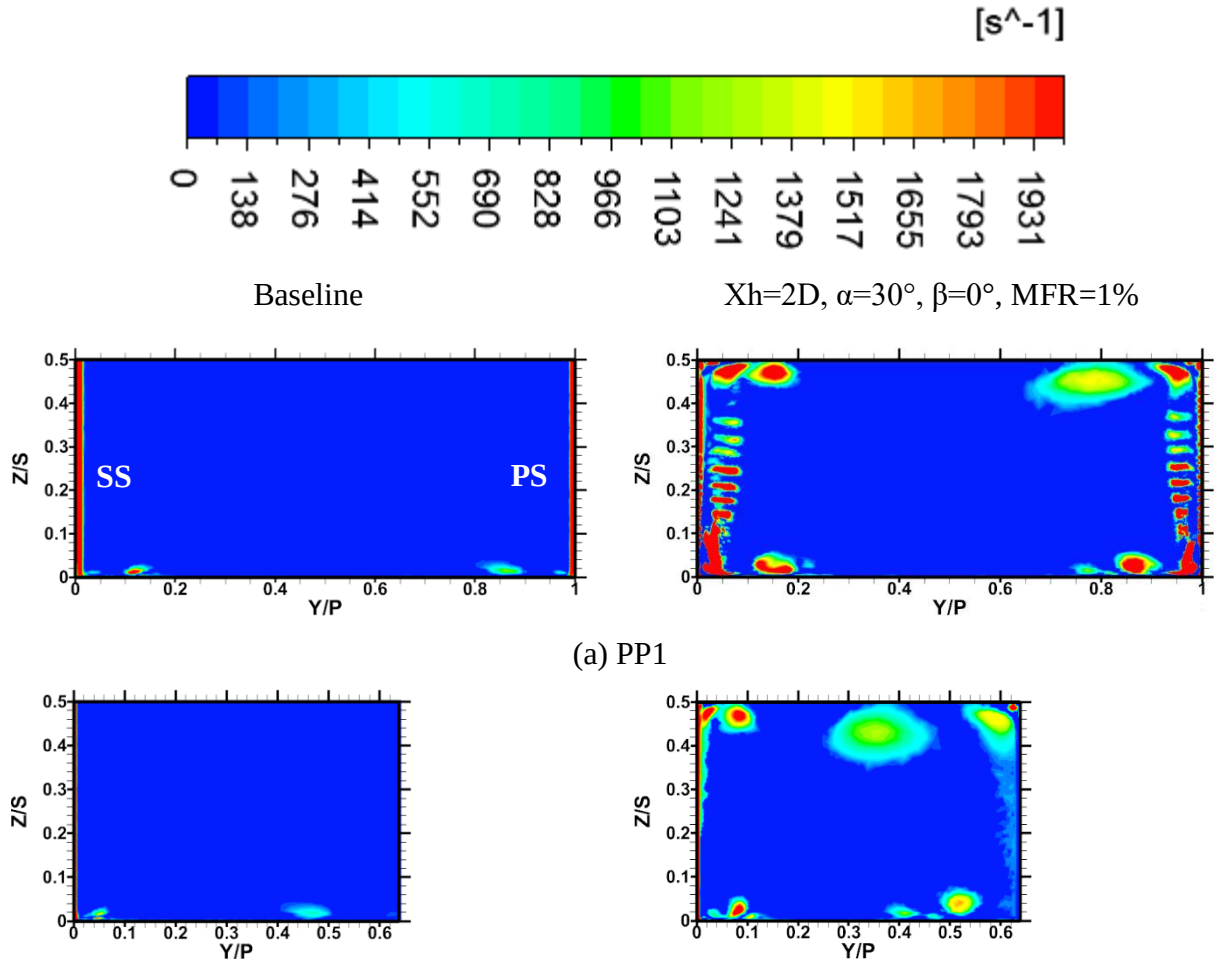

(a) PP1

(b) PP2

(c) PP3

(d) PP4

(c) PP5

(f) PP6

(g) PP7

Figure 29: Swirling strength contours located at planes PP1-PP7 in the vane passage

For the 30 degree hole inclination, the swirling strength contours plotted on planes PP1-PP7 for the cases MFR=0.1%-1% were compared against one another and against the baseline case. It was observed that in the cases MFR=0.1% and 0.25%, there was no change with respect to the secondary flow structure close to the endwall which reflected the ineffectiveness of the injected fluid. For the cases 0.5%-1%, the injected coolant appeared to have fragmented the pressure side leg of the horseshoe vortex into vortex filaments with the effect being more pronounced with the increase in mass flow ratio. In the cases with MFR=0.5% and 0.75%, one fragment of the vortex traversed the passage in the pitch-wise direction quicker than the other. Still, there was no large scale difference in the location (axial length) traversed by the entire passage vortex while being convected across the passage as compared to the baseline case (i.e. The passage vortex was completely convected across the passage at 100% of the vane axial chord distance downstream of the passage inlet) . In the case with 1% MFR, the effect was much more pronounced with the passage vortex being disintegrated into clear fragments with one fragment continuing close to the pressure side vane while the other fragment was swept by the cross passage gradient onto the suction side. Thus in the cases of MFR=0.5%-1%, there appeared to be a scope for further exploration in diminishing the passage vortex while no major difference was observed in the swirling strength/trajectory of the passage vortex in the entire range of the mass flow ratios tested.

3.2.3 Exit Plane Loss Coefficients

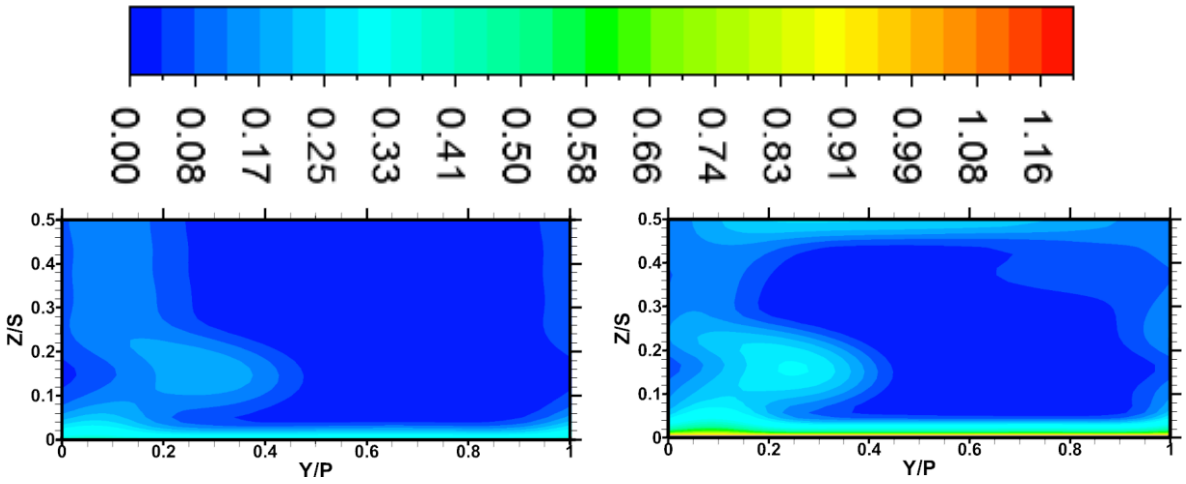

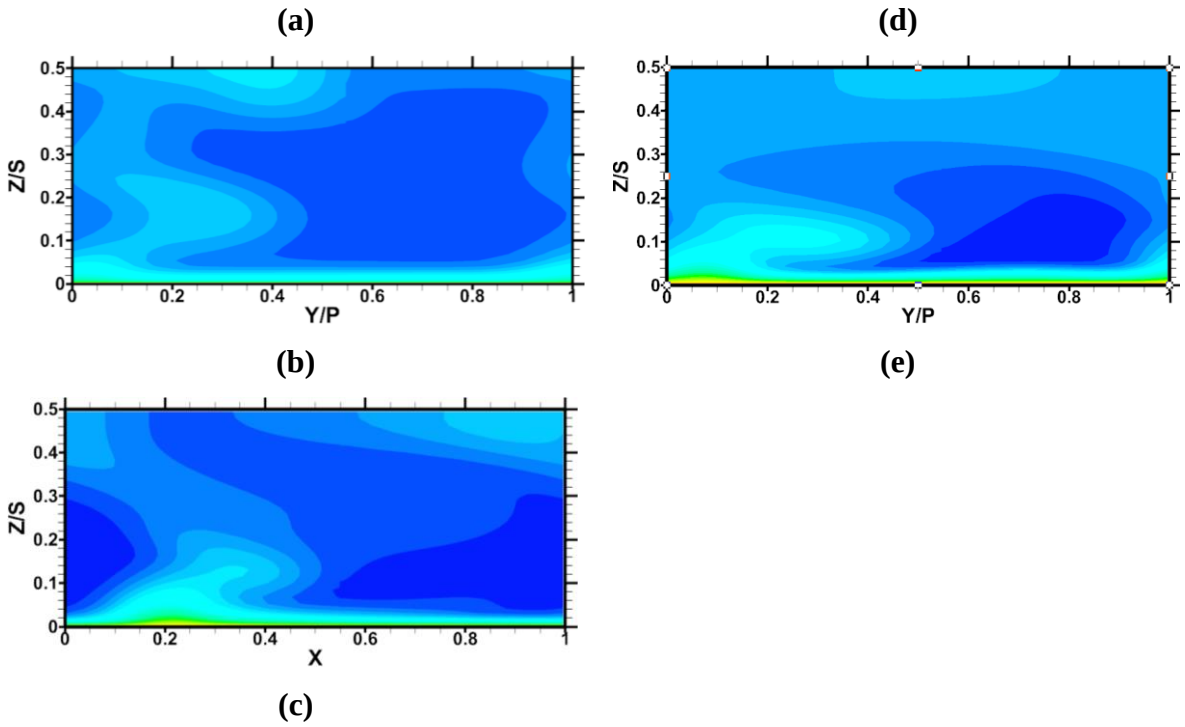

Figure 30: Total pressure loss coefficient contours for (a) Baseline case (b) α=30°, MFR=0.5% (c) α=30°, MFR=1% (d) α=90°, MFR=0.5% (e) α=90°, MFR=1%

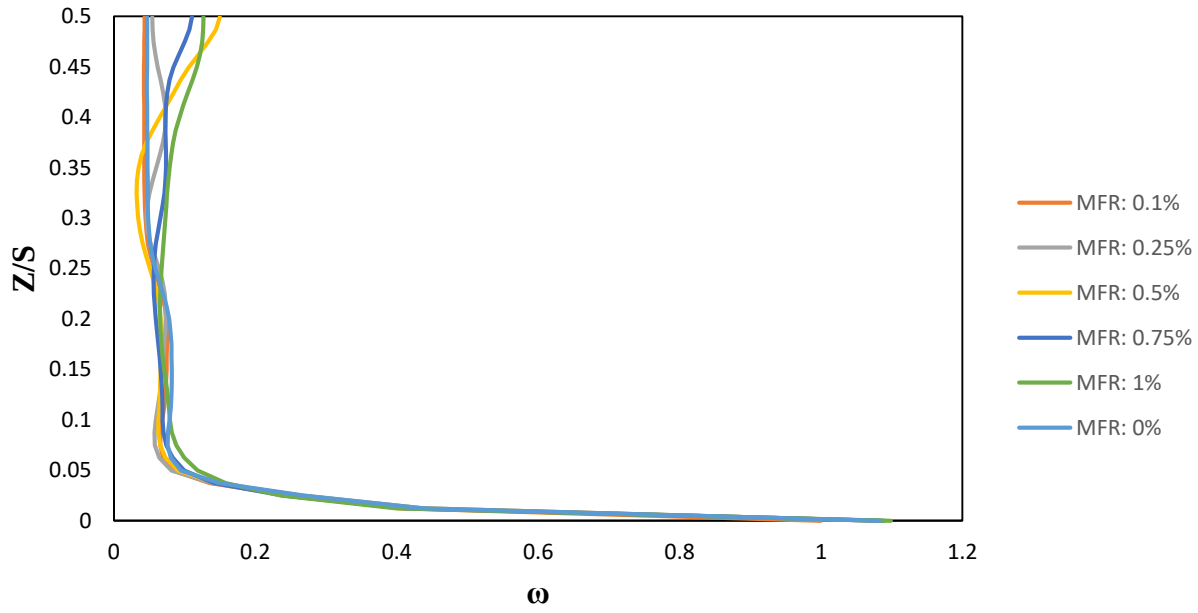

Figure 31: Pitch-wise averaged total pressure loss coefficient for different MFRs for α=30°

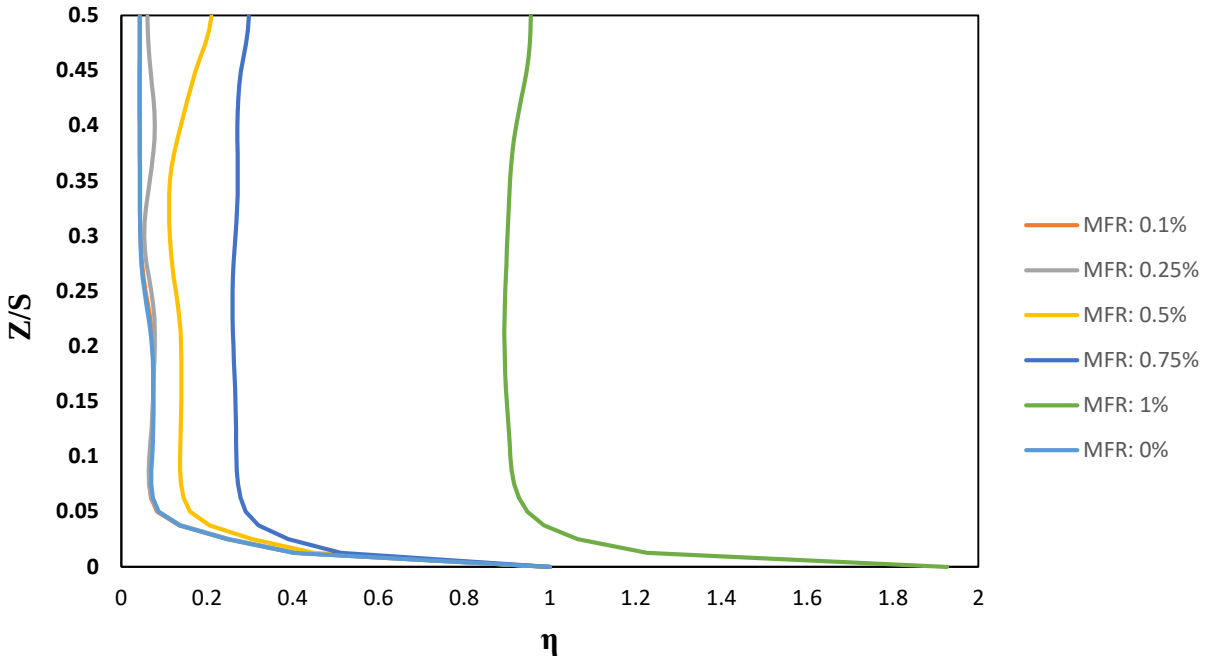

Figure 32: Pitch-wise averaged kinetic energy loss coefficient for different MFRs for α=30°

Table 8: Mass averaged total pressure loss coefficient and kinetic energy loss coefficient values for cases with α=30° and X/D=2 for different values of MFR

X/D	α (deg)	β (deg)	MFR	ω	% change w.r.t baseline	η	% change w.r.t baseline
N/A	N/A	N/A	N/A	0.0823	-baseline-	0.0760	-baseline-
2	30	0	0.1	0.0821	-0.2774	0.0757	-0.4217
2	30	0	0.25	0.0835	1.4163	0.0877	15.3842
2	30	0	0.5	0.0856	4.0534	0.1562	105.3762
2	30	0	0.75	0.0898	9.1712	0.2832	272.3802
2	30	0	1	0.0984	19.5750	0.4297	464.9989

Table 9: Mass averaged total pressure loss coefficient and kinetic energy loss coefficient values for for cases with α=90° and X/D=2 for different values of MFR

X/D	α (deg)	β (deg)	MFR	ω	% change w.r.t baseline	η	% change w.r.t baseline
N/A	N/A	N/A	N/A	0.0823	-baseline-	0.0760	-baseline-
2	90	0	0.1	0.0818	-0.6463	0.0753	-0.9761
2	90	0	0.25	0.0814	-1.0210	0.0795	4.5385
2	90	0	0.5	0.0875	6.3487	0.1157	52.1255
2	90	0	0.75	0.1226	48.9823	0.2102	176.3837
2	90	0	1	0.1456	76.9377	0.3202	320.9826

The total pressure loss coefficient contours and the kinetic energy loss coefficient loss contours were compared against the baseline case. From the loss contours and the pitch averaged and mass averaged values, a suitable conclusion could not be drawn primarily due to the fact that as the mass flow rate increased, the losses increased and at no particular mass flow ratio was there an appreciable change in the loss values due to a change in the flow structure. These trends were echoed in the hole with 90° inclination (See Appendix).

Using the patterns observed in the path of the passage vortex using the swirling strength plots, the range of mass flow ratios to be further studied was decided as MFR=0.5% to 1%. In order to save on computational time and because of the lack of much distinction between the results of the MFR=0.75% case from other two MFR values, two mass flow ratios chosen were 0.5% and 1%.

3.2.4 Vane surface Mach number plots

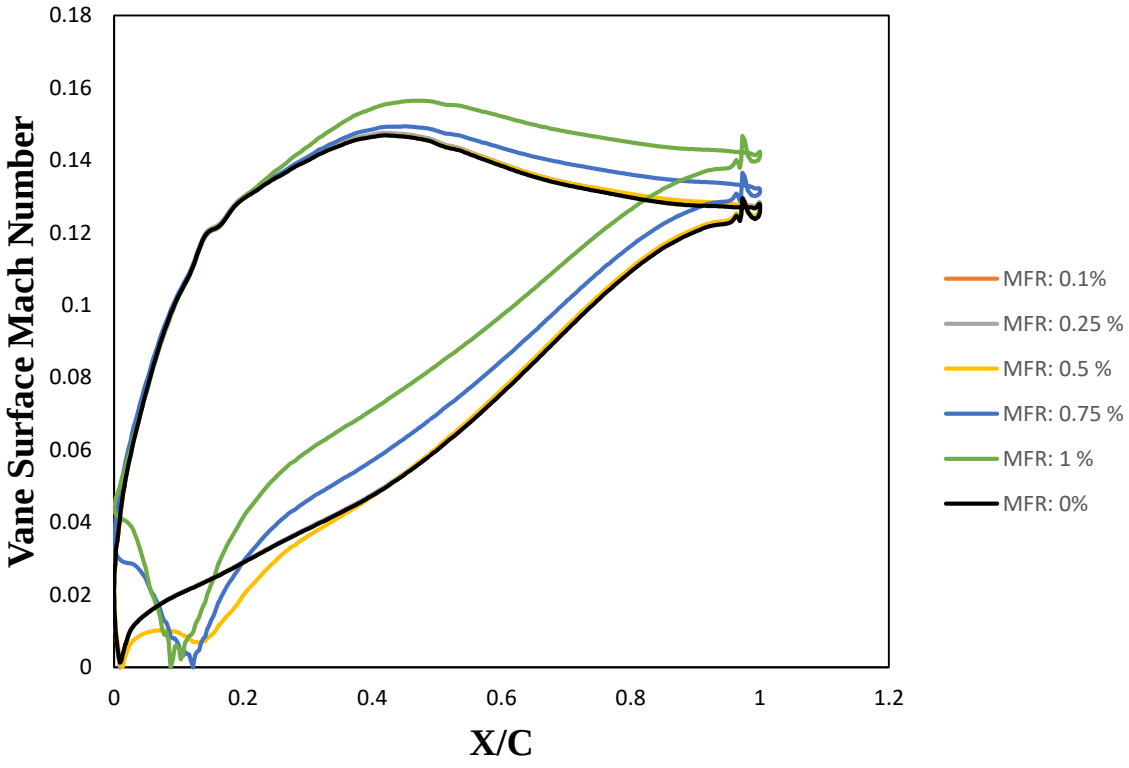

Figure 33: Midspan vane surface Mach number distribution for 30° hole

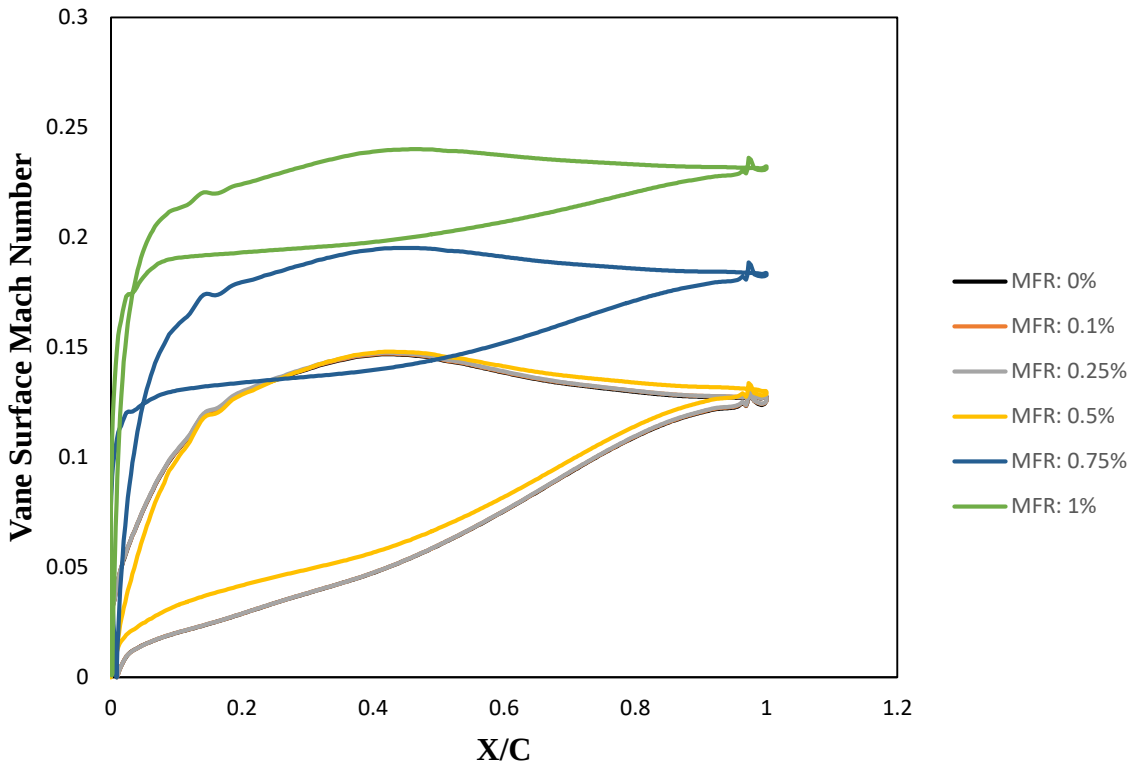

Figure 34: Midspan vane surface Mach number distribution for 90° hole

From the above vane surface Mach number in figures 35 and 36 at the vane midspan, it can be noticed that for the 30° streamwise inclination angle, for all of the mass flow ratios, there is no shift from the surface Mach number profiles on the suction side until an axial chord location of 0.25 C downstream of the leading edge of the vane. Downstream of this point, the vane surface Mach number profiles are similar to the baseline case for low mass flow ratios (0.1%, 0.25% and 0.5%) while for the higher mass flow ratios (0.75% and 1%) the suction side surface Mach numbers tend to be higher. On the pressure side too, a similar trend of the surface Mach number variation was noticed. For the 90° case, it could be noticed from figure 25 that there are major aerodynamic shifts for the blade with respect to the vane surface Mach number profiles in that both the pressure side as well as suction side Mach number profiles are higher that the baseline case for the higher mass flow ratio cases as opposed to the lower mass flow ratio cases (0.1%, 0.25%, and 0.5%) which almost completely trace the Mach number profile of the baseline case of 0% MFR.

3.3 Alpha Study

Table 10: Test matrix for Alpha study

x/d	α (deg)	β (deg)	MFR (%)
1	30	0	0.5
1	90	0	0.5
1	150	0	0.5
1	30	0	1
1	90	0	1
1	150	0	1
2	30	0	0.5
2	90	0	0.5
2	150	0	0.5
2	30	0	1
2	90	0	1
2	150	0	1

In order to identify the ideal inclination of hole angle, studies were conducted to compare the effect of changing the angle of inclination at 3 different hole inclination angles(30°,90°, and 150°) at 2 different hole locations(X=D and 2D) at 2 different mass flow ratios(MFR=0.5% and 1%). In order to make comparisons simpler, the list of test cases was classified into low MFR cases and high MFR cases, and each of these was classified based on distance of the hole from the leading edge (X=D and X=2D). This resulted in four subsets of test cases.

3.1.1 Leading edge Vortex

In order to study the aerodynamic performance of the different streamwise inclination angles to be tested based on the selection of MFRs in the previous study the leading edge flowfield was

simulated and the velocity streamlines and vectors were visualized. These were overlaid with total pressure contours in order to clearly see the fluid jet injected through hole in the endwall. From the velocity vectors and streamlines, one could notice the fact that the horseshoe vortex. For the case with α=30°, the flowfields were similar to those observed in the MFR study for the same mainstream inclination angle. One commonality with respect to all the cases tested in the alpha study for alpha=30 degrees was that the leading edge horseshoe vortex was uniformly absent in all of them. Also evident in all the cases was the presence of a secondary vortex induced due to a low pressure region induced underneath the jet mainstream near the endwall. This vortex occupied a greater region in case of the X/D=2 case as opposed to the X/D=1 case, regardless of the MFR, thus showing that the larger the low pressure region, greater the size of the vortex (though not necessarily the speed of rotation of the vortex).

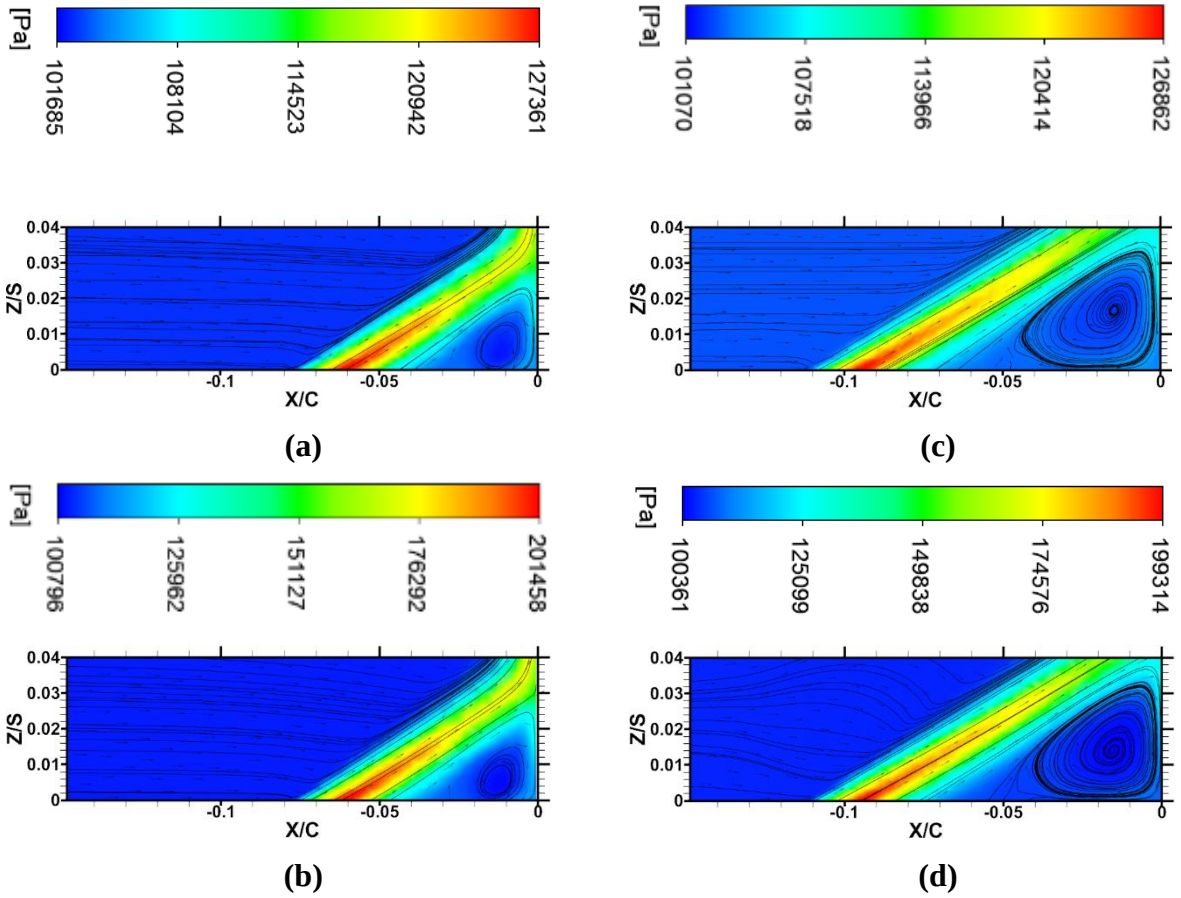

Figure 37: Leading edge vortex streamlines and velocity vectors overlaid with total pressure contours for a)X=D,0.5%MFR b)X=D,1%MFR c)X=2D, 0.5% MFR d) X=2D, 1% MFR

For the case with the 90 degree streamwise inclination angle, the leading edge vortex was visibly absent in all of the tested cases barring the high momentum injection (MFR=1%) at the hole position X/D=1. This was because the high velocity fluid acted as a physical barrier and the flow mechanics causing the leading edge horseshoe vortex caused the vortex to form just as in the case with no injection. The position of core of the vortex was the same position as before, i.e. 0.05 C upstream of the vane leading edge. Also noticeably, the size of the induced vortex in (a), (c), and (d) in Figure 30 was greater with greater distance from the endwall of the jet injected.

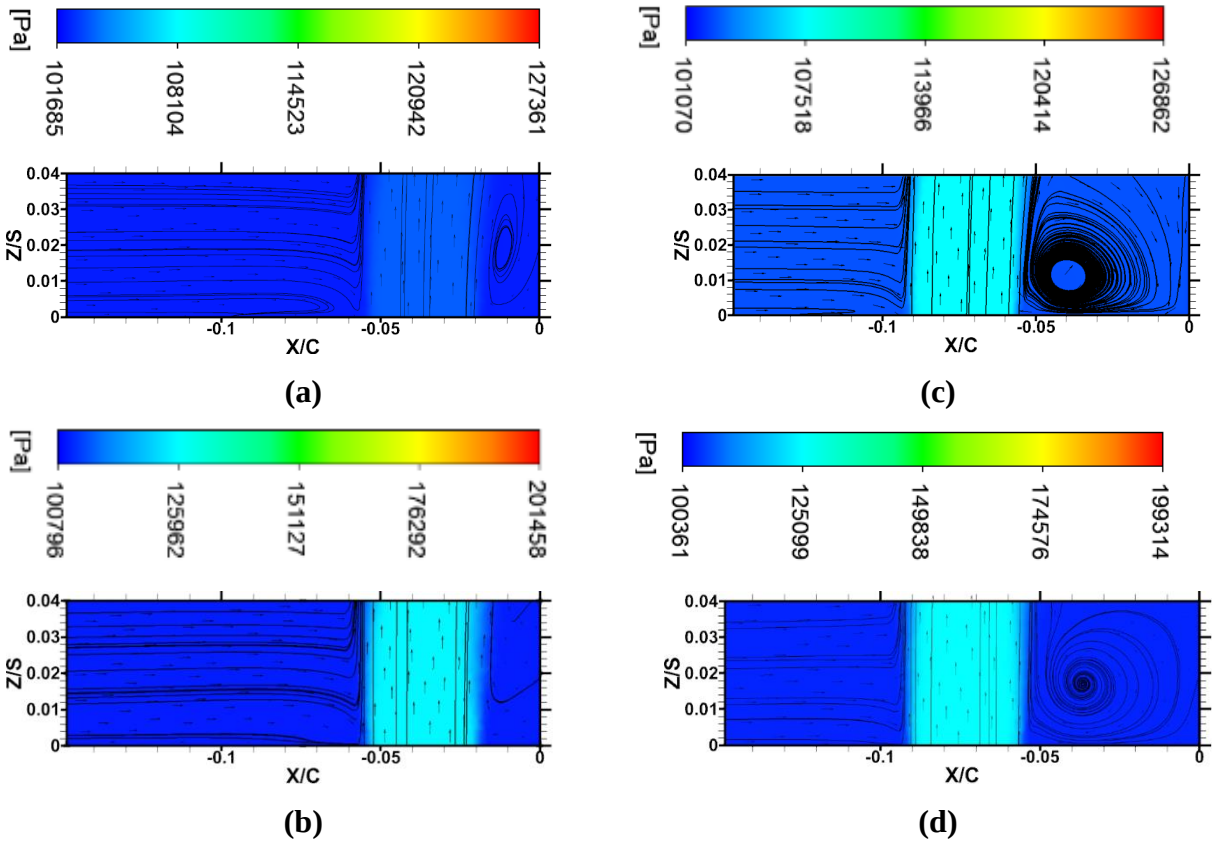

Figure 38: Leading edge vortex streamlines and velocity vectors overlaid with total pressure contours for α=90° a)X=D,0.5%MFR b)X=D,1%MFR c)X=2D, 0.5% MFR d) X=2D, 1% MFR

For the case with 150°streamwise inclination with the jet appearing to pointing in the opposite direction as the mainstream flow, there appears to be no leading edge vortex for the low momentum cases in either hole location, due to the fact that there is no drastic pressure change near the leading edge unlike in previous cases where a spanwise pressure gradient was caused at the leading edge due to the flow from the jet having a high dynamic component which was converted to a static component upon impingement and the relatively lower pressure closer to the endwall/leading edge

junction drawing portions of the fluid down to the into a spiraling motion. However, for a high momentum case, as can be seen in Figure 39 (b) and (d), the high flow velocity tends to entrain flow from above the jet down to the endwall due to the high velocity. This tends to cause another induced vortex albeit in the direction opposite that of the induced vortex caused in the 30 degree streamwise inclination angle which implies that the vortex was created by a spanwise component of velocity rather that a streamwise component, which further affirms the proposition that the fluid entrained by the jet induced the corner vortex.

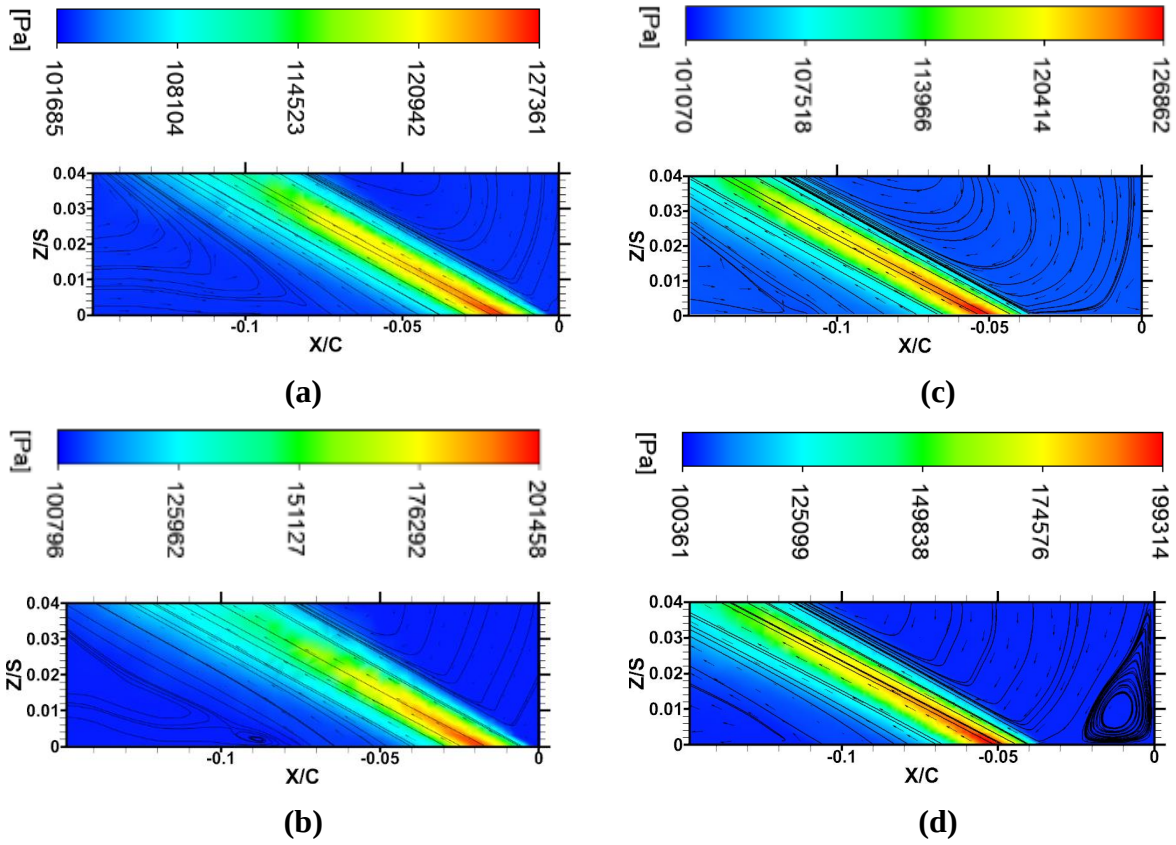

Figure 39: Leading edge vortex streamlines and velocity vectors overlaid with total pressure contours for α=150° a)X=D,0.5%MFR b)X=D,1%MFR c)X=2D, 0.5% MFR d) X=2D, 1% MFR

3.1.2 Passage vortex

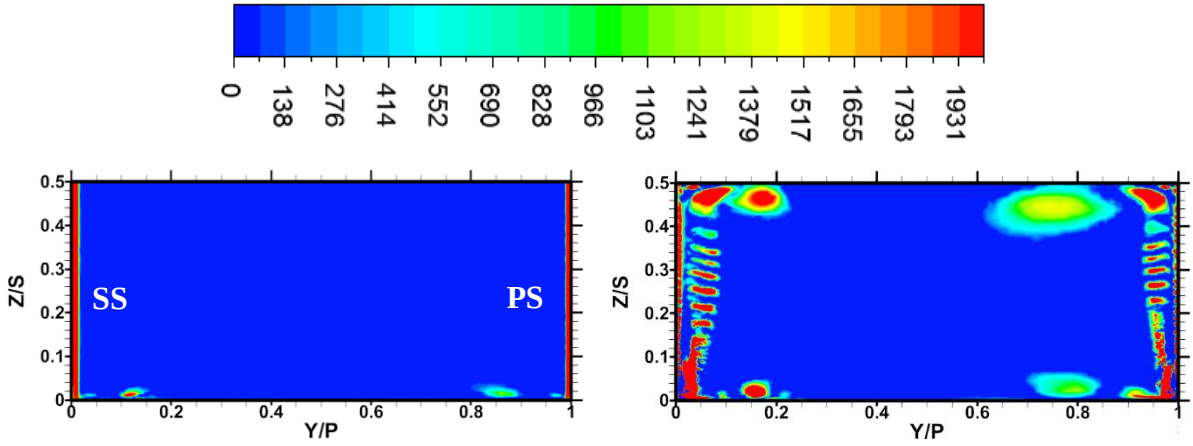

(a) PP1

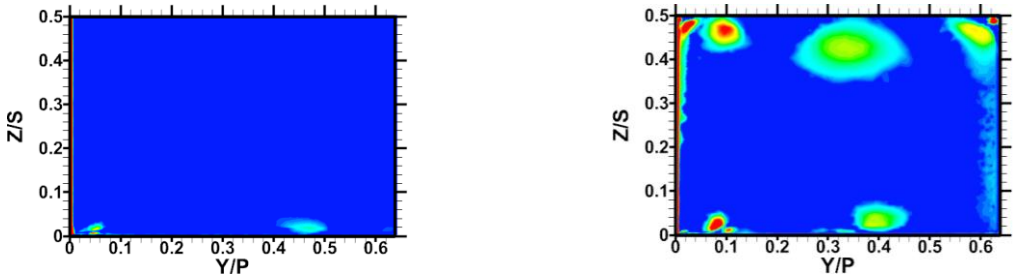

(b) PP2

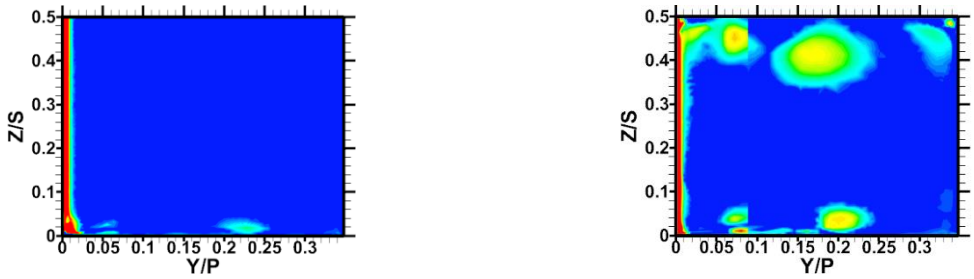

(c) PP3

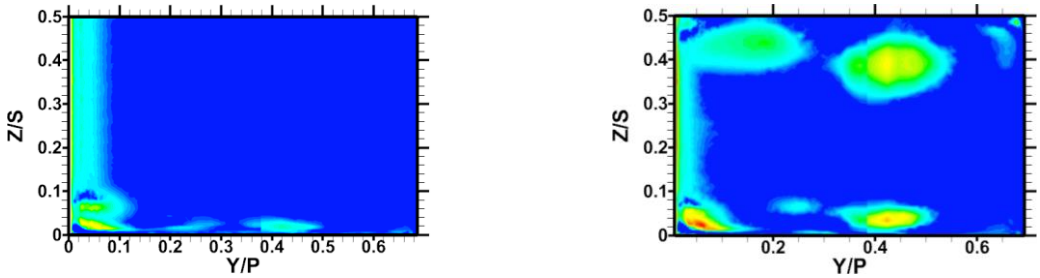

(d) PP4

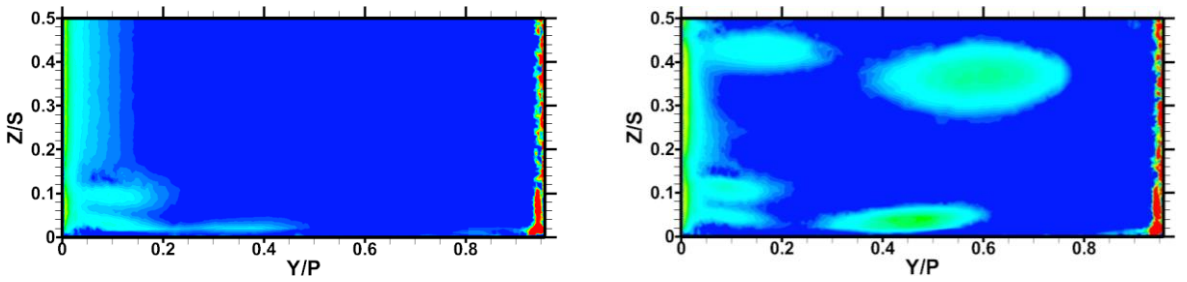

(c) PP5

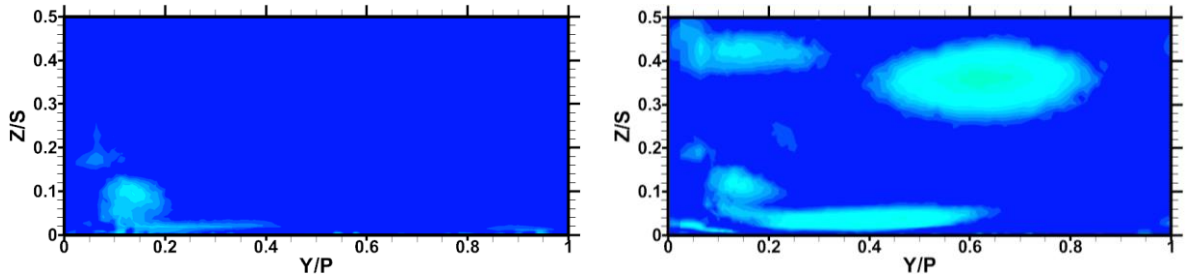

(f) PP6

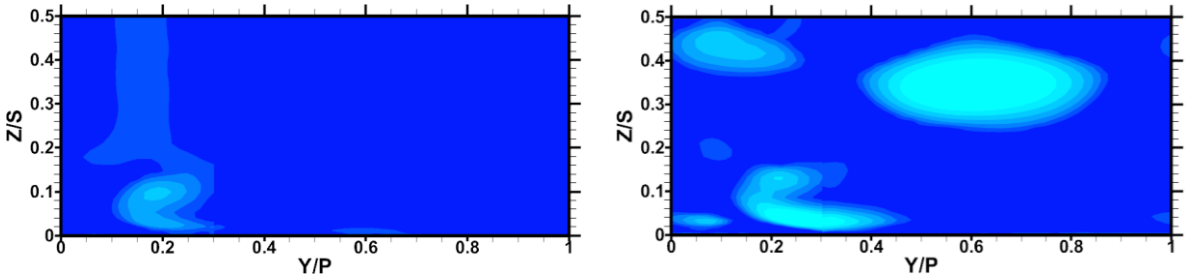

(g) PP7

Figure 40: Swirling strength contours located at planes PP1-PP7 in the vane passage

As before, the passage vortex was monitored through planes placed perpendicular to the inlet mainstream flow direction in different axial locations (PP1-PP7) and the swirling strength contours in each of these planes was plotted in order to track the movement of the passage vortex. The passage vortex shows up as a small region of swirling motion typically within 5% of the total span of the blade. The aim of the present study is to identify those alpha angles of the coolant which result in a fragmentation, weakening of the spiraling movement or delay of the passage of the vortex due to the cross passage gradient. This would be a direct result of the coolant interacting with the passage vortex in the leading edge region and altering its passage downstream in the pitchwise direction. In case of the 30° alpha angle at X/D=1 and 0.5% MFR, it was observed that there was some interaction of the vortex with the injected jet, due to the fact that there was a slight

shedding of smaller vortex filaments from the relatively larger vortex at 50% of the vane axial chord and 75% of the vane axial chord. Also visible was the slight enlargement (1-2%) of the diameter of the swirling motion and a small intensification of the rotational motion at the core of the vortex. Still, the overall path of the vortex remained mostly unaltered and the vortex, which began its pitchwise movement at the leading edge, reached the adjacent vane's suction side flow near the trailing edge of the vane cascade. One drawback noted was the creation of a large cloud of swirling fluid close to the mainstream which was caused due to the lifting of the injected fluid off the endwall surface and folding against the blade surface post impingement and a similar jet injected from the opposite endwall. This was a common drawback noted across different hole inclination angles, mass flow ratios and hole positions. For the same streamwise inclination angle (30°) and hole location, there was a more delayed traversal of the passage vortex from the pressure to the suction side which was evident by the fact that the vortex reached the suction side beyond the end of the vane cascade, at PP6 located 10% downstream of the trailing edge of the vane passage. The strength of the swirling motion was also strengthened, albeit by a greater factor than in the X/D=1, 0.5% MFR case. For the X/D=2 hole location, similar results were noted with respect to the fact that there was no appreciable change in the passage vortex's path through the cascade for the 0.5% MFR case but a delayed migration coupled with fragmentation for the 1% MFR case. For the 90° hole inclination angle, no interaction whatsoever with the passage vortex, except in the leading edge region could be deduced owing to the fact that the size and the path followed by the passage vortex remained virtually undisturbed by changing the hole location and the flow rate through the hole. For the 150° inclination angle of the hole, in all four instances of its usage (two hole locations for two mass flow ratios), the passage vortex seemed much more intense and larger in diameter as compared to the baseline case. Thus based on the monitoring of the passage vortex, it was concluded that aiming the injected flow in the direction of the flow as opposed to against the mainstream would be suitable if the disruption or delay in formation/migration of the passage vortex was sought. Injecting the flow perpendicular to the endwall would simply result in a localized weakening of the vortex close to the vane stagnation point, but no large-scale change in the behavior of the vortex. Thus the 30° angle seemed most promising among the angles chosen for this study in positively changing the path of the passage vortex by disrupting the flow near the region of formation of the passage vortex and delaying the cross-passage migration of the passage vortex.

3.1.3 Exit Plane Loss Coefficients

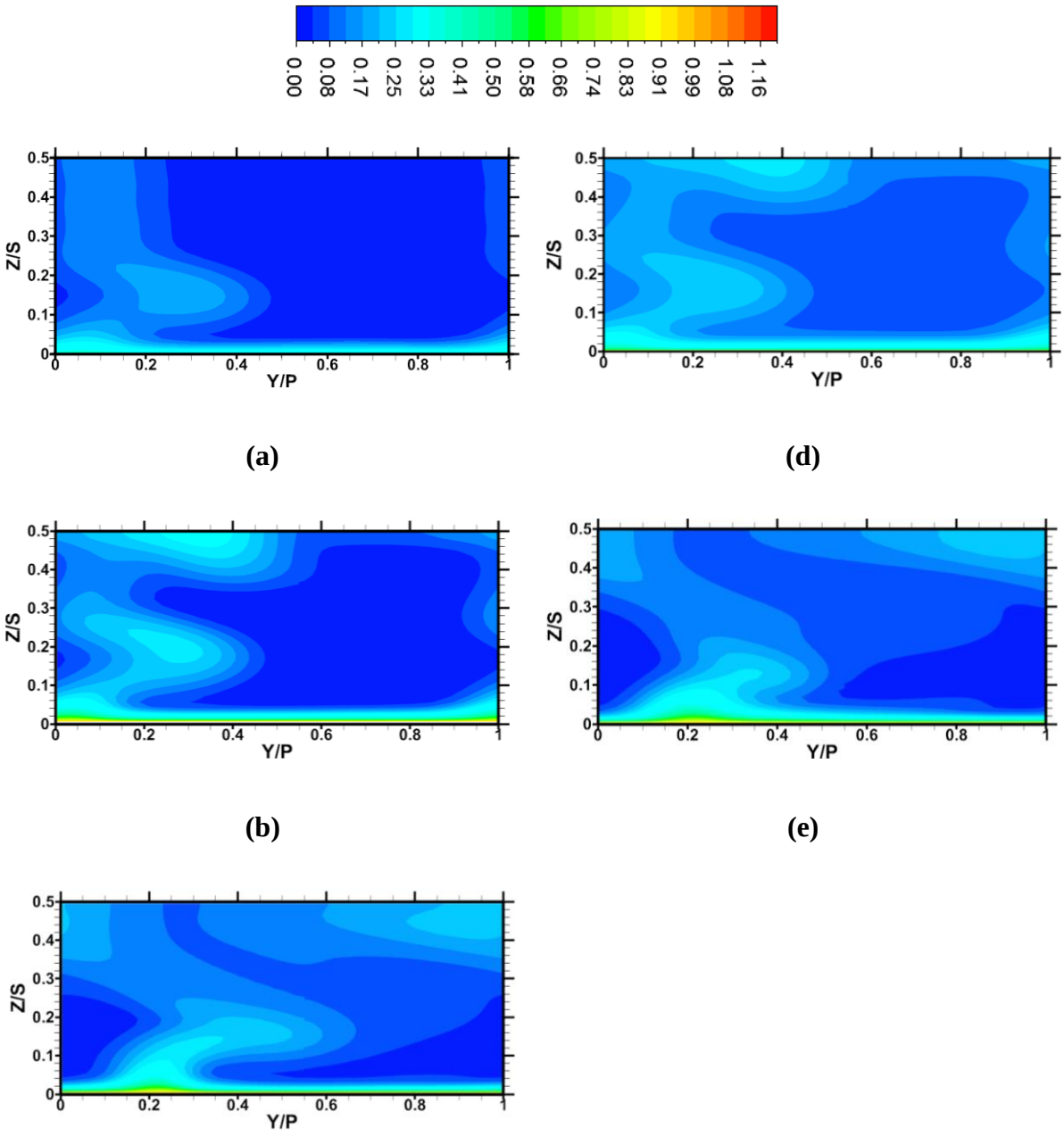

Figure 41: Total Pressure Loss coefficient contours for α=30°, β=0° for (a) Baseline (b) MFR=0.5%, X=D (c) MFR=1%, X=D (d) MFR=0.5%, X=2D (e) MFR=0.5%, X=2D

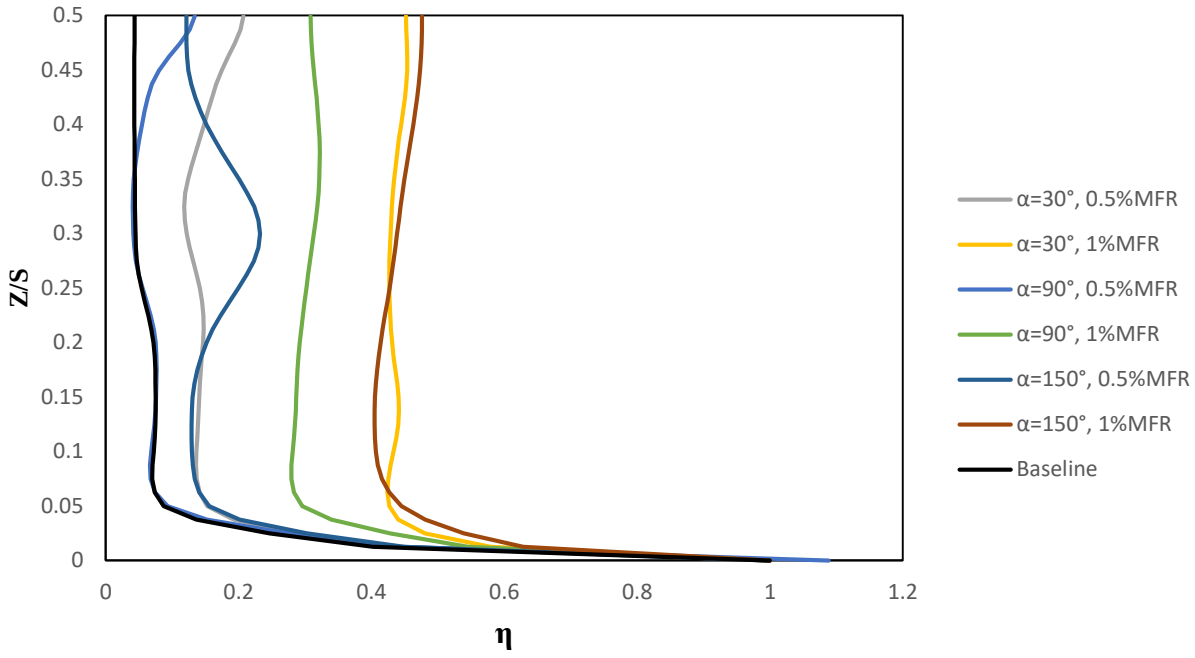

Figure 42: Pitch-wise averaged kinetic energy loss coefficient for different α angles at X/D=1

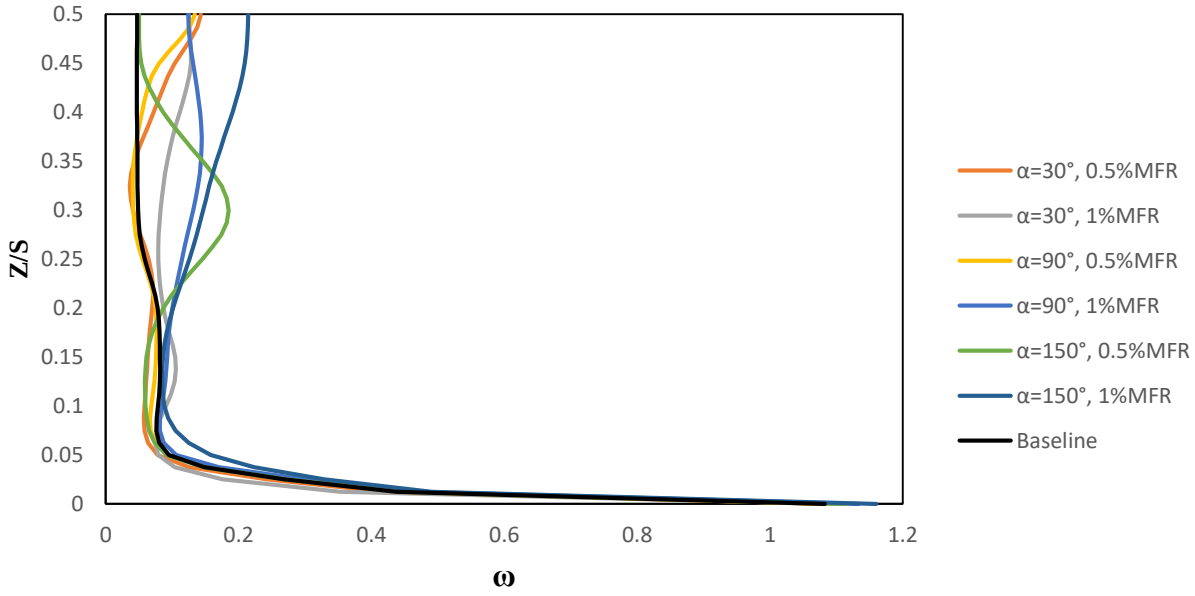

Figure 43: Pitch-wise averaged total pressure loss coefficient for different α angles at X/D=1

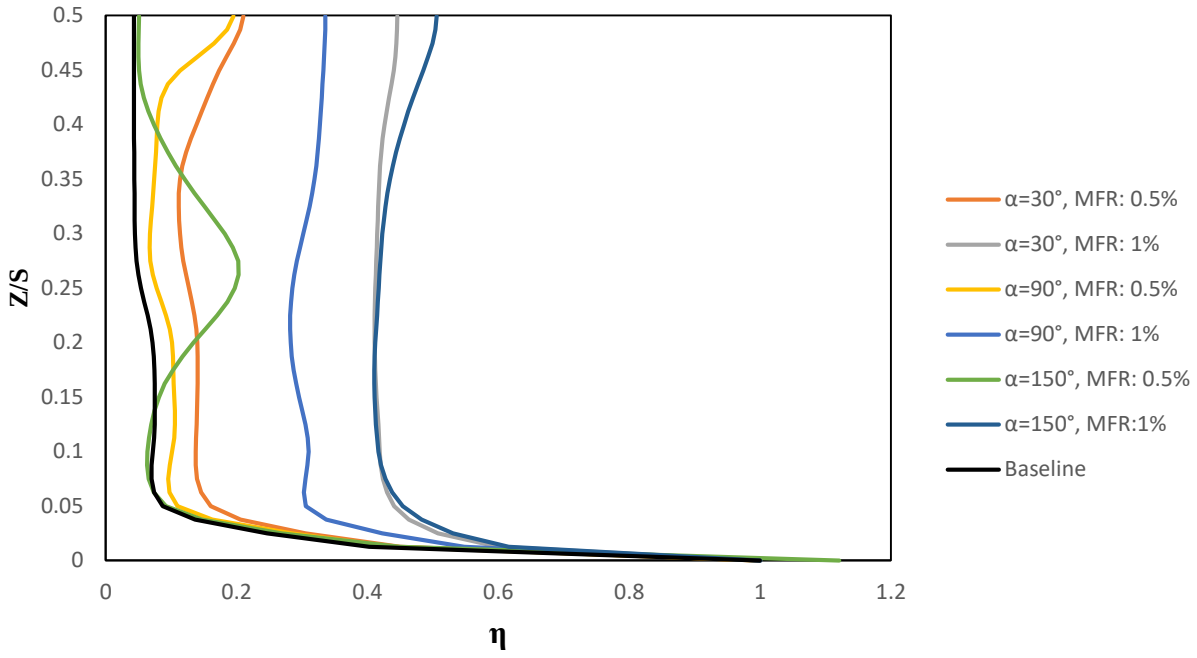

Figure 44: Pitch-wise averaged kinetic energy loss coefficient for different α angles at X/D=2

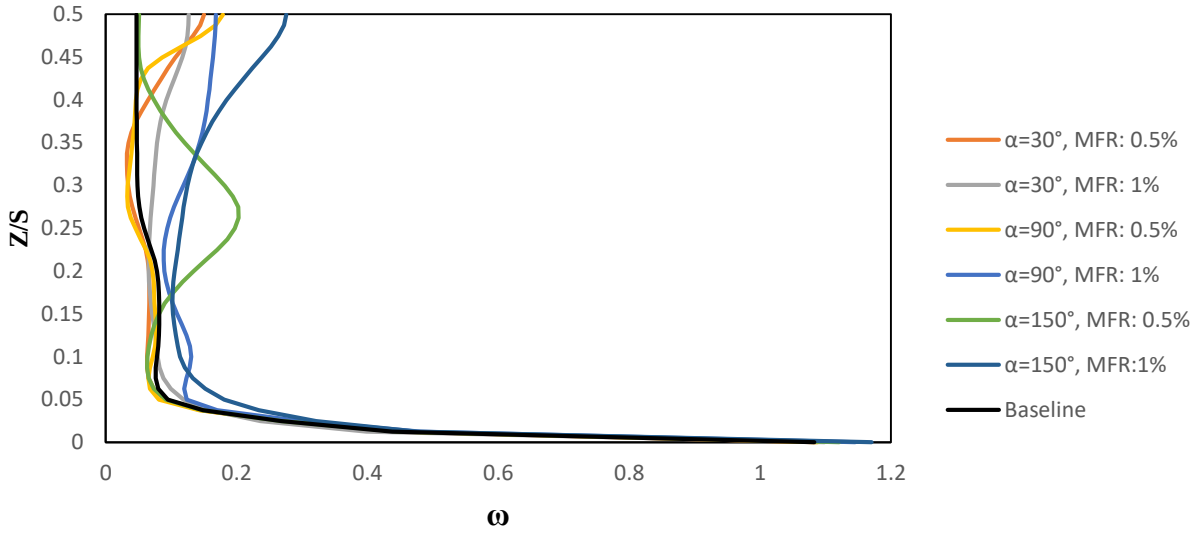

Figure 45: Pitch-wise averaged total pressure loss coefficient for different α angles at X/D=2

Table 11: Mass averaged total pressure loss coefficient and kinetic energy loss coefficient values for cases with X/D=1, MFR=0.5% for different values of α

X/D	α (deg)	β (deg)	MFR (%)	ω	% change w.r.t baseline	η	% change w.r.t baseline
N/A	N/A	N/A	N/A	0.0823	-baseline-	0.0760	-baseline-
1	30	0	0.5	0.0877	6.5906	0.1604	110.9568
1	90	0	0.5	0.0886	7.6685	0.1161	52.6199
1	150	0	0.5	0.1150	39.7001	0.1748	129.8050

Table 12: Mass averaged total pressure loss coefficient and kinetic energy loss coefficient values for cases with X/D=1, MFR=1% for different values of α

X/D	α (deg)	β (deg)	MFR	ω	% change w.r.t baseline	η	% change w.r.t baseline
N/A	N/A	N/A	N/A	0.0823	-baseline-	0.0760	-baseline-
1	30	0	1	0.1064	29.2770	0.4418	480.9924
1	90	0	1	0.1361	65.3417	0.3153	314.6407
1	150	0	1	0.1601	94.5604	0.4462	486.6913

Table 13: Mass averaged total pressure loss coefficient and kinetic energy loss coefficient values for cases with X/D=2, MFR=0.5% for different values of α

X/D	α (deg)	β (deg)	MFR	ω	% change w.r.t baseline	η	% change w.r.t baseline
N/A	N/A	N/A	N/A	0.0823	-baseline-	0.0760	-baseline-
2	30	0	0.5	0.0856	4.0534	0.1562	105.3762
2	90	0	0.5	0.0875	6.3487	0.1157	52.1255
2	150	0	0.5	0.1209	46.9709	0.1786	134.8727

Table 14: Mass averaged total pressure loss coefficient and kinetic energy loss coefficient values for cases with X/D=2, MFR=1% for different values of α

X/D	α (deg)	β (deg)	MFR	ω	% change w.r.t baseline	η	% change w.r.t baseline
N/A	N/A	N/A	N/A	0.0823	-baseline-	0.0760	-baseline-
2	30	0	1	0.0984	19.5750	0.4297	464.9989
2	90	0	1	0.1456	76.9377	0.3202	320.9826
2	150	0	1	0.1710	107.8317	0.4478	488.7794

The pitch averaged values of the total pressure loss coefficients and kinetic energy loss coefficients were studied to quantify the losses caused by the secondary flow and the endwall fluid injection. In this study, the entire test matrix of 12 cases was segregated into four sets of cases (based on hole location and for each hole location, two sets of mass flow ratios) with three streamwise inclination angles for each set of cases. Based on the pitchwise averaged distributions of the kinetic energy loss coefficient and the pitchwise averaged total pressure loss coefficient profiles, it was observed that for each hole location and each hole inclination angle, though the total pressure loss coefficient was measured to be the least for the 30° inclination angle as opposed to the 90° and 150° angles, the kinetic energy loss coefficient was the least for the 90° hole in each case. This was mainly because of the large difference in kinetic energies possessed by the jets ejected from the 30° and the 150° holes as opposed to the 90° hole. Since the exit area of the 30° and the 150° holes was nearly twice that the 90°hole, the velocity of the flow coming out of them was double the velocity of the fluid being ejected by the 30°hole which led to the kinetic energy energy loss coefficient being lower than the other two angles. Thus there was an ambiguity in the selection of the streamwise inclination angle since for the same mass flow rate, there were two different blowing ratios and two trends based on the two different loss coefficients measured.

3.1.4 Vane surface Mach number

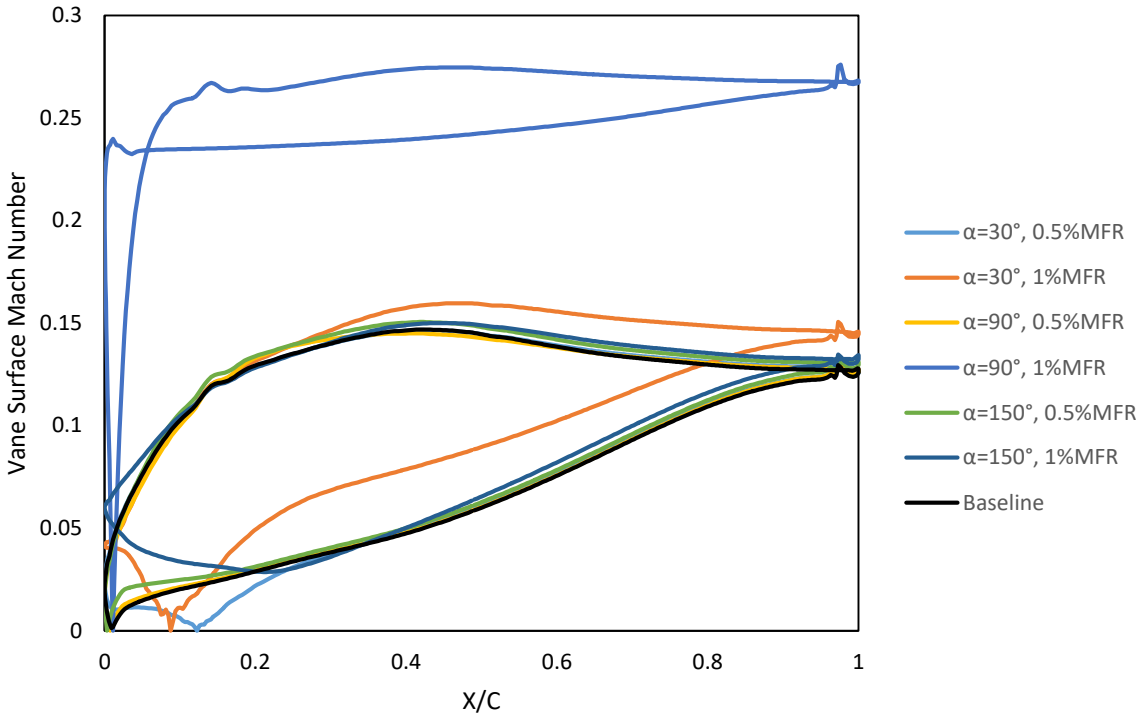

Figure 46: Midspan vane surface Mach number for cases with hole location at X/D=1

Based on the observations of the vane surface Mach number profiles at the two hole locations, it can be seen that apart from two cases (α=90° 1% MFR, α=30° 1% MFR case), most other hole geometries do not cause a major shift in the surface velocities at the vane midspan. For the α=30° 1% MFR case on the pressure side, a marked change in the vane surface Mach number can be noticed which is characterized by an increase in the pressure side vane surface Mach number from 0.2 C downstream of the vane onwards while for the suction side the change in the Mach number is prominent from 0.4 C downwards. For the 90° case there is a complete shift of the entire profile by over 100%, thus making it unfeasible for using this configuration for further use. Thus looking at the passage vortex patterns and the vane surface Mach number profiles, in combination with total pressure loss coefficient values and the overarching aim of studying the interaction between the passage vortex and the injected fluid, the 30° streamwise inclination angle was chosen.

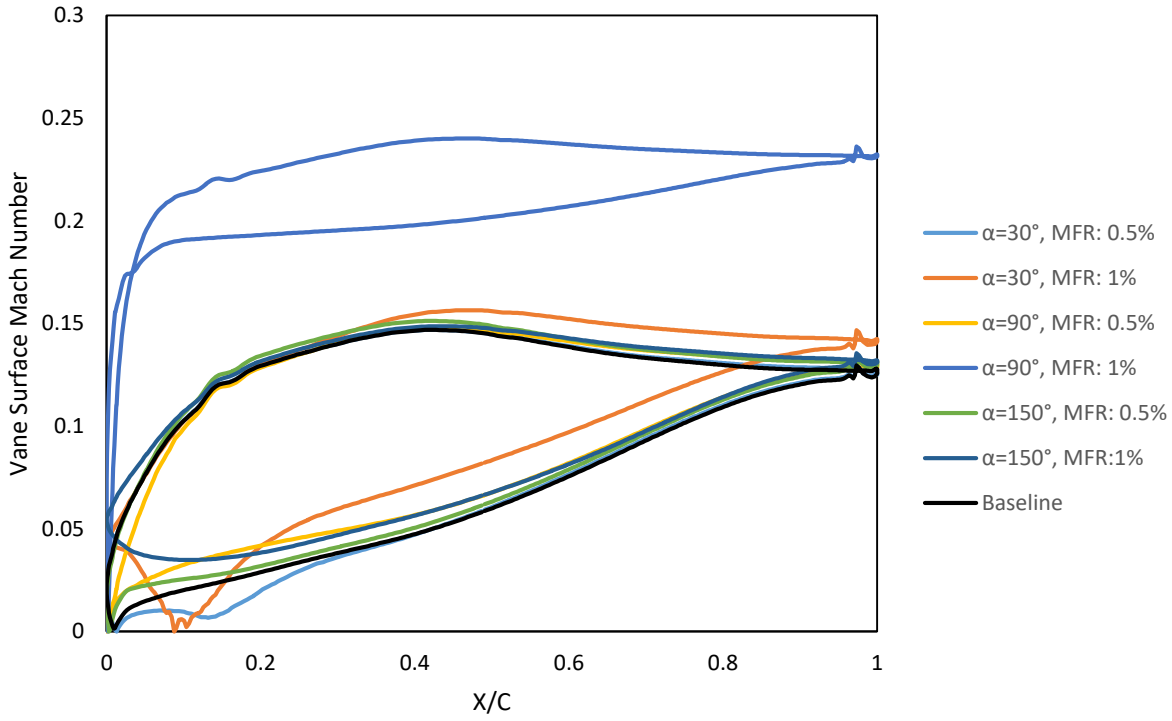

Figure 47: Midspan vane surface Mach number for cases with hole location at X/D=2

3.4 Beta Study

In combination with the optimized streamwise inclination angle (30°) identified in the previous study, five different compound angles were used to test the performance of the endwall injection on the leading edge vortex structure and the passage vortex. Two different hole positions (X/D=1, 2) and two different MFRs (0.5%, 1%) were chosen for this study. Table 15 shows the list of cases tested in the β study.

Table 15: Test Matrix for β-study

X/D	α (deg)	β (deg)	MFR
1	30	0	0.5
1	30	30	0.5
1	30	45	0.5
1	30	60	0.5
1	30	90	0.5
1	30	0	1
1	30	30	1
1	30	45	1
1	30	60	1
1	30	90	1
2	30	0	0.5
2	30	30	0.5
2	30	45	0.5
2	30	60	0.5
2	30	90	0.5
2	30	0	1
2	30	30	1
2	30	45	1
2	30	60	1
2	30	90	1

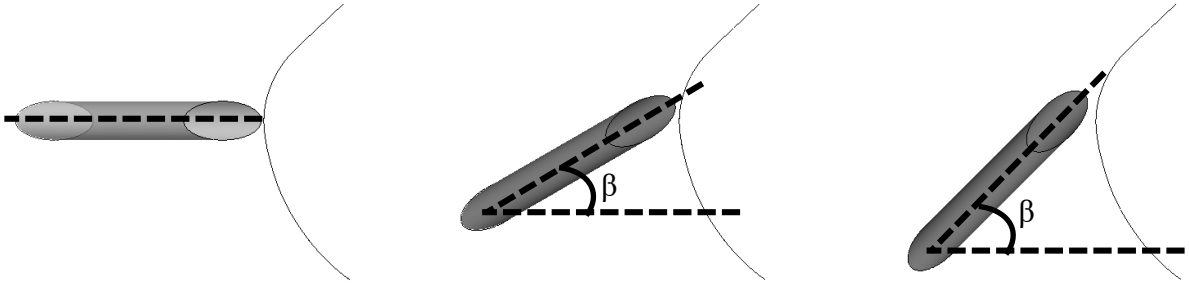

a) β=0° b) β=30° c) β=45°

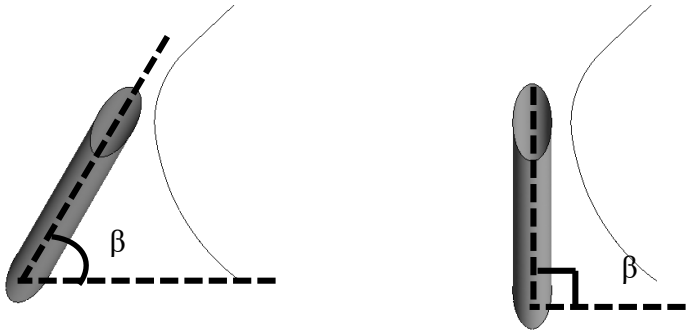

d) β=60° e) β=90°

Figure 48: Graphical depiction of hole compound angles tested in the β-study

3.4.1 Leading Edge Vortex

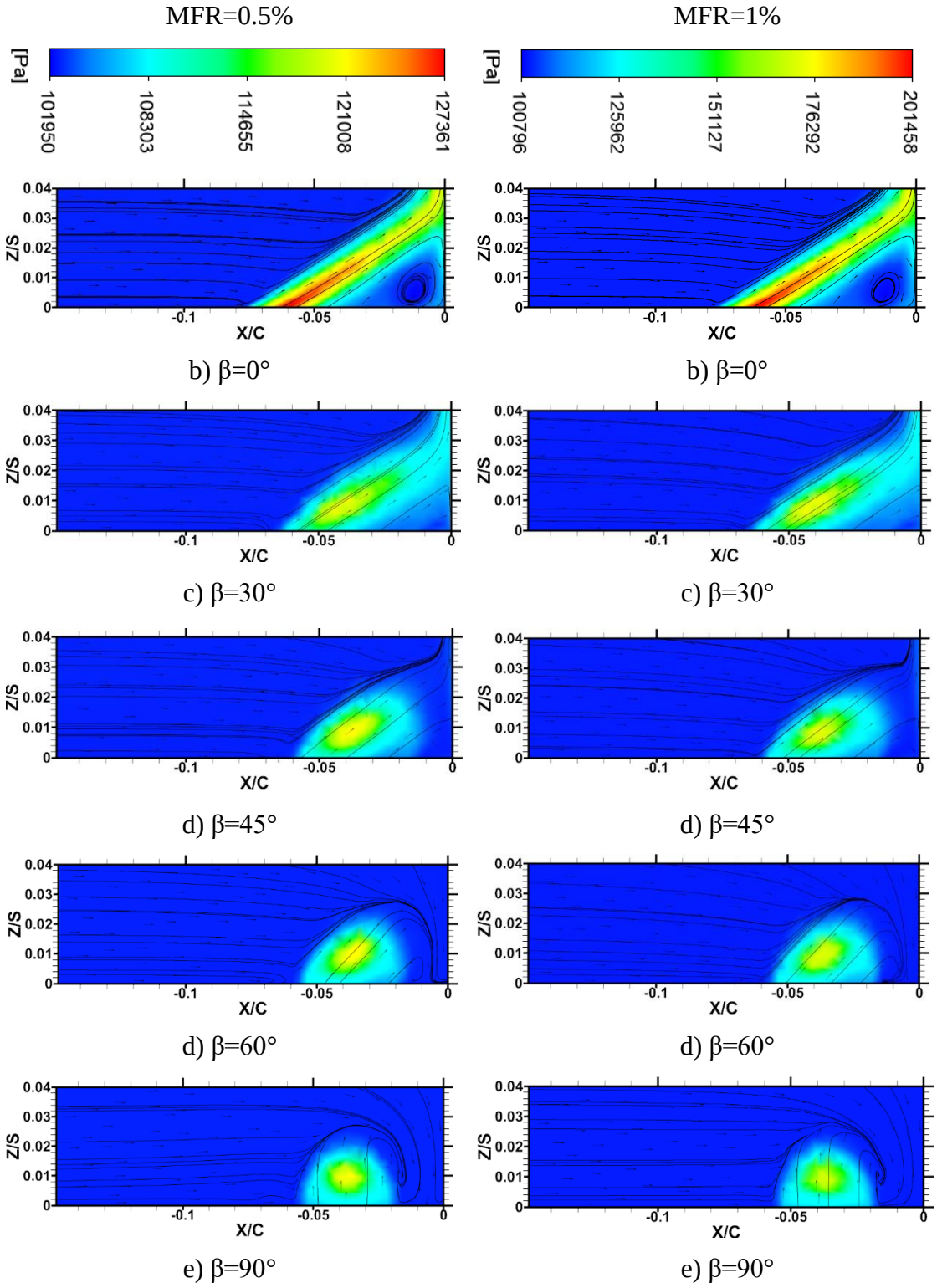

Figure 49: Leading edge velocity streamlines and vectors overlaid with total pressure (absolute) contours at different β values at α=30°, and X=D

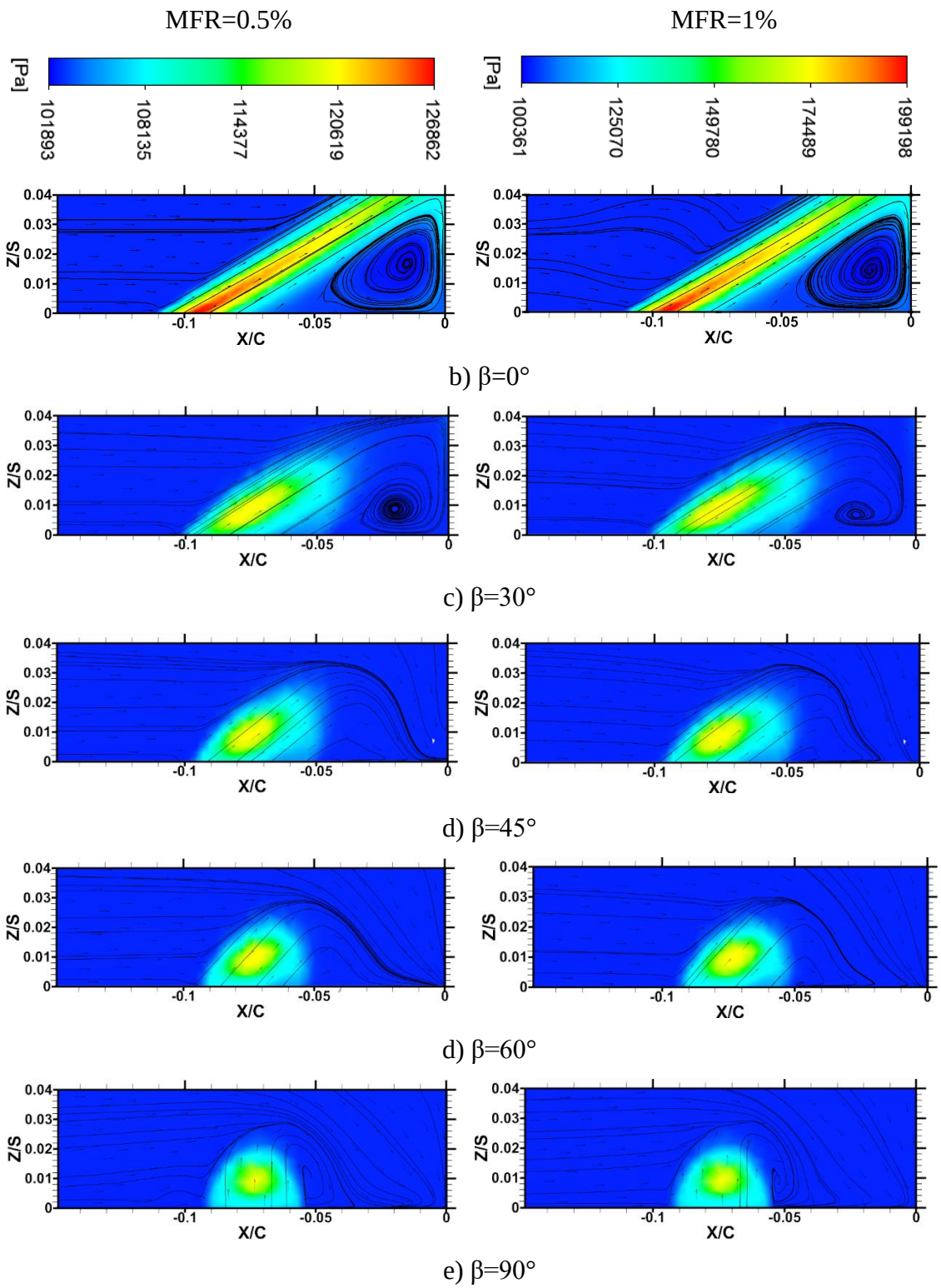

Figure 50: Leading edge velocity streamlines and vectors overlaid with total pressure (absolute) contours at different β values at α=30°, and X=2D

The leading edge flowfield was studied by plotting velocity streamlines overlaid with velocity vectors and velocity streamlines were plotted with velocity vectors and total pressure contours in order to trace the flow patterns and the trajectory of the injected jet in the leading edge plane in the stagnation region. One common feature noticed in all the different compound angles, mass flow ratios and hole positions studied was the absence of a leading edge horseshoe vortex. This is due to the counter momentum provided opposite to the direction of the pressure gradient caused due to the stagnation of the oncoming boundary layer flow which results in the spiraling of the flow. Also noticeable was the diminishing of the induced corner vortex with the increase in the compound angle. One can clearly notice the presence of induced vortex in the case of the 0°compound angle and to a reduced extent in the instance with the 30° compound angle. This is due to the absence of a well-defined low pressure region in the stagnation plane of the vane. Thus there is no driving force to draw the fluid from the injected jet down to the endwall to form another induced vortex. As the compound angle increases beyond 30°, there is no evidence of a leading edge vortex in the 45° and 60° compound angle instances. However for the 90° instance, the leading edge vortex is not completely eliminated but some elements of the vortex remain as can be seen from figure. This is because the injected jet is completely aligned in the pitchwise direction and the spanwise component of the velocity, which would provide the momentum to break the vortex is quite low. Thus remnants of the vortical motion can still be seen in the 90° compound angle flowfield results for all X/D locations of the hole and MFR values.

3.4.2 Passage Vortex

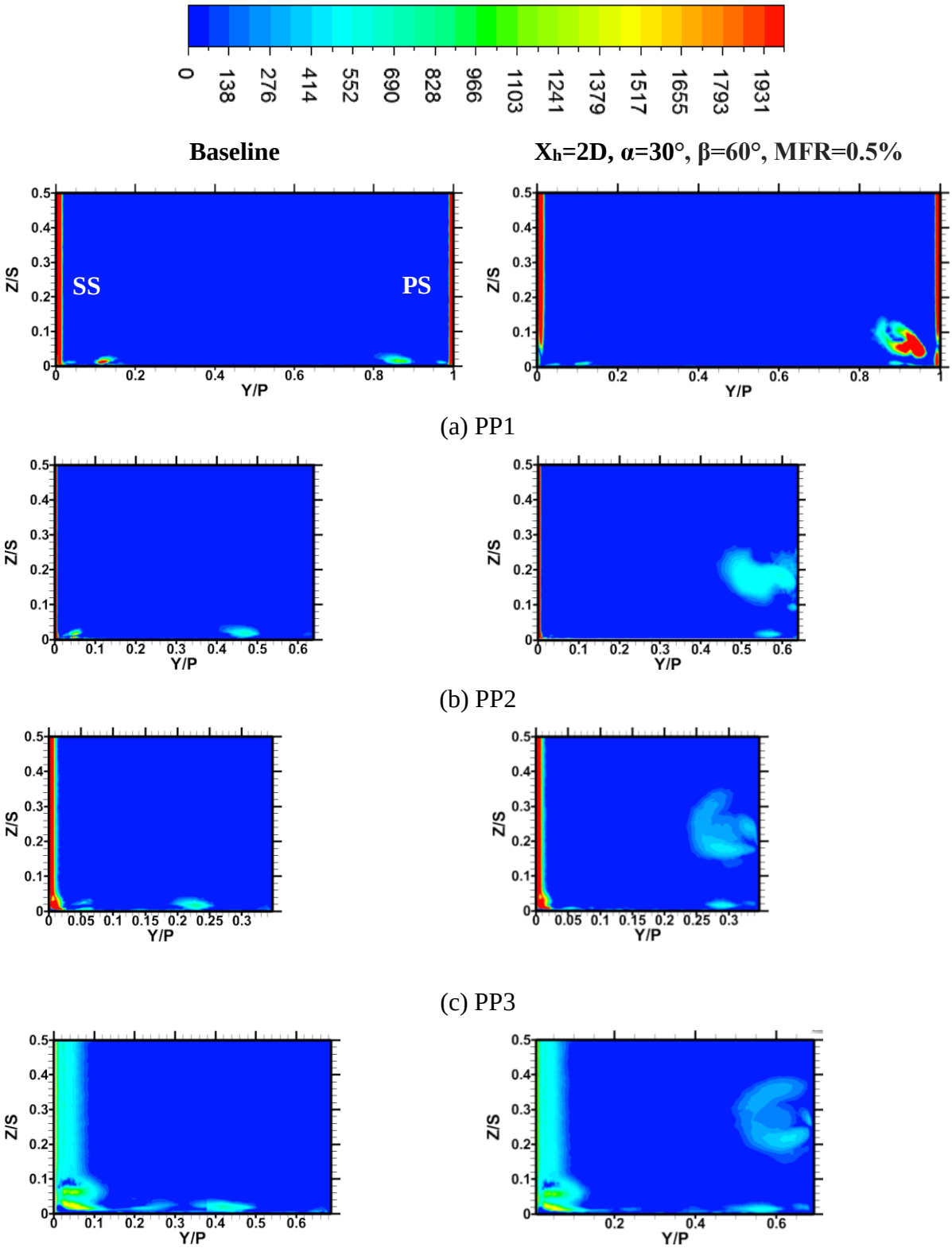

(a) PP1

(b) PP2

(c) PP3

(d) PP4

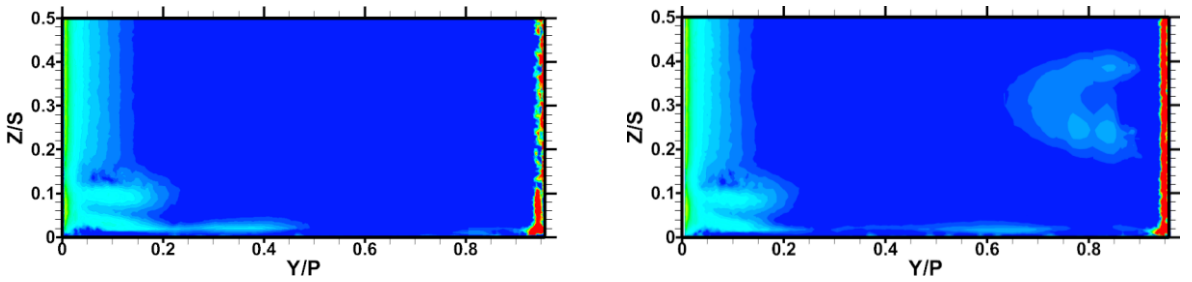

(e) PP5

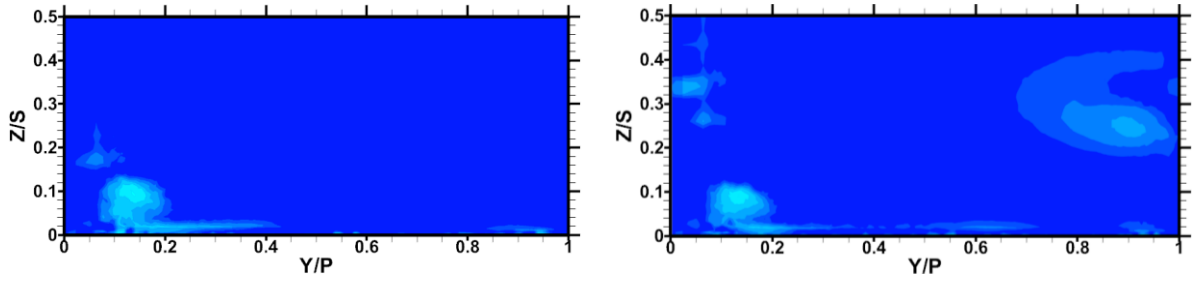

(f) PP6

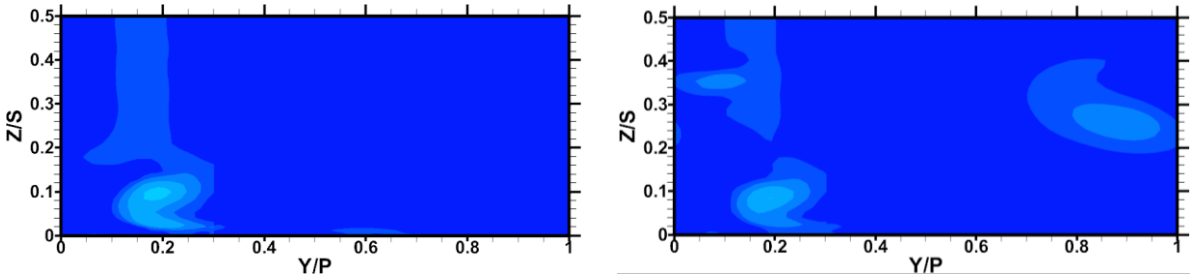

(g) PP7

Figure 51: Swirling strength contours located at planes PP1-PP7 in the vane passage

As the swirling strength contours were plotted and the trajectory of the passage vortex monitored it was seen that for each set of mass flow rates and each set of hole locations, the 60° compound angle provided the best delaying effect of the pitchwise motion of the horseshoe vortex near the endwall. In **Figure 51**, both the delaying effect as well as the weakening of the passage vortex can be seen at 0.1 C downstream of the trailing edge of the vane cascade, with the bulk of the swirling motion at 60% of the passage in the cross passage direction for the X/D=2, β=60° case while the passage vortex in the baseline case has begun the process of merging with the suction side secondary flow. This is assumed to be due to the fact that it matches up best with the compound angle of the passage vortex itself (as can be seen in **Figure 65**) and thus enables the

disruption of the passage vortex, forcing it to develop at a later point as opposed to the leading edge in the baseline case.

3.4.3 Exit plane loss coefficients

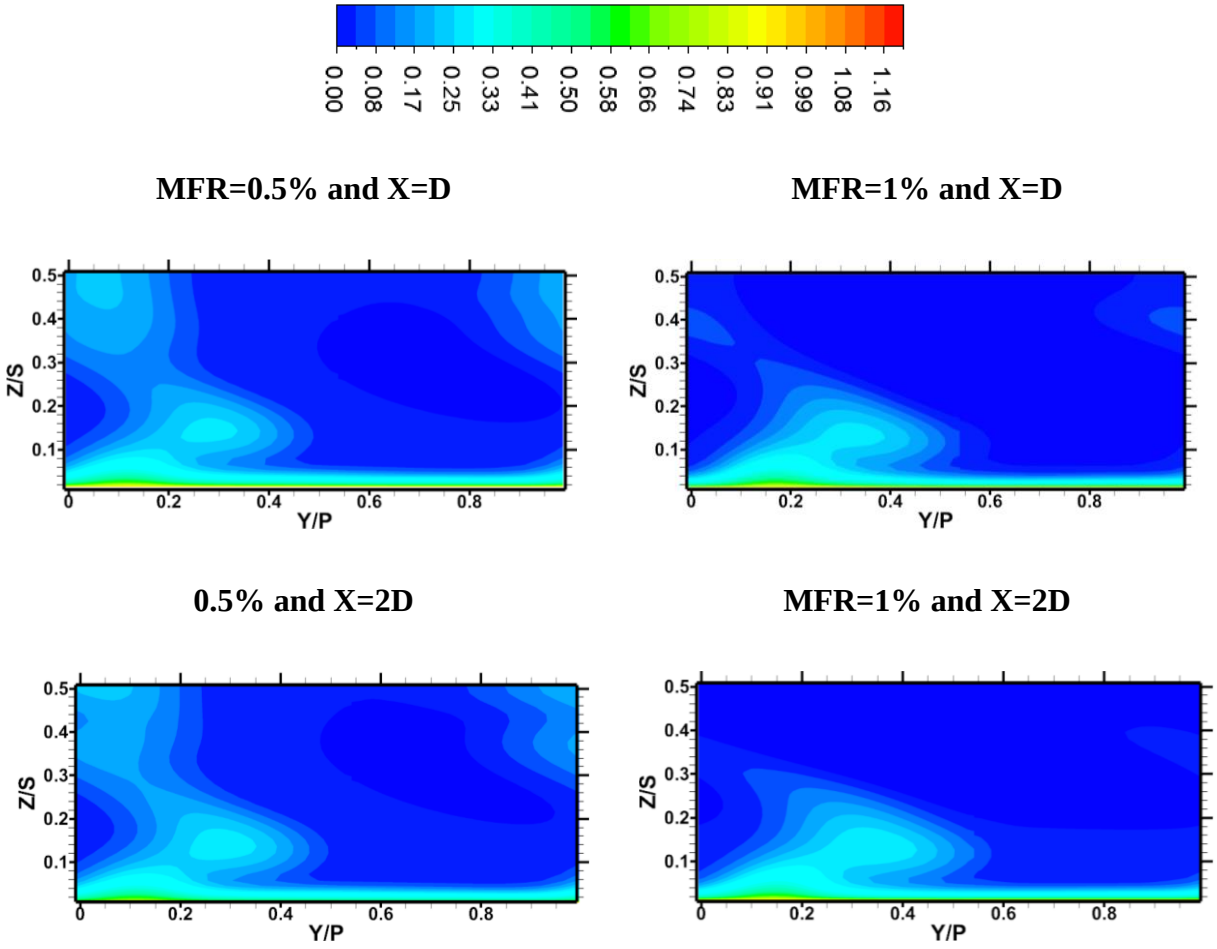

Figure 52: Total Pressure Loss coefficient contours for β=60°

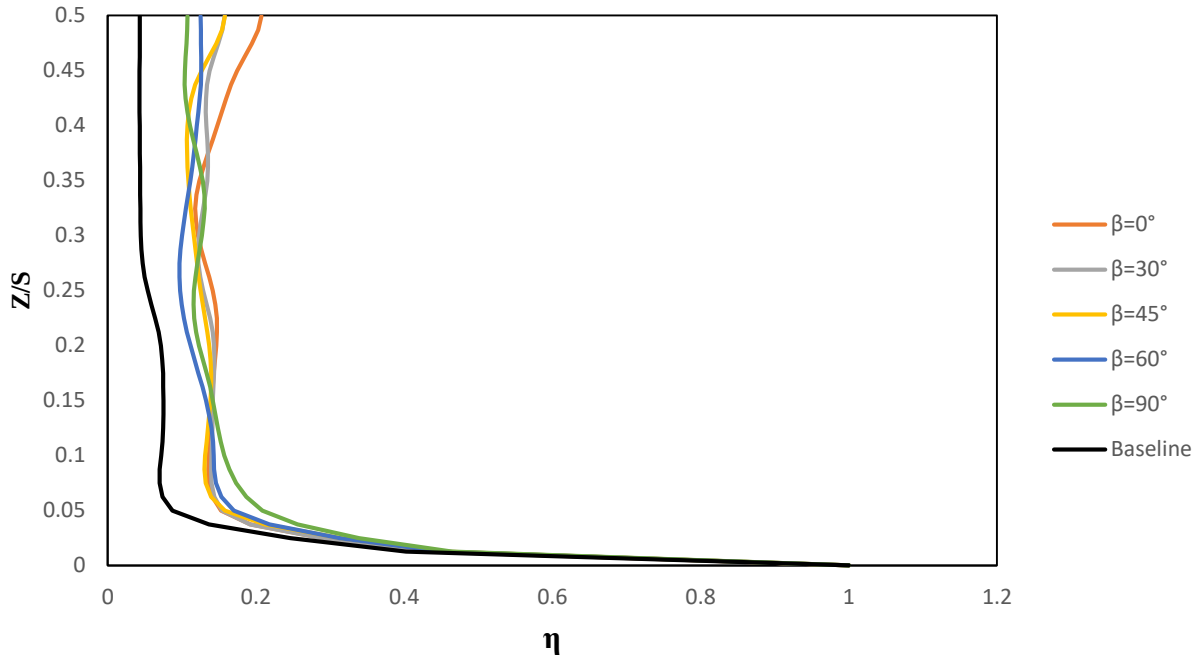

Figure 53: Pitch-wise averaged kinetic energy loss coefficient for X/D=1, 0.5 MFR

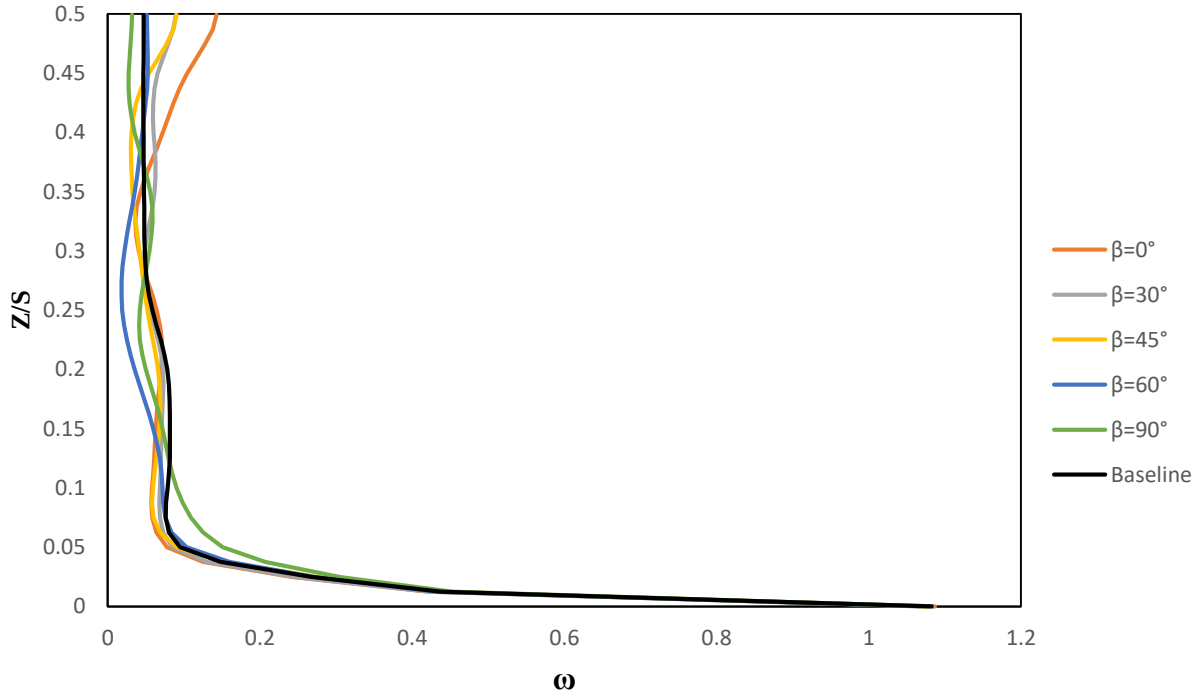

Figure 54: Pitch-wise averaged total pressure loss coefficient for X/D=1, 0.5 MFR

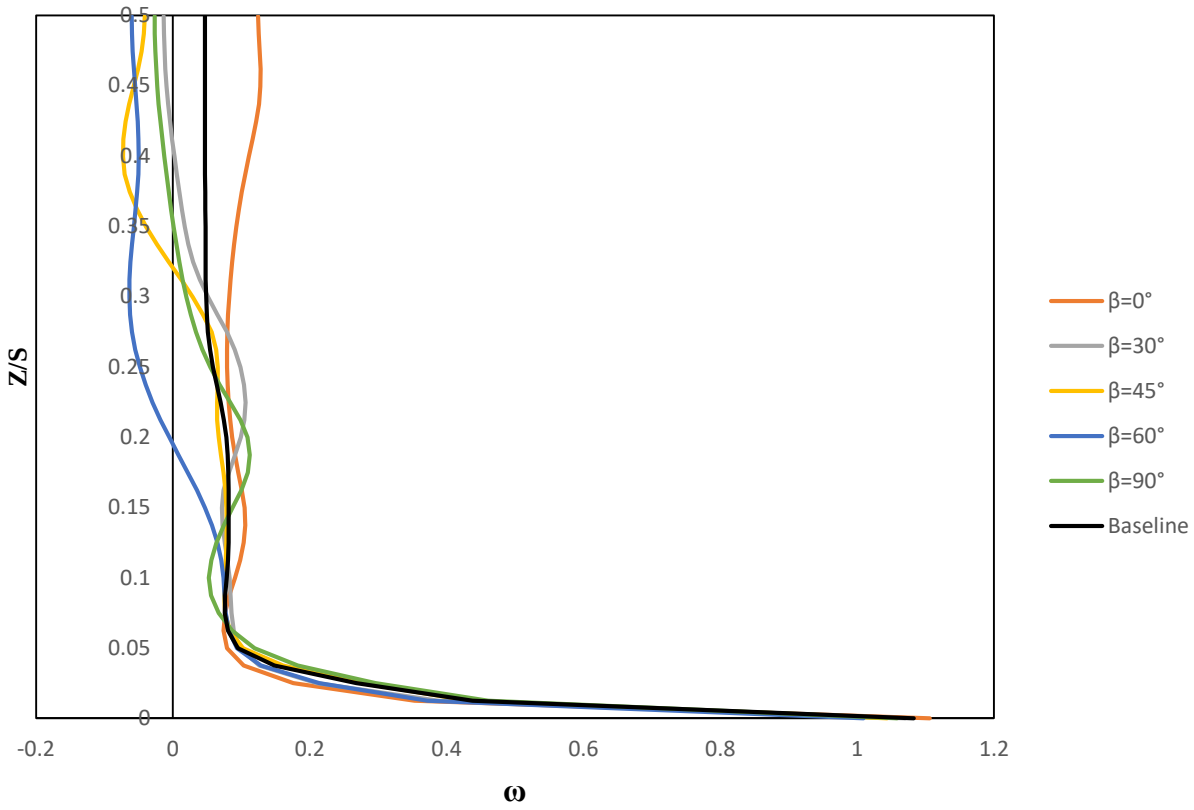

Figure 55: Pitch-wise averaged total pressure loss coefficient for X/D=1, MFR=1%

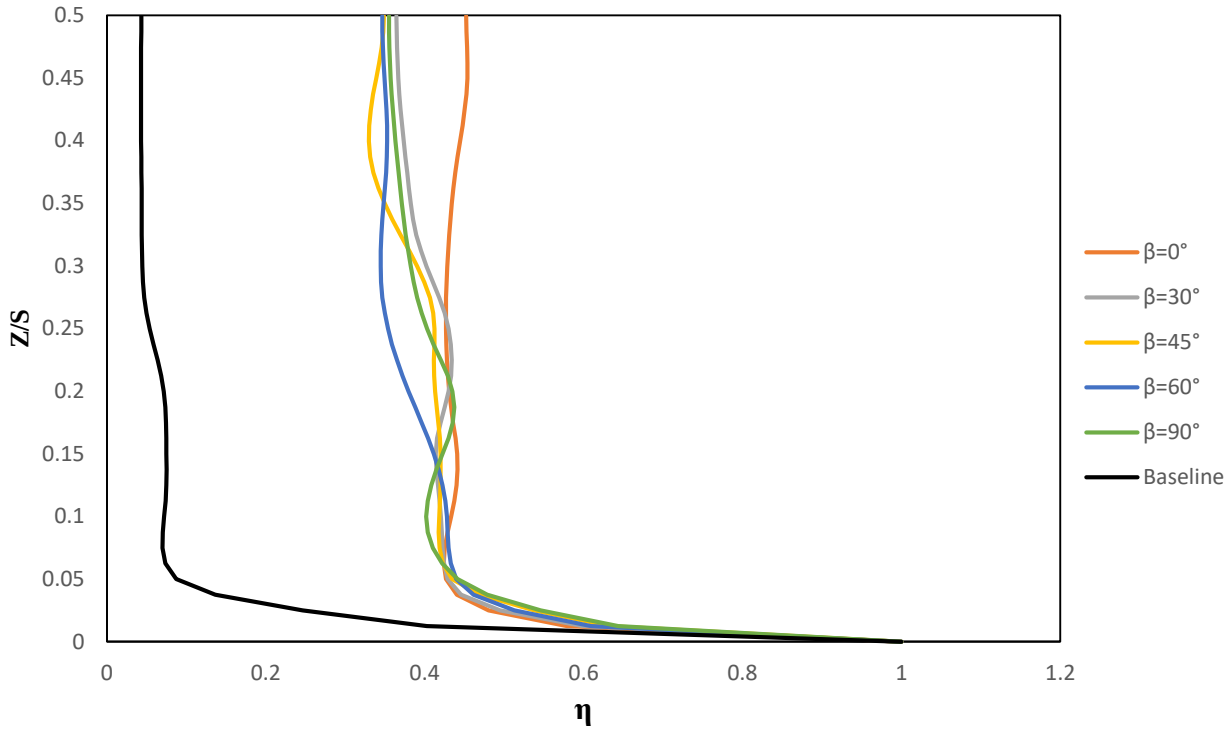

Figure 56: Pitch-wise averaged kinetic energy loss coefficient for X/D=1, MFR=1%

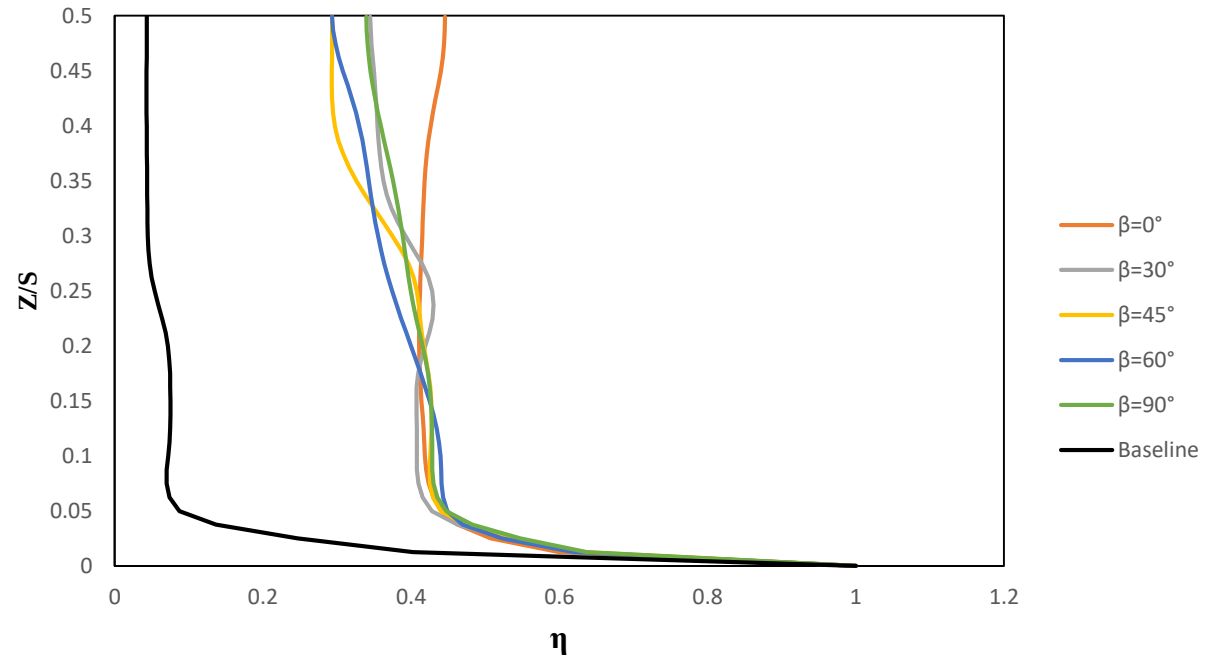

Figure 57: Pitch-wise averaged kinetic energy loss coefficient for X/D=2, MFR=1%

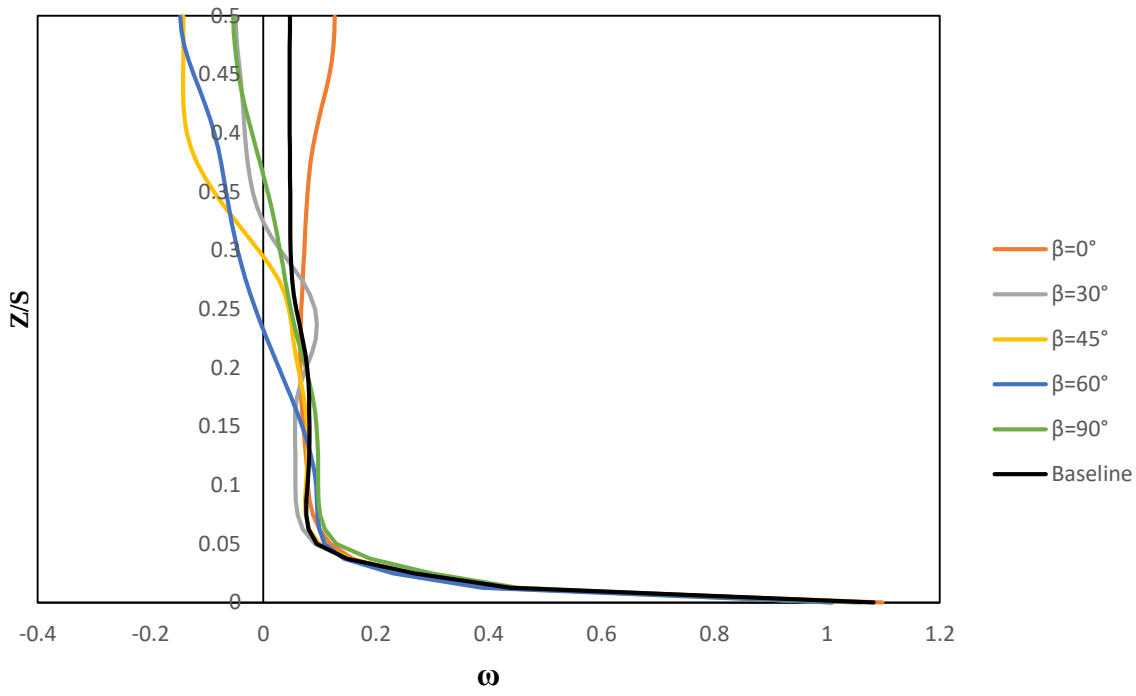

Figure 58: Pitch-wise averaged total pressure loss coefficient for X/D=2, MFR=1%

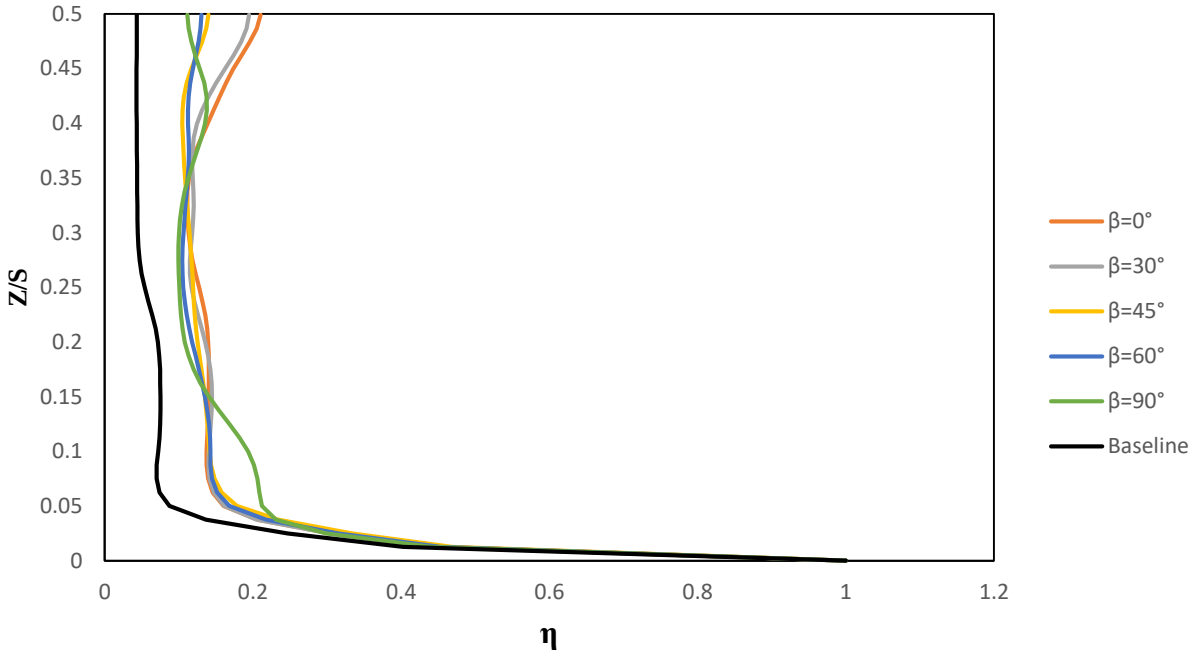

Figure 59: Pitch-wise averaged kinetic energy loss coefficient for X/D=2, MFR=0.5%

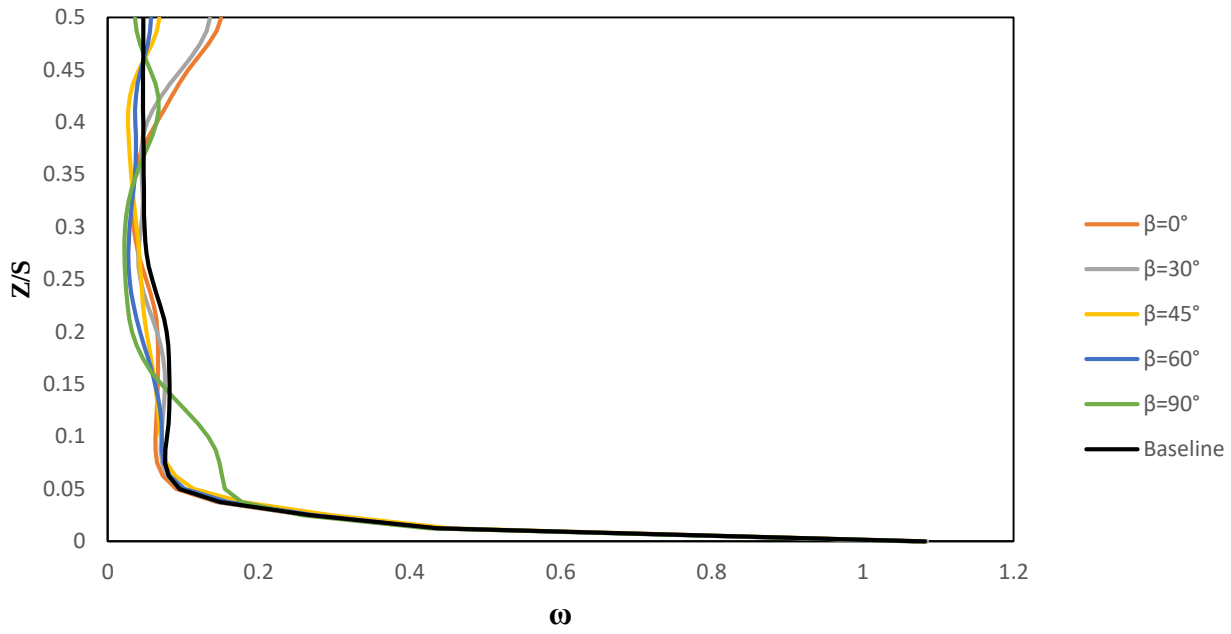

Figure 60: Pitch-wise averaged total pressure loss coefficient for X/D=2, MFR=0.5%

Table 16: Mass averaged total pressure loss coefficient and kinetic energy loss coefficient values for cases with X/D=1, α=30°, MFR=0.5% for different values of β

X/D	α (deg)	β (deg)	MFR (%)	ω	% change w.r.t baseline	η	% change w.r.t baseline
N/A	N/A	N/A	N/A	0.0823	-baseline-	0.0760	-baseline-
1	30	0	0.5	0.0877	6.5906	0.1604	110.9568
1	30	30	0.5	0.0848	3.0270	0.1534	101.7220
1	30	45	0.5	0.0758	-7.8782	0.1450	90.6924
1	30	60	0.5	0.0681	-17.2927	0.1394	83.2394
1	30	90	0.5	0.0786	-4.4404	0.1478	94.3847

Table 17: Mass averaged total pressure loss coefficient and kinetic energy loss coefficient values for cases with X/D=1, α=30°, MFR=1% for different values of β

X/D	α (deg)	β (deg)	MFR (%)	ω	% change w.r.t baseline	η	% change w.r.t baseline
N/A	N/A	N/A	N/A	0.0823	-baseline-	0.0760	-baseline-

1	30	0	1	0.1064	29.2770	0.4418	480.9924
1	30	30	1	0.0703	-14.5162	0.4132	443.3328
1	30	45	1	0.0440	-46.5709	0.3994	425.2302
1	30	60	1	0.0104	-87.4067	0.3889	411.4169
1	30	90	1	0.0589	-28.4580	0.4052	432.7963

Table 18: Mass averaged total pressure loss coefficient and kinetic energy loss coefficient values for cases with X/D=2, α=30°, MFR=0.5% for different values of β

X/D	α (deg)	β (deg)	MFR (%)	ω	% change w.r.t baseline	η	% change w.r.t baseline
N/A	N/A	N/A	N/A	0.0823	-baseline-	0.0760	-baseline-
2	30	0	0.5	0.0856	4.0534	0.1562	105.3762
2	30	30	0.5	0.0851	3.3675	0.1529	101.1145
2	30	45	0.5	0.0737	-10.3944	0.1441	89.4564
2	30	60	0.5	0.0690	-16.1841	0.1408	85.0961
2	30	90	0.5	0.0805	-2.1435	0.1488	95.7220

Table 19: Mass averaged total pressure loss coefficient and kinetic energy loss coefficient values for cases with X/D=2, α=30°, MFR=1% for different values of β

X/D	α (deg)	β (deg)	MFR (%)	ω	% change w.r.t baseline	η	% change w.r.t baseline
N/A	N/A	N/A	N/A	0.0823	-baseline-	0.0760	-baseline-
2	30	0	1	0.0984	19.5750	0.4297	464.9989
2	30	30	1	0.0499	-39.3714	0.4033	430.3663
2	30	45	1	0.0102	-87.5937	0.3855	406.9277
2	30	60	1	0.0094	-88.6230	0.3884	410.7502
2	30	90	1	0.0600	-27.1023	0.4066	434.6030

From the exit plane loss contour plots and pitchwise averaged loss plots, we can see that the 60° compound angle presents the best case for endwall injection with respect to the fact that for each mass flow ratio, for the 30° streamwise inclination angle the 60° compound angle provides

the lowest pitchwise averaged loss profile as well as the mass averaged loss value. Tables 16-19 quantify the losses caused by the endwall injection. The increase in the losses with respect to the baseline case have been shown to be minimized while the effect on the pressure side leg of the horseshoe vortex is maximized for the 60° compound angle injection. This was true for both hole locations, since no clear pattern could be established, since for the X/D=2 location, there was a 1% drop in the kinetic energy loss coefficient for the 1% MFR case as compared to the X/D=1 hole location. As opposed to this there was a 2% increase in kinetic energy losses for the 0.5% MFR case for the X/D=2 hole location as opposed to the X/D=1 hole location. There, however, is a clear trend of increasing losses with increasing MFR, as there tends to be a higher kinetic energy loss resulting in a higher kinetic energy loss coefficient.

3.4.4 Vane Surface Mach number Plots

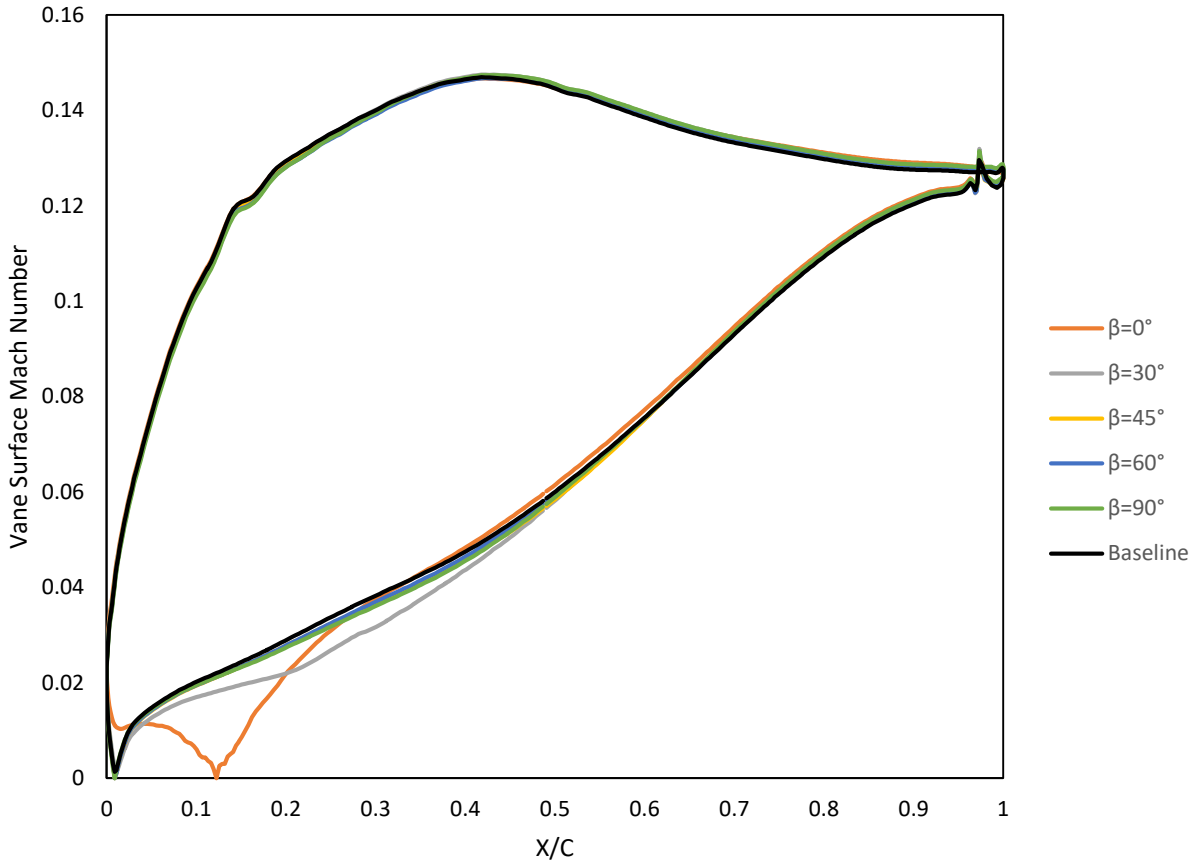

Figure 61: Midspan vane surface Mach number at X/D=1, α=30° and MFR=0.5%

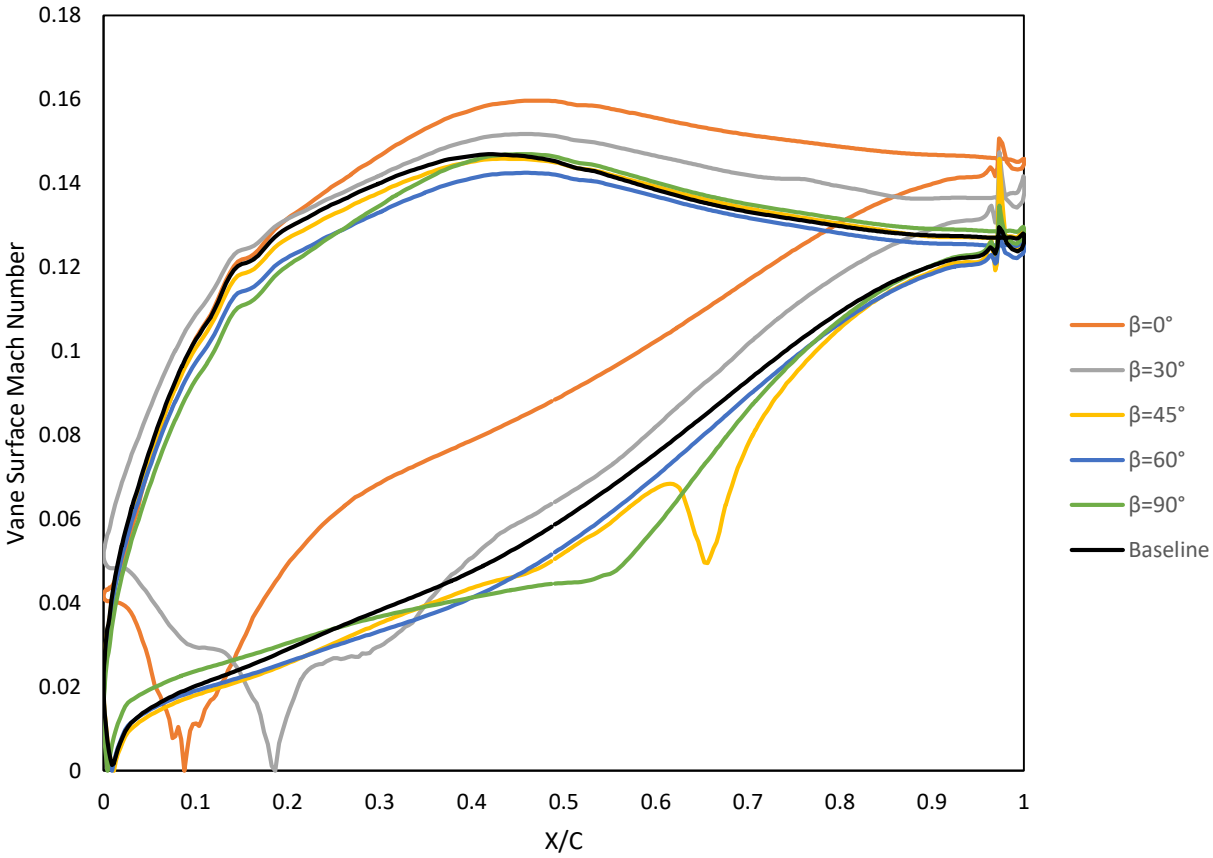

Figure 62: Midspan vane surface Mach number at X/D=1, α=30° and MFR=1%

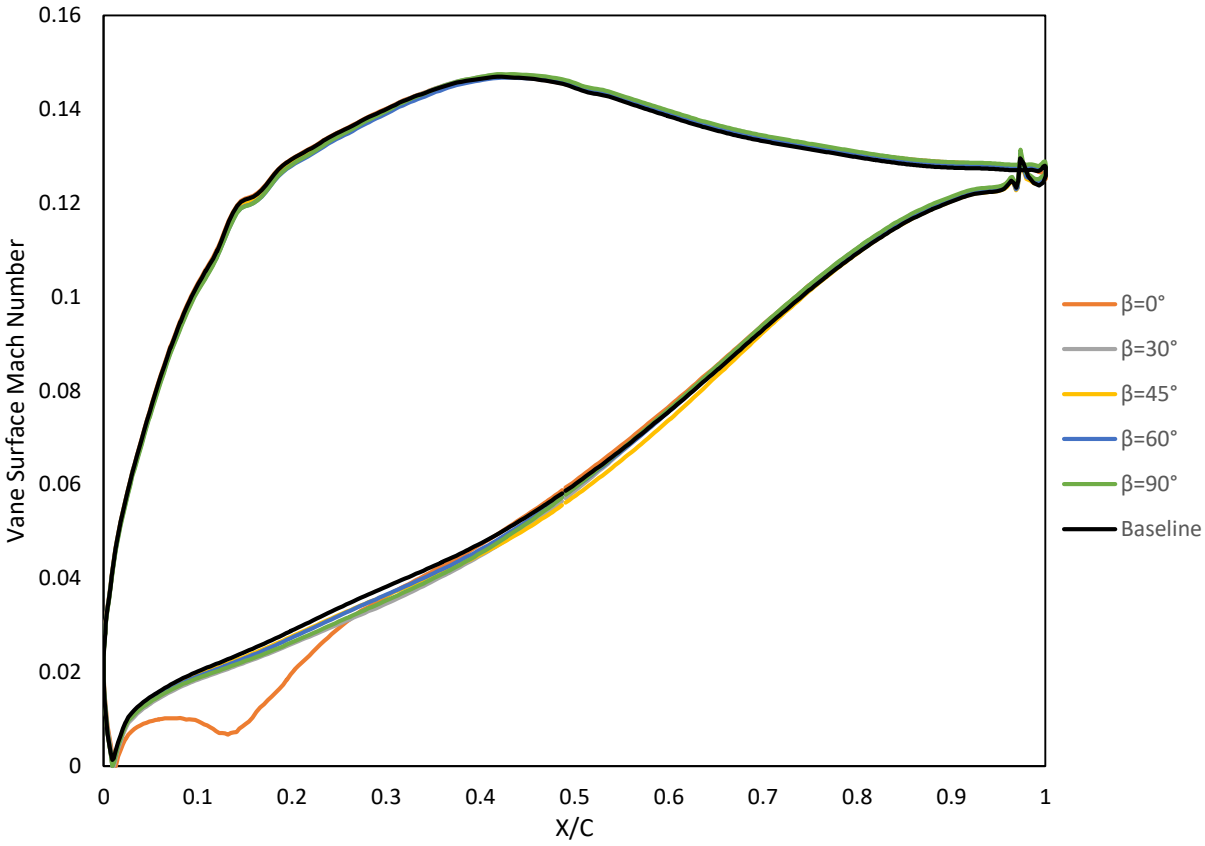

Figure 63: Midspan vane surface Mach number at X/D=2, α=30° and MFR=0.5%

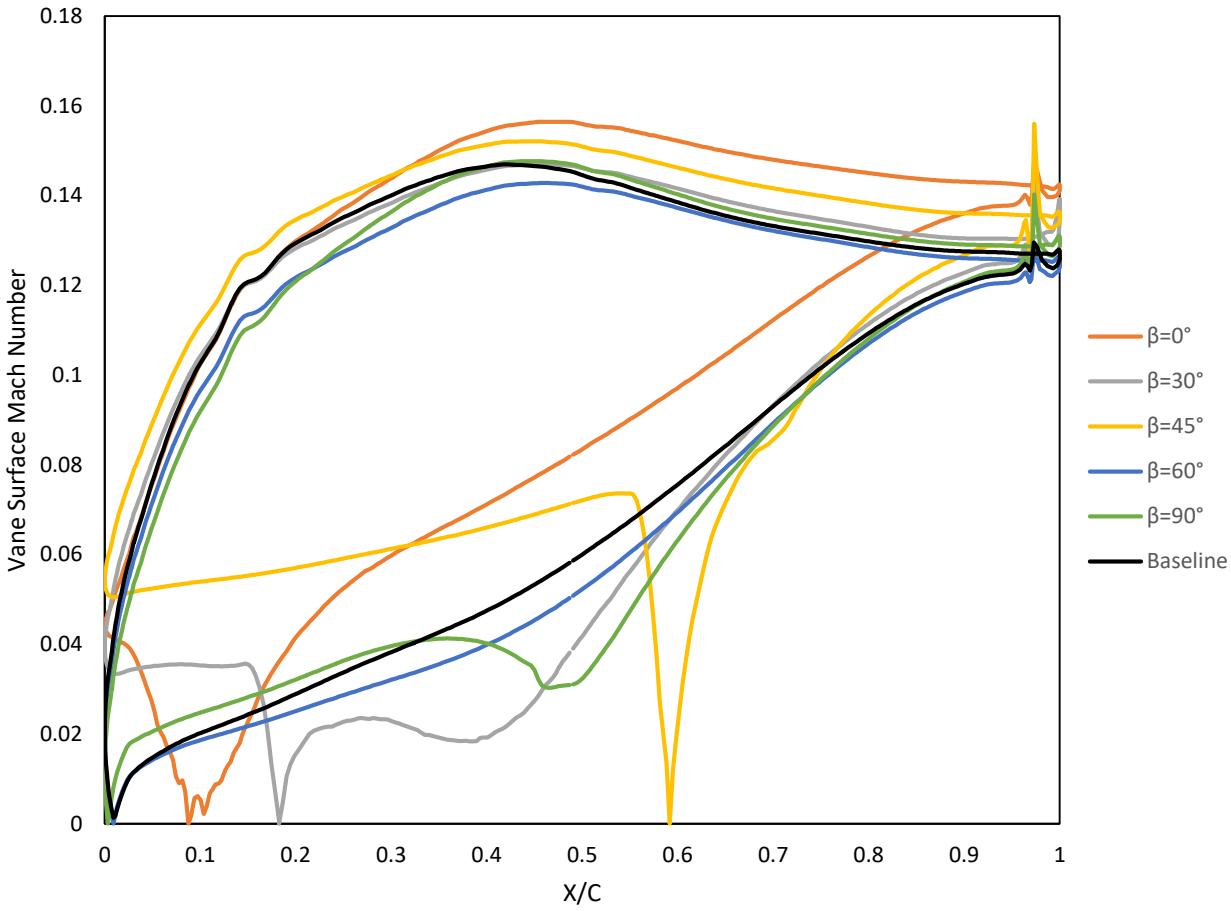

Figure 64: Midspan vane surface Mach number at X/D=2, α=30° and MFR=1%

When the vane surface Mach number profiles were compared with the baseline case, it was observed that the 60° compound angle presented the best case from the aerodynamic perspective, since it minimized the variation of the surface Mach number profile from the baseline case as opposed to the other compound angles.

3.5 Heat Transfer Study

To further confirm that the 60° compound angle combined with the 30° streamwise inclination angle is beneficial towards weakening the leading edge horseshoe vortex and delaying the pitchwise movement of the passage vortex towards the suction side of the vane passage, heat transfer studies were conducted by heating the mainstream air inlet combined with an endwall held at constant temperature. The leading edge vortex tends to cause intense mixing of flow at the leading edge and as the pressure side leg of the passage vortex is convected downstream develops into the passage vortex which also causes increased heat transfer. The passage vortex tends to cause creates a separation line along its path and directs the endwall boundary layer flow along the separation line towards the suction side of vane passage. A virtual barrier to the oncoming boundary layer is caused by the separation line and a new boundary layer begins developing downstream of the separation line. This boundary layer flow is very thin and is continuously removed by the cross-passage pressure gradient from the endwall region and pushed to the suction side even as new fluid from the mainstream migrates toward the gap left by the fluid convected away. This causes large portions of the endwall to be exposed to high heat transfer even when film cooling is employed upstream of the vane passage, since the coolant entering the vane passage tends to be low momentum fluid (in order to prevent separation from the endwall surface it aims to cool) which cannot surpass the passage vortex and feeds into it. Thus one can easily “see” the presence of the passage vortex merely by conducting a heat transfer study and identifying regions of high heat transfer in the vane passage stretching from the leading edge region downstream into the vane passage marked by the separation line which is traced by the passage vortex.

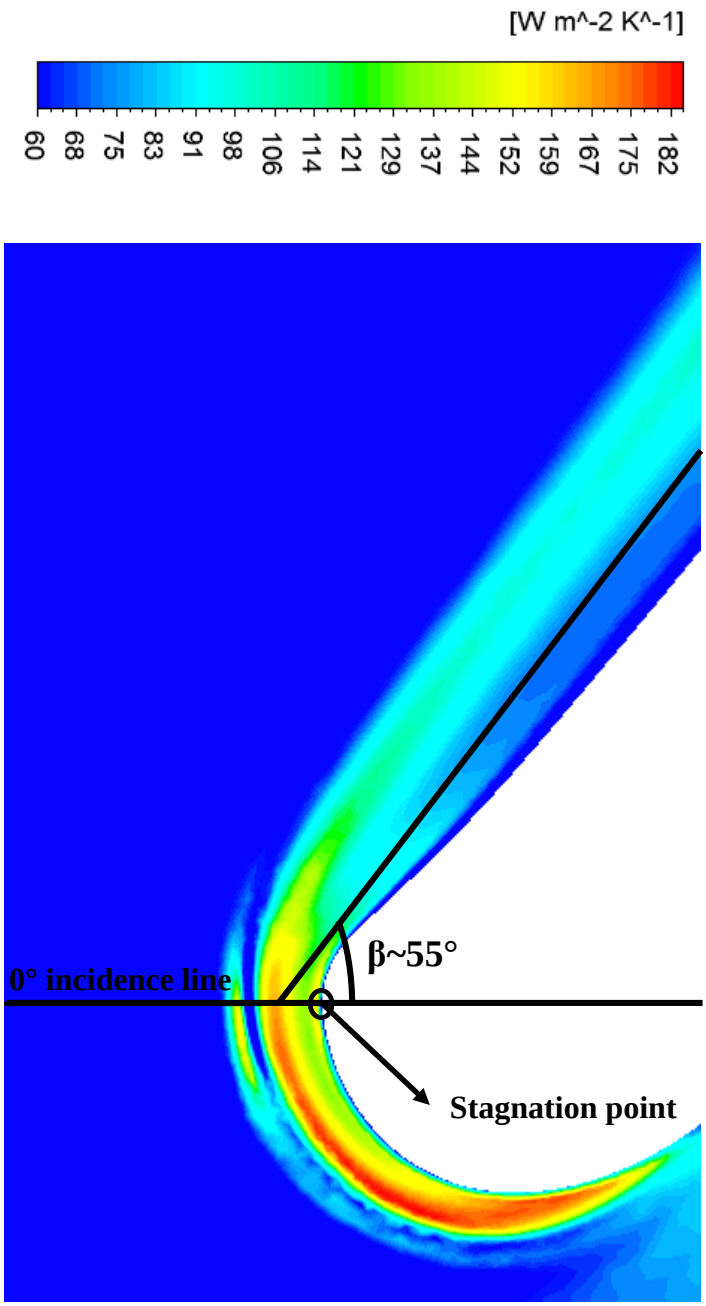

Figure 65: Depiction of high heat transfer bands at the endwall near the leading edge junction.

Thus an increased amount of coolant by way of increasing the mass flow ratio through the coolant and the use of cooling schemes to prevent flow separation from the endwall such as the tripod hole/trenched hole concept to prevent separation of flow from the endwall even at high coolant to mainstream mass flow ratios is required. An alternative to increasing the coolant flow would be to try and weaken the passage vortex, or delay the movement of the passage vortex to

the suction side (thereby moving the separation line further downstream and causing a net drop). The present heat transfer study is intended to be illustrative of the concept of using endwall fluid injection to weaken the leading edge horseshoe vortex and modify the separation line by delaying the movement of the passage vortex and reducing the area exposed to high heat flux values.

3.5.1 Boundary Conditions

The main domain used in the heat transfer study was similar to the one used in the previous studies. Four different cases in addition to the baseline were simulated with a mainstream heated to 325 K at the inlet and the endwall temperature held at 300K. A second order accurate Finite Volume discretization scheme Steady state RANS equations solve the mass and momentum conservation equations similar to the flowfield studies. The heat flux and the heat transfer contour profiles were studied at the endwall upstream of the guide vanes and in the vane passage.

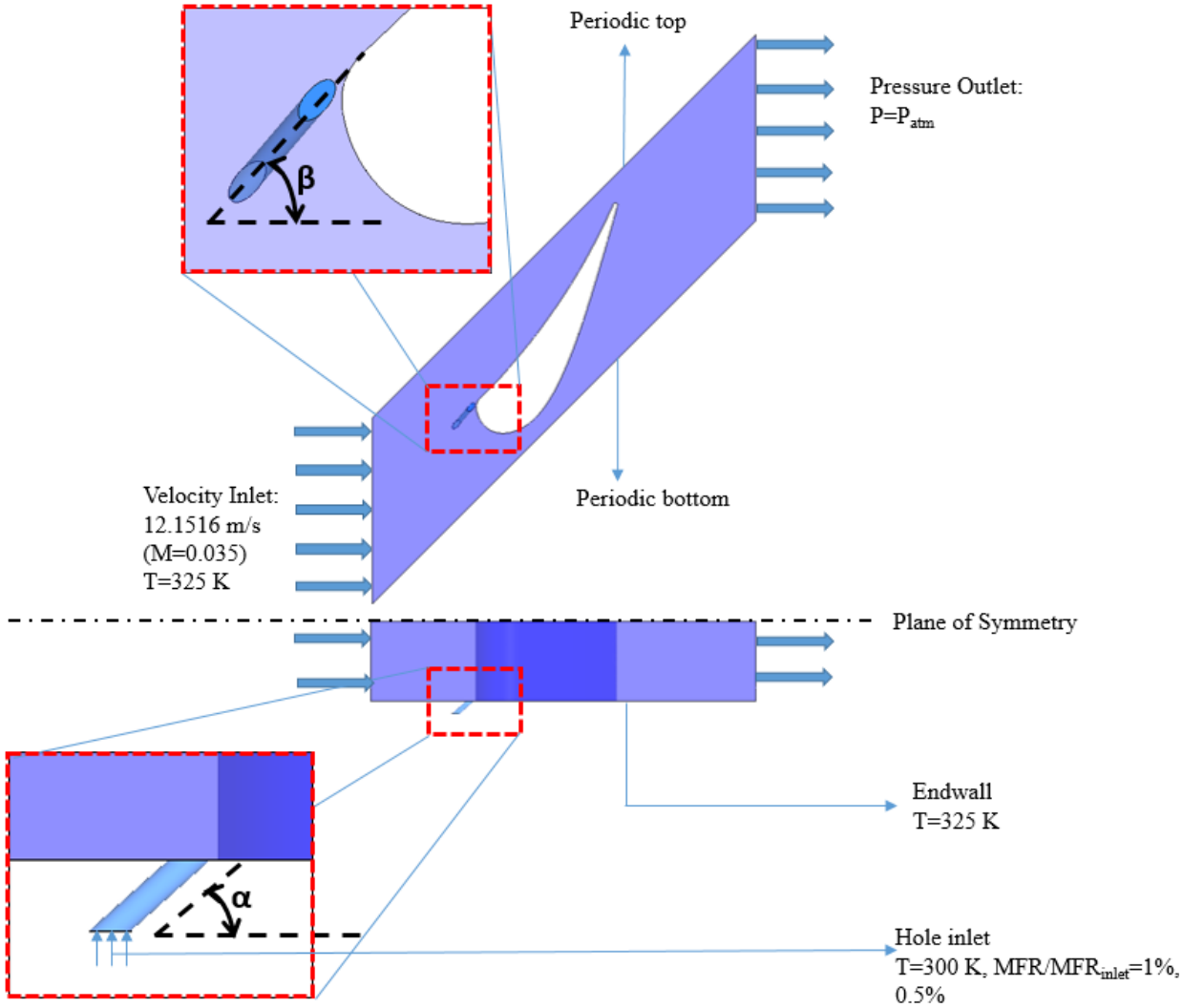

Figure 66: Schematic of the Vane Cascade geometry with boundary conditions indicated

3.5.2 Heat Transfer Study Results

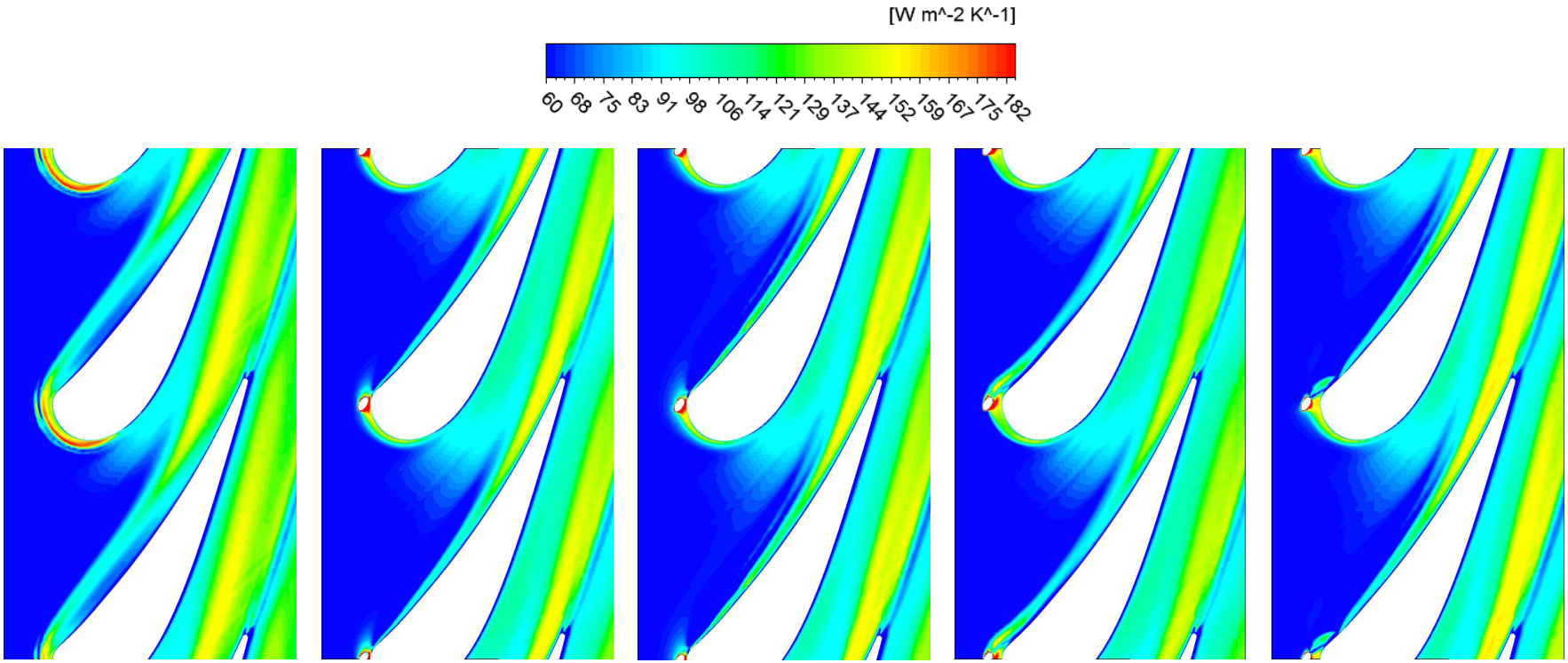

a) Baseline **b) X=D, α=30°, β=60°, MFR: 0.5%** **c) X=D, α=30°, β=60°, MFR: 1%** **d) X=2D, α=30°, β=60°, MFR: 0.5%** **e) X=2D, α=30°, β=60°, MFR: 1%**

Figure 67: Endwall Heat Transfer Coefficient Contours depicting passage vortex path

Figure 67: Endwall Heat Transfer Coefficient Contours depicting passage vortex path shows the endwall heat transfer coefficient contours for each of the cases tested in the heat transfer study. Each of the cases depicts the change in the path of the passage vortex and the change in the scouring effect caused by the change in the passage vortex. Table 20 shows the average heat transfer coefficient values on the endwall calculated using the heat flux values on the endwall surface and the mainstream temperature. It is clearly visible that the injection of fluid from the endwall has had a positive effect on the heat transfer of the endwall due to the fact that the separation of the endwall boundary layer by the passage vortex in the vane passage is delayed as compared to the baseline. This allows a greater portion of the endwall to remain covered by the lower temperature endwall boundary layer preventing direct exposure to the hotter mainstream gas.

Table 21: Average endwall heat transfer coefficient values for heat transfer studies

Case	Average HTC on Endwall (W/m^2-K)	% change with respect to baseline
Baseline	92.354	0(Baseline)
X/D=1, α=30°, β=60°, MFR: 0.5%	85.540	-7.378
X/D=1, α=30°, β=60°, MFR: 1%	85.093	-7.862
X/D=2, α=30°, β=60°, MFR: 0.5%	84.073	-8.966
X/D=2, α=30°, β=60°, MFR: 1%	84.251	-8.774

It can be seen from the above results that there is a drop in heat transfer in all the above cases with the low MFR case for the hole located at X/D=2 with the streamwise inclination angle of 30° and compound angle of 60° providing nearly 9% drop in the heat transfer coefficient in the vane passage.

CHAPTER 4: CONCLUSIONS

The flowfield close to the endwall upstream of a first stage nozzle guide vane and the inter-vane passage in a vane cascade was simulated and the formation of the leading edge horseshoe vortex and the passage vortex was studied. Endwall fluid injection through a cylindrical hole was employed to study the effects on the passage vortex and the injection parameters namely the hole location on the endwall, the mass flow rate of the fluid injected, the streamwise inclination angle, and the compound angle. These were varied and the results analyzed in a series of studies to pick the corresponding parameter that would cause the least harm to the vane aerodynamics while disrupting the leading edge vortex and altering the passage vortex trajectory positively. During the study to identify the most suitable MFR for the endwall injection, it was decided based on the leading edge velocity streamlines and swirling strength contours in the vane passage in combination with loss coefficient values that the MFR range that would best serve the purpose was 0.5% to 1% of the mainstream mass flow. Thus two mass flow rates (0.5% and 1%) were selected and used for further testing in order to save on computational time rather than test the entire range of mass flow ratios. For the α-angle study, three streamwise inclination angles were studied and the 30° hole was shown to have the least adverse effect on the loss coefficient values while having a potential to disturb the passage vortex. Five different β-angles from 0° to 90° were tested and during the study, and the 60° compound angle was chosen based on the absence of the leading edge vortex, delaying of the passage vortex development. In all, four cases with the compound angle 60° were chosen for conducting heat transfer studies. Heat transfer studies were conducted to observe the benefits of altering the passage vortex path by looking at the imprint of the passage vortex on the endwall, which is separated into regions of high and low heat transfer. Based on the average HTC drop in the vane passage, it was seen that there were drops in heat transfer in each of the 60° cases as compared with the baseline ranging from 7.3% to 9% with the X/D=2, MFR=0.5 case having the largest drop in heat transfer.

REFERENCES

[1] L. S. Langston, "Secondary flows in axial turbines--a review.," *Annals of the New York Academy of Sciences*, vol. 934, no. 1. pp. 11–26, 2001.

[2] W. A. Eckerle and L. S. Langston, "Horseshoe Vortex For ' mation Around a Cylinder," vol. 109, no. April, 1987.

[3] S. Hada, M. H. Industries, K. Takeishi, Y. Oda, S. Mori, and Y. Nuta, "the Effect of Leading Edge Diameter," *Cycle*, pp. 813–823, 2008.

[4] K. S. Hermanson and K. a. Thole, "Effect of Inlet Conditions on Endwall Secondary Flows," *J. Propuls. Power*, vol. 16, no. 2, pp. 286–296, 2000.

[5] J. D. Denton, "Loss Mechanisms in Turbomachines," *J. TurboMach.*, vol. 115, no. 4, p. 621, 1993.

[6] S. Harrison, "Secondary Loss Generation in a Linear Cascade of High-Turning Turbine Blades," *J. TurboMach.*, vol. 112, no. 4, p. 618, 1990.

[7] L. S. Langston, M. L. Nice, and R. M. Hooper, "Three-Dimensional Flow Within a Turbine Cascade Passage," *J. Eng. Power*, vol. 99, no. 1, p. 21, 1977.

[8] L. S. Langston, "Crossflows in a Turbine Cascade Passage," *J. Eng. Power*, vol. 102, no. 4, p. 866, 1980.

[9] C. H. Sieverding, "Recent Progress in the Understanding of Basic Aspects of Secondary Flows in Turbine Blade Passages," *J. Eng. Gas Turbines Power*, vol. 107, no. April 1985, p. 248, 1985.

[10] O. P. Sharma and T. L. Butler, "Predictions of Endwall Losses and Secondary Flows in Axial Flow Turbine Cascades," *J. TurboMach.*, vol. 109, no. 86, p. 229, 1987.

[11] H. Wang, S. J. Olson, R. J. Goldstein, and E. R. G. Eckert, "s FLOW VISUALIZATION IN A LINEAR TURBINE CASCADE," no. 1985, 2015.

[12] C. H. Sieverding and P. Van den Bosche, "The use of coloured smoke to visualize secondary flows in a turbine-blade cascade," *J. Fluid Mech.*, vol. 134, no. -1, p. 85, 1983.

[13] R. J. Goldstein and R. a. Spores, "Turbulent Transport on the Endwall in the Region Between Adjacent Turbine Blades," *J. Heat Transfer*, vol. 110, no. November 1988, p. 862, 1988.

[14] T. J. Praisner and C. R. Smith, "The Dynamics of the Horseshoe Vortex and Associated

Endwall Heat Transfer—Part I - Temporal Behavior," *J. TurboMach.*, vol. 128, no. 4, p. 755, 2006.

[15] M. B. Kang, a. Kohli, and K. a. Thole, "Heat Transfer and Flowfield Measurements in the Leading Edge Region of a Stator Vane Endwall," *J. TurboMach.*, vol. 121, no. 3, pp. 558–568, 1999.

[16] J. T. Chung, T. W. Simon, and J. Buddhavarapu, "Three-dimensional flow near the blade/endwall junction of a gas turbine: application of a boundary layer fence," in *ASME 1991 International Gas Turbine and Aeroengine Congress and Exposition*, 1991, pp. V004T09A008–V004T09A008.

[17] N. V Aunapu, R. J. Volino, K. A. Flack, and R. M. Stoddard, "Secondary Flow Measurements in a Turbine Passage With Endwall Flow Modification," *J. TurboMach.*, vol. 122, no. 4, p. 651, 2000.

[18] T. Kawai, S. Shinoki, and T. Adachi, "Secondary flow control and loss reduction in a turbine cascade using endwall fences," *JSME Int. journal Ser. 2, Fluids Eng. heat Transf. power, Combust. Thermophys. Prop.*, vol. 32, no. 3, pp. 375–387, 1989.

[19] L. Qi, Z. Zou, P. Wang, T. Cao, and H. Liu, "Control of secondary flow loss in turbine cascade by streamwise vortex," *Comput. Fluids*, vol. 54, no. 1, pp. 45–55, 2012.

[20] P. Doerffer, P. Flaszynski, and F. Magagnato, "Streamwise vortex interaction with a horseshoe vortex," *J. Therm. Sci.*, vol. 12, no. 4, pp. 304–309, 2003.

[21] K. V. Panchal, S. Abraham, S. V Ekkad, W. Ng, A. S. Lohaus, and M. E. Crawford, "Effect of Endwall Contouring on a Transonic Turbine Blade Passage: Part 2—Heat Transfer Performance," *Vol. 4 Heat Transf. Parts A B*, p. 151, 2012.

[22] A. Roy, "Experimental Study of Gas Turbine Endwall Cooling with Endwall Contouring under Transonic Conditions Arnab Roy Dissertation submitted to the faculty of Virginia Polytechnic Institute and State University in partial fulfillment of the requirement for the d," *Dissertation*, 2014.

[23] G. A. Zess and K. A. Thole, "Computational design and experimental evaluation of using a leading edge fillet on a gas turbine vane," in *ASME Turbo Expo 2001: Power for Land, Sea, and Air*, 2001, pp. V003T01A083–V003T01A083.

[24] A. A. Thrift and K. A. Thole, "Influence of flow injection angle on a leading-edge horseshoe vortex," *Int. J. Heat Mass Transf.*, vol. 55, no. 17–18, pp. 4651–4664, 2012.

[25] N. Sundaram and K. A. Thole, “Film-Cooling Flowfields With Trenched Holes on an Endwall,” *ASME Conf. Proc.*, vol. 2008, no. 43147, pp. 121–132, 2008.

[26] A. M. Levchenya, E. M. Smirnov, and V. D. Goryachev, “RANS-based numerical simulation and visualization of the horseshoe vortex system in the leading edge endwall region of a symmetric body,” *Int. J. Heat Fluid Flow*, vol. 31, no. 6, pp. 1107–1112, 2010.

[27] K. Takeishi, Y. Oda, J. Seguchi, and S. Kozono, “Effect of endwall film cooling upstream of an airfoil/endwall junction to suppress the formation of horseshoe vortex in a symmetric airfoil,” in *ASME Turbo Expo 2013: Turbine Technical Conference and Exposition*, 2013, pp. V03BT13A052–V03BT13A052.

[28] Y. Oda, K. Takeishi, S. Hada, and Y. Nuta, “Large eddy simulations of endwall heat transfer around junction of a symmetric vane,” in *ICHMT DIGITAL LIBRARY ONLINE*, 2009.

[29] F. Kost and M. Nicklas, “Film-cooled turbine endwall in a transonic flow field: Part I - Aerodynamic measurements,” *J. TurboMach.*, vol. 123, no. 4, pp. 709–719, 2001.

[30] B. V. Ravi, S. Deshpande, S. Ramesh, P. D. Dhilipkumar, and S. Ekkad, “Film Cooling Performance of Tripod Holes on the Endwall Upstream of a First Stage Nozzle Guide Vane,” in *ASME 2015 International Mechanical Engineering Congress and Exposition*, 2015, pp. V08BT10A021–V08BT10A021.

[31] T. I.-P. Shih and Y.-L. Lin, “Controlling Secondary-Flow Structure by Leading-Edge Airfoil Fillet and Inlet Swirl to Reduce Aerodynamic Loss and Surface Heat Transfer,” *ASME Conf. Proc.*, vol. 2002, no. 36088, pp. 1023–1032, 2002.

[32] A. Mensch and K. A. Thole, “Overall Effectiveness and Flowfield Measurements for an Endwall With Nonaxisymmetric Contouring,” *J. TurboMach.*, vol. 138, no. 3, p. 031007, 2015.

[33] A. M. Levchenya and E. M. Smirnov, “CFD-analysis of 3D flow structure and endwall heat transfer in a transonic turbine blade cascade: effects of grid refinement,” *CD ROM Proc. West East High Speed Flow F. Conf.*, no. November, 2007.

[34] D. M. Blot, A. Roy, S. V Ekkad, W. Ng, A. S. Lohaus, and M. E. Crawford, “GT2013-94591,” pp. 1–12, 2014.

[35] K. Sangston, J. Little, M. E. Lyall, and R. Sondergaard, “End Wall Loss Reduction of High Lift Low Pressure Turbine Airfoils Using Profile Contouring -- Part II: Validation,” *J. TurboMach.*, vol. 136, no. 8, p. 081006, 2014.

[36] P. Chakraborty, S. Balachandar, and R. J. Adrian, “On the relationships between local vortex identification schemes,” *J. Fluid Mech.*, vol. 535, pp. 189–214, 2005.

[37] J. Zhou, R. J. Adrian, S. Balachandal, and T. M. Kendall, “Mechanisms for generating coherent packets of hairpin vortices in channel flow,” *J. Fluid Mech.*, vol. 387, p. S002211209900467X, 1999.

[38] M. Raffel and F. Kost, “Investigation of aerodynamic effects of coolant ejection at the trailing edge of a turbine blade model by PIV and pressure measurements,” *Exp. Fluids*, vol. 24, no. 5–6, pp. 447–461, 1998.

APPENDIX

MFR Study

Table 22: Details of parameters tested in MFR study for 30 degree hole

x/d	α	β	MFR
2	30	0	0.1
2	30	0	0.25
2	30	0	0.5
2	30	0	0.75
2	30	0	1

Table 23: Details of parameters tested in MFR study for 90 degree hole

x/d	α (deg)	β (deg)	MFR (%)
2	90	N/A	0.1
2	90	N/A	0.25
2	90	N/A	0.5
2	90	N/A	0.75
2	90	N/A	1

Leading Edge Vortex Streamlines

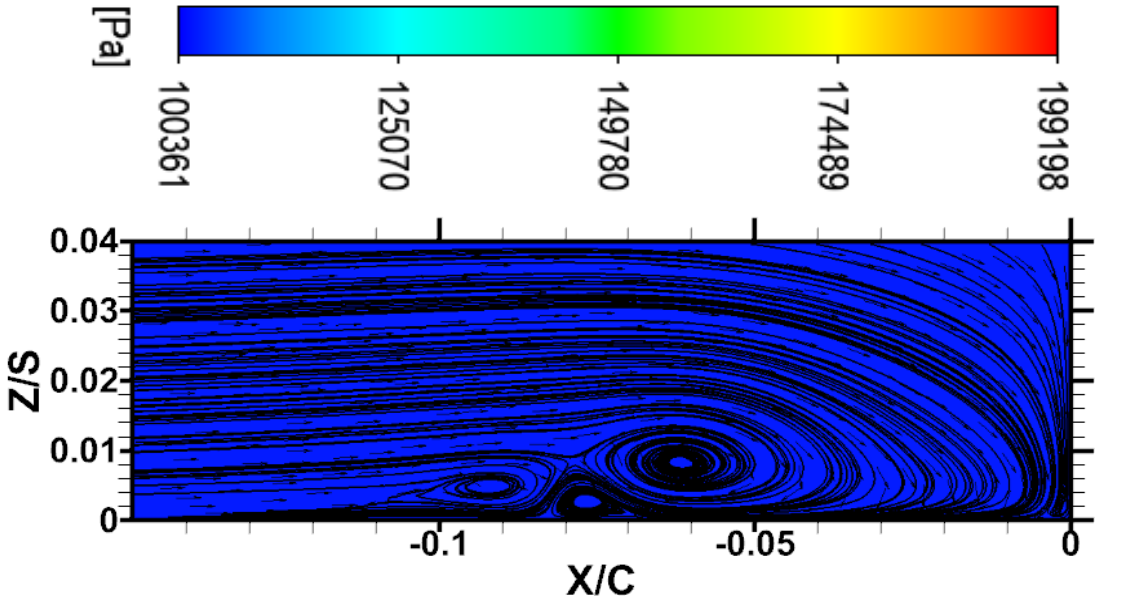

a) Baseline

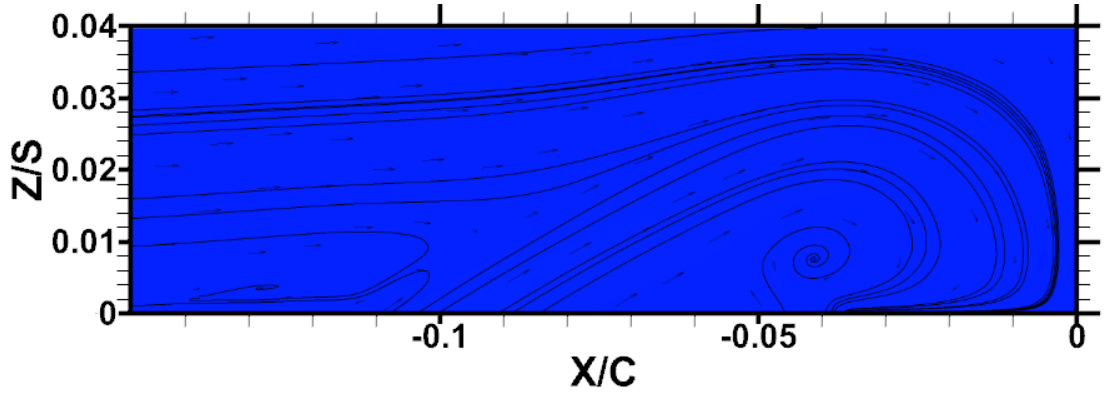

b) MFR: 0.1%

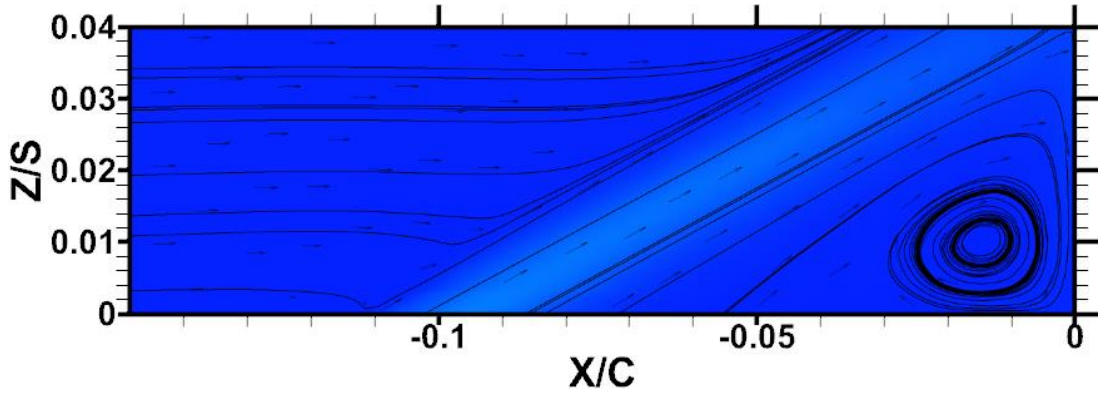

c) MFR: 0.25%

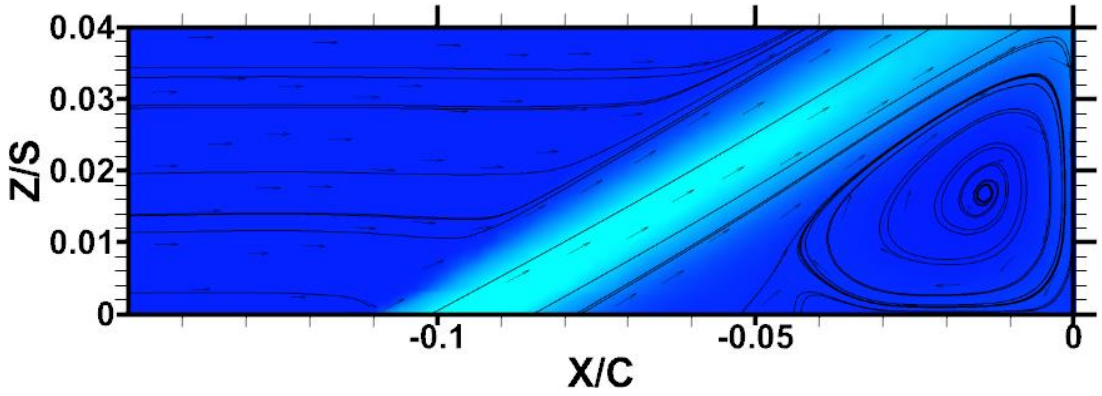

d) MFR: 0.5%

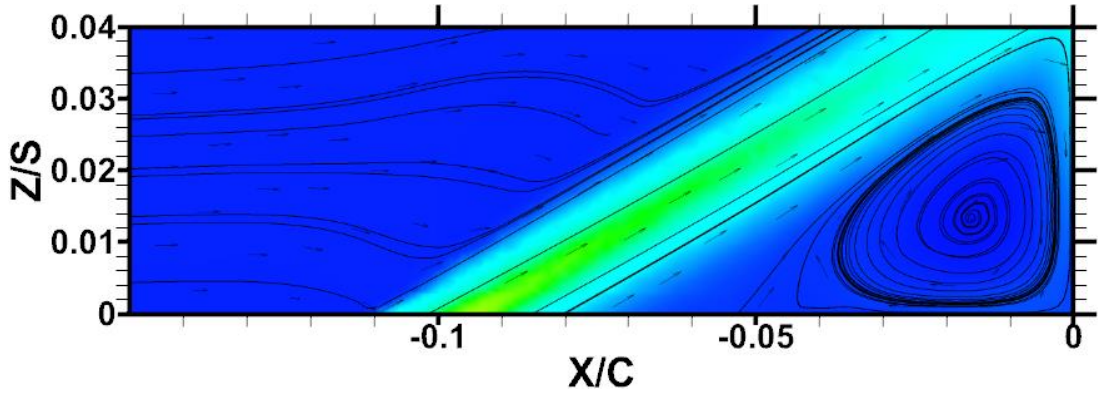

e) MFR: 0.75%

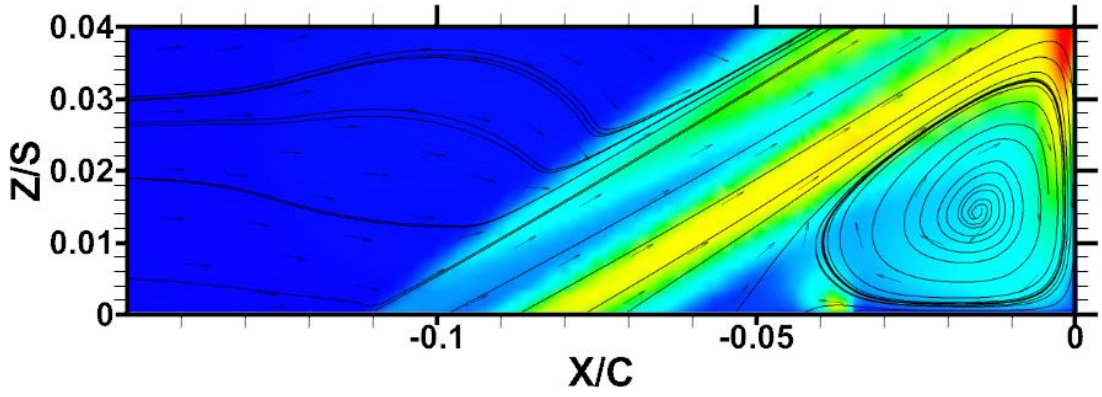

f) MFR: 1%

Figure 68: Leading edge velocity streamlines and vectors overlaid with total pressure (absolute) contours at different mass flow ratios for α=30° and X=2D

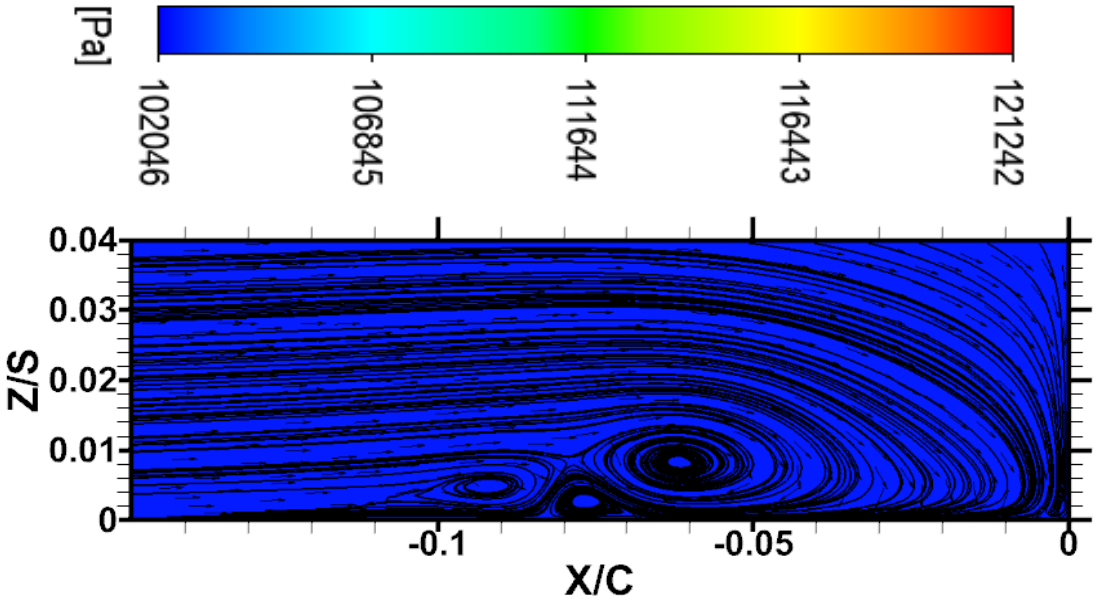

a) Baseline

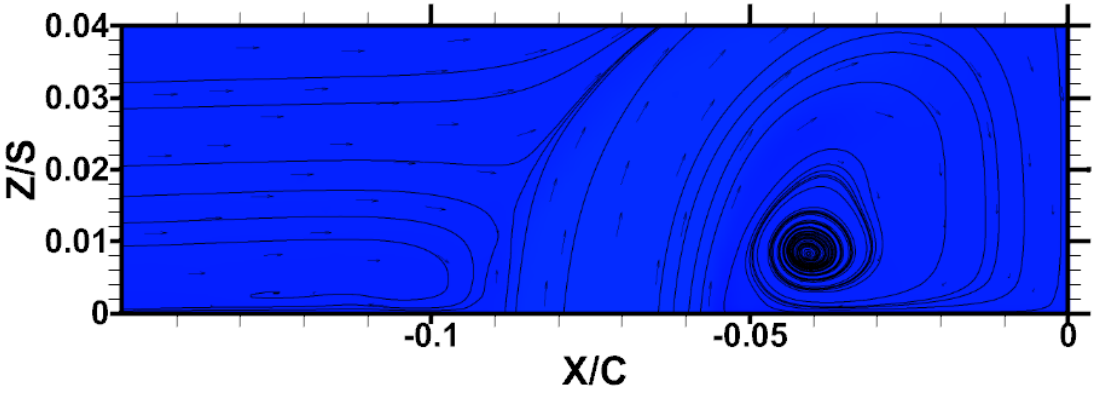

b) MFR: 0.1%

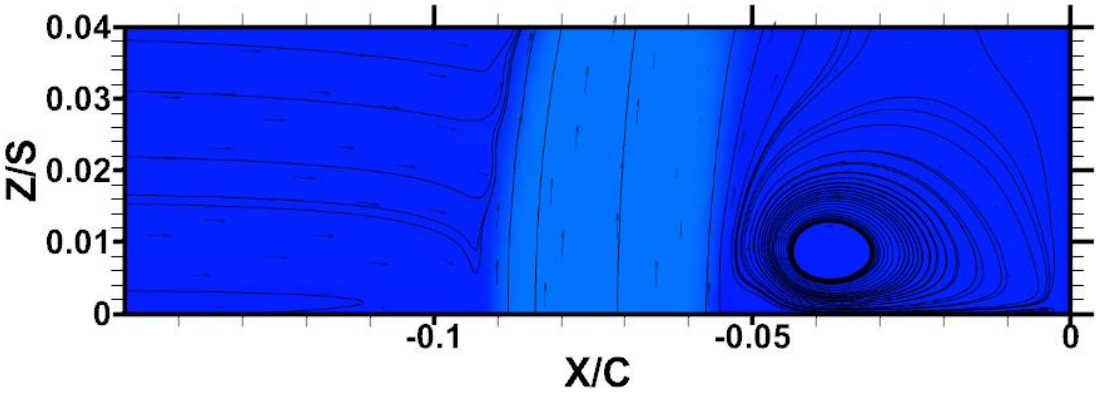

c) MFR: 0.25%

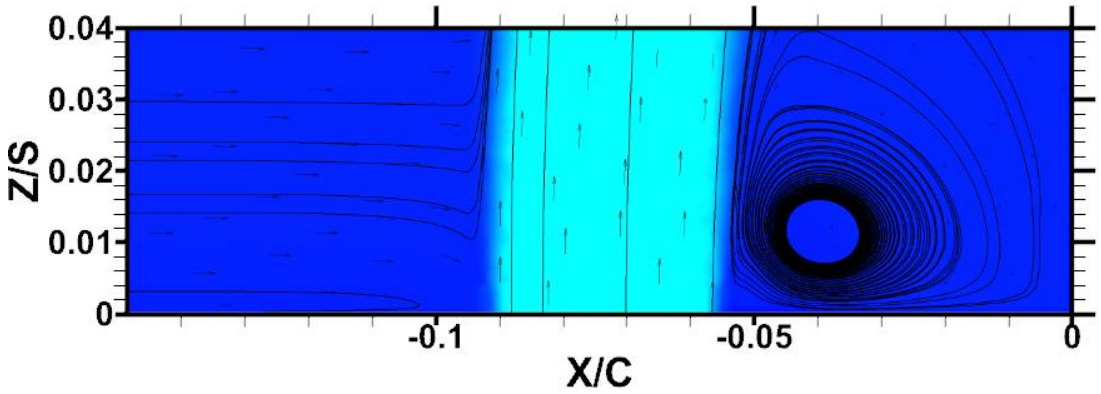

d) MFR: 0.5%

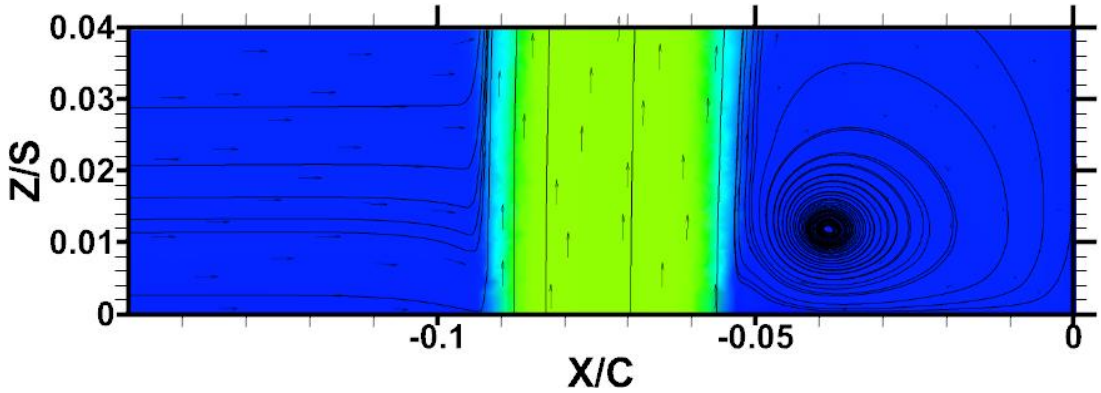

e) MFR: 0.75%

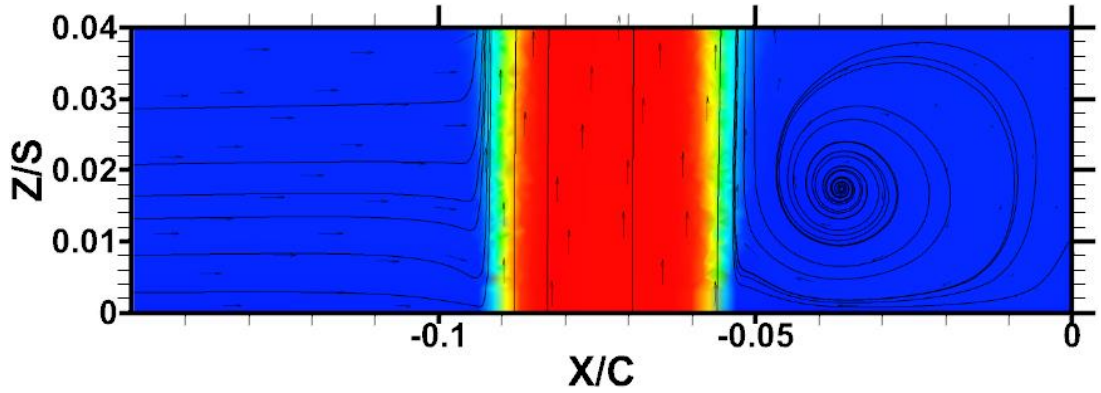

f) MFR: 1%

Figure 69: Leading edge velocity streamlines and vectors overlaid with total pressure (absolute) contours at different mass flow ratios for α=90° and X=2D.

Passage Vortex Swirling Strength Plots

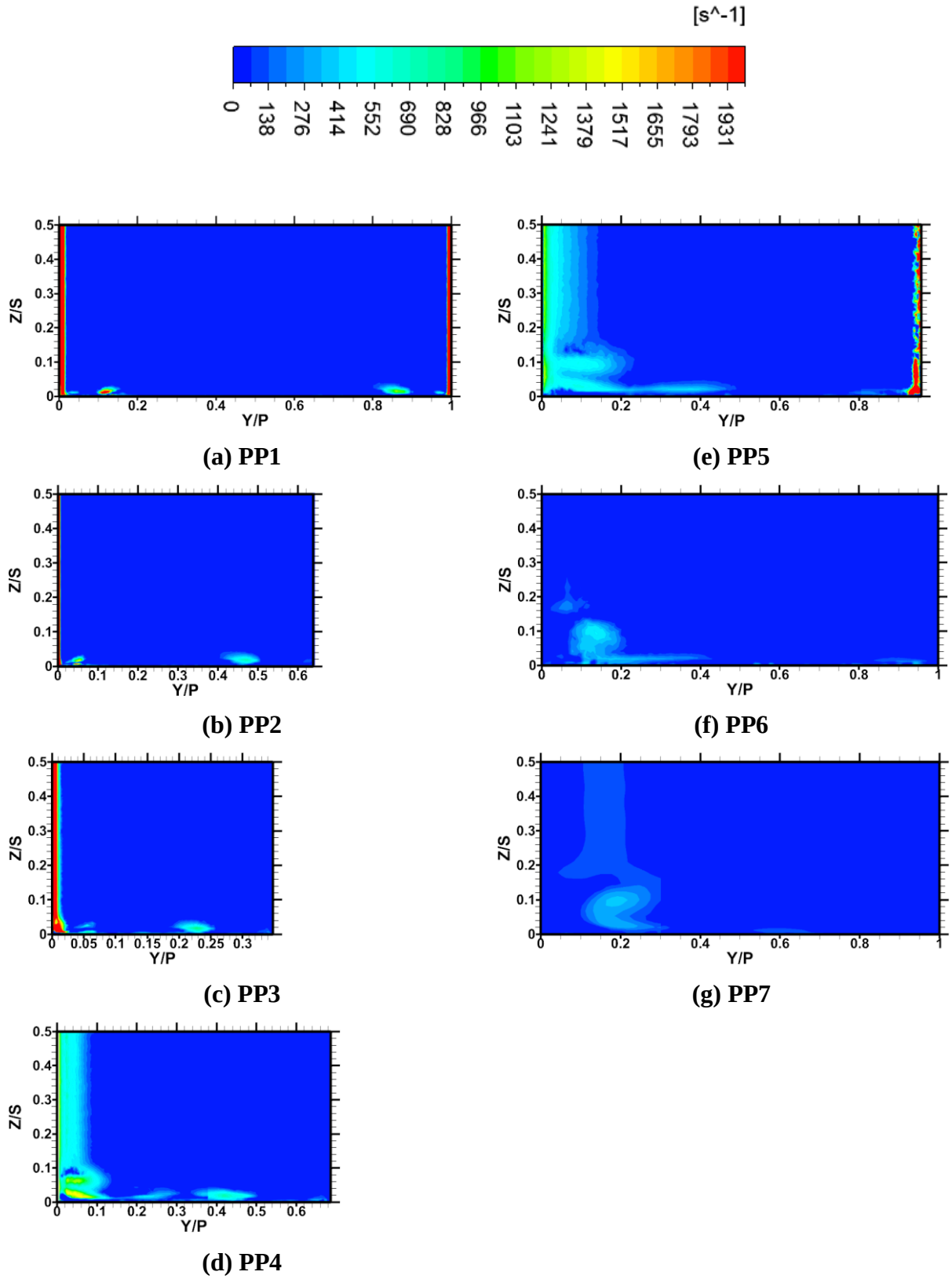

(a) PP1

(e) PP5

(b) PP2

(f) PP6

(c) PP3

(g) PP7

(d) PP4

Figure 70: Swirling Strength Contours at various axial planes through the passage for the baseline case

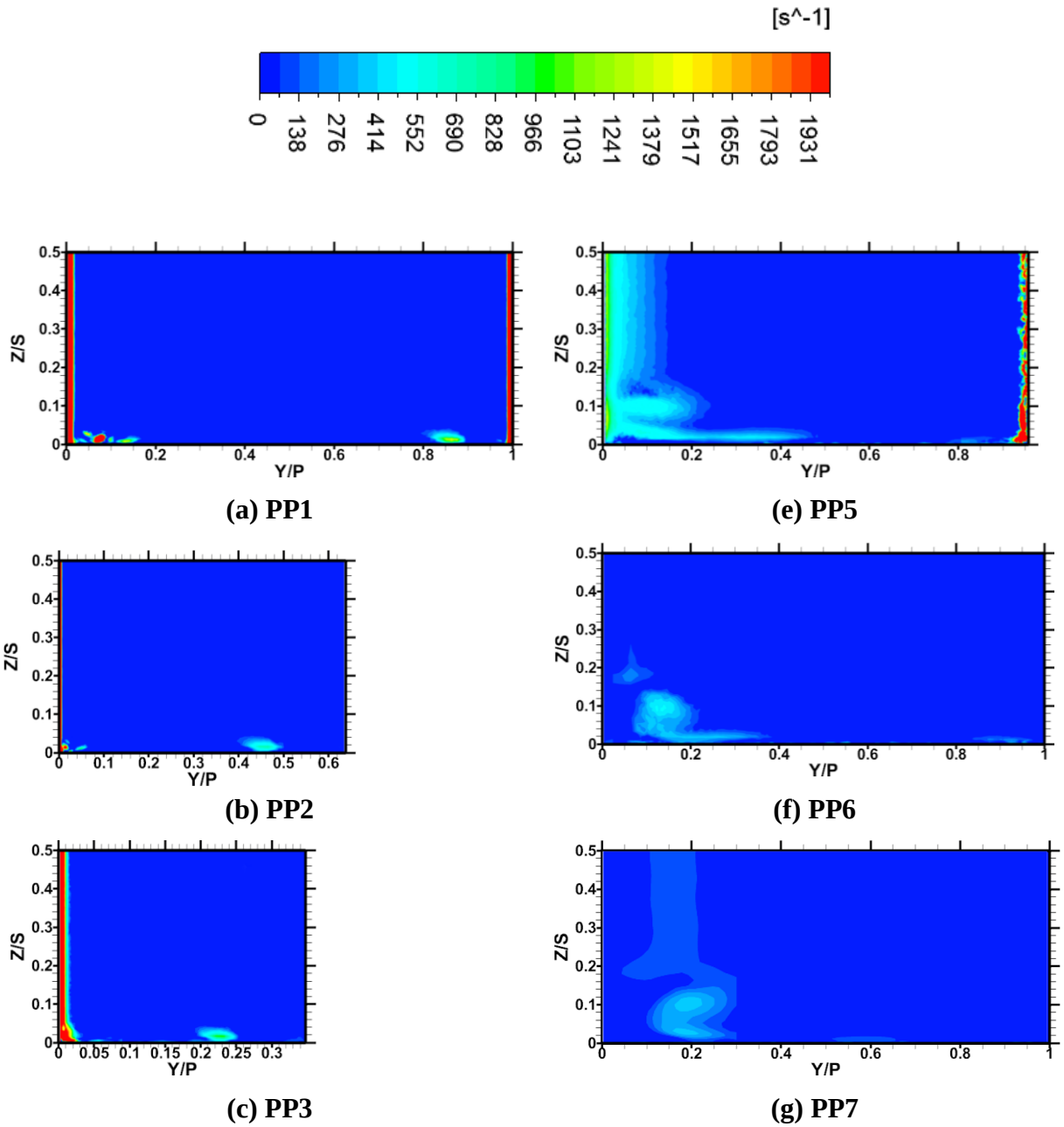

(a) PP1

(e) PP5

(b) PP2

(f) PP6

(c) PP3

(g) PP7

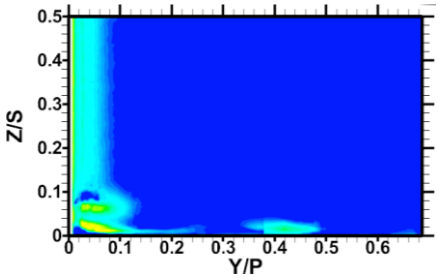

(d) PP4

Figure 71: Swirling Strength Contours at various axial planes through the passage for the case X_h=2D, α=30°, β=0, MFR=0.1%

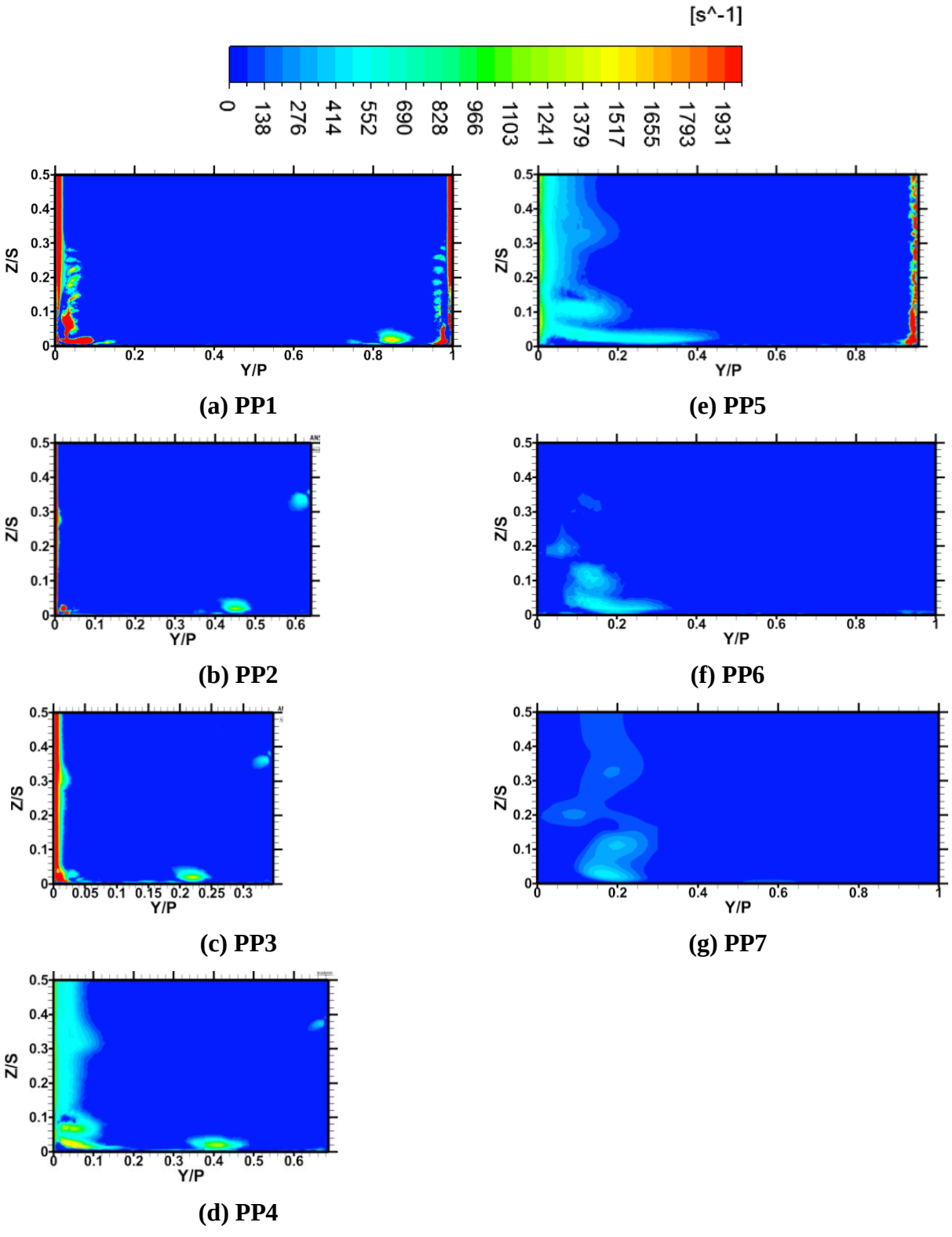

Figure 72: Swirling Strength Contours at various axial planes through the passage for the case X_h=2D, α=30°, β=0, MFR=0.25%

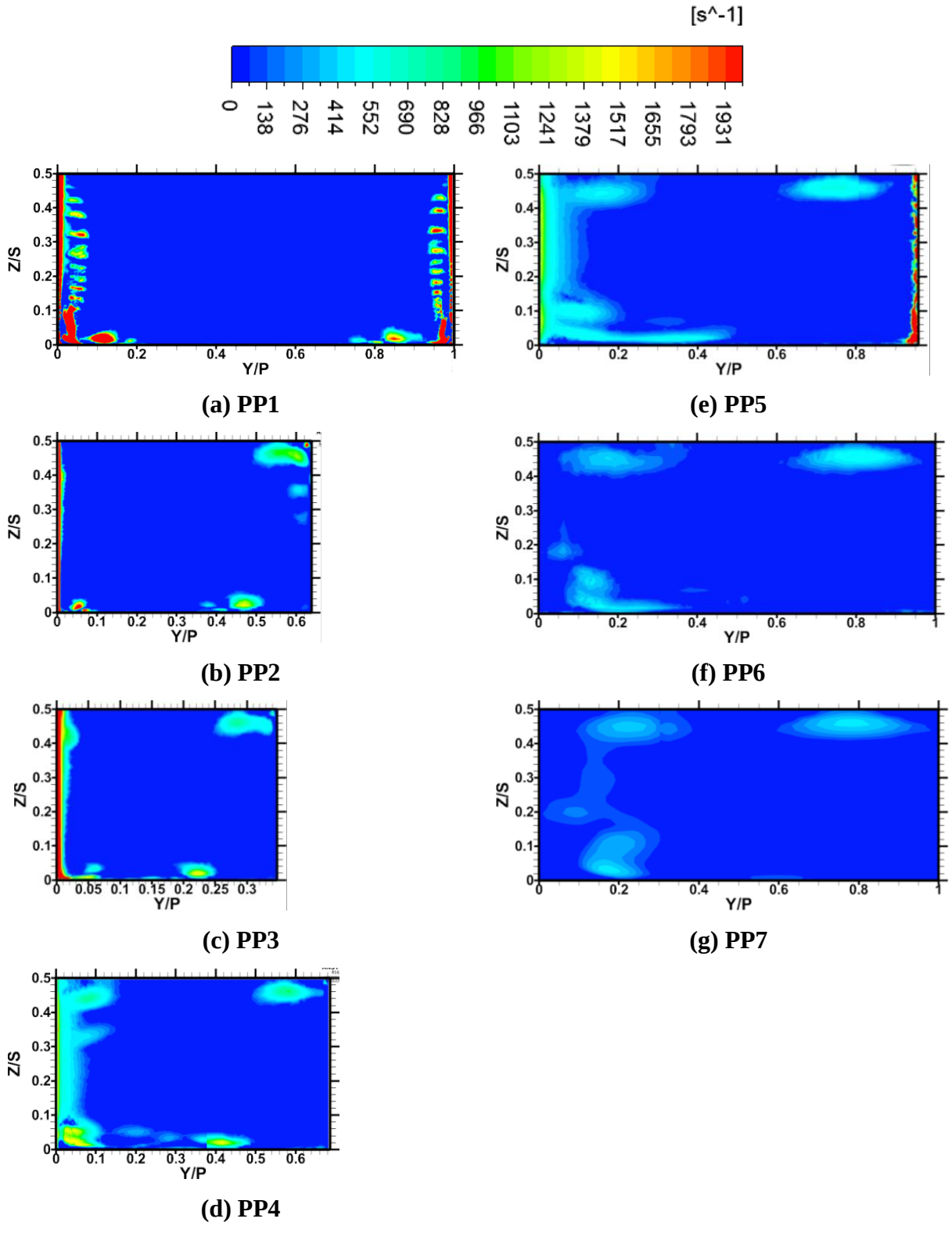

(a) PP1

(e) PP5

(b) PP2

(f) PP6

(c) PP3

(g) PP7

(d) PP4

Figure 73: Swirling Strength Contours at various axial planes through the passage for the case X_h=2D, α=30°, β=0, MFR=0.5%

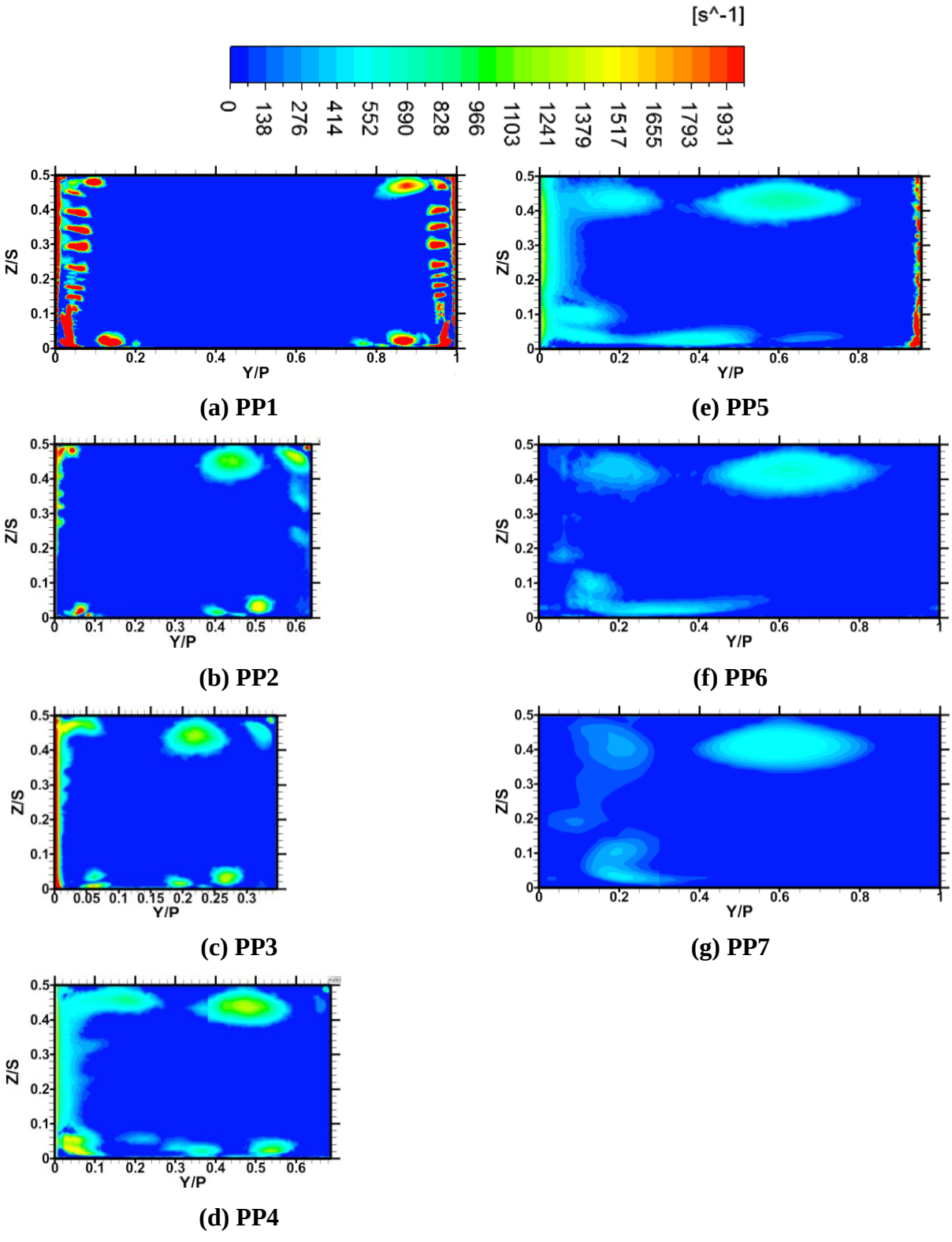

(a) PP1

(e) PP5

(b) PP2

(f) PP6

(c) PP3

(g) PP7

(d) PP4

Figure 74: Swirling Strength Contours at various axial planes through the passage for the case X_h=2D, α=30°, β=0, MFR=0.75%

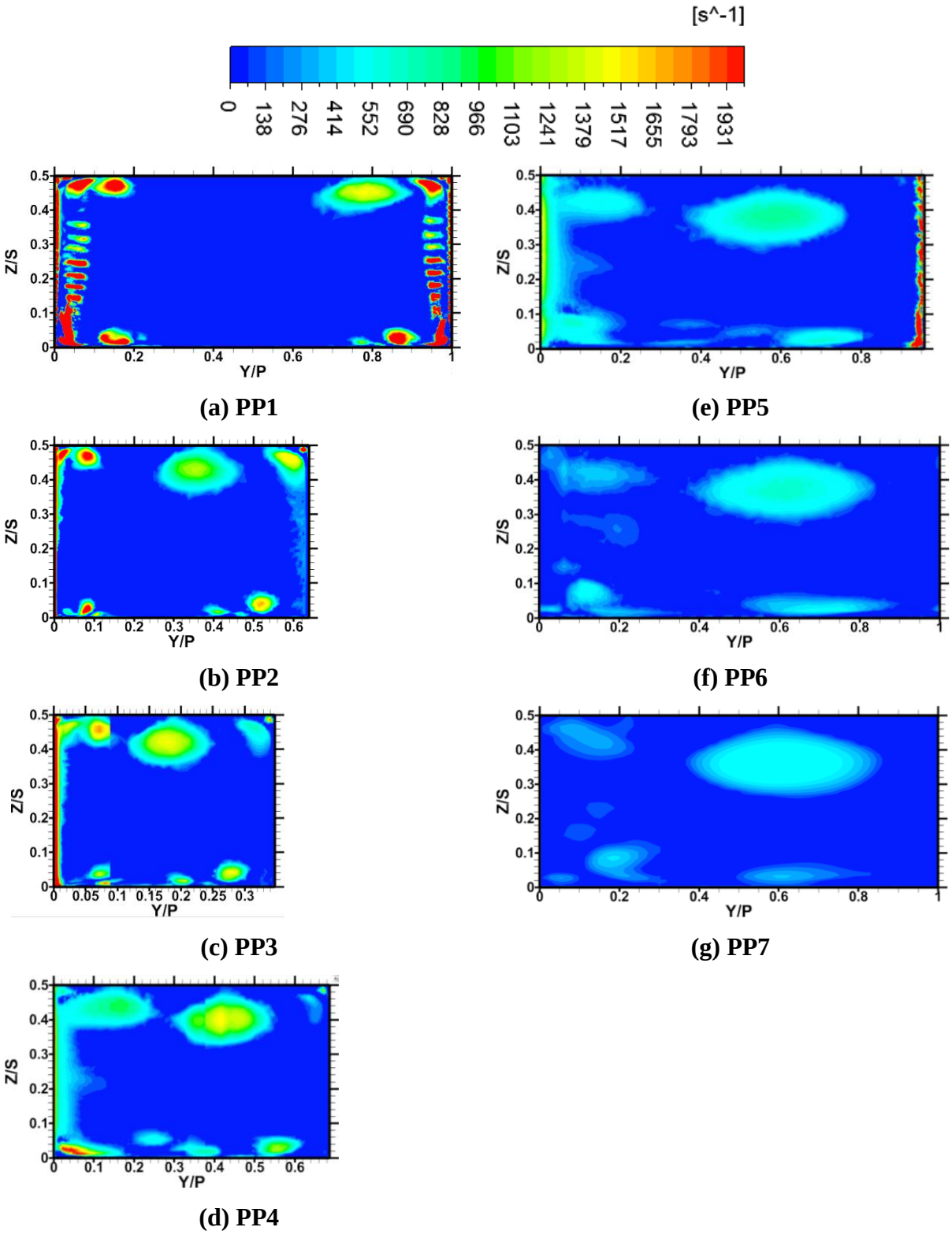

Figure 75: Swirling Strength Contours at various axial planes through the passage for the case X_h=2D, α=30°, β=0, MFR=1%

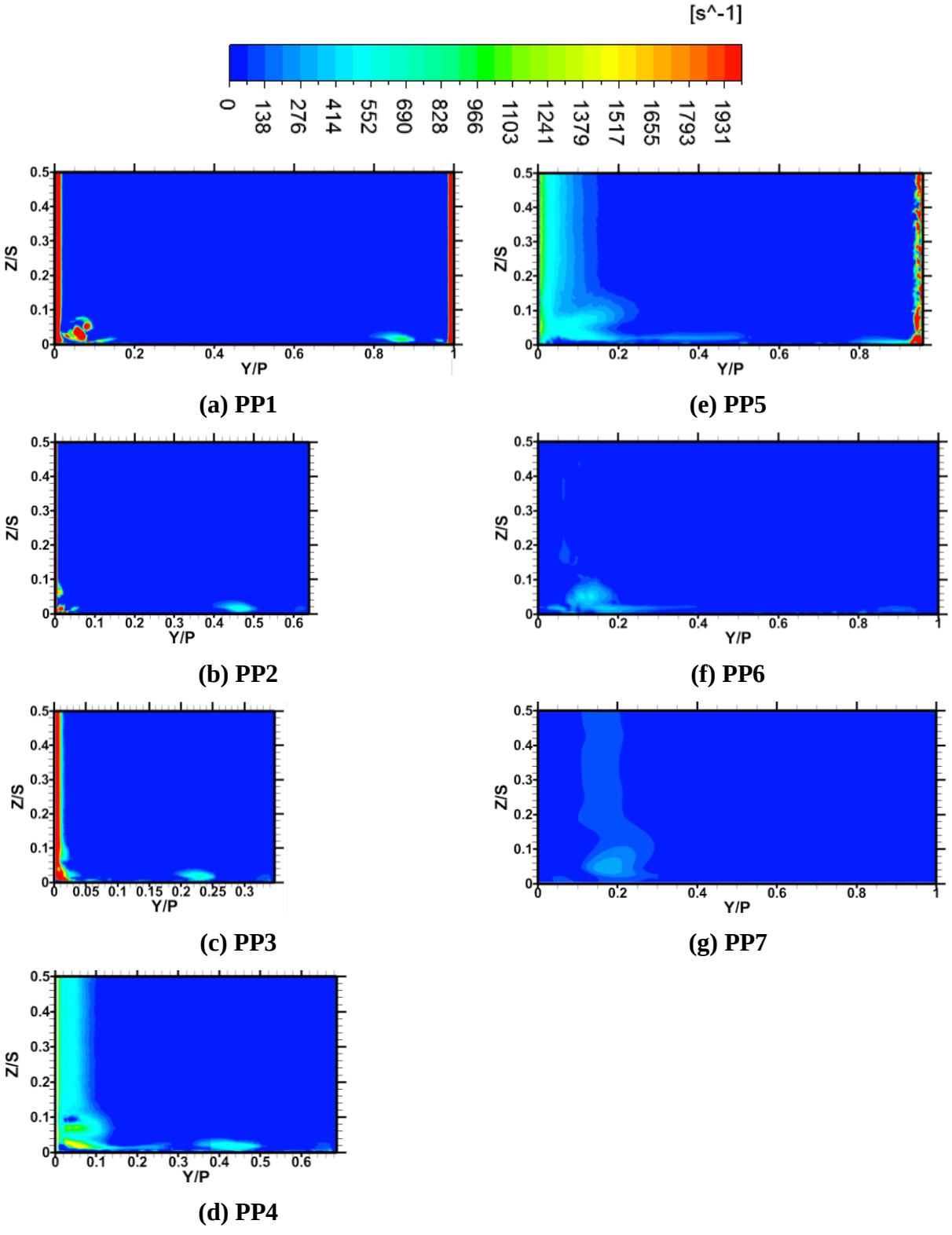

Figure 76: Swirling Strength Contours at various axial planes through the passage for the case X_h=2D, α=90°, β=0, MFR=0.1%

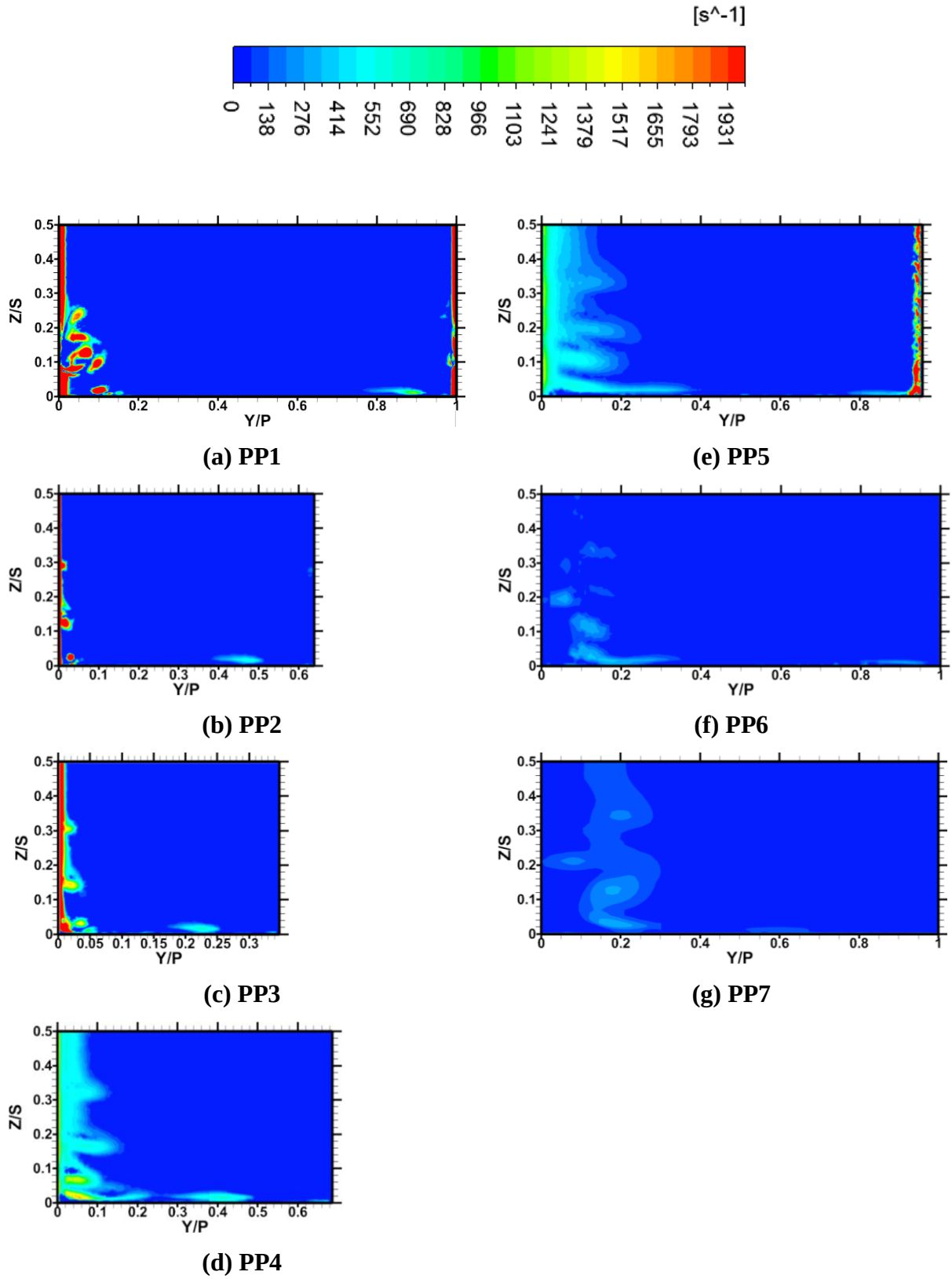

Figure 77: Swirling Strength Contours at various axial planes through the passage for the case X_h=2D, α=90°, β=0, MFR=0.25%

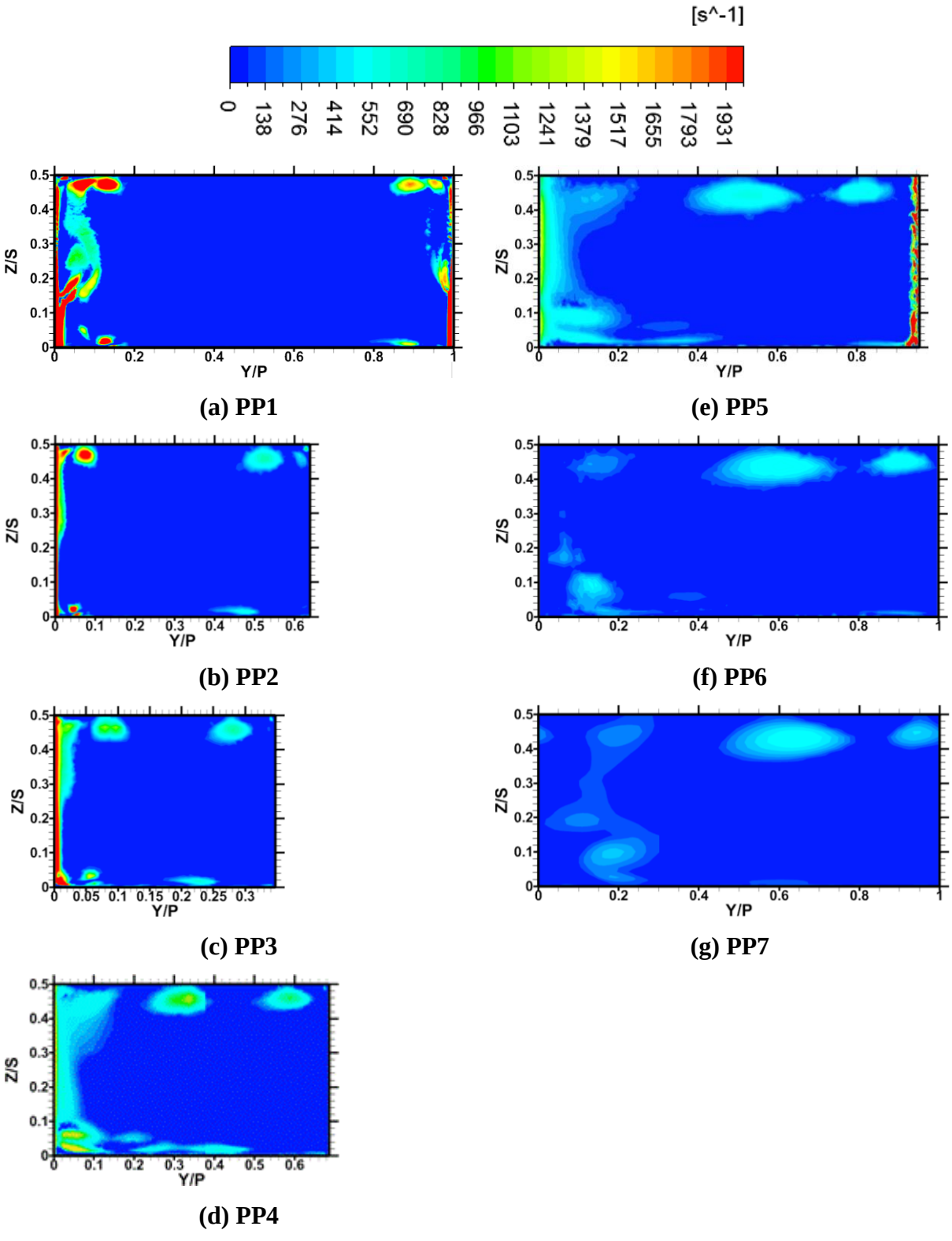

(a) PP1

(e) PP5

(b) PP2

(f) PP6

(c) PP3

(g) PP7

(d) PP4

Figure 78: Swirling Strength Contours at various axial planes through the passage for the case X_h=2D, α=90°, β=0, MFR=0.5%

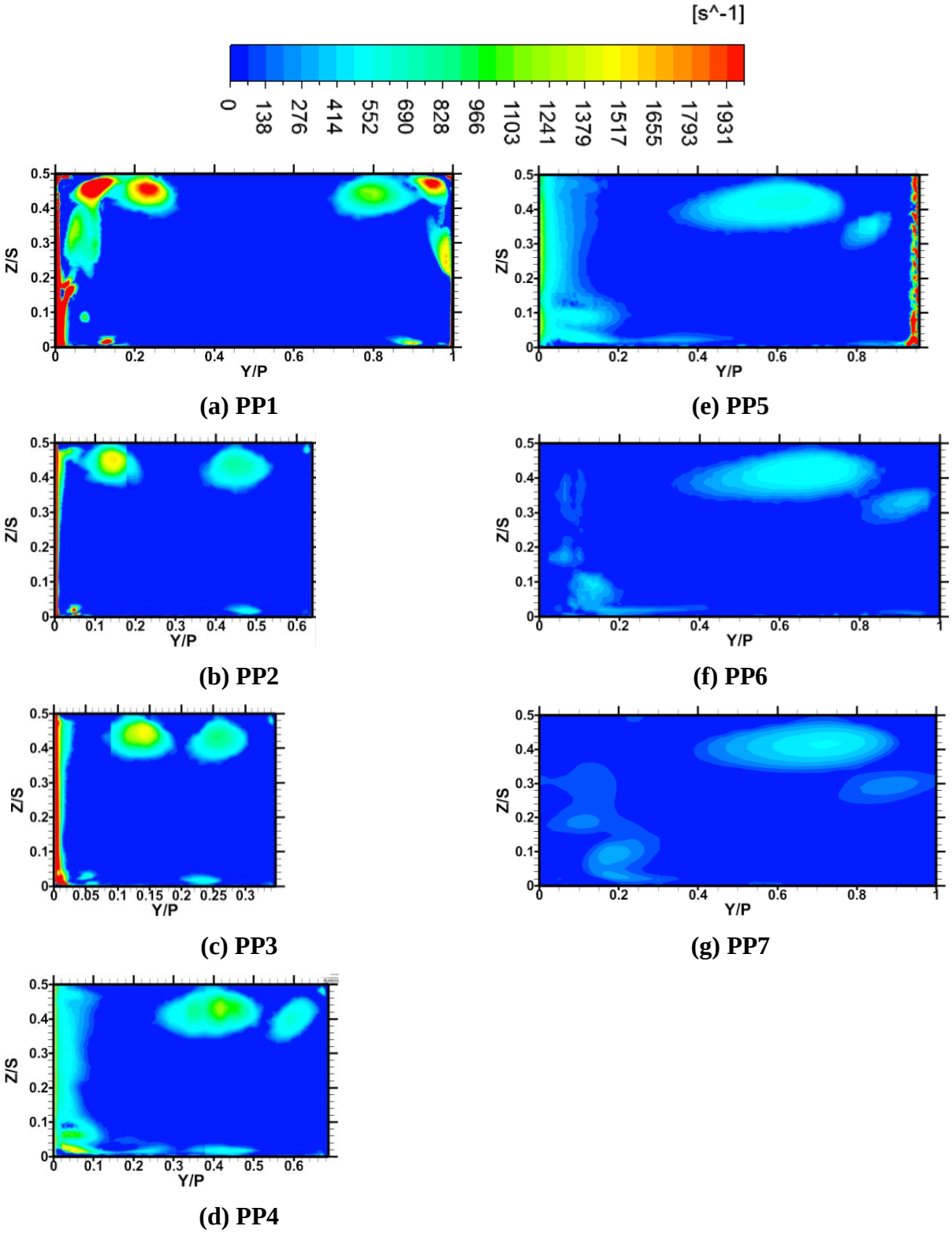

Figure 79: Swirling Strength Contours at various axial planes through the passage for the case X_h=2D, α=90°, β=0, MFR=0.75%

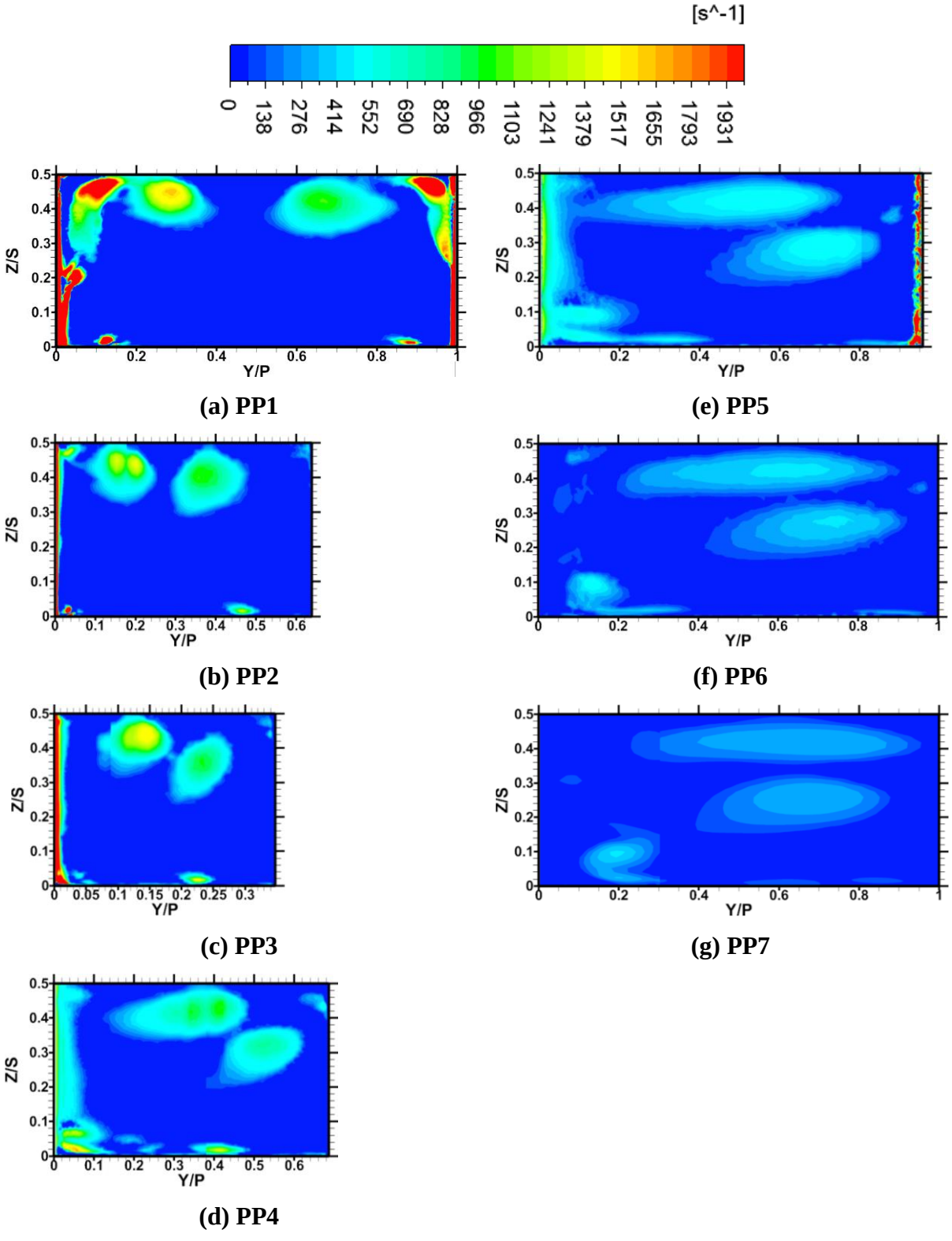

Figure 80: Swirling Strength Contours at various axial planes through the passage for the case X_h=2D, α=90°, β=0, MFR=1%

Exit Plane Total Pressure Loss Coefficient

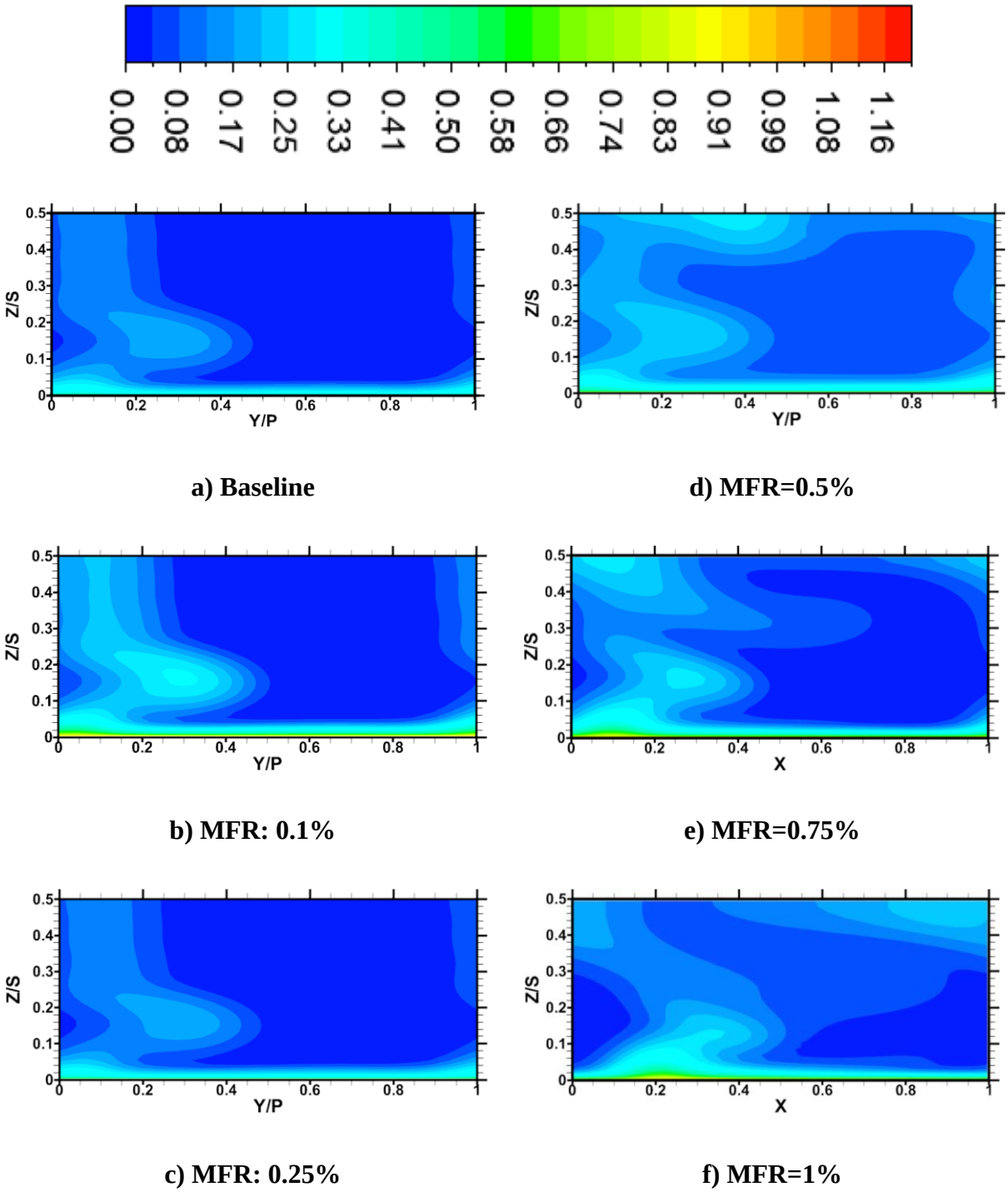

a) Baseline

d) MFR=0.5%

b) MFR: 0.1%

e) MFR=0.75%

c) MFR: 0.25%

f) MFR=1%

Figure 81: Exit plane total pressure loss coefficient contours for different MFRs at α=30° and X=2D

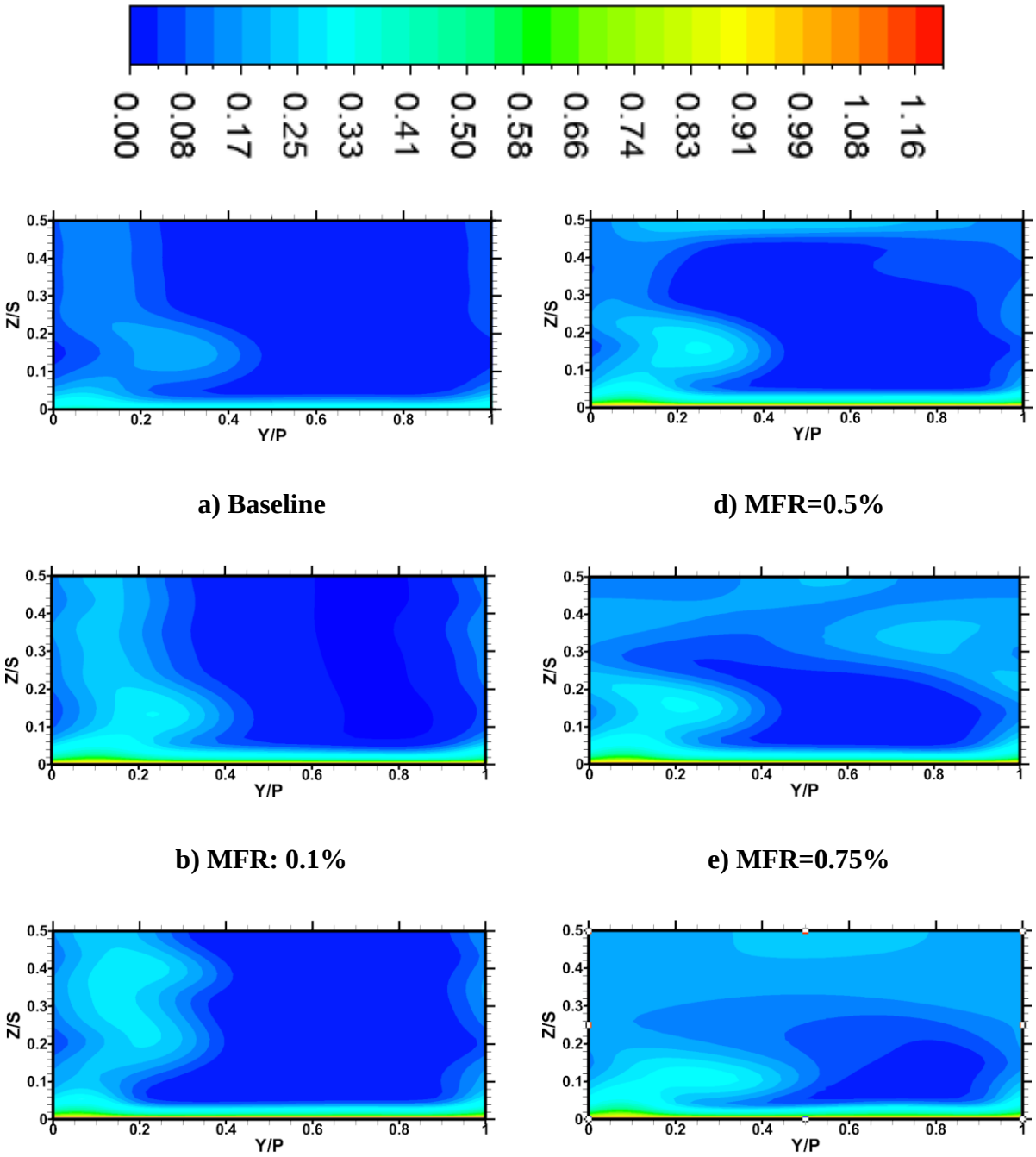

Figure 82: Exit plane total pressure loss coefficient contours for different MFRs at α=90° and X=2D

Exit Plane Kinetic Energy Loss Coefficient Plots

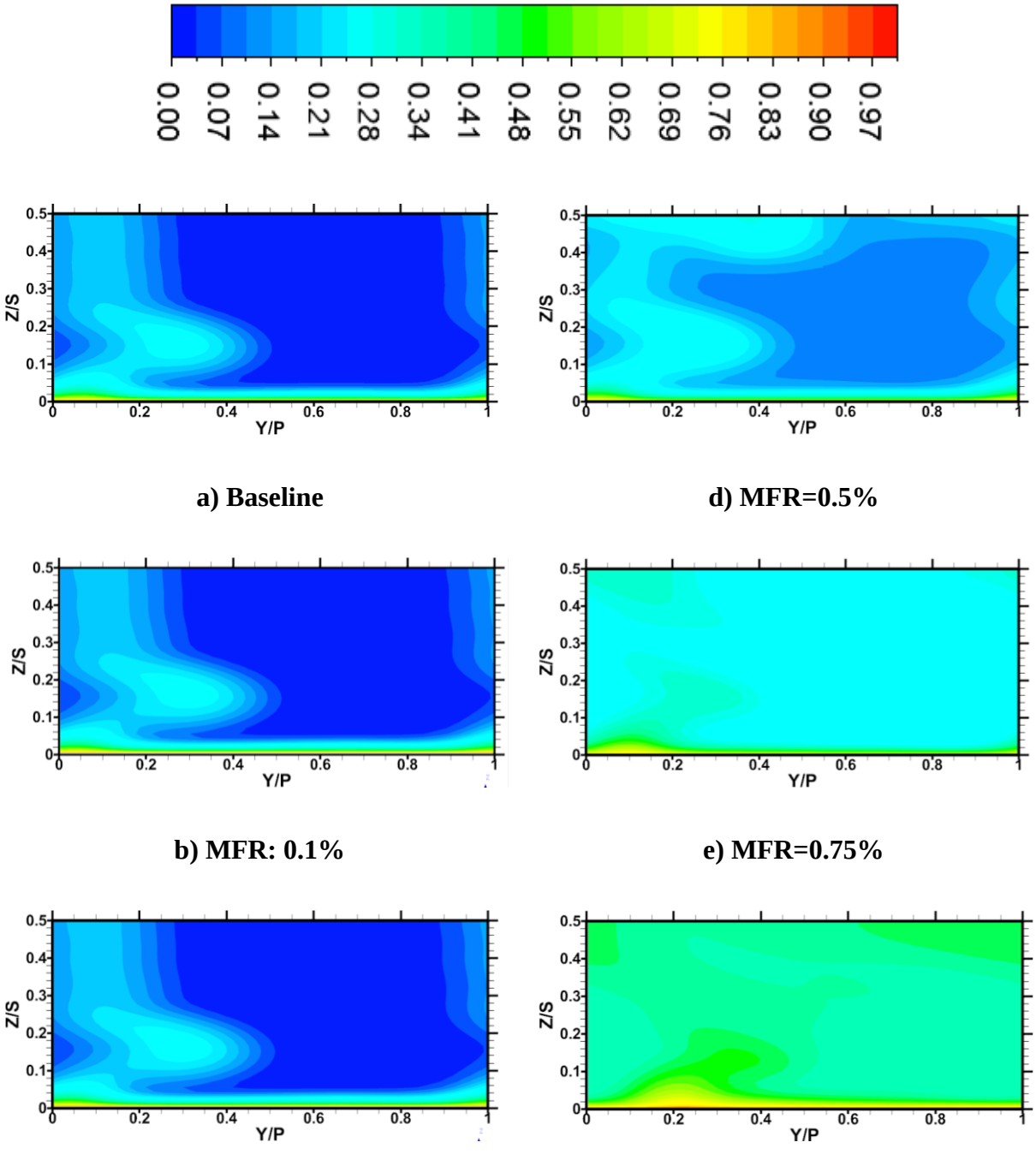

Figure 83: Exit plane kinetic energy loss coefficient contours for different MFRs at α=30° and X=2D

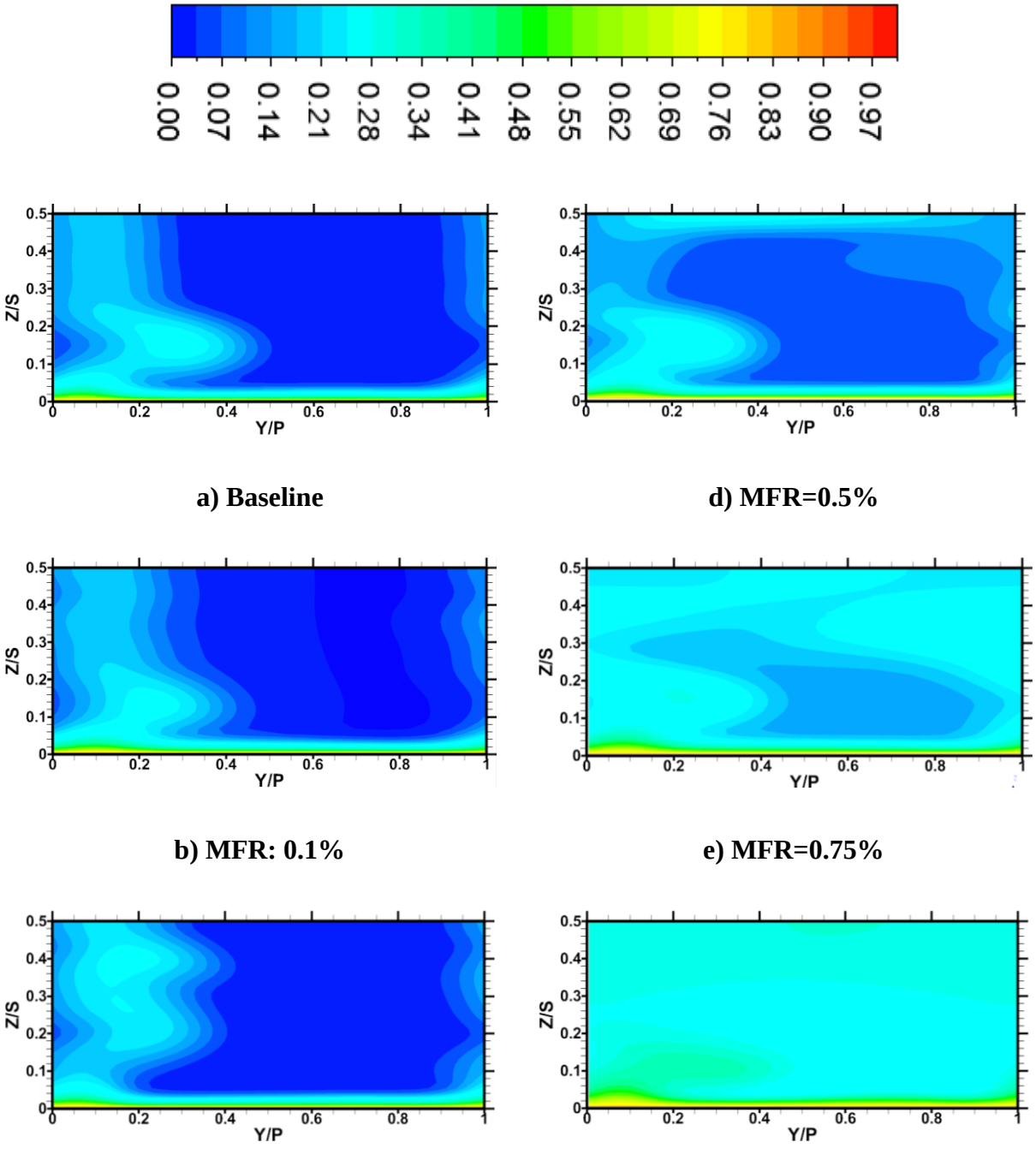

a) Baseline

d) MFR=0.5%

b) MFR: 0.1%

e) MFR=0.75%

c) MFR: 0.25%

f) MFR=0.1%

Figure 84: Exit plane kinetic energy loss coefficient contours for different MFRs at α=90° and X=2D

Alpha Study

Table 24: Details of parameters tested in Alpha study

x/d	α (deg)	β (deg)	MFR (%)
1	30	0	0.5
1	90	0	0.5
1	150	0	0.5
1	30	0	1
1	90	0	1
1	150	0	1
2	30	0	0.5
2	90	0	0.5
2	150	0	0.5
2	30	0	1
2	90	0	1
2	150	0	1

Leading Edge Vortex Streamlines

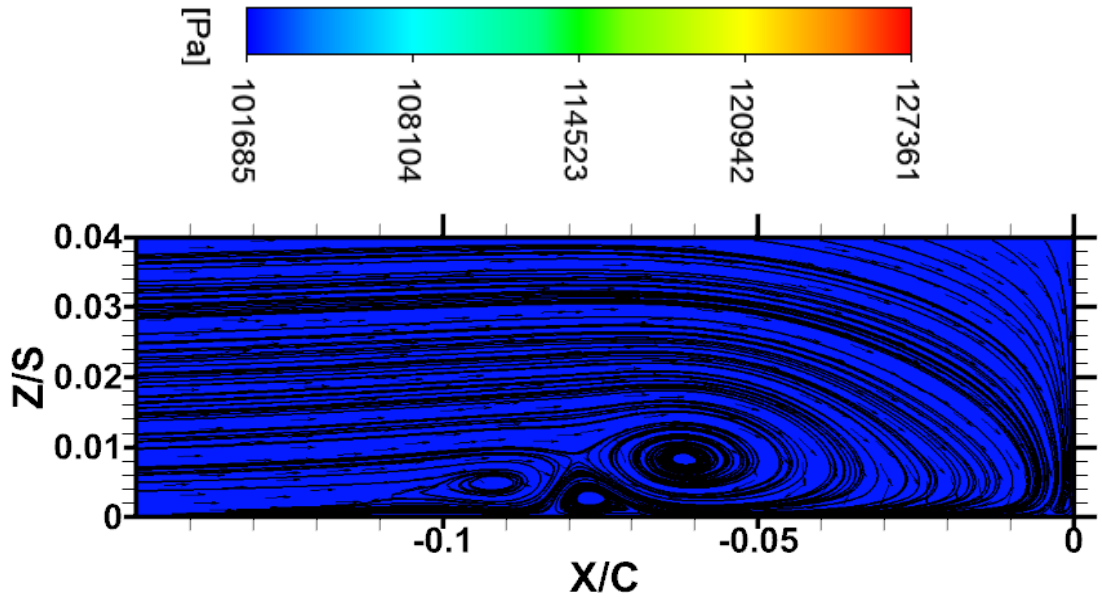

a) Baseline

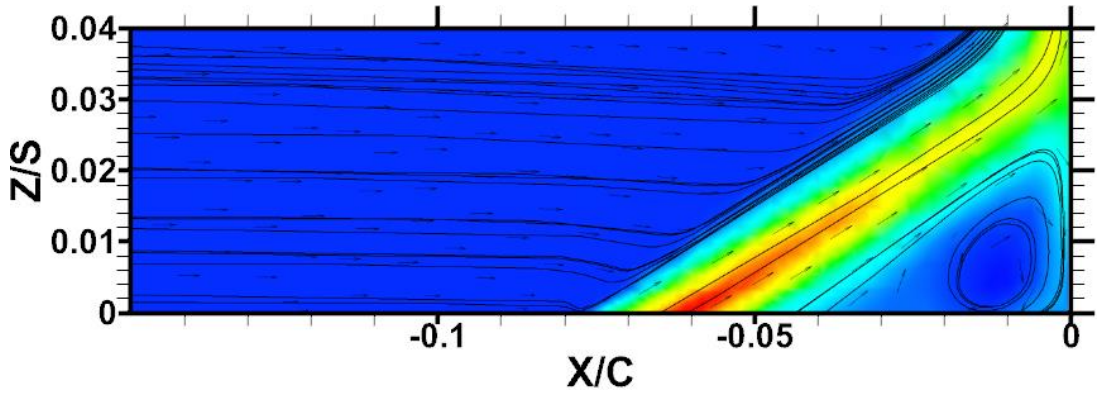

b) α=30°

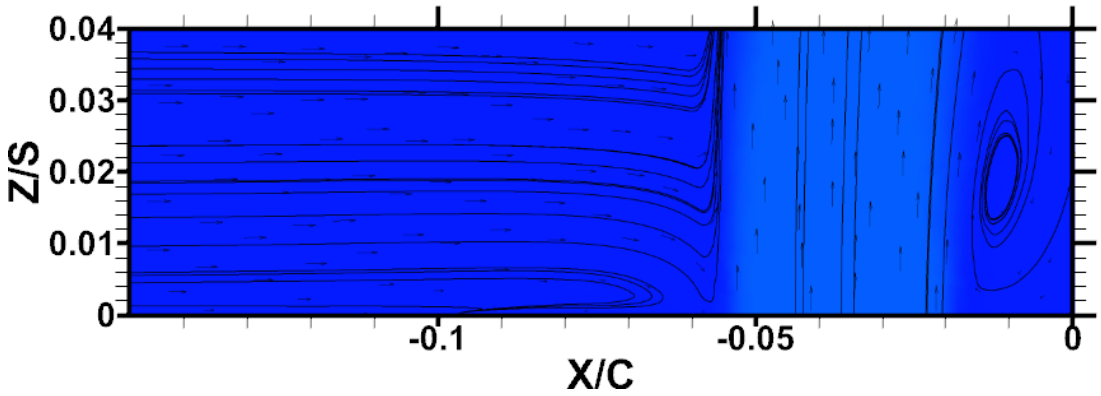

c) α=90°

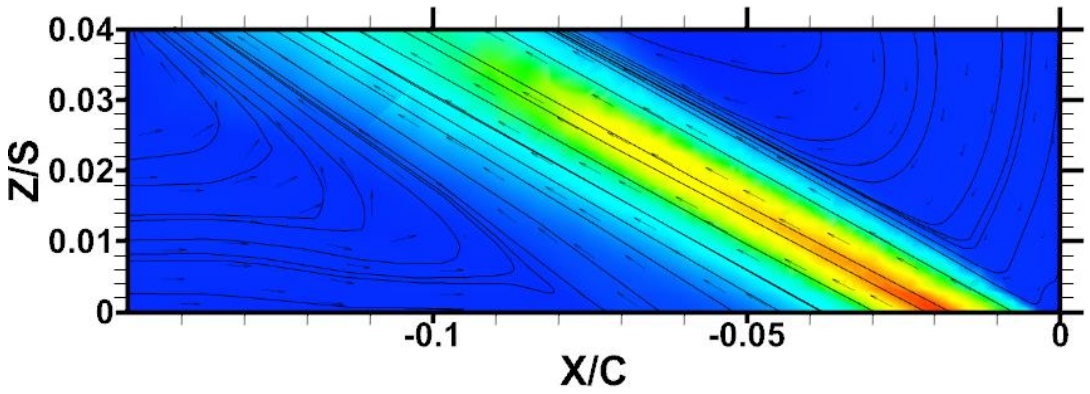

d) α=150°

Figure 85: Leading edge velocity streamlines and vectors overlaid with total pressure (absolute) contours at different α values at MFR=0.5% and X=D

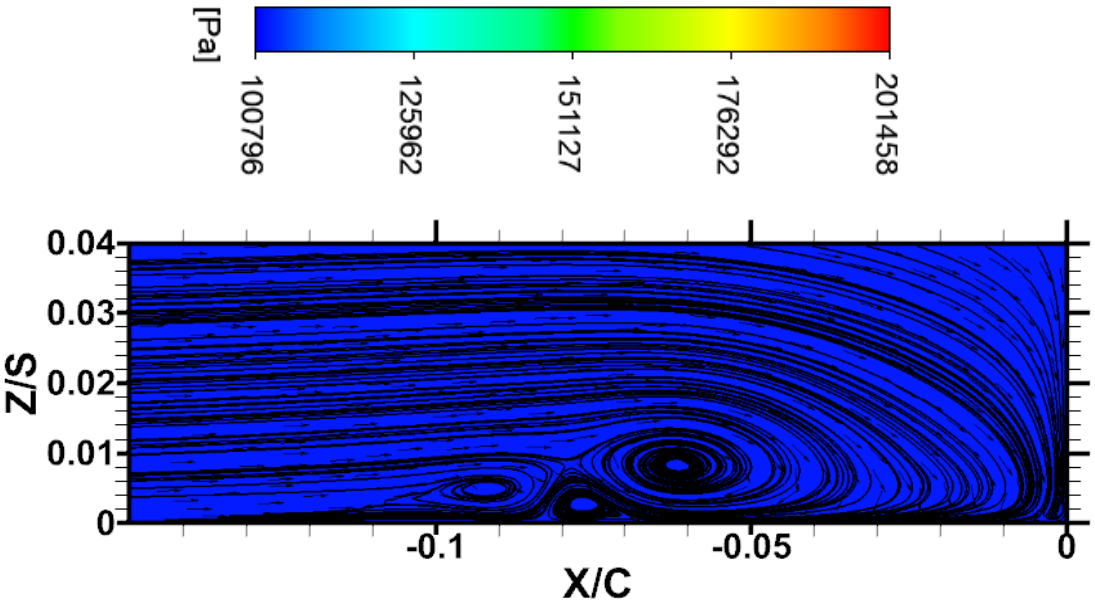

a) Baseline

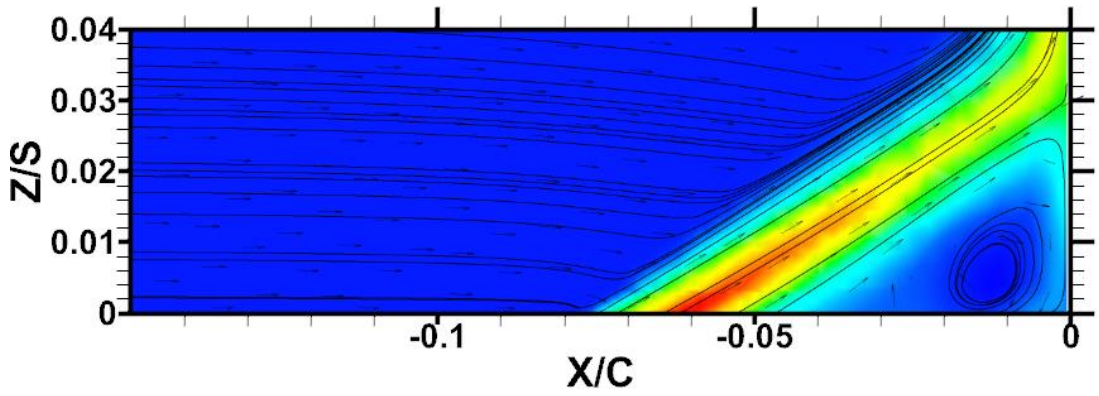

b) α=30°

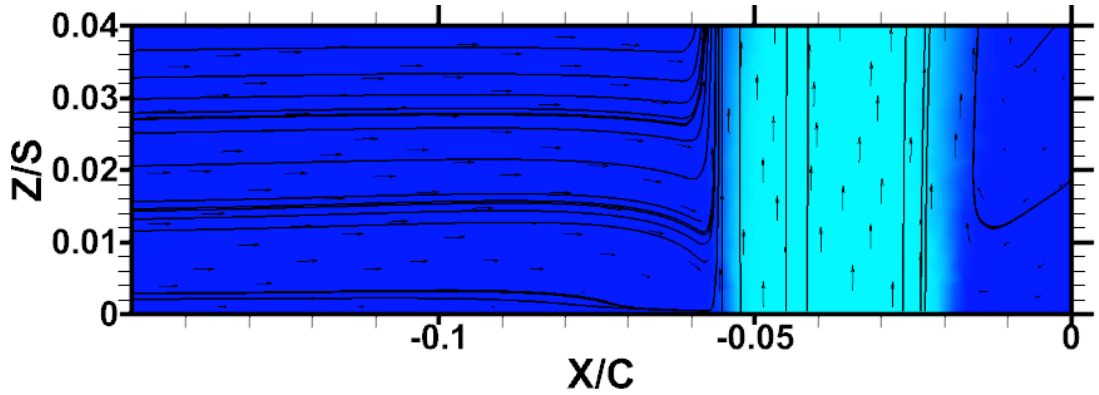

c) α=90°

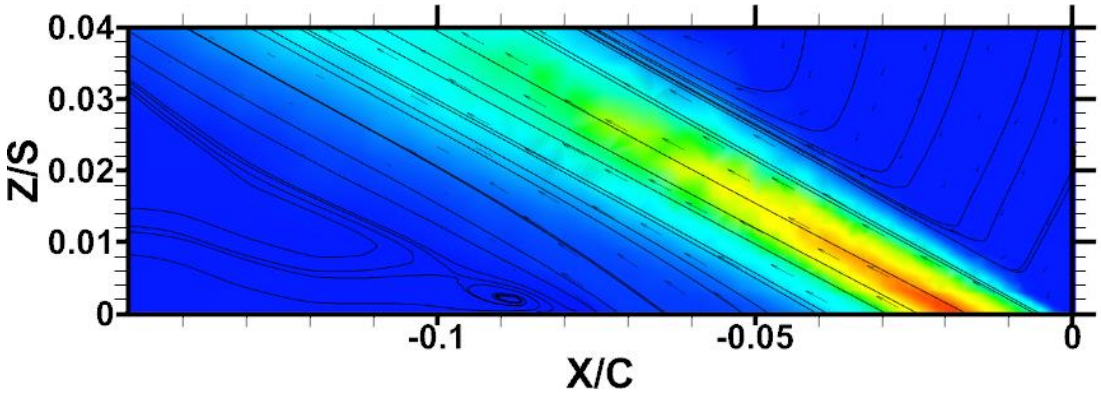

d) α=150°

Figure 86: Leading edge velocity streamlines and vectors overlaid with total pressure (absolute) contours at different α values at MFR=1% and X=D

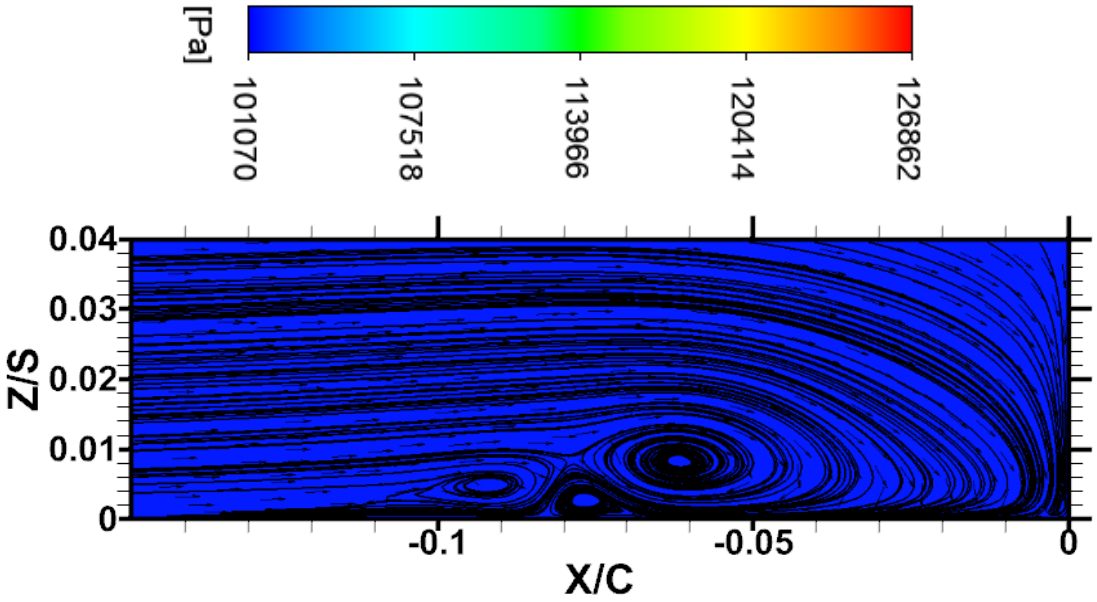

a) Baseline

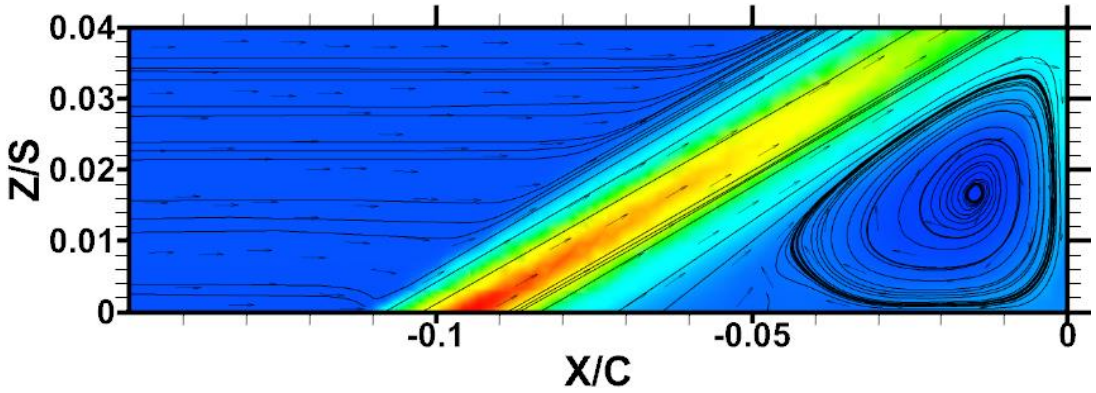

b) α=30°

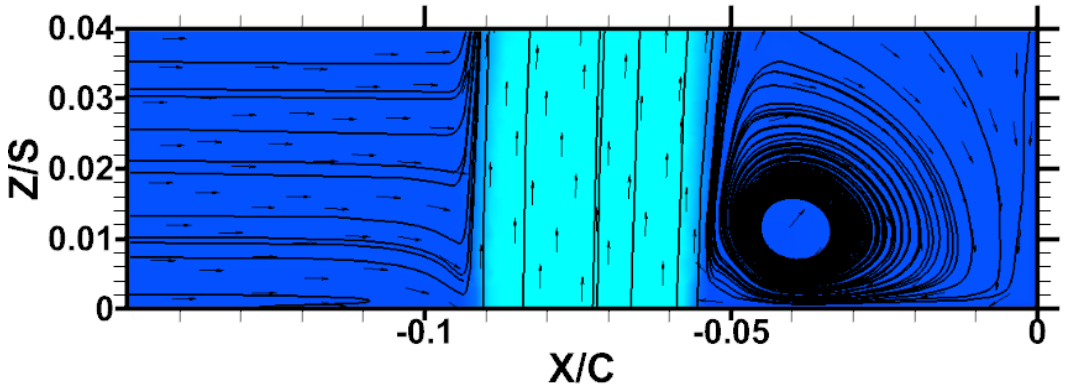

c) α=90°

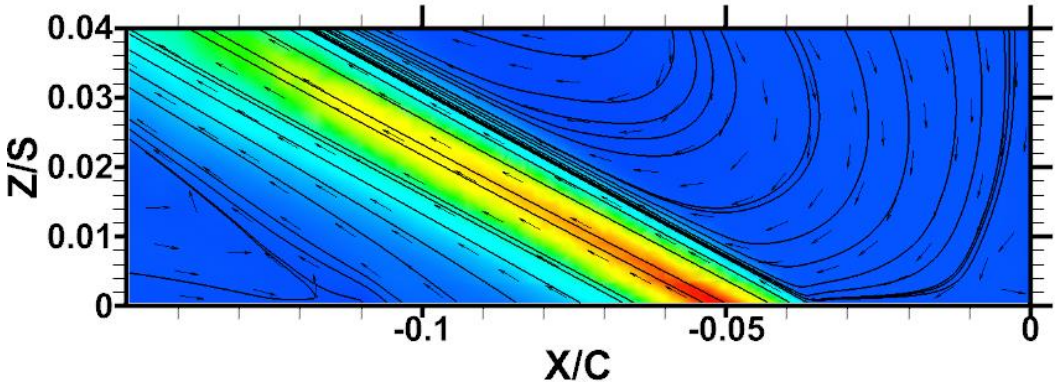

d) α=150°

Figure 87: Leading edge velocity streamlines and vectors overlaid with total pressure (absolute) contours at different α values at MFR=0.5% and X=2D

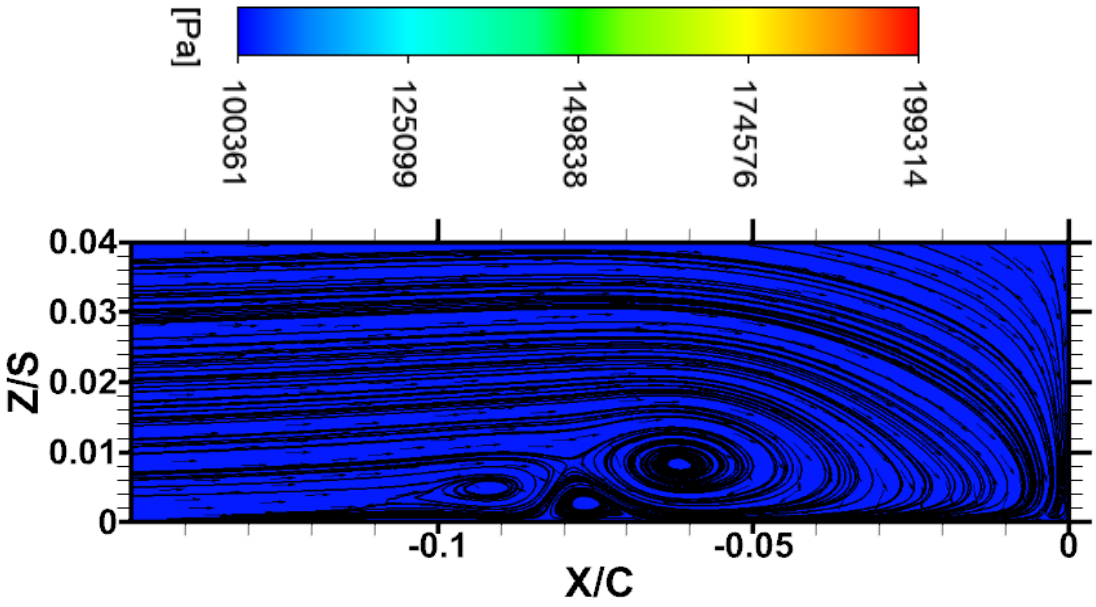

a) Baseline

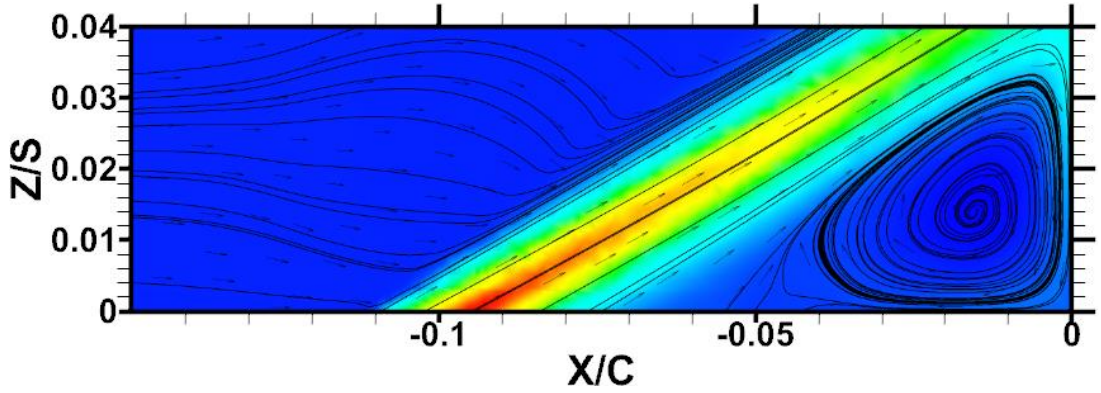

b) α=30°

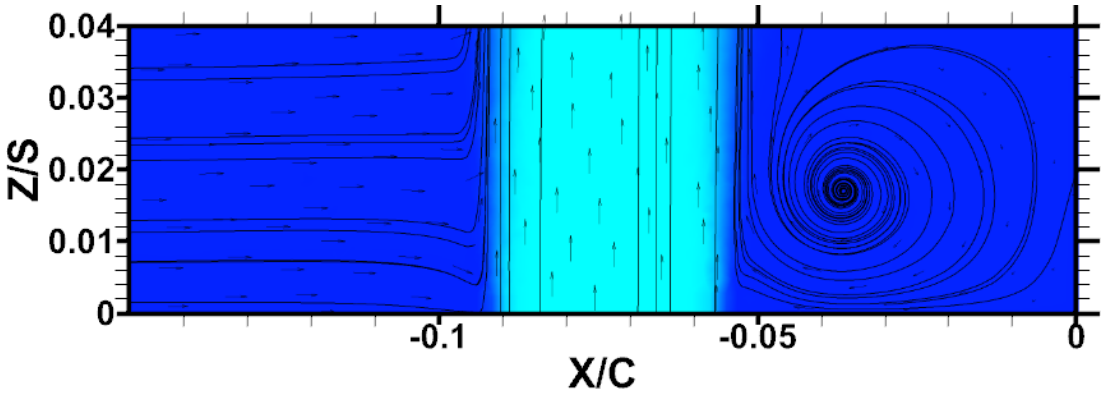

c) α=90°

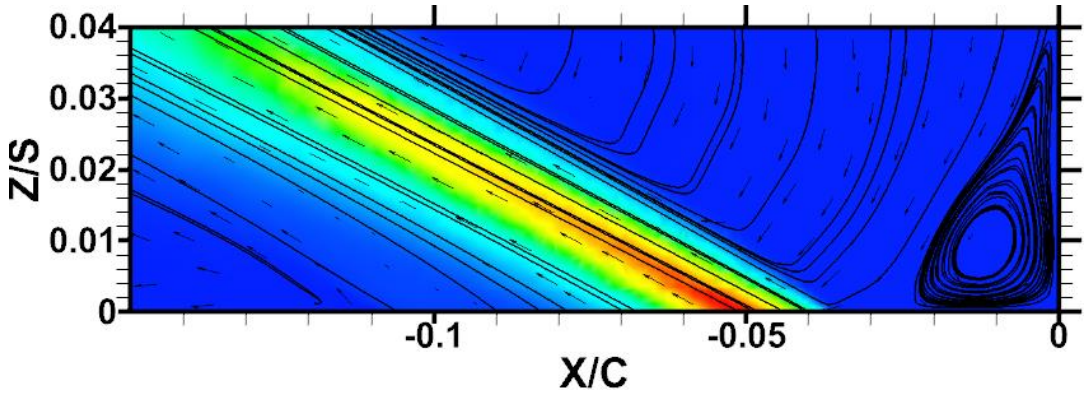

d) α=150°

Figure 88: Leading edge velocity streamlines and vectors overlaid with total pressure (absolute) contours at different α values at MFR=1% and X=2D

Passage Vortex Swirling Strength Plots

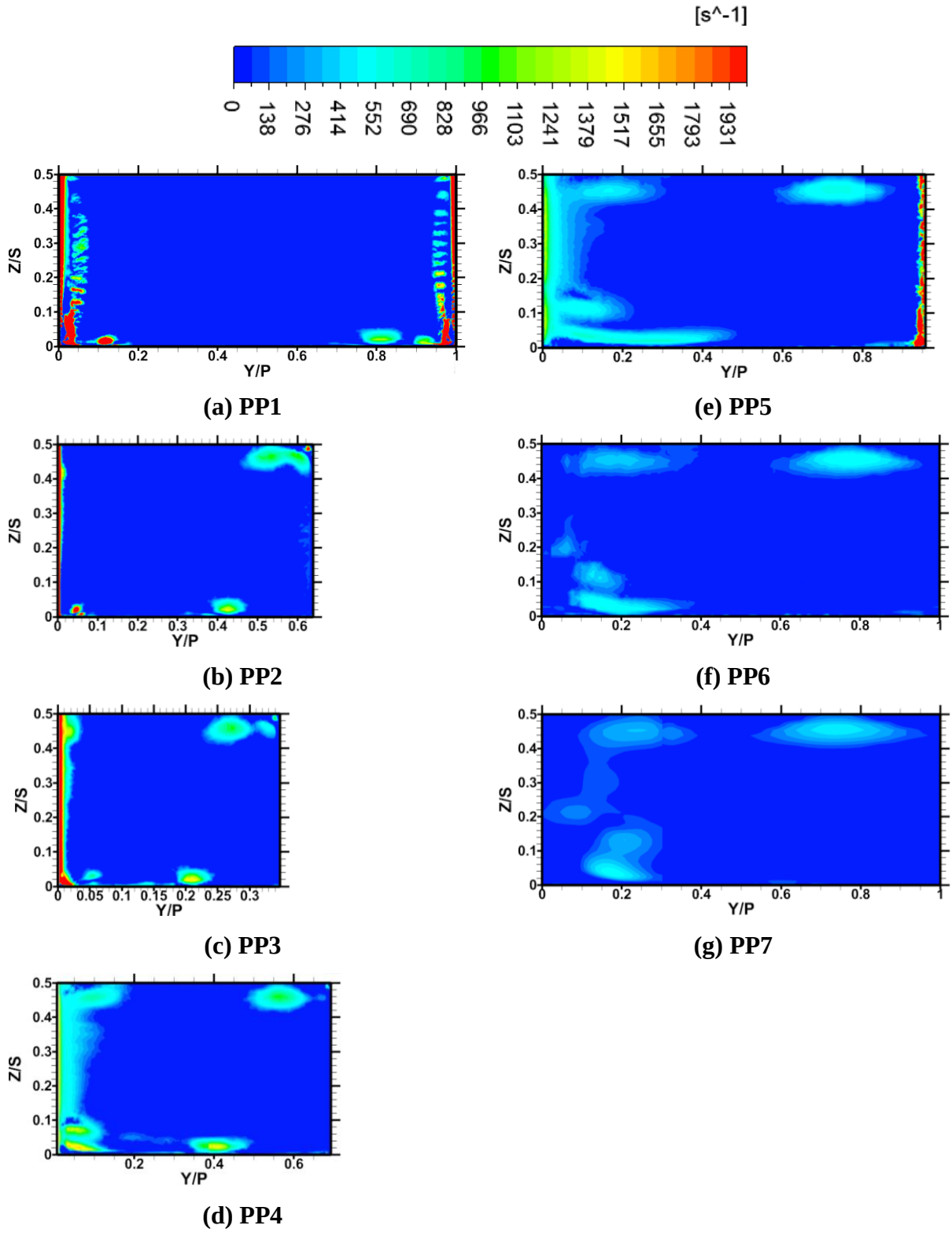

Figure 89: Swirling Strength Contours at various axial planes through the passage for the case X_h=D, α=30°, β=0, MFR=0.5%

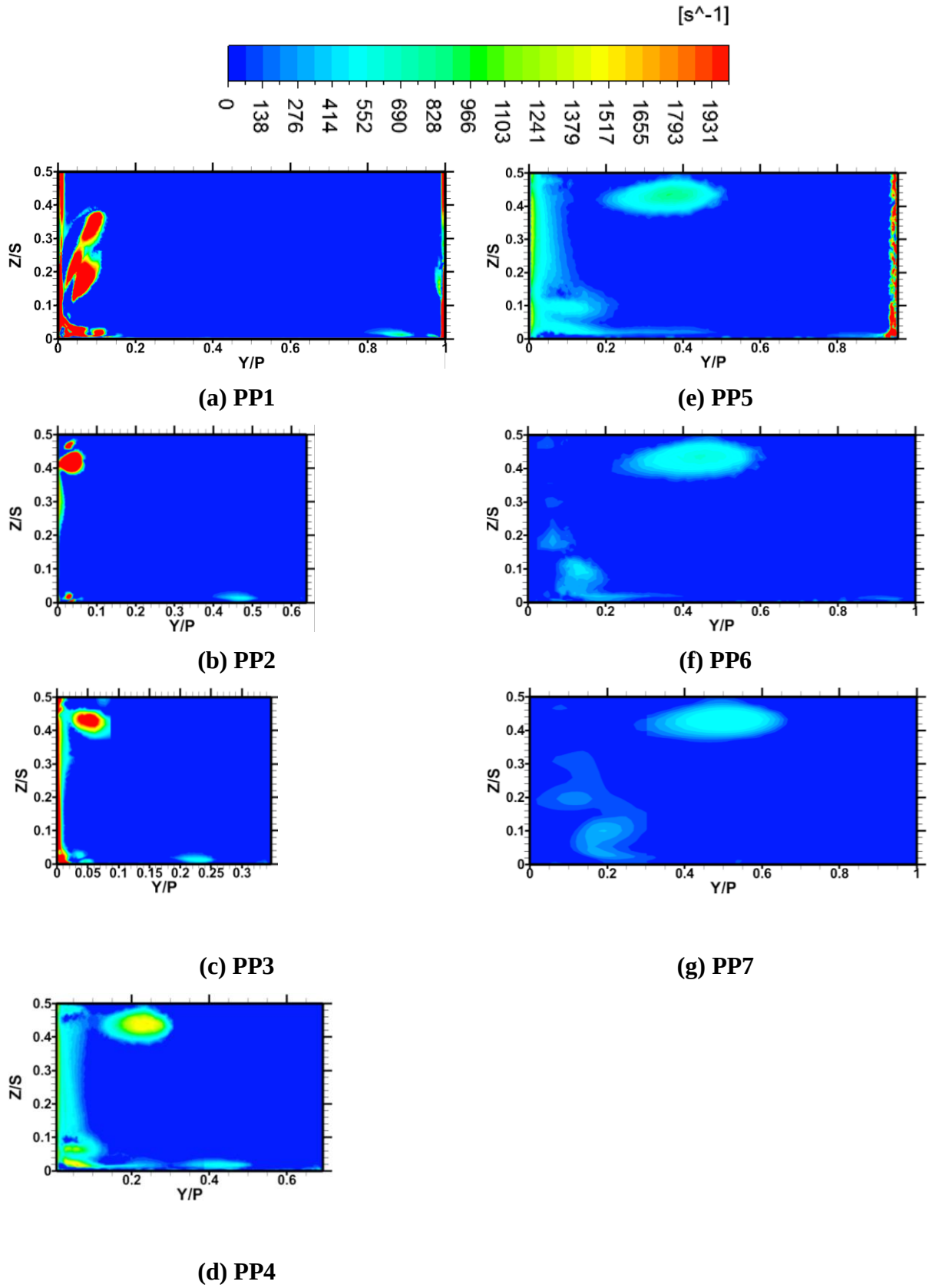

Figure 90: Swirling Strength Contours at various axial planes through the passage for the case X_h=D, α=90°, β=0, MFR=0.5%

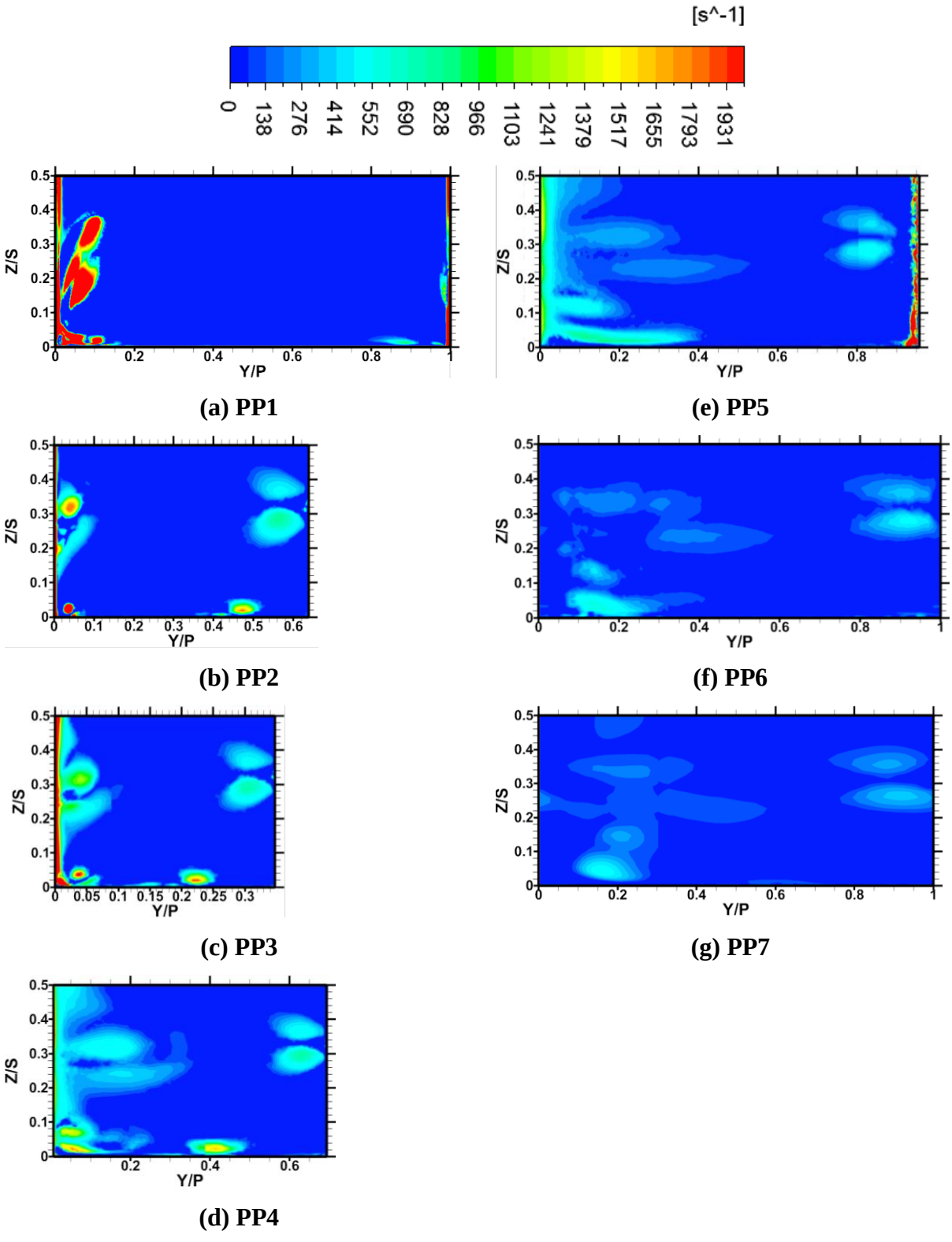

(a) PP1

(e) PP5

(b) PP2

(f) PP6

(c) PP3

(g) PP7

(d) PP4

Figure 91: Swirling Strength Contours at various axial planes through the passage for the case X_h=D, α=150°, β=0, MFR=0.5%

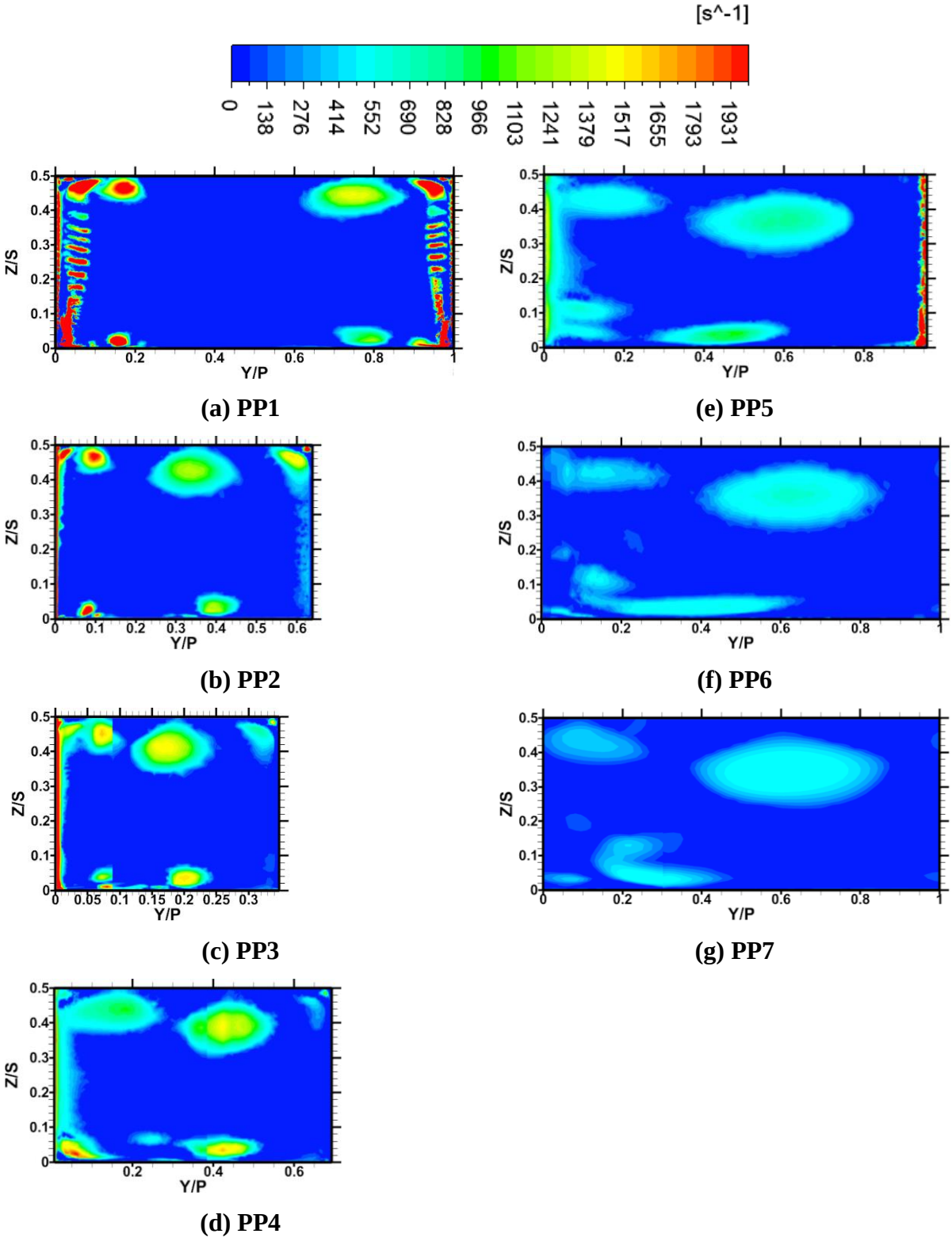

Figure 92: Swirling Strength Contours at various axial planes through the passage for the case X_h=D, α=30°, β=0, MFR=1%

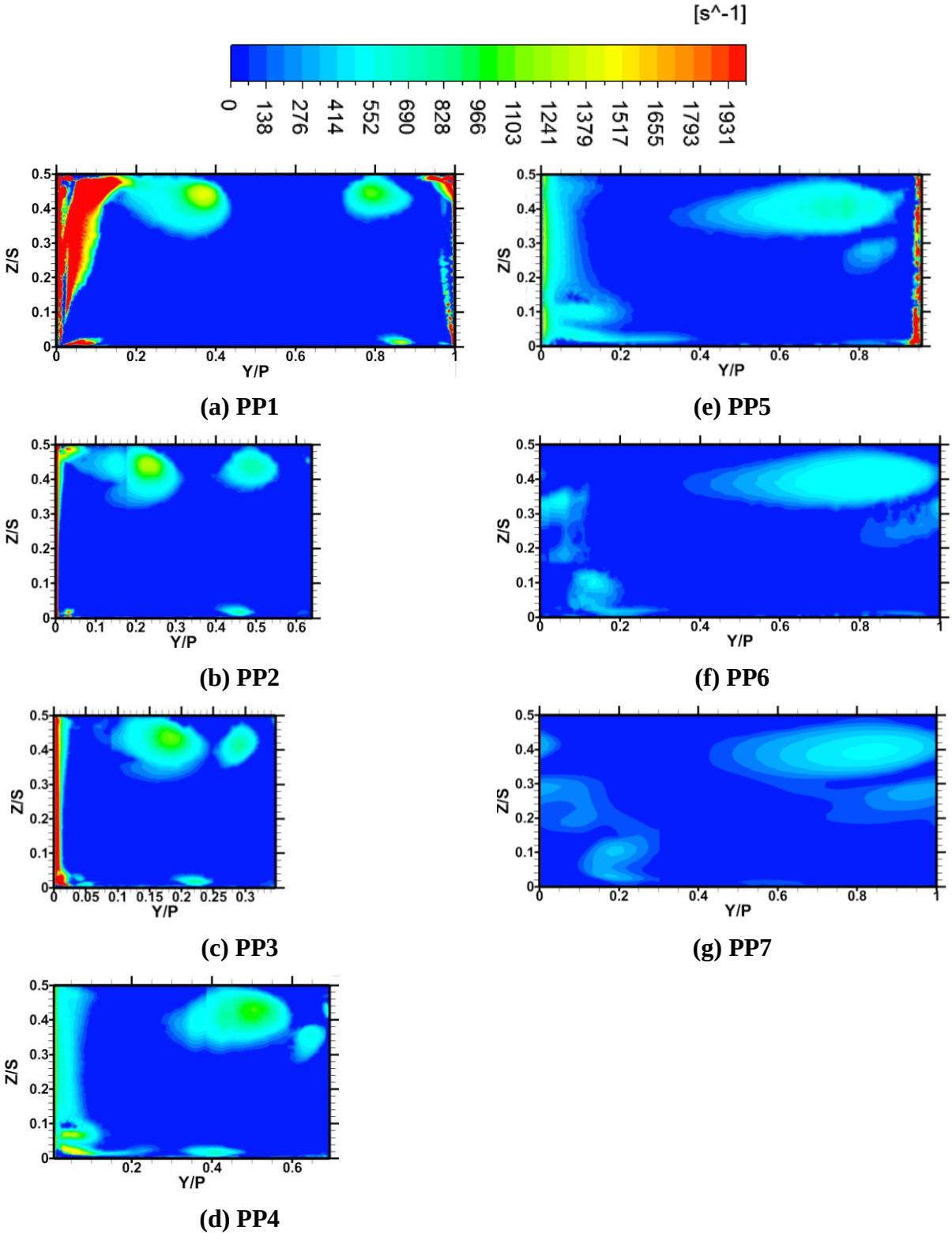

Figure 93: Swirling Strength Contours at various axial planes through the passage for the case X_h=D, α=90°, β=0, MFR=1%

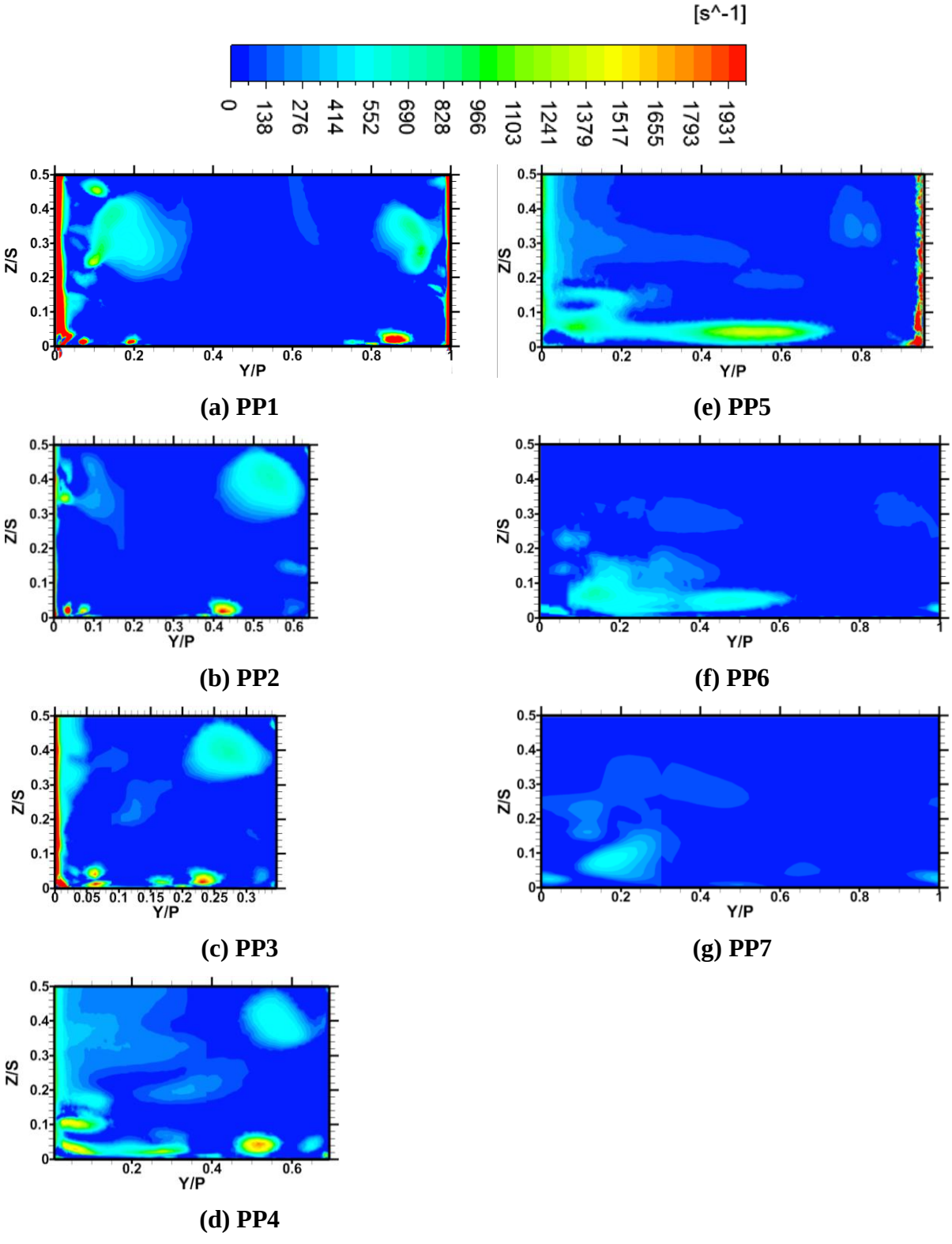

(a) PP1

(e) PP5

(b) PP2

(f) PP6

(c) PP3

(g) PP7

(d) PP4

Figure 94: Swirling Strength Contours at various axial planes through the passage for the case X_h=D, α=150°, β=0, MFR=1%

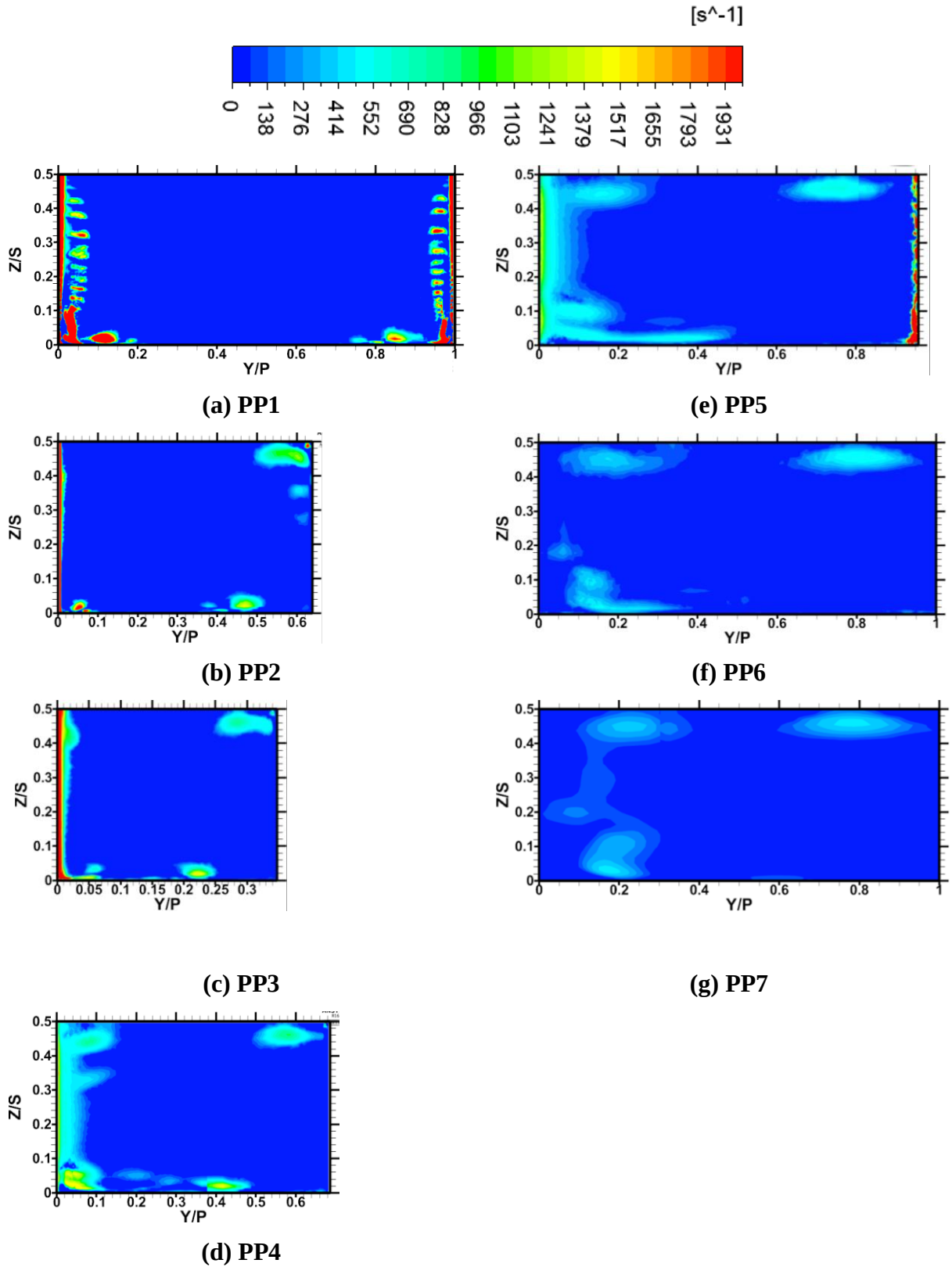

(a) PP1

(e) PP5

(b) PP2

(f) PP6

(c) PP3

(g) PP7

(d) PP4

Figure 95: Swirling Strength Contours at various axial planes through the passage for the case X_h=2D, α=30°, β=0, MFR=0.5%

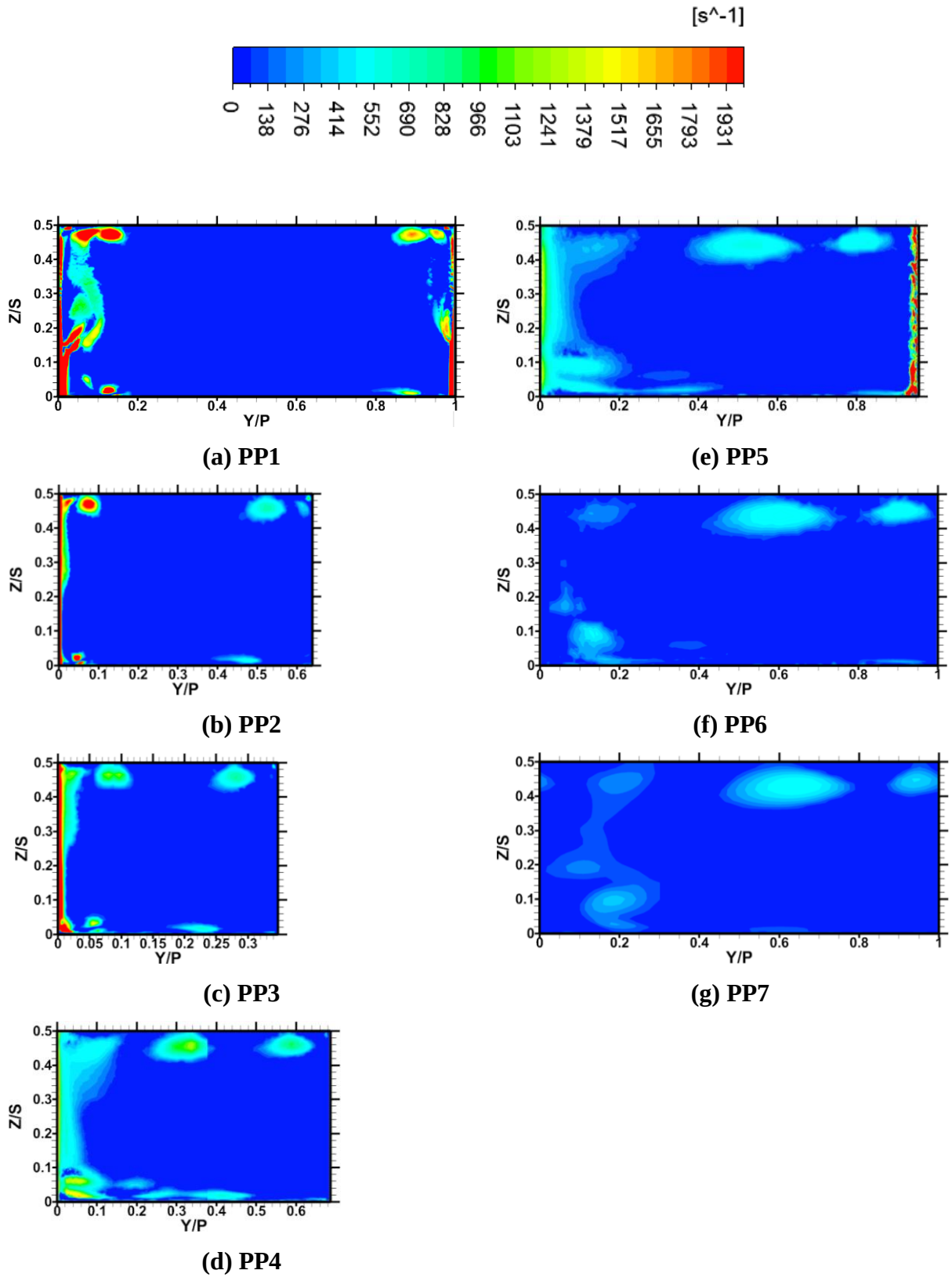

Figure 96: Swirling Strength Contours at various axial planes through the passage for the case X_h=2D, α=90°, β=0, MFR=0.5%

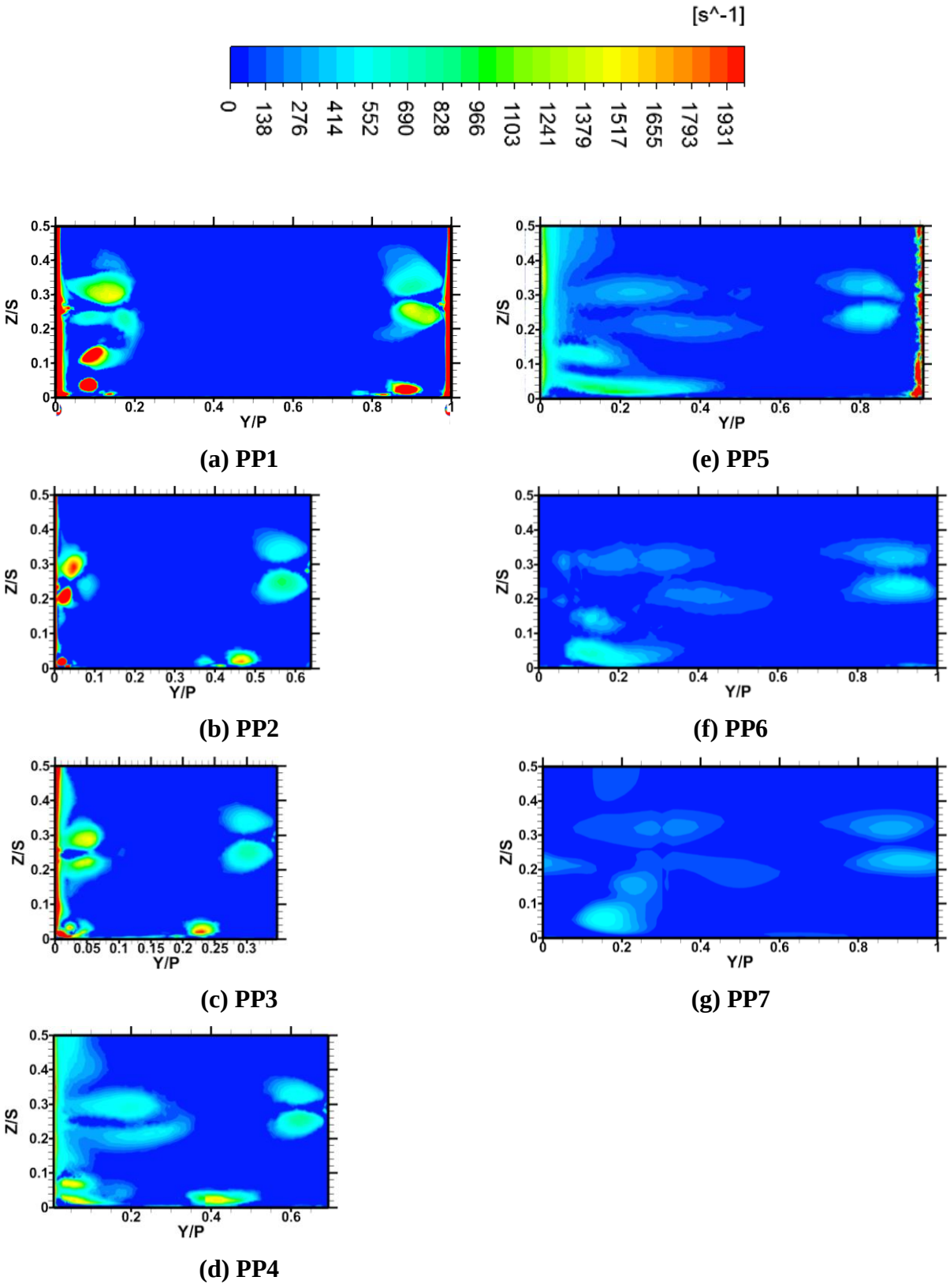

(a) PP1

(e) PP5

(b) PP2

(f) PP6

(c) PP3

(g) PP7

(d) PP4

Figure 97: Swirling Strength Contours at various axial planes through the passage for the case X_h=2D, α=150°, β=0, MFR=0.5%

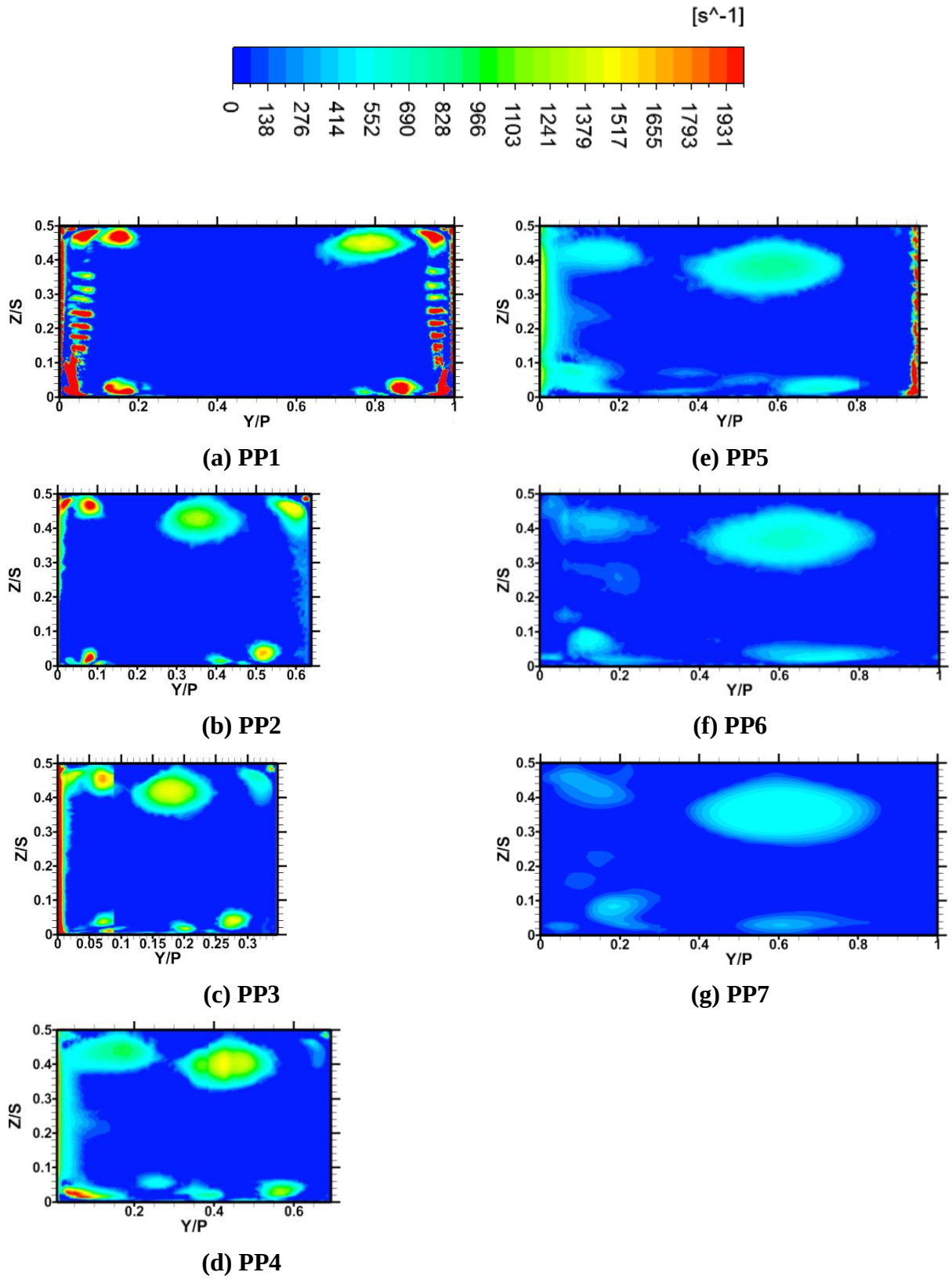

Figure 98: Swirling Strength Contours at various axial planes through the passage for the case X_h=2D, α=30°, β=0, MFR=1%

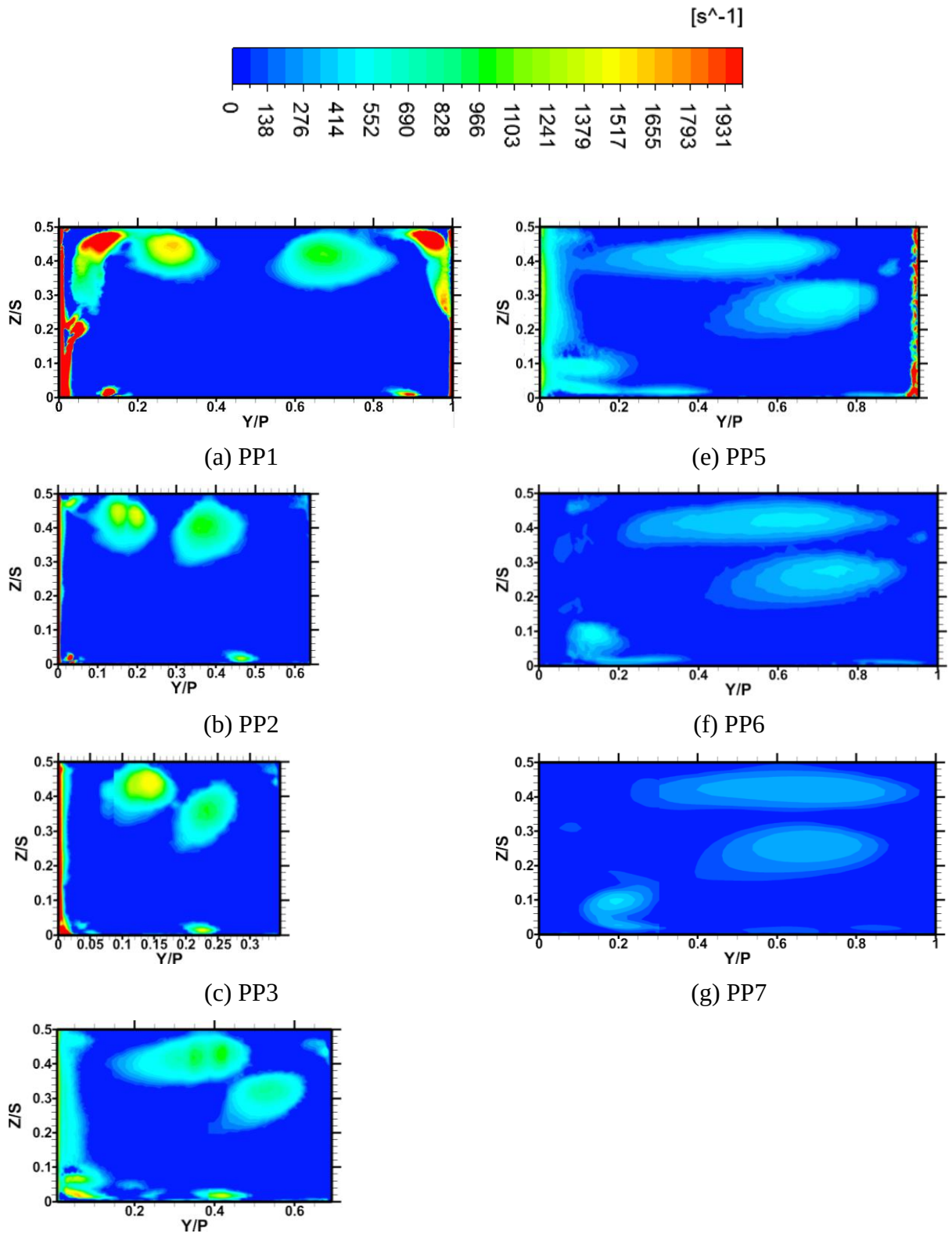

(a) PP1

(e) PP5

(b) PP2

(f) PP6

(c) PP3

(g) PP7

(d) PP4

Figure 99: Swirling Strength Contours at various axial planes through the passage for the case X_h=2D, α=90°, β=0, MFR=1%

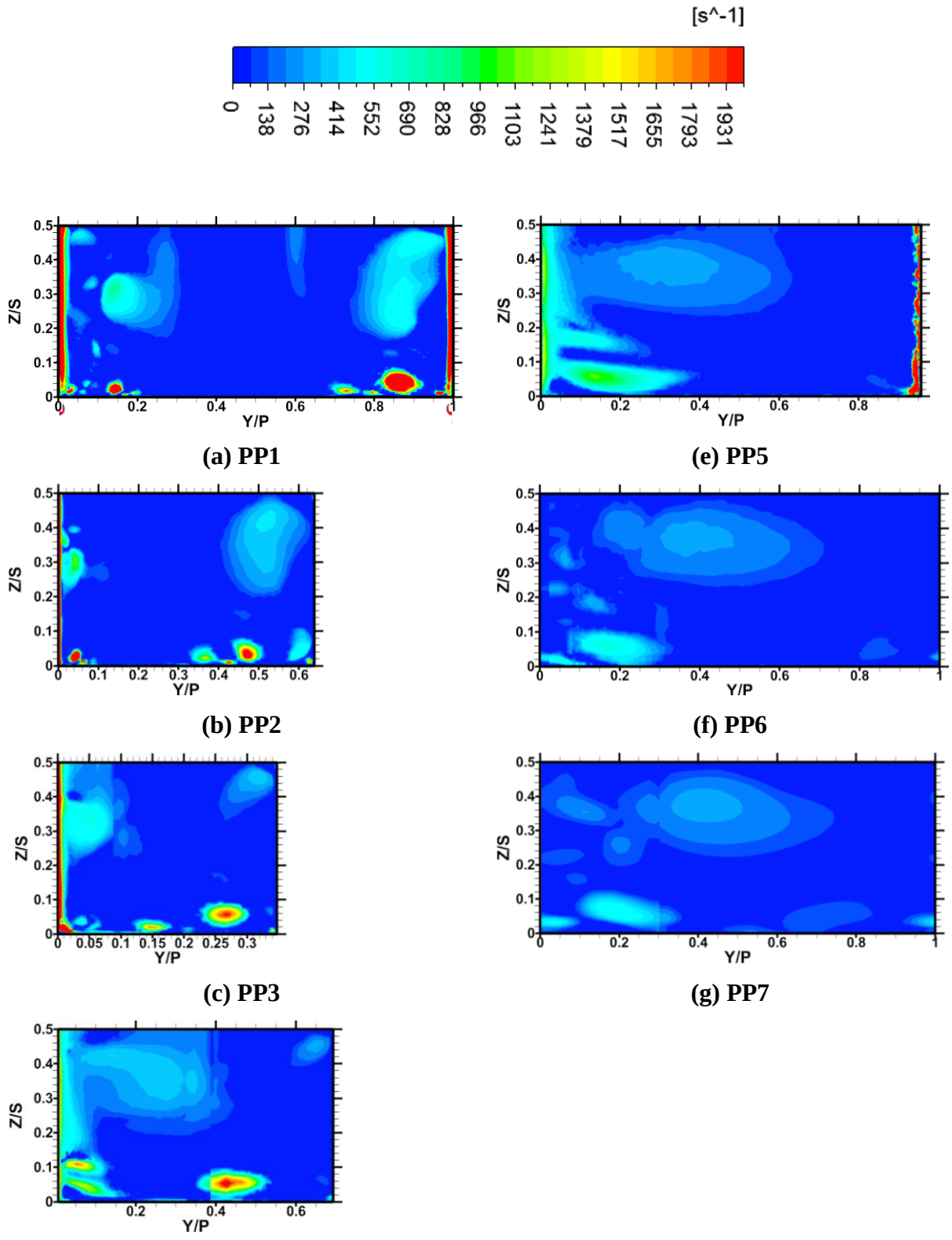

Figure 100: Swirling Strength Contours at various axial planes through the passage for the case X_h=2D, α=150°, β=0, MFR=1%

Exit Plane Total Pressure Loss Coefficient Plots

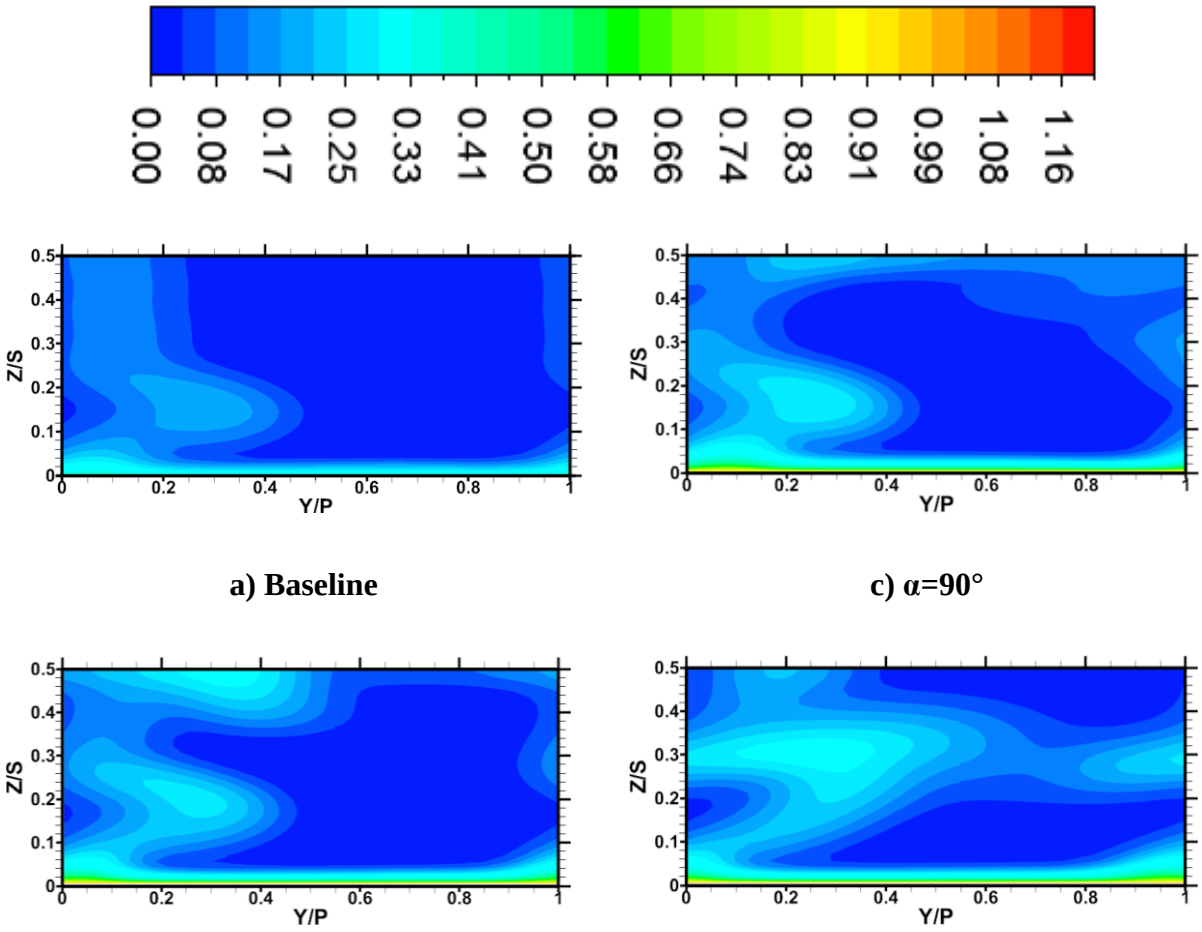

a) Baseline

c) α=90°

b) α=30°

d) α=150°

Figure 101: Exit plane total pressure loss coefficient contours for different α values at MFR=0.5% and X=D

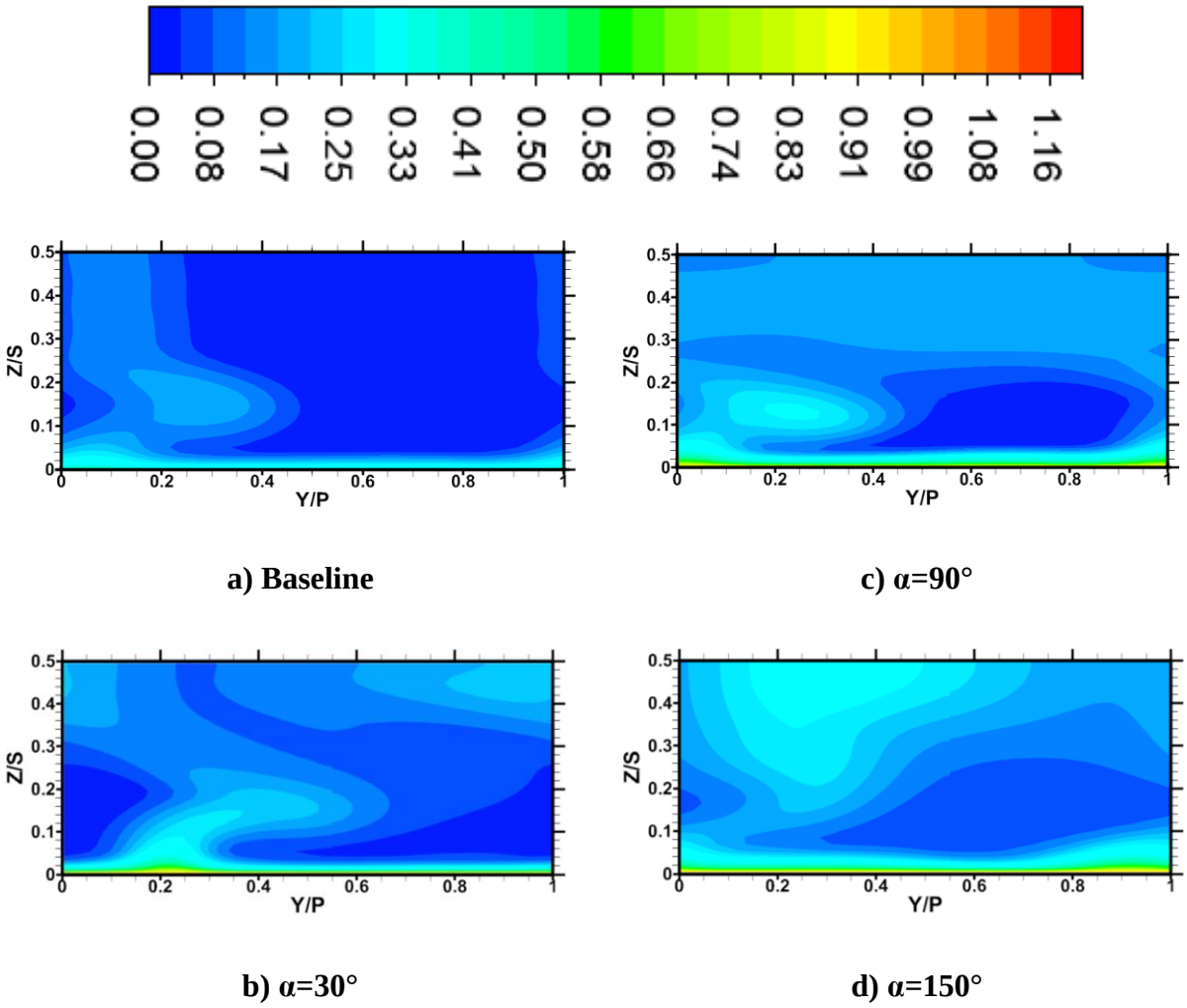

a) Baseline

c) α=90°

b) α=30°

d) α=150°

Figure 102: Exit plane total pressure loss coefficient contours for different α values at MFR=1% and X=D

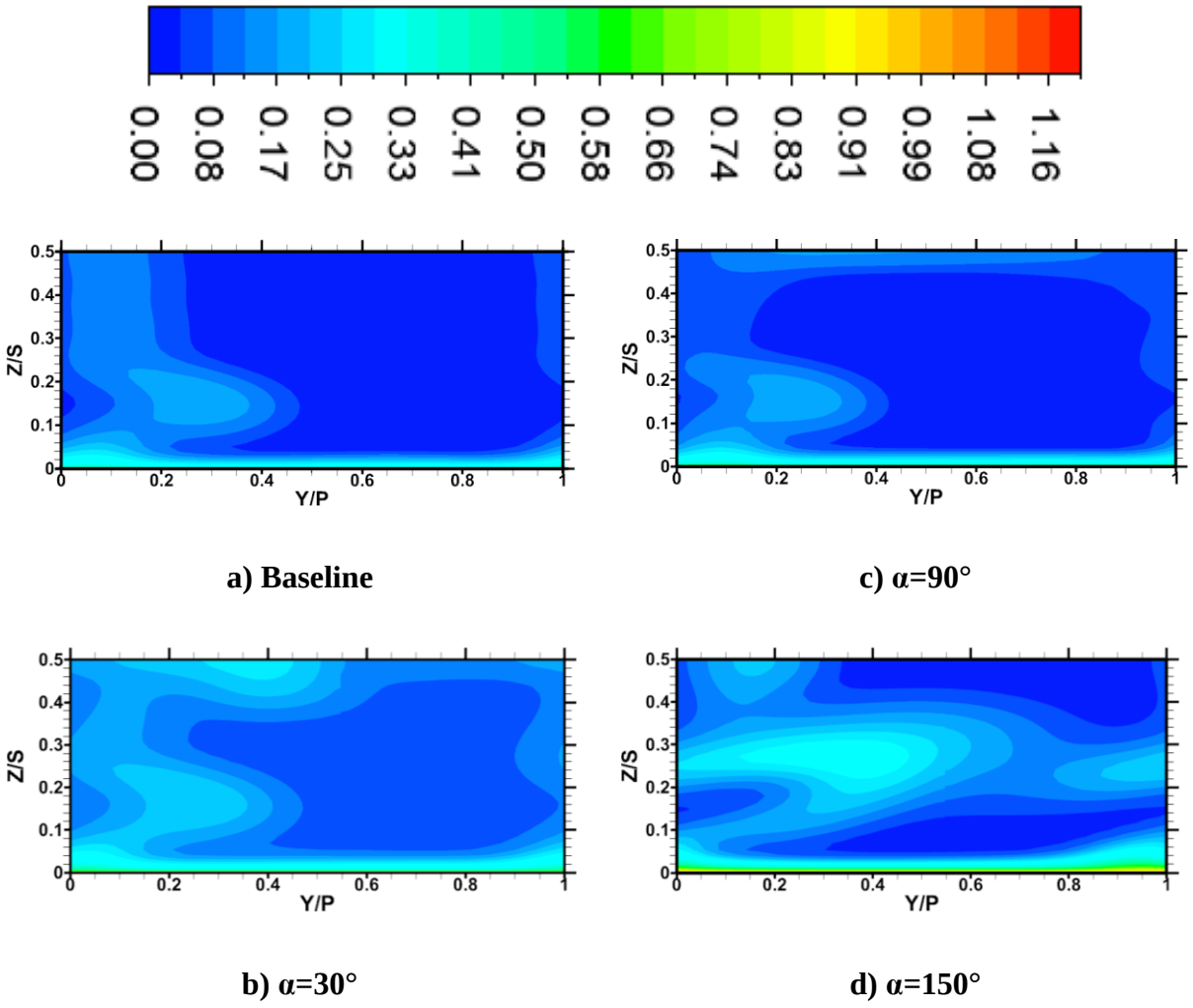

a) Baseline **c) α=90°**

b) α=30° **d) α=150°**

Figure 103: Exit plane total pressure loss coefficient contours for different α values at MFR=0.5% and X=2D

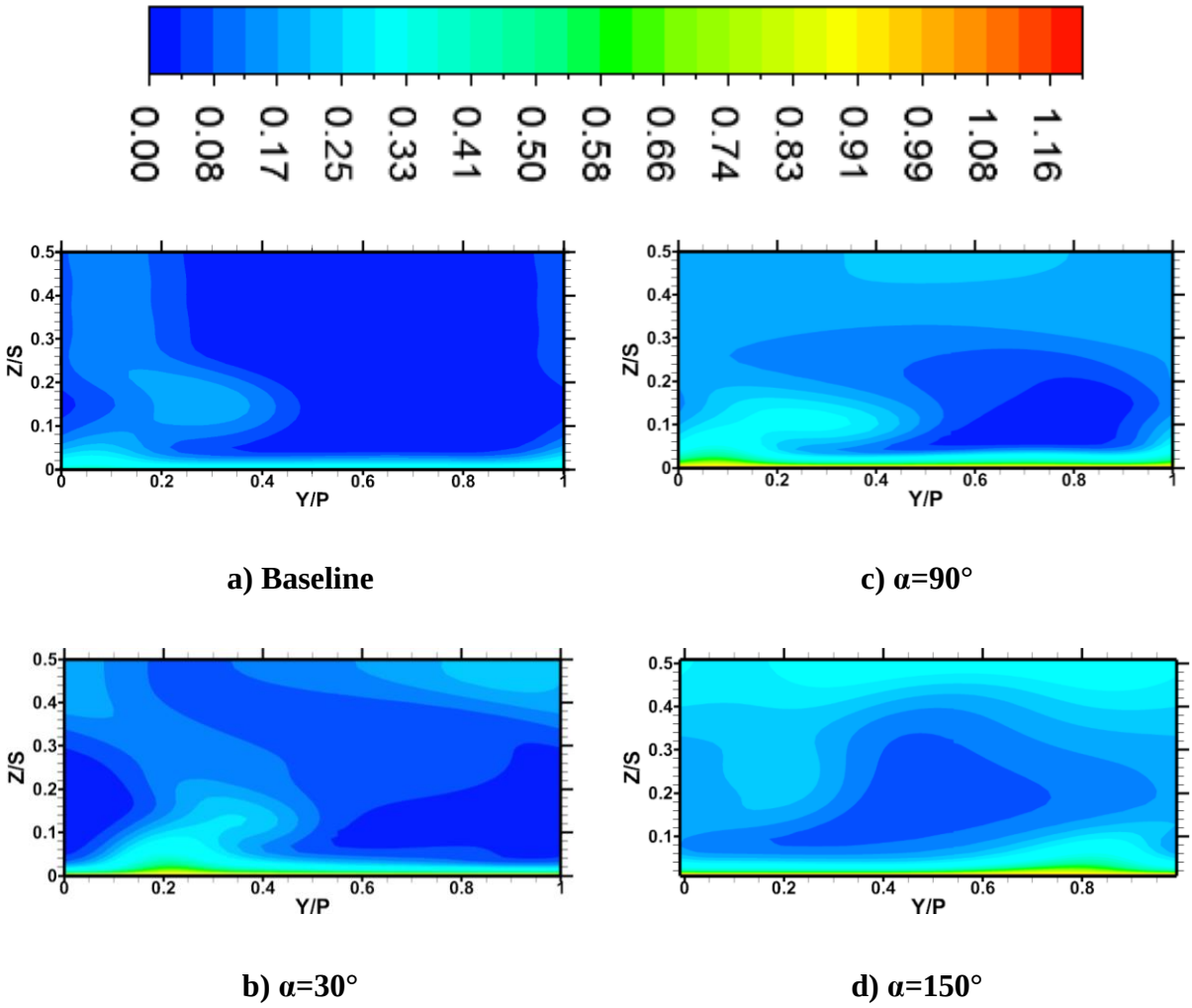

Figure 104: Exit plane total pressure loss coefficient contours for different α values at MFR=1% and X=2D

Exit plane Kinetic Energy Loss Coefficient Plots

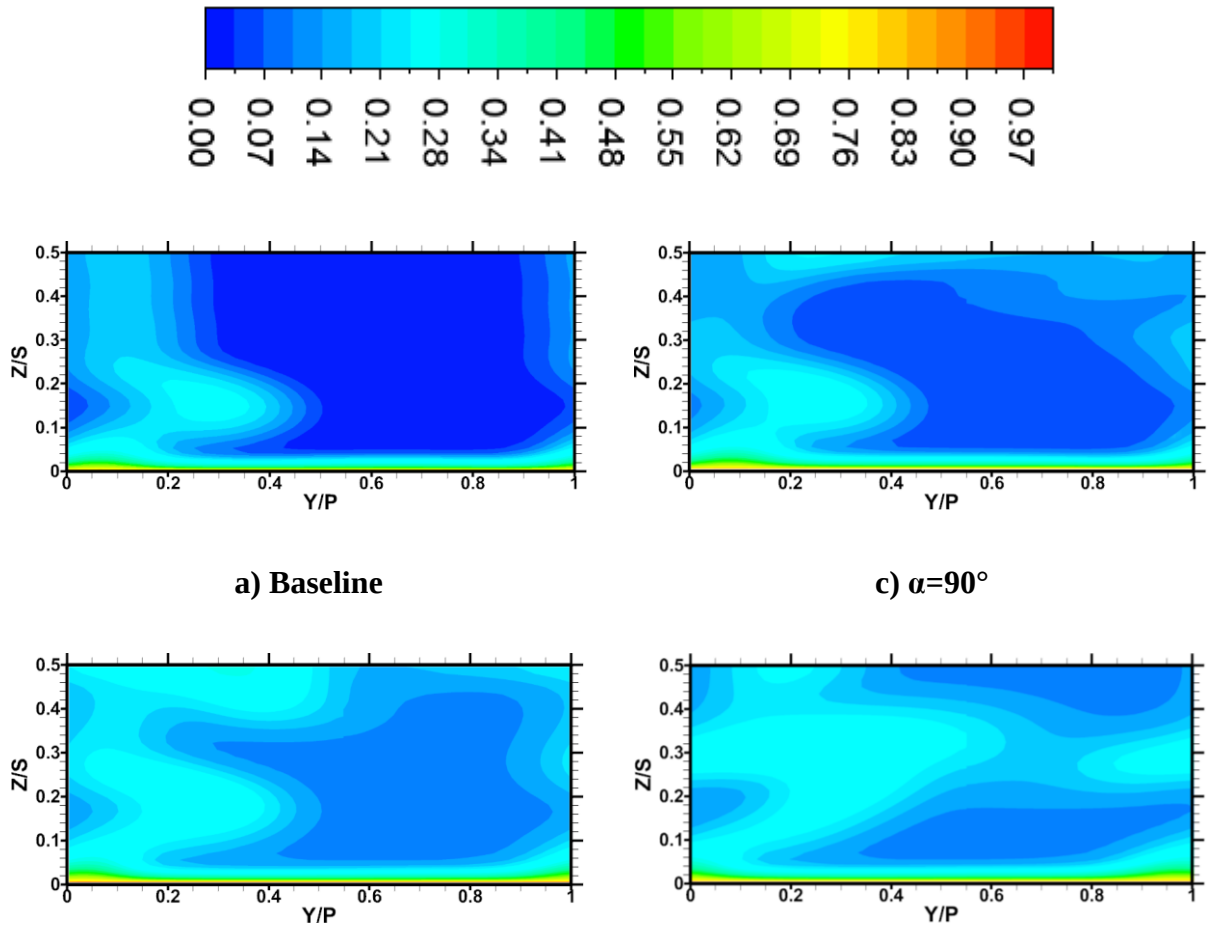

a) Baseline

c) α=90°

b) α=30°

d) α=150°

Figure 105: Exit plane kinetic energy loss coefficient contours for different α values at MFR=0.5% and X=D

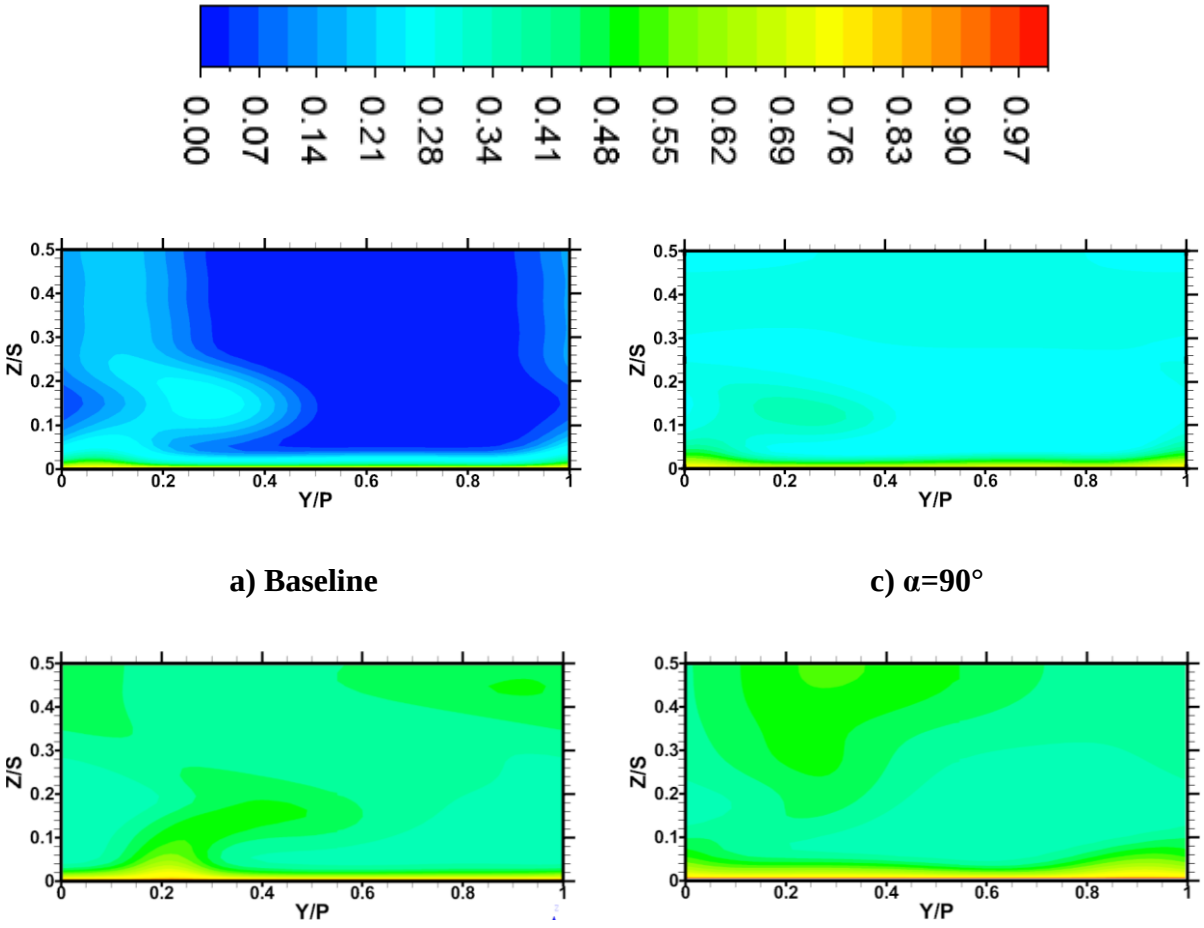

Figure 106: Exit plane kinetic energy loss coefficient contours for different α values at MFR=1% and X=D

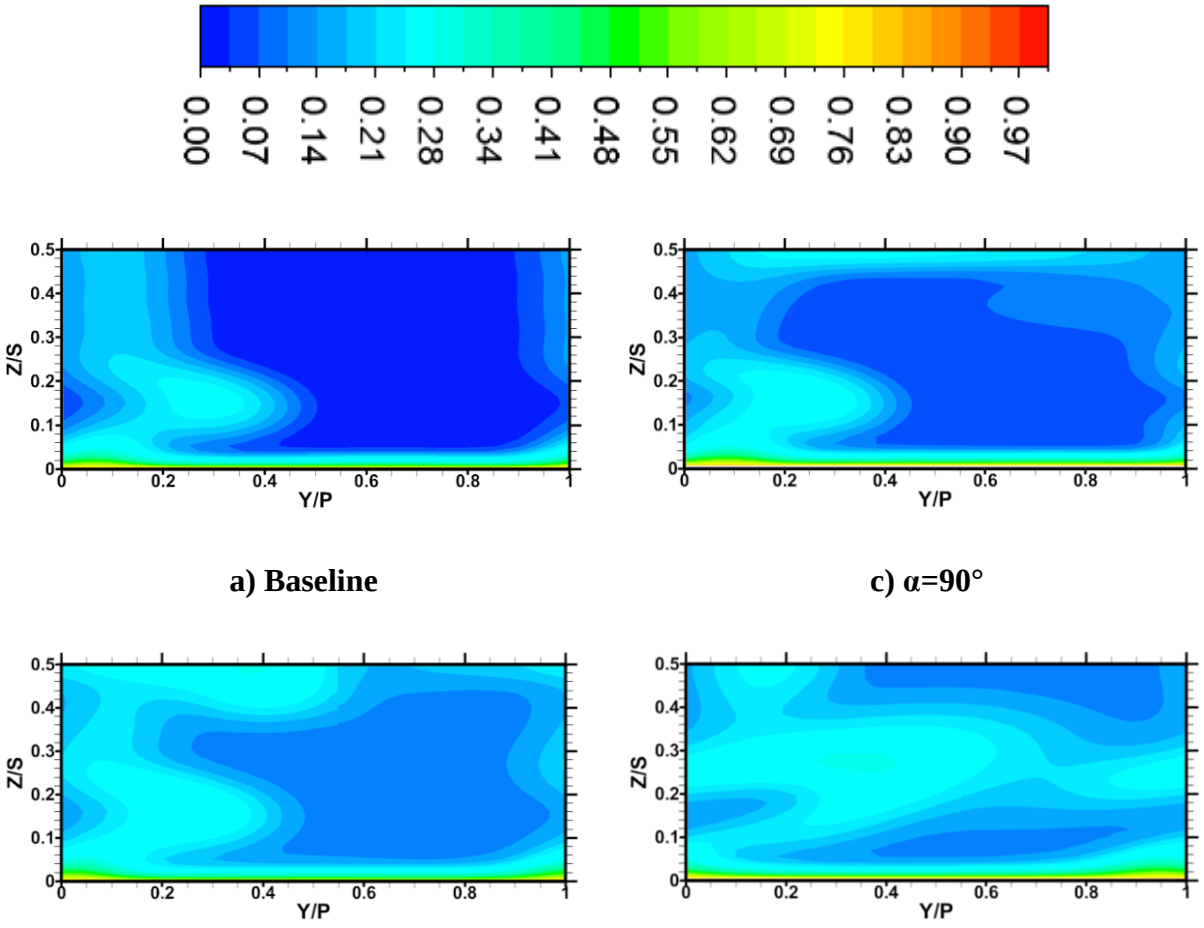

a) Baseline **c) α=90°**

b) α=30° **d) α=150°**

Figure 107: Exit plane kinetic energy loss coefficient contours for different α values at MFR=0.5% and X=2D

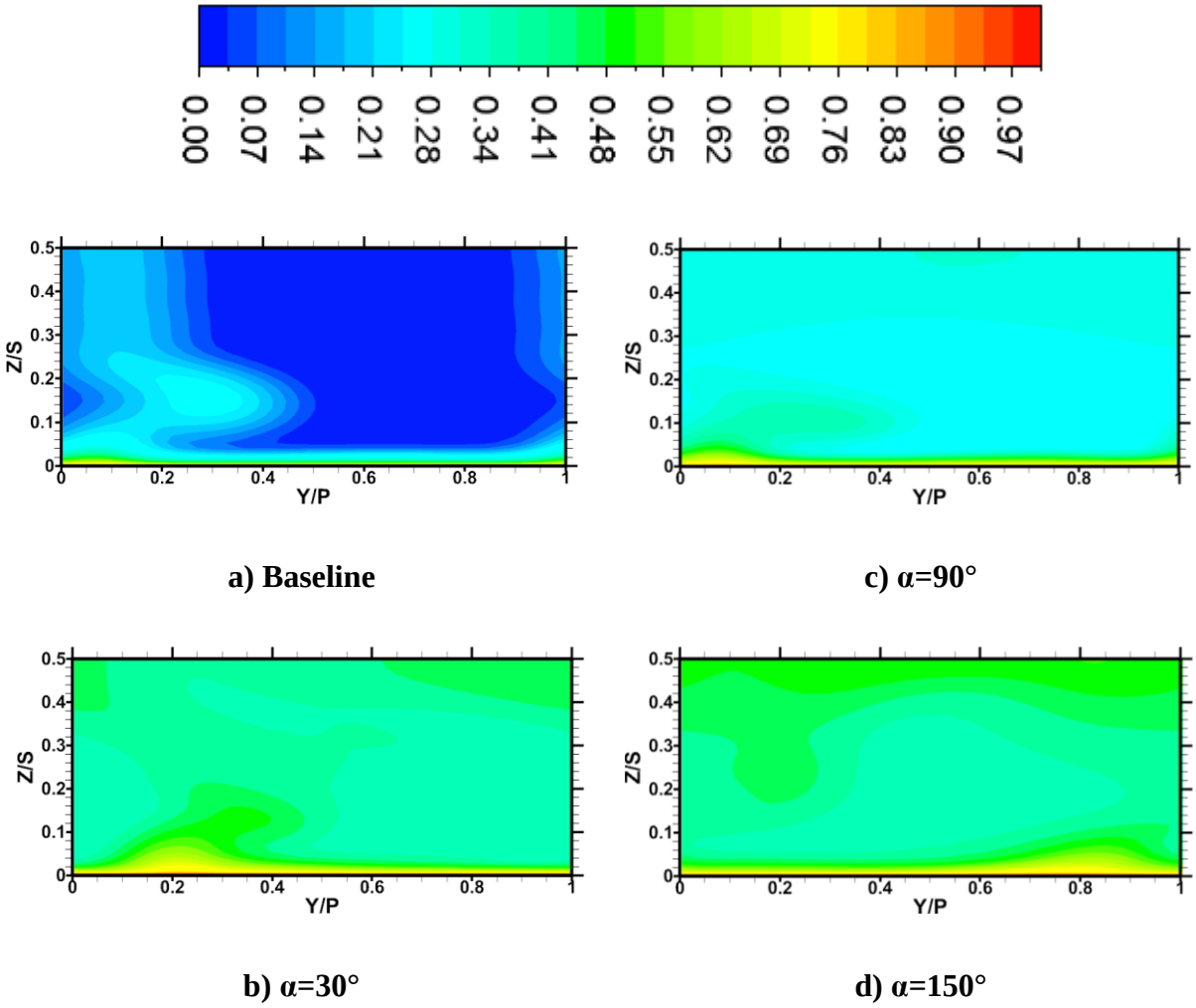

a) Baseline **c) α=90°**

b) α=30° **d) α=150°**

Figure 108: Exit plane kinetic energy loss coefficient contours for different α values at MFR=1% and X=2D

Beta Study

Table 25: Details of parameters tested in Beta study for X=D

X/D	α (deg)	β (deg)	MFR
1	30	0	0.5
1	30	30	0.5
1	30	45	0.5
1	30	60	0.5
1	30	90	0.5
1	30	0	1
1	30	30	1
1	30	45	1
1	30	60	1
1	30	90	1

Table 26: Details of parameters tested in Beta study for X=2D

X/D	α (deg)	β (deg)	MFR
2	30	0	0.5
2	30	30	0.5
2	30	45	0.5
2	30	60	0.5
2	30	90	0.5
2	30	0	1
2	30	30	1
2	30	45	1
2	30	60	1
2	30	90	1

Leading edge Vortex Streamlines

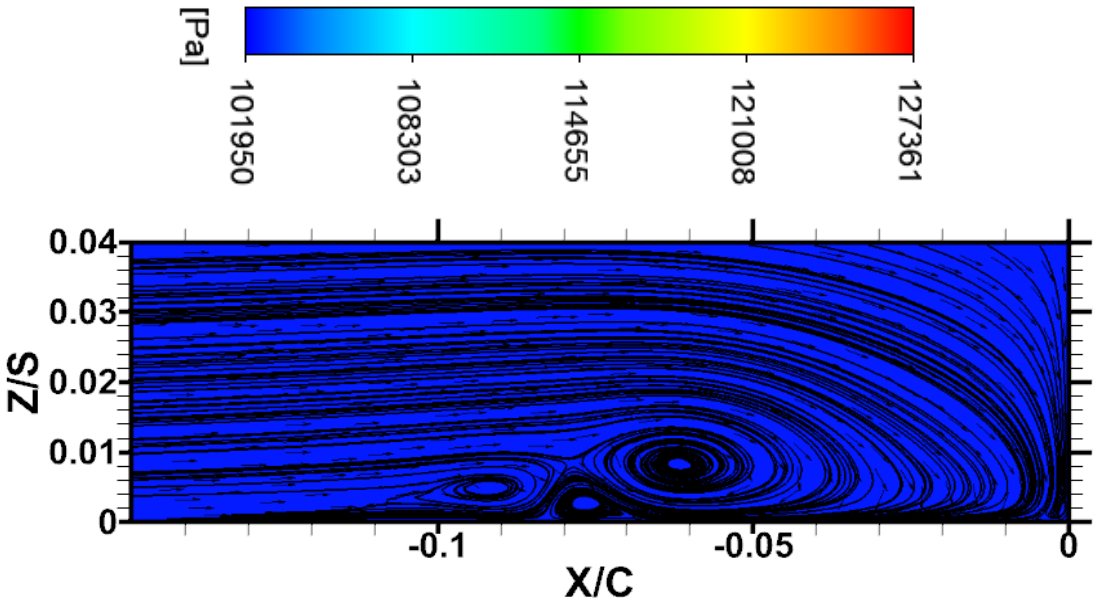

a) Baseline

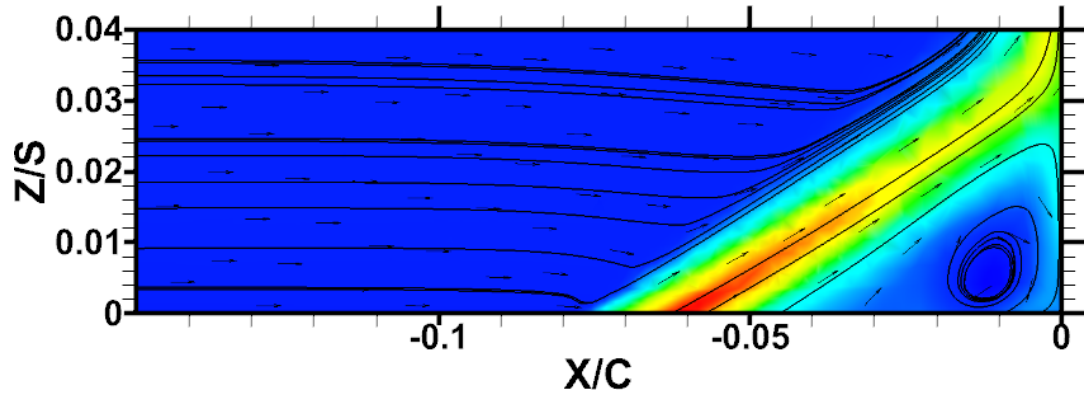

b) β=0°

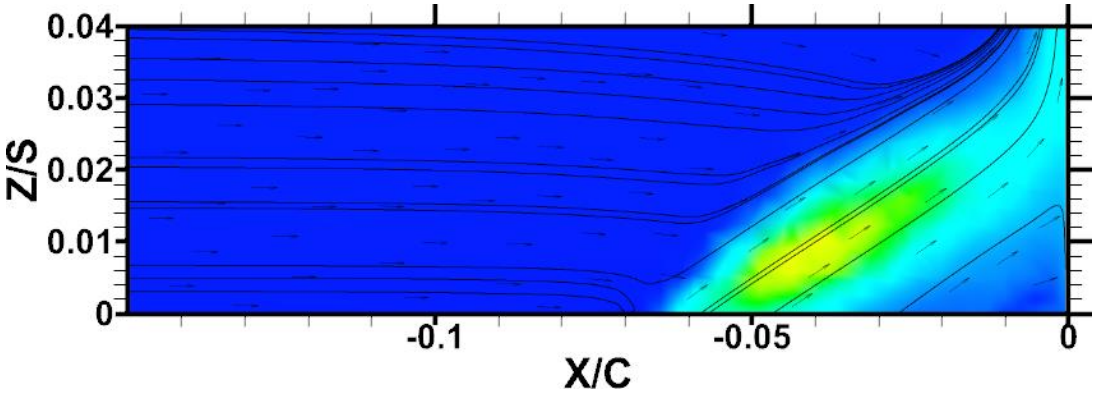

c) β=30°

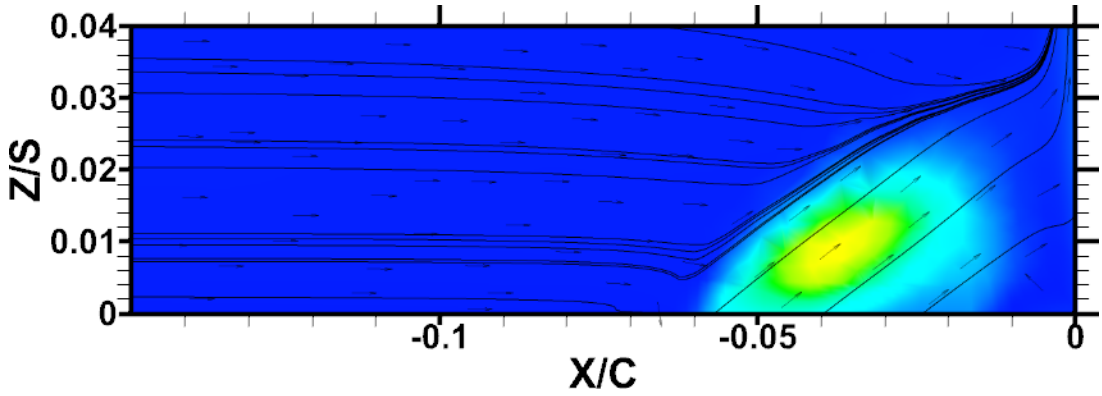

d) β=45°

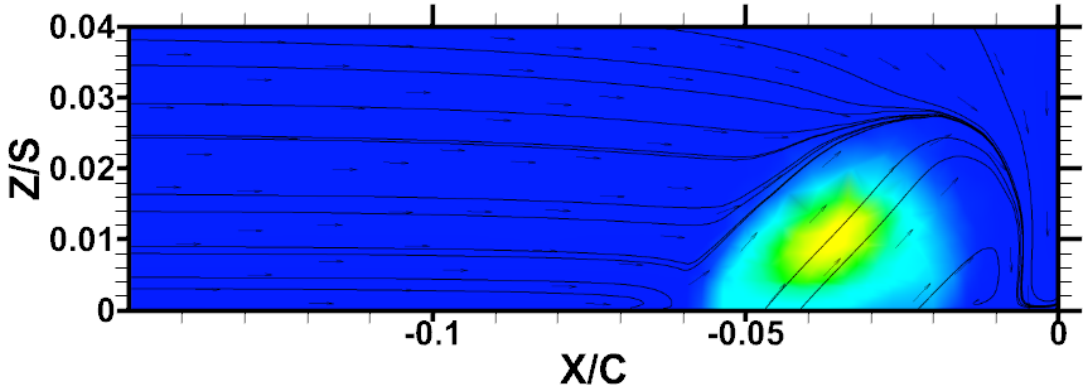

d) β=60°

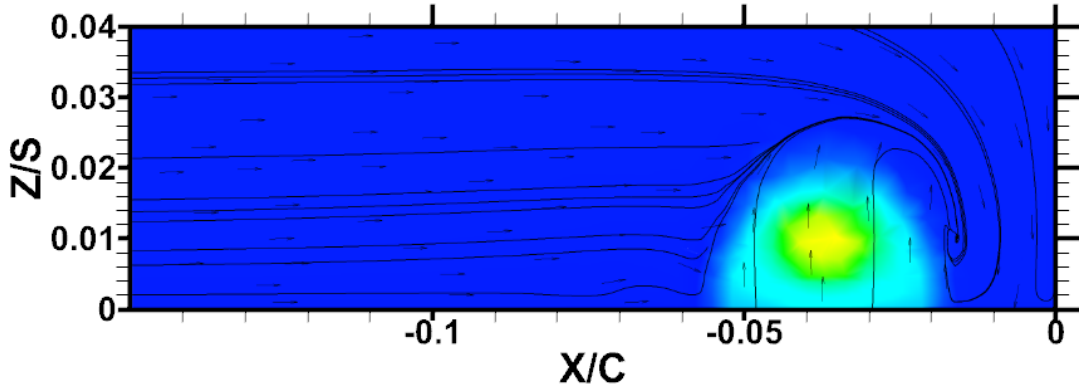

e) β=90°

Figure 109: Leading edge velocity streamlines and vectors overlaid with total pressure (absolute) contours at different β values at MFR=0.5%, α=30°, and X=D

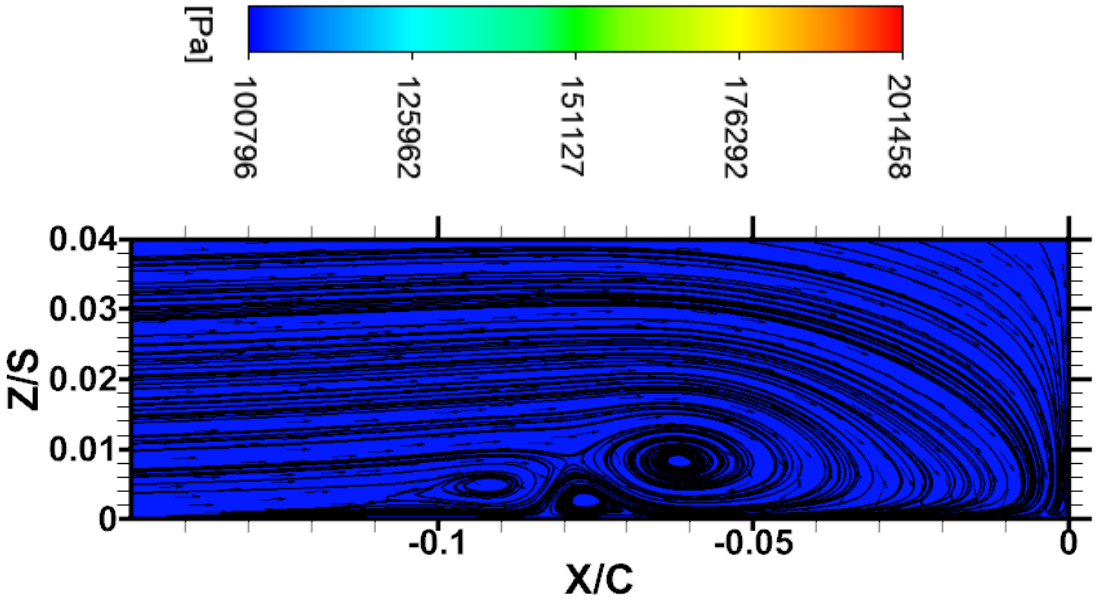

a) Baseline

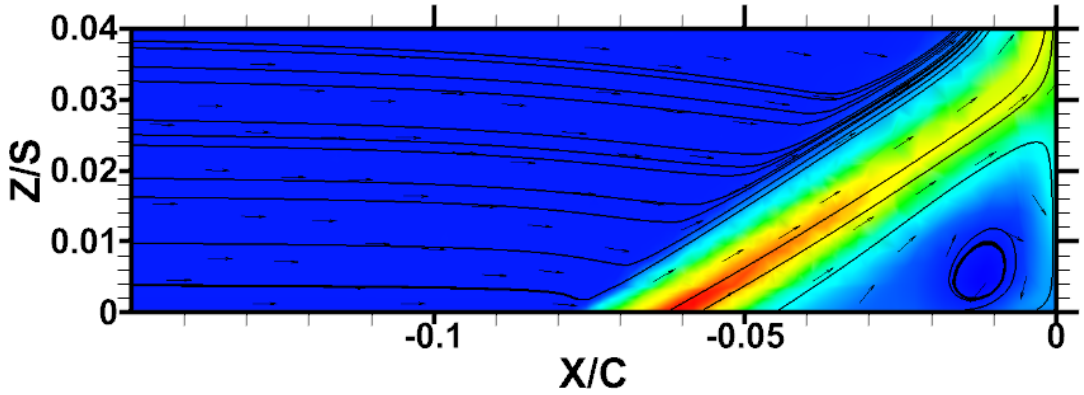

b) β=0°

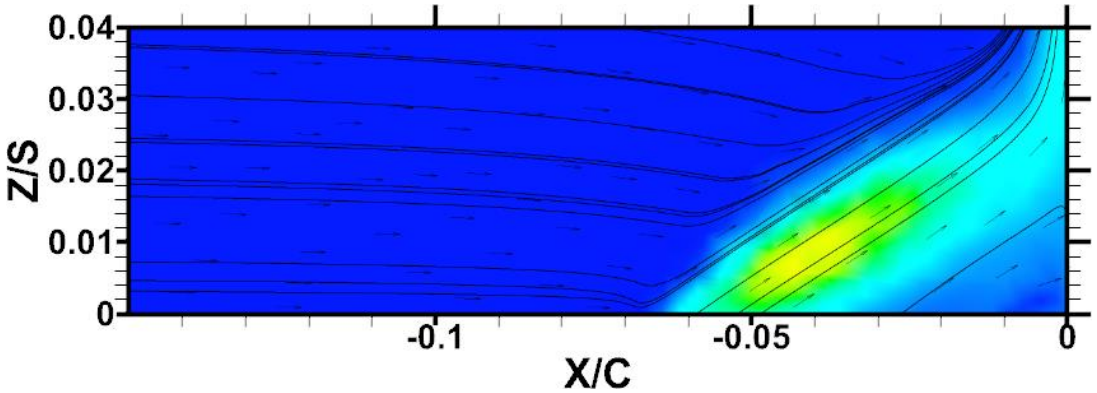

c) β=30°

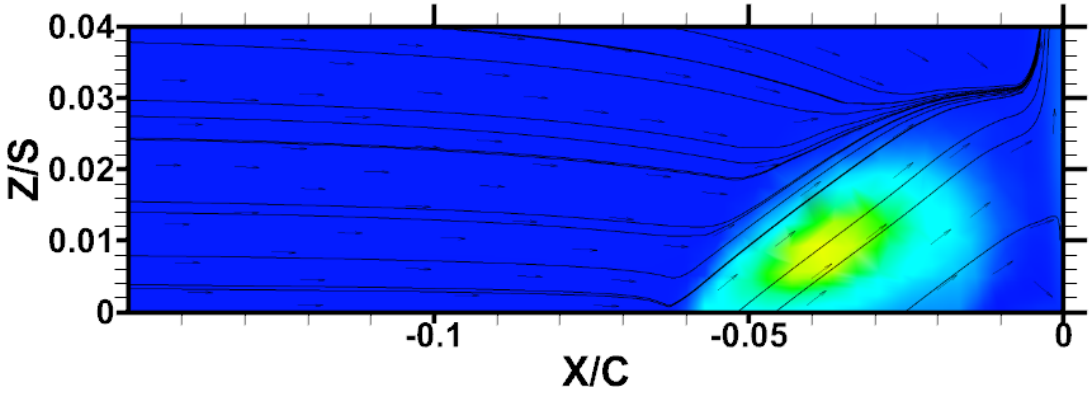

d) β=45°

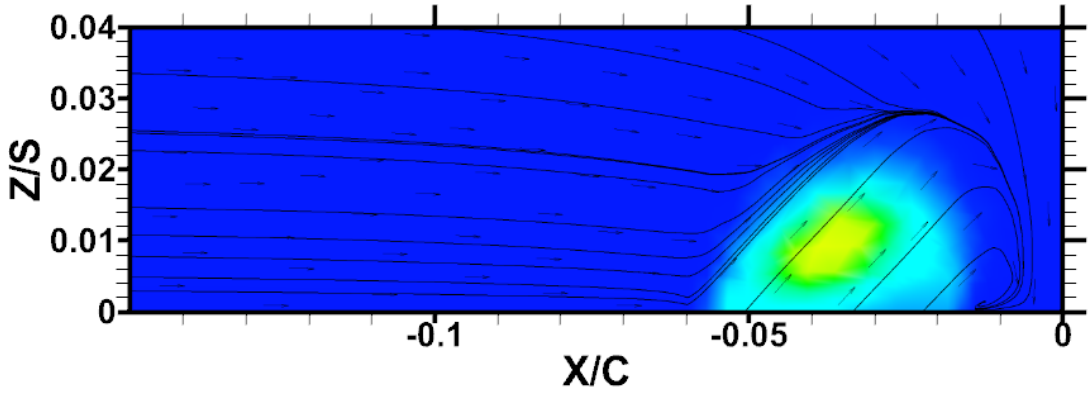

d) β=60°

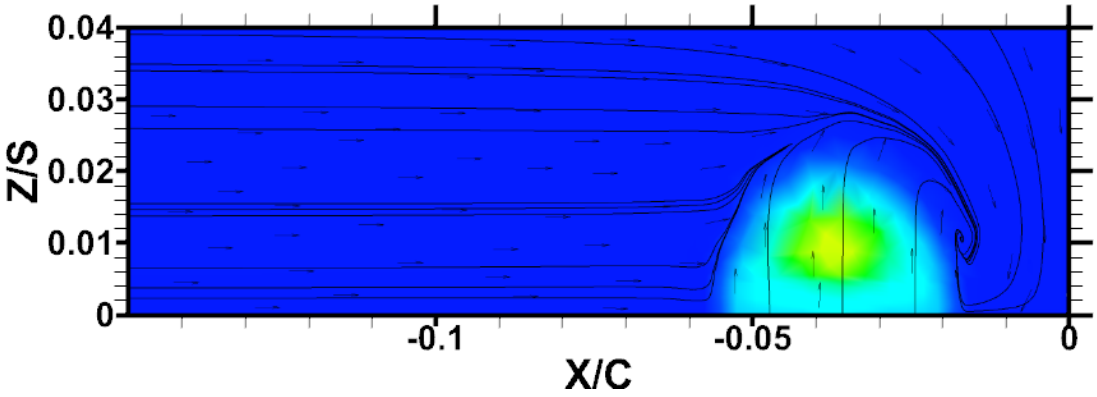

e) β=90°

Figure 110: Leading edge velocity streamlines and vectors overlaid with total pressure (absolute) contours at different β values at MFR=1%, α=30°, and X=D

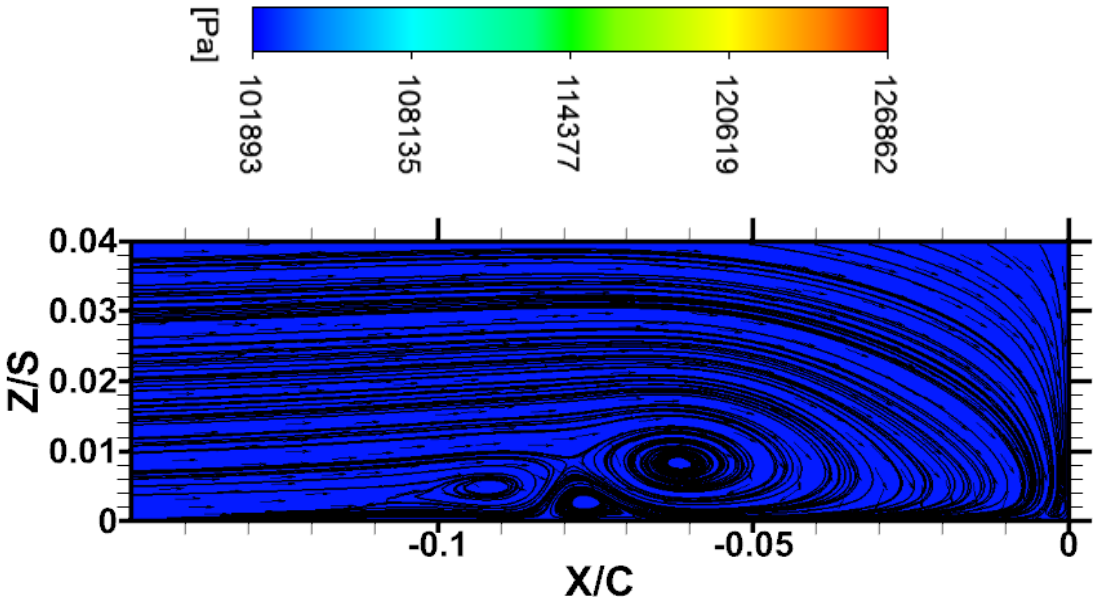

a) Baseline

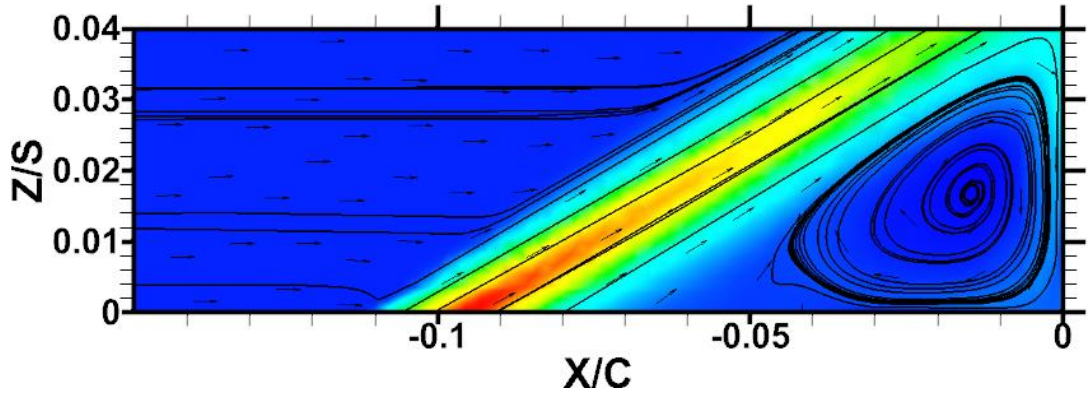

b) β=0°

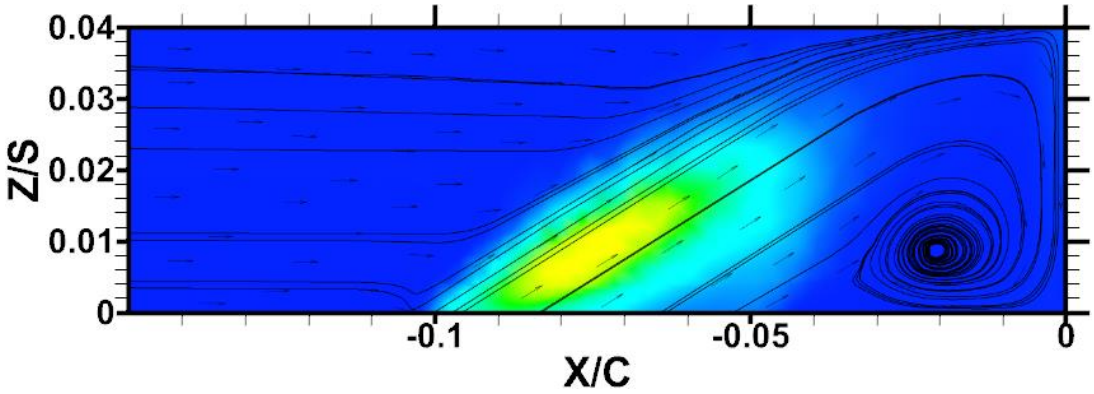

c) β=30°

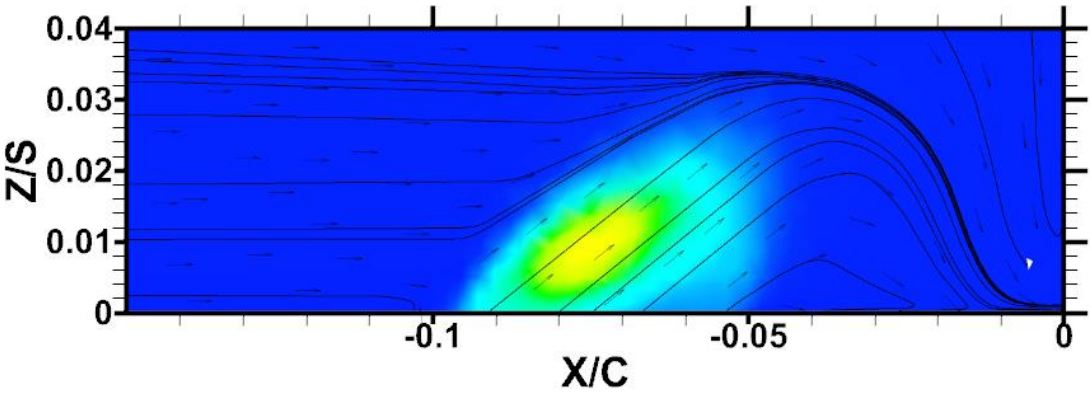

d) β=45°

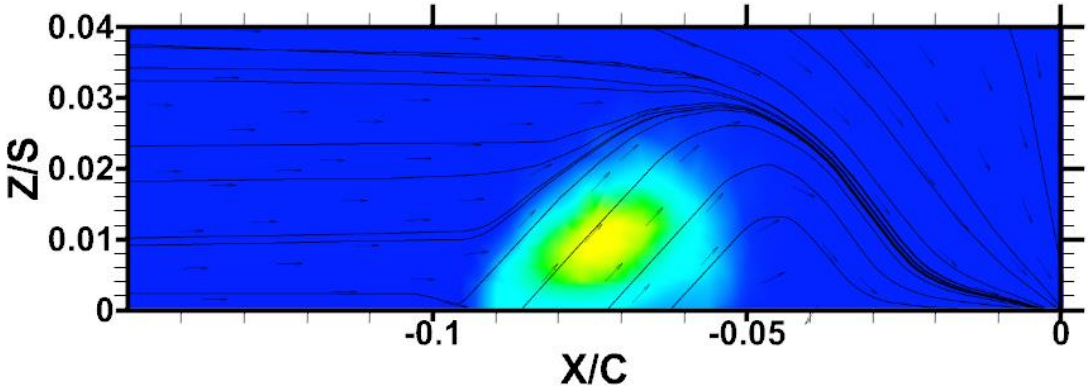

d) β=60°

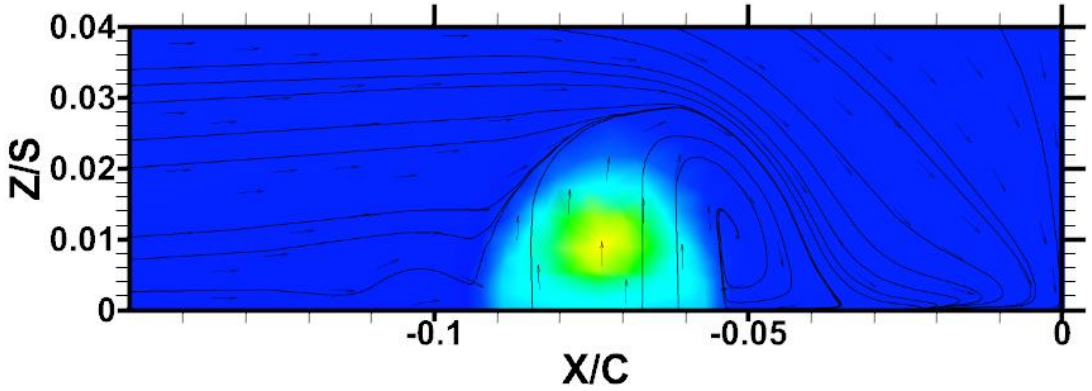

e) β=90°

Figure 111: Leading edge velocity streamlines and vectors overlaid with total pressure (absolute) contours at different β values at MFR=0.5%, α=30°, and X=2D

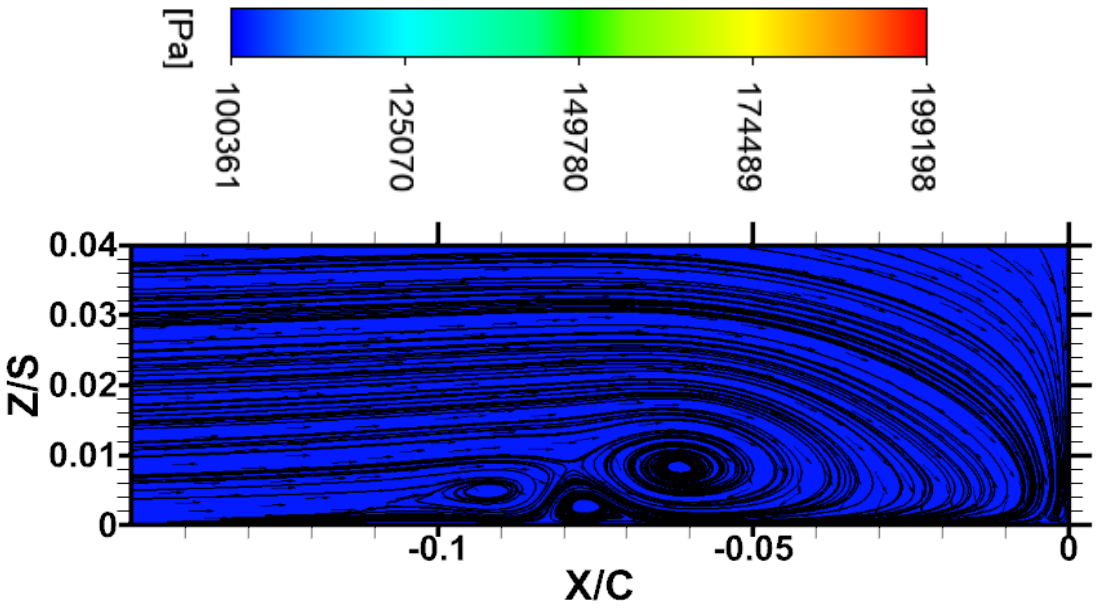

a) Baseline

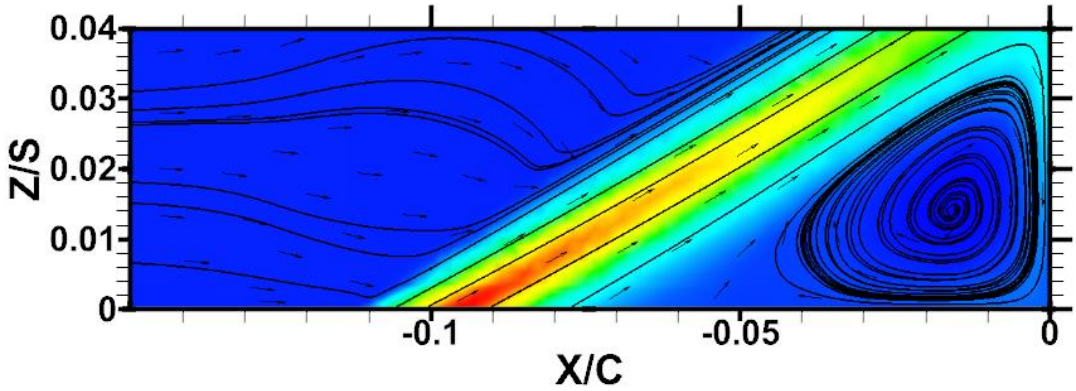

b) β=0°

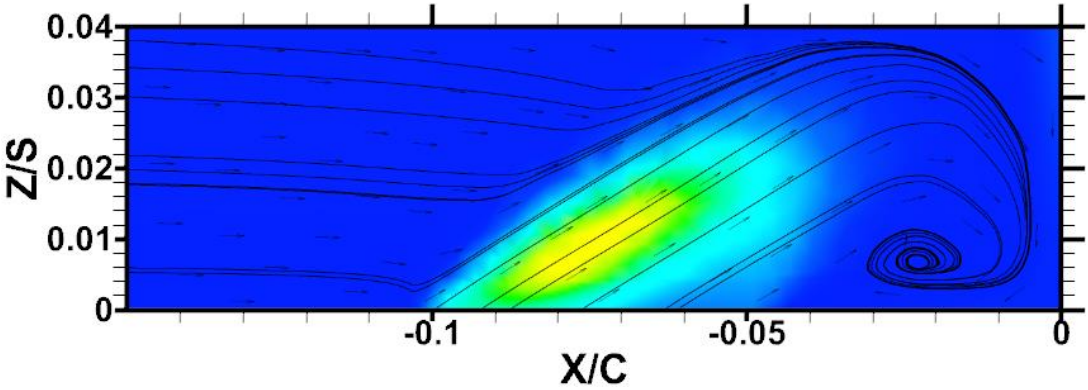

c) β=30°

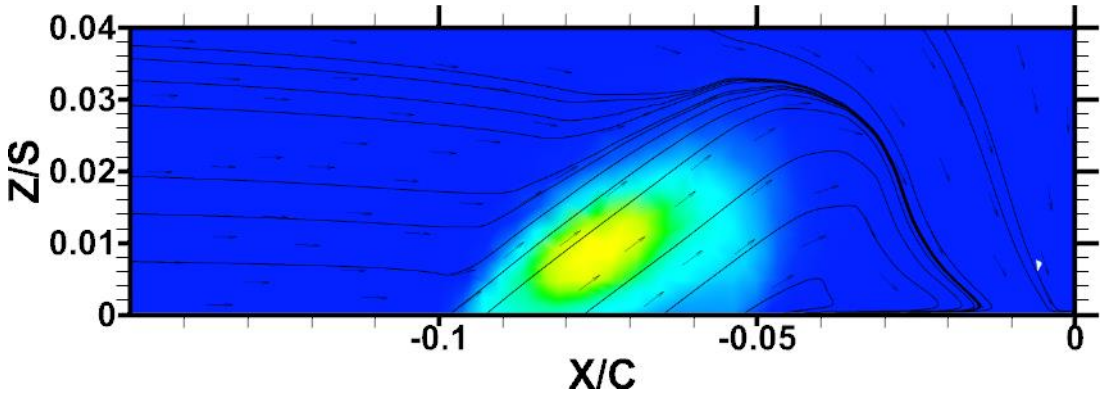

d) β=45°

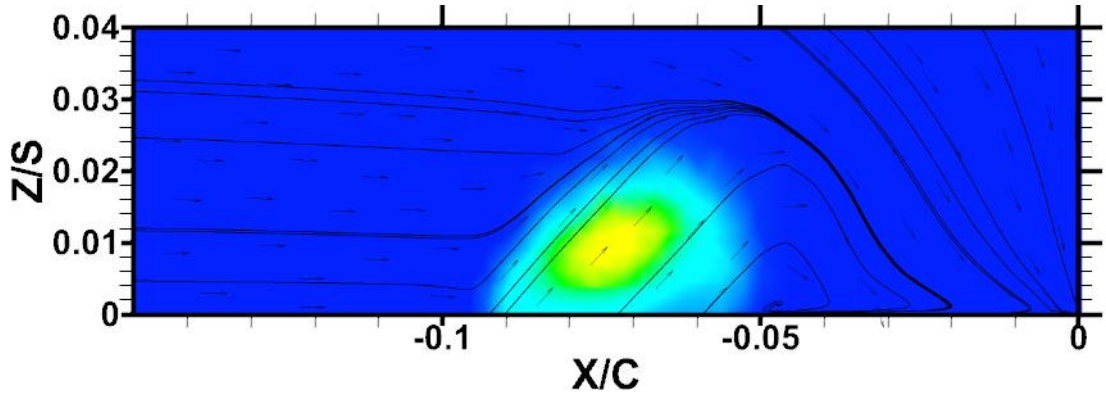

d) β=60°

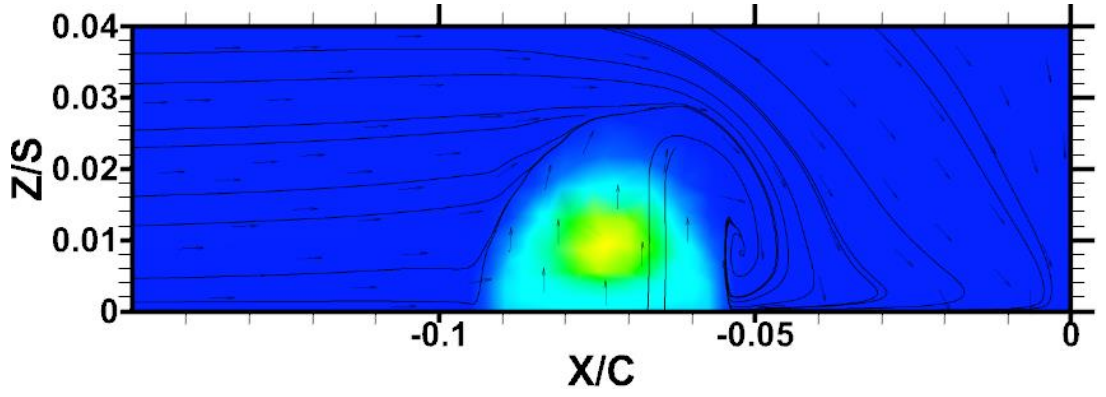

e) β=90°

Figure 112: Leading edge velocity streamlines and vectors overlaid with total pressure (absolute) contours at different β values at MFR=1%, α=30°, and X=2D

Passage Vortex Swirling Strength Plots

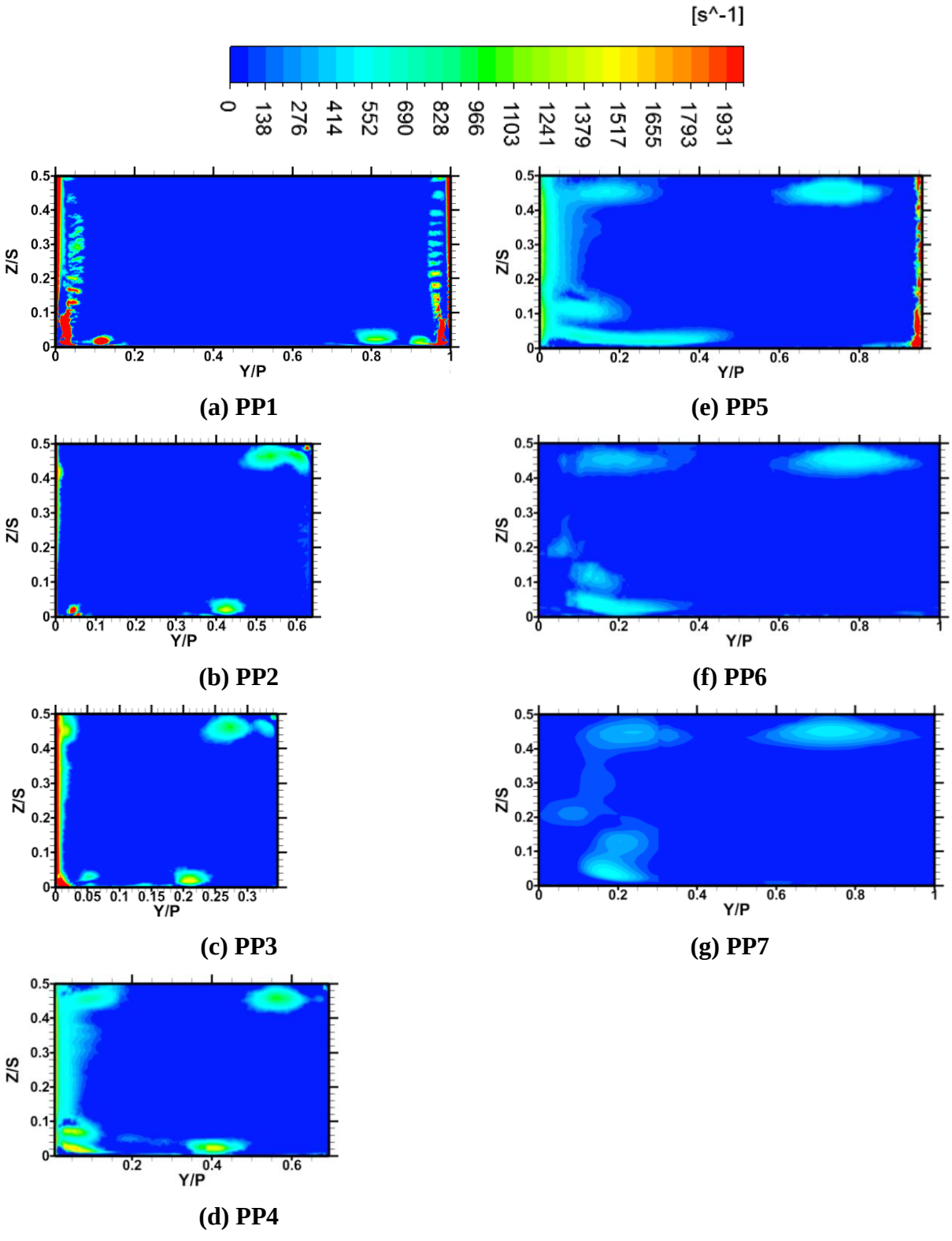

Figure 113: Swirling Strength Contours at various axial planes through the passage for the case X_h=D, α=30°, β=0°, MFR=0.5%

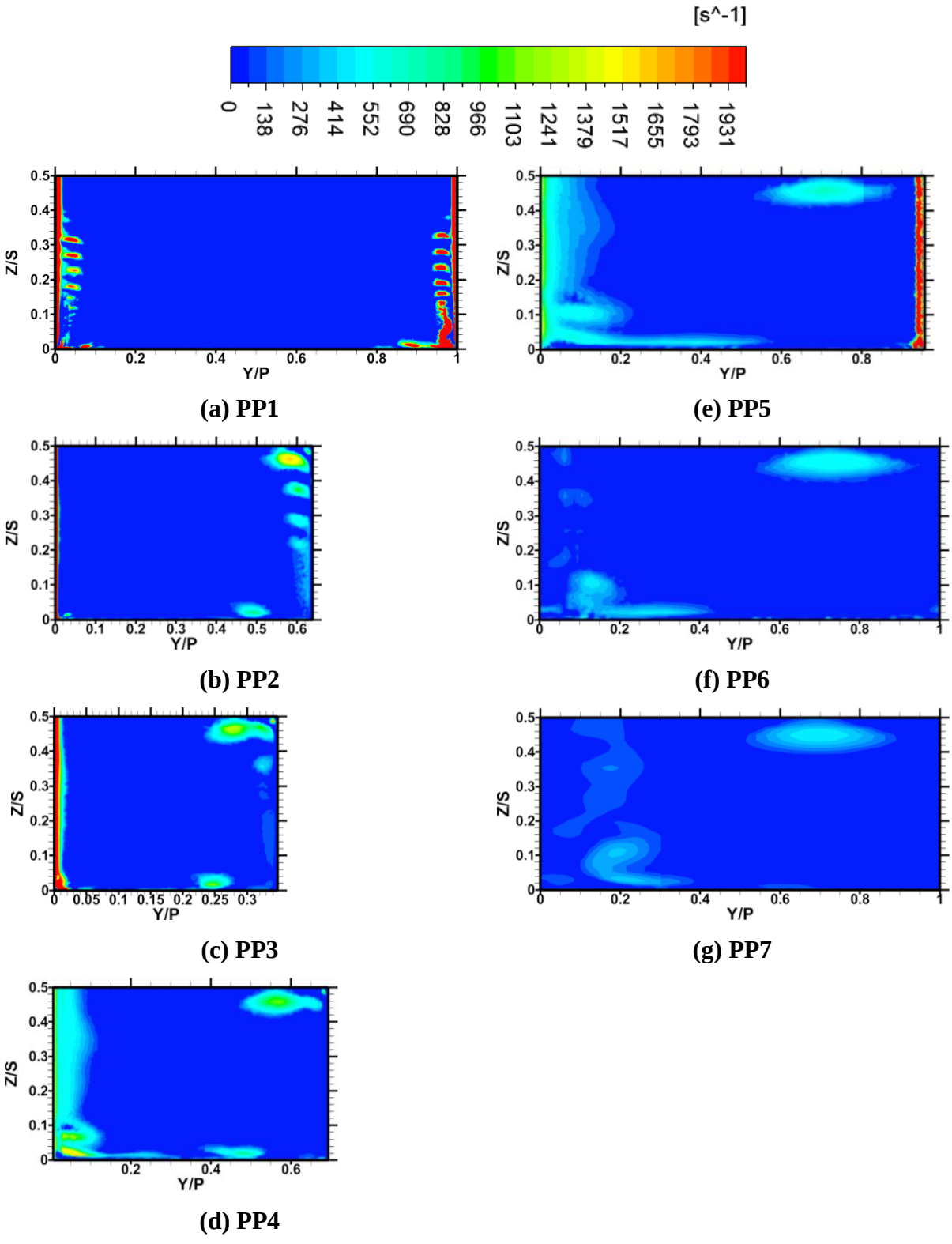

Figure 114: Swirling Strength Contours at various axial planes through the passage for the case X_h=D, α=30°, β=30°, MFR=0.5%

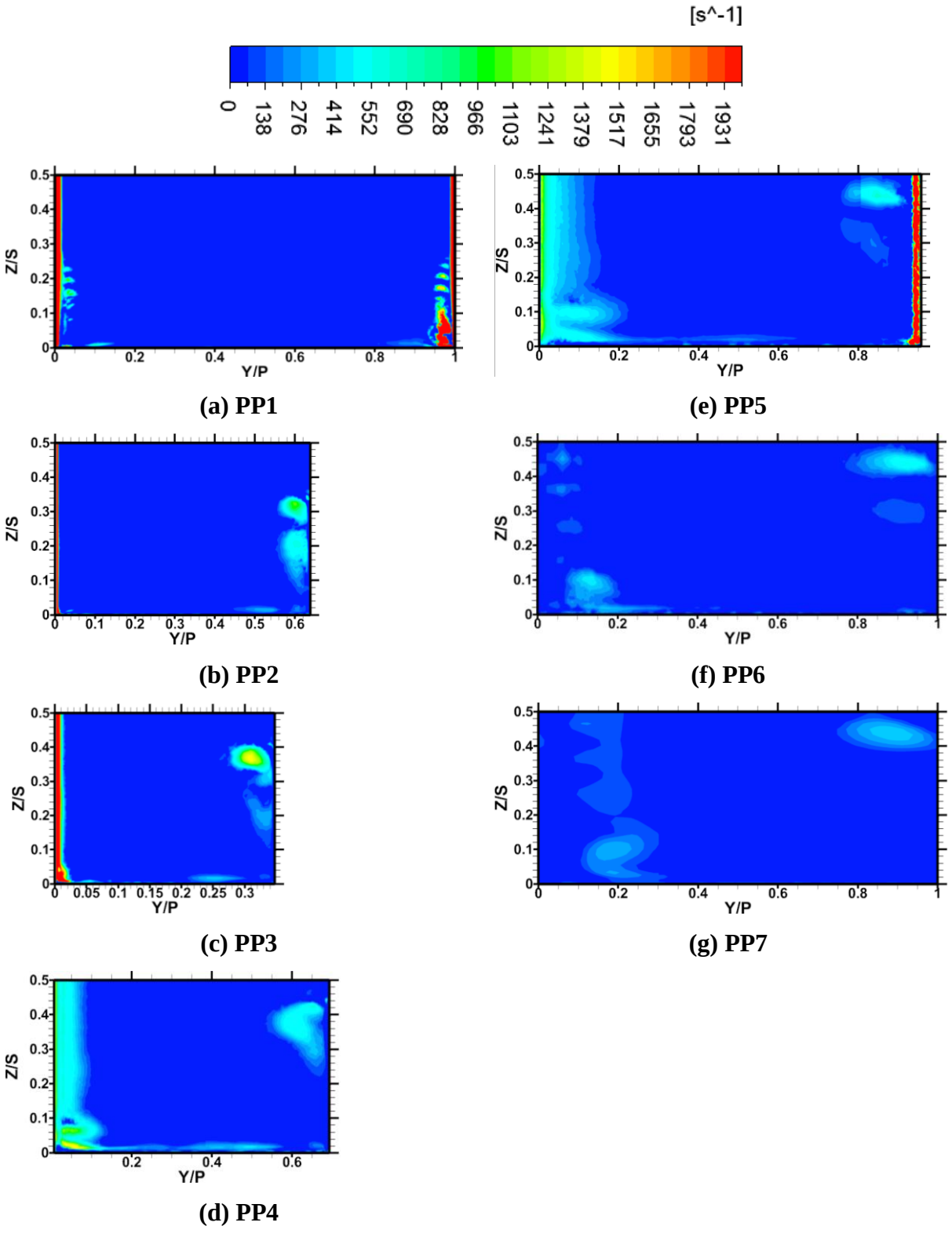

Figure 115: Swirling Strength Contours at various axial planes through the passage for the case X_h=D, α=30°, β=45°, MFR=0.5%

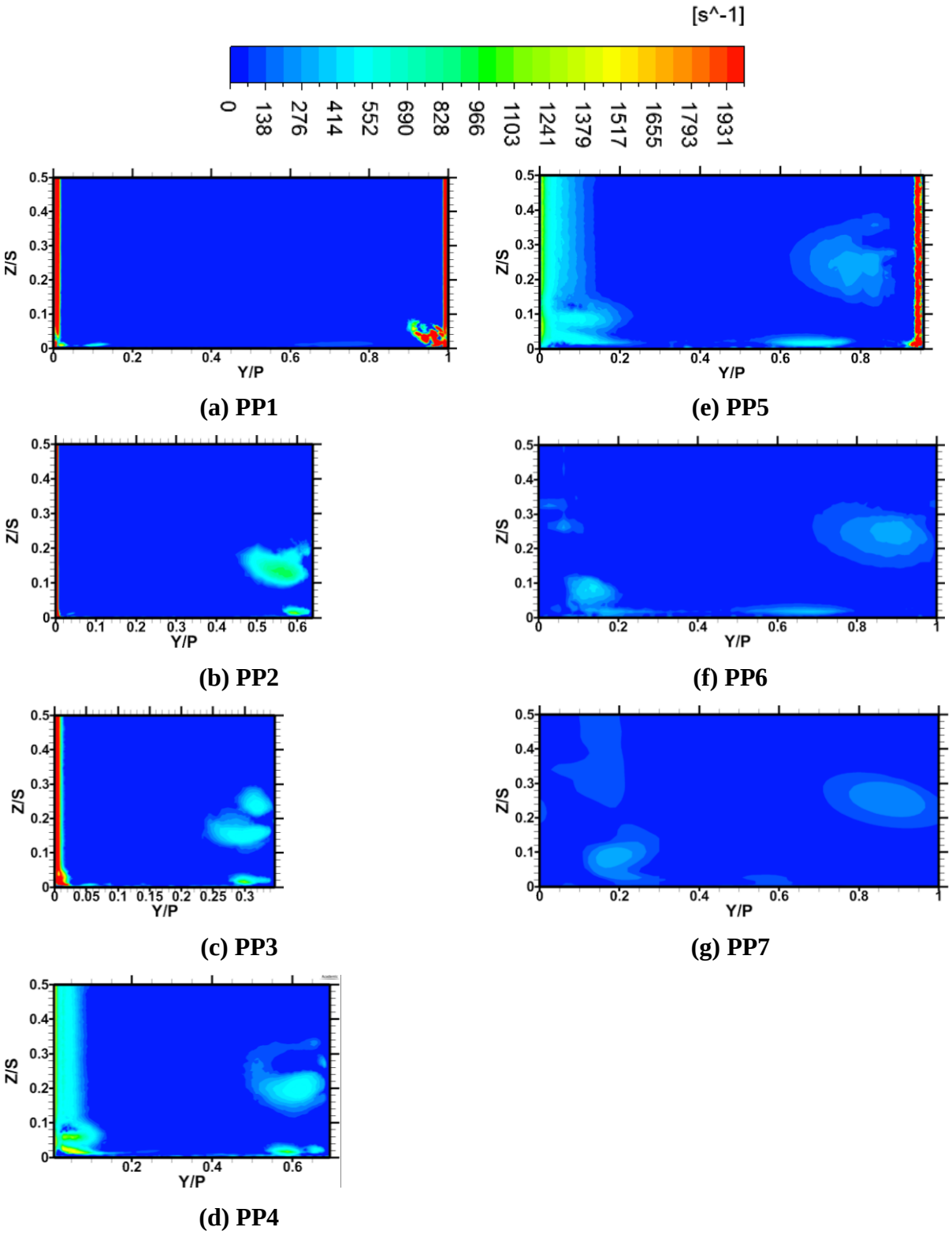

Figure 116: Swirling Strength Contours at various axial planes through the passage for the case X_h=D, α=30°, β=60°, MFR=0.5%

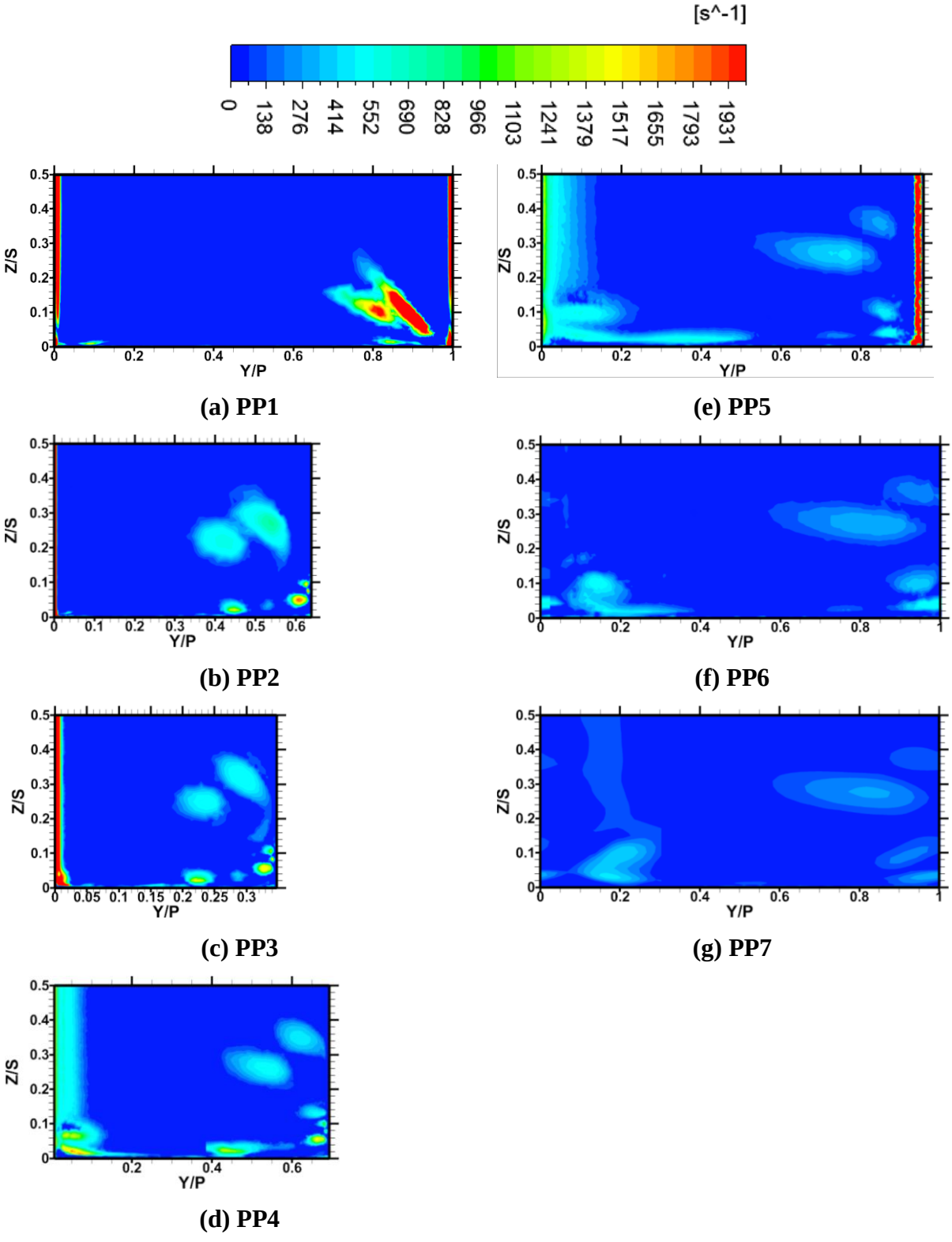

(a) PP1

(e) PP5

(b) PP2

(f) PP6

(c) PP3

(g) PP7

(d) PP4

Figure 117: Swirling Strength Contours at various axial planes through the passage for the case X_h=D, α=30°, β=90°, MFR=0.5%

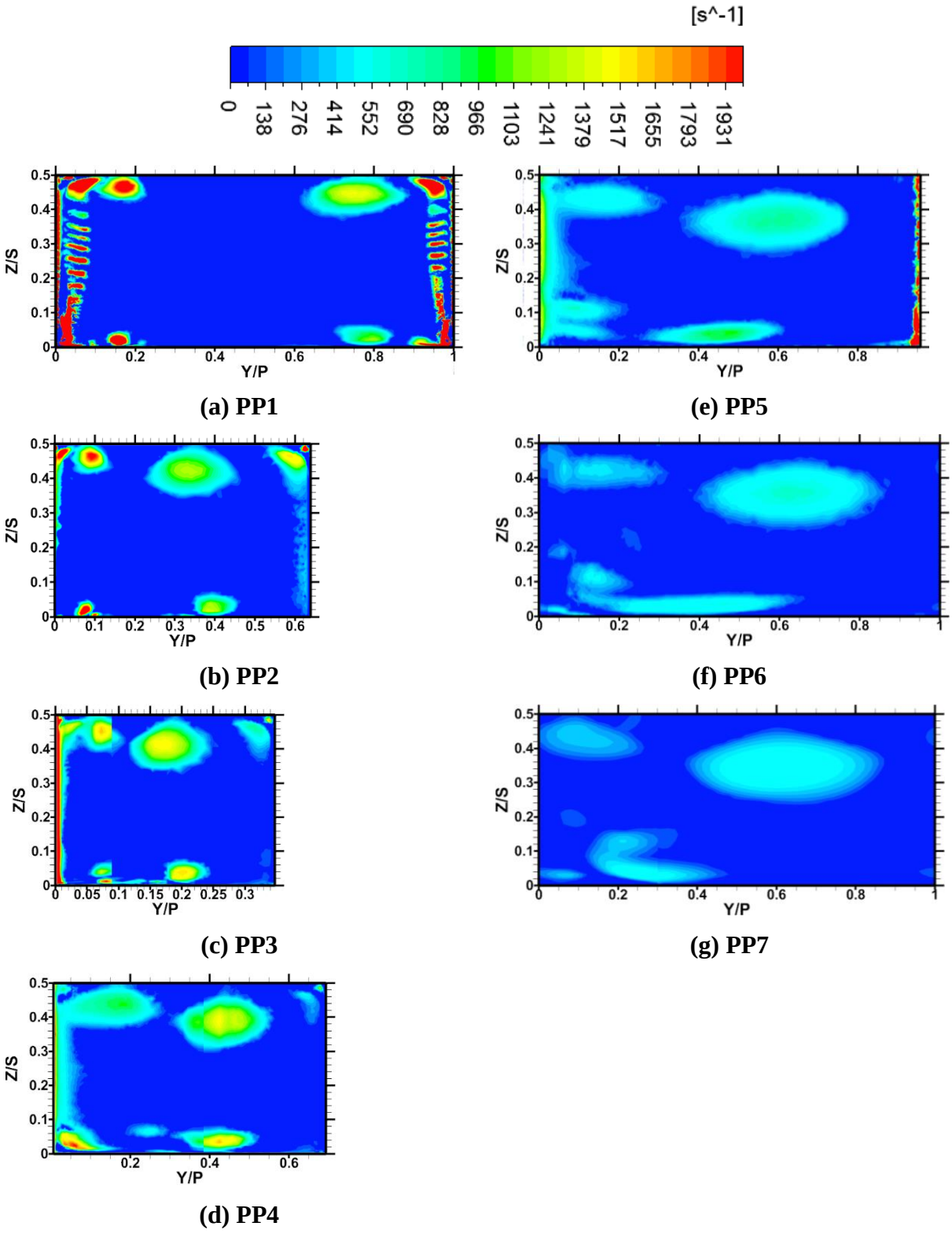

Figure 118: Swirling Strength Contours at various axial planes through the passage for the case X_h=D, α=30°, β=0°, MFR=1%

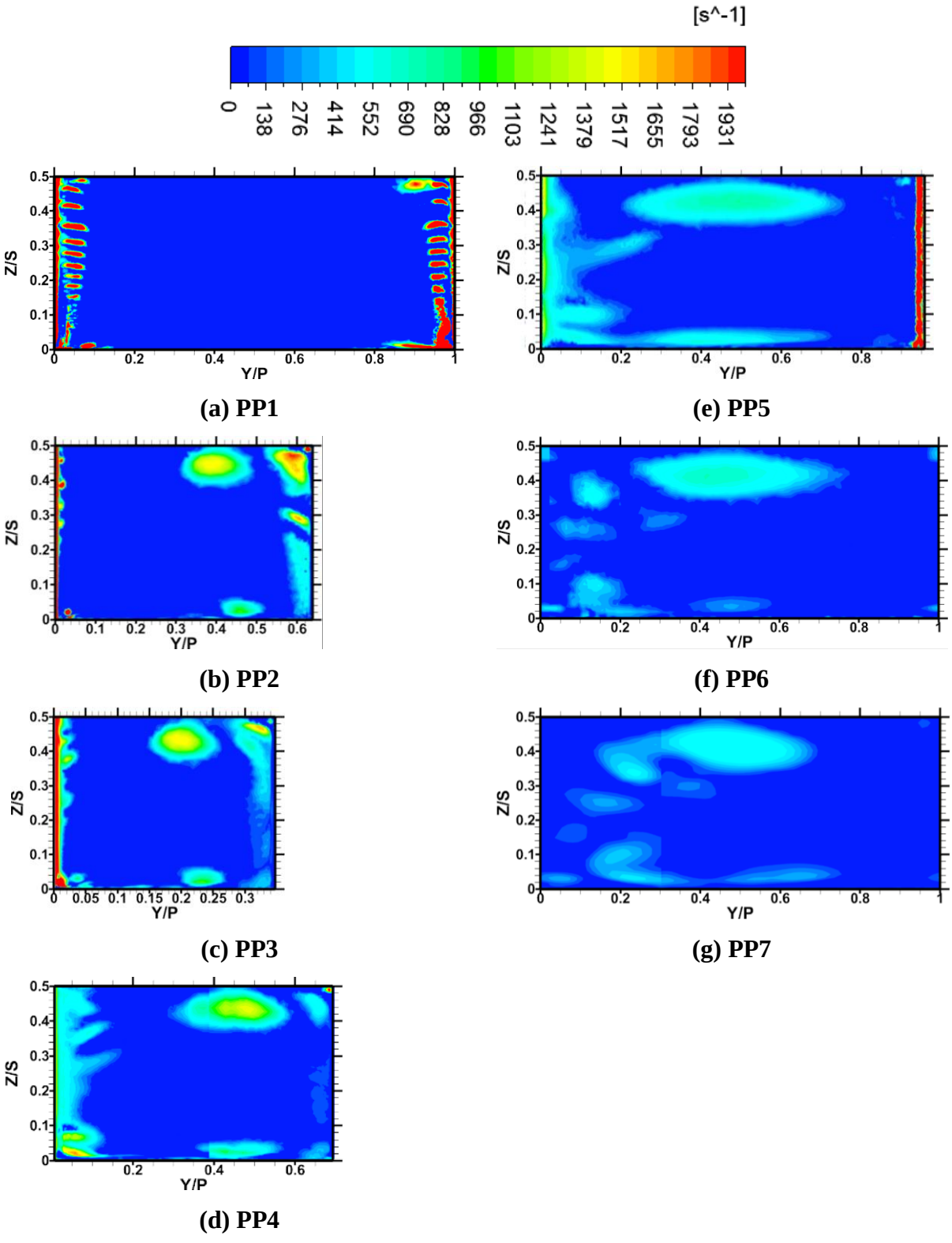

Figure 119: Swirling Strength Contours at various axial planes through the passage for the case X_h=D, α=30°, β=30°, MFR=1%

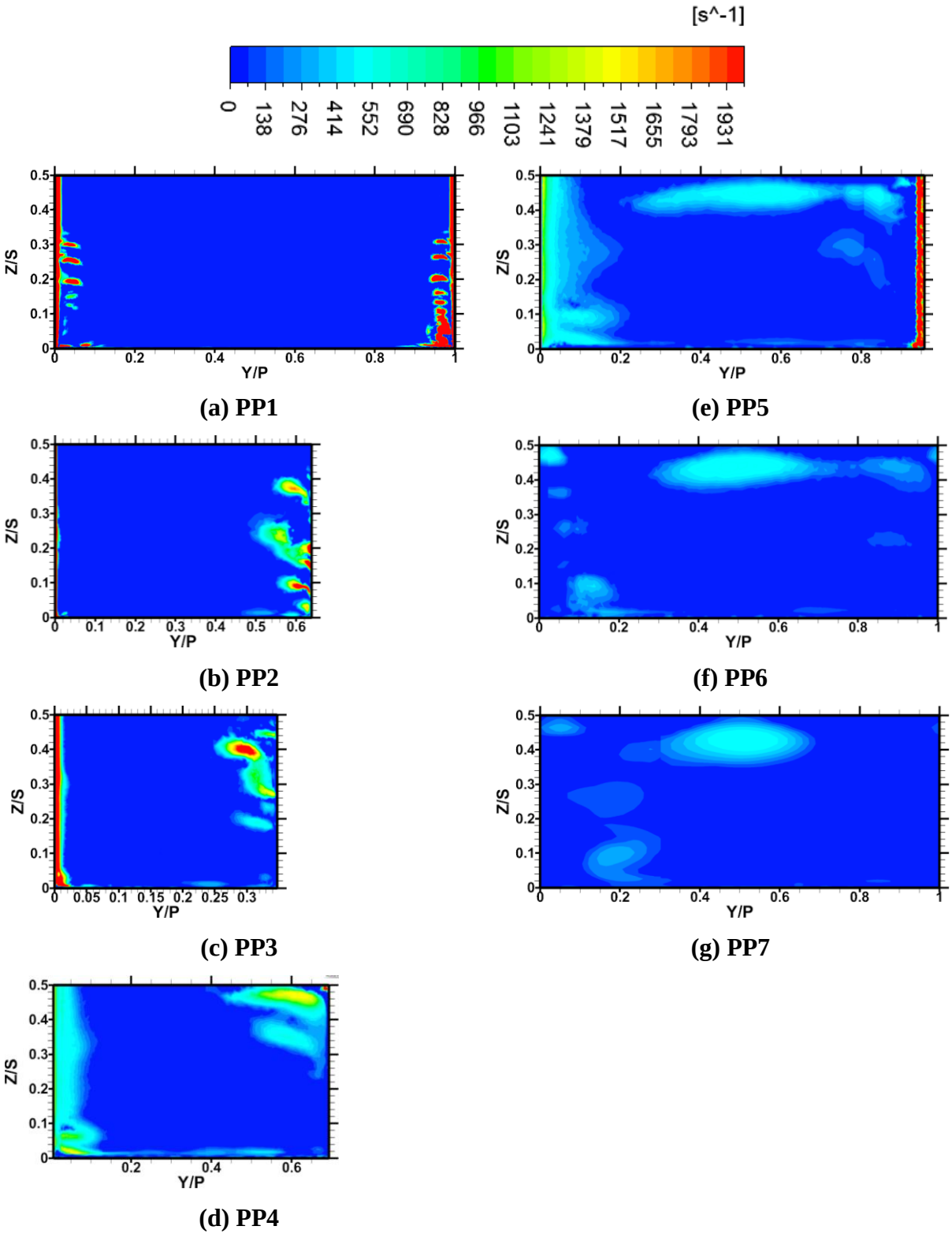

Figure 120: Swirling Strength Contours at various axial planes through the passage for the case X_h=D, α=30°, β=45°, MFR=1%

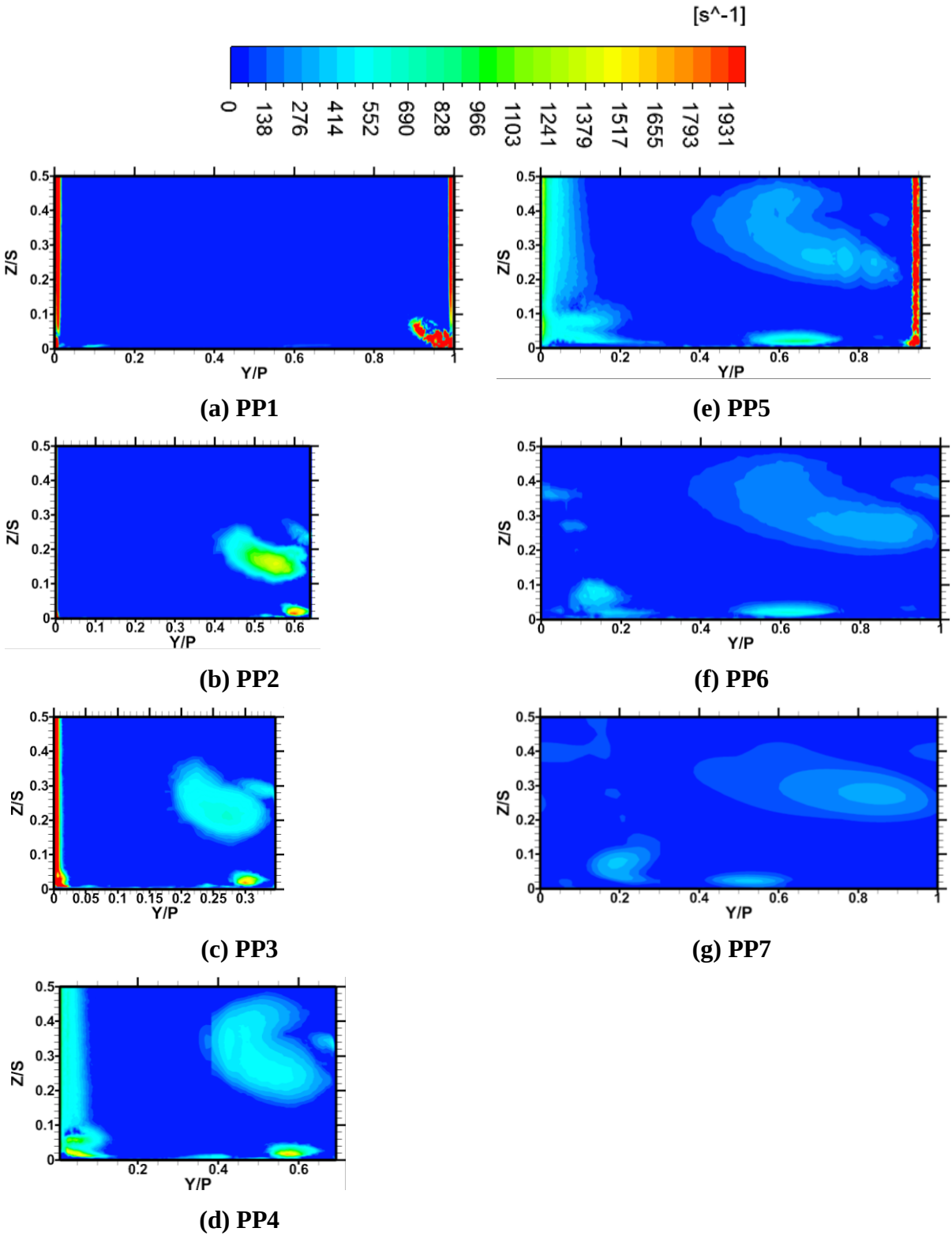

(a) PP1

(e) PP5

(b) PP2

(f) PP6

(c) PP3

(g) PP7

(d) PP4

Figure 121: Swirling Strength Contours at various axial planes through the passage for the case X_h=D, α=30°, β=60°, MFR=1%

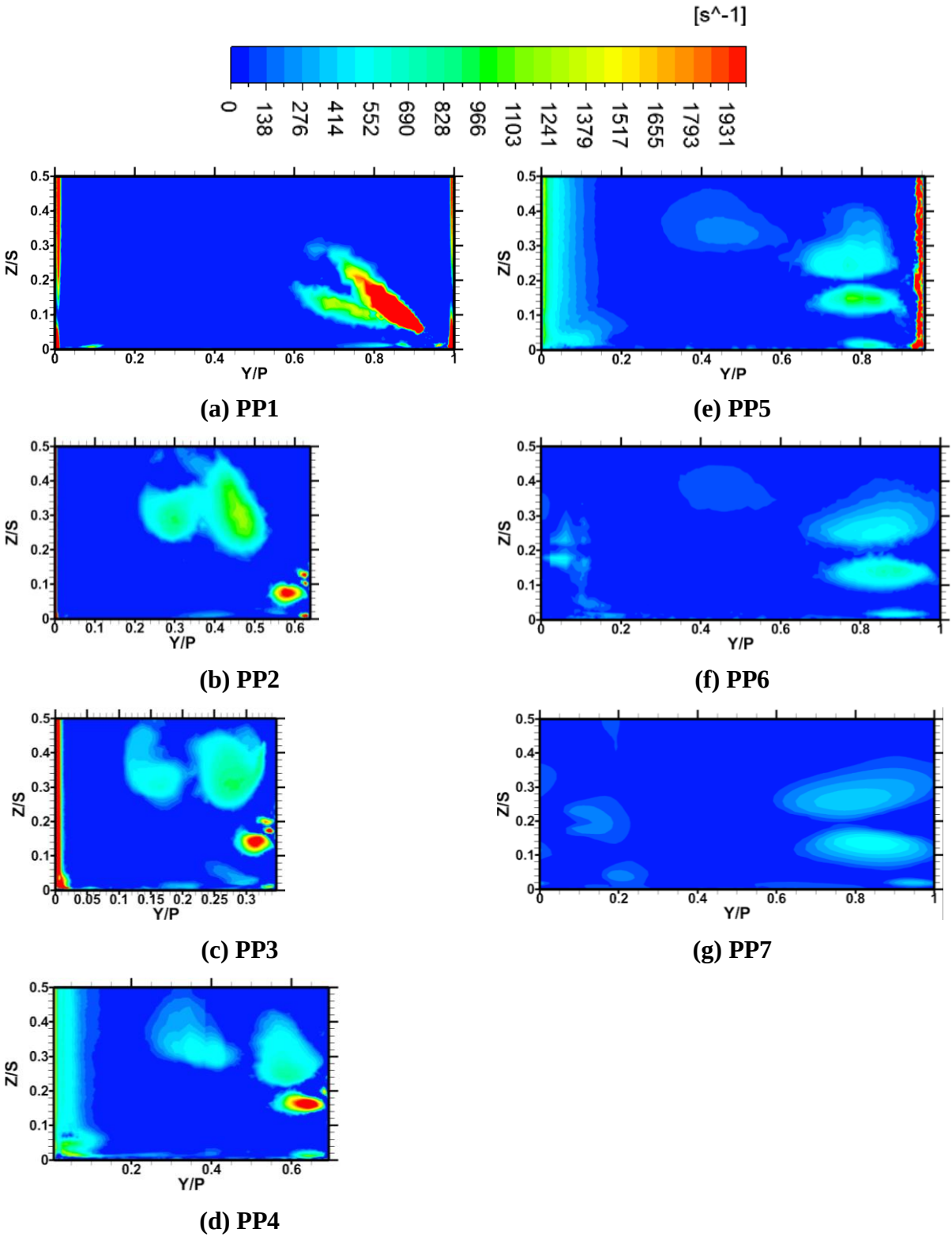

Figure 122: Swirling Strength Contours at various axial planes through the passage for the case X_h=D, α=30°, β=90°, MFR=1%

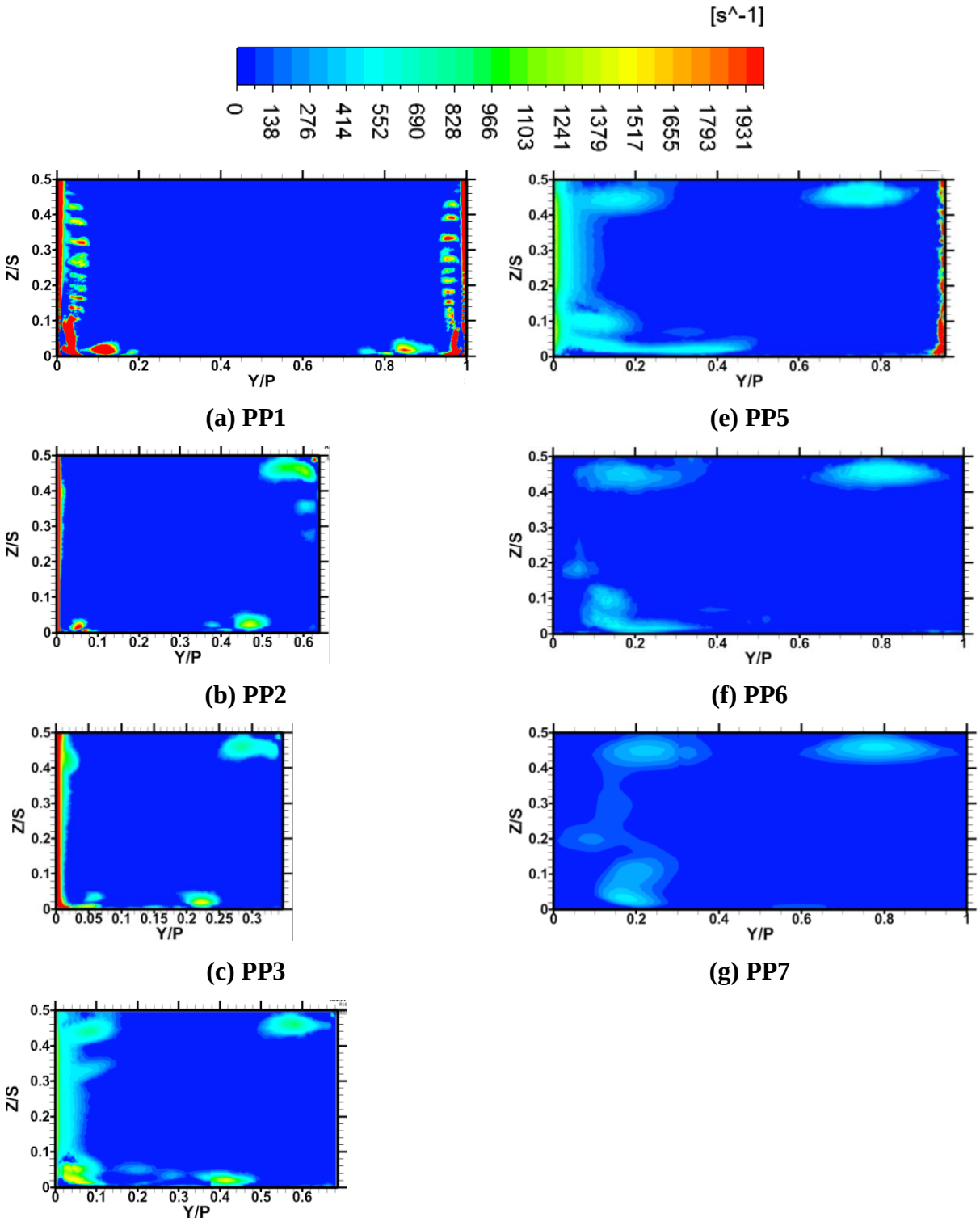

Figure 123: Swirling Strength Contours at various axial planes through the passage for the case X_h=2D, α=30°, β=0°, MFR=0.5%

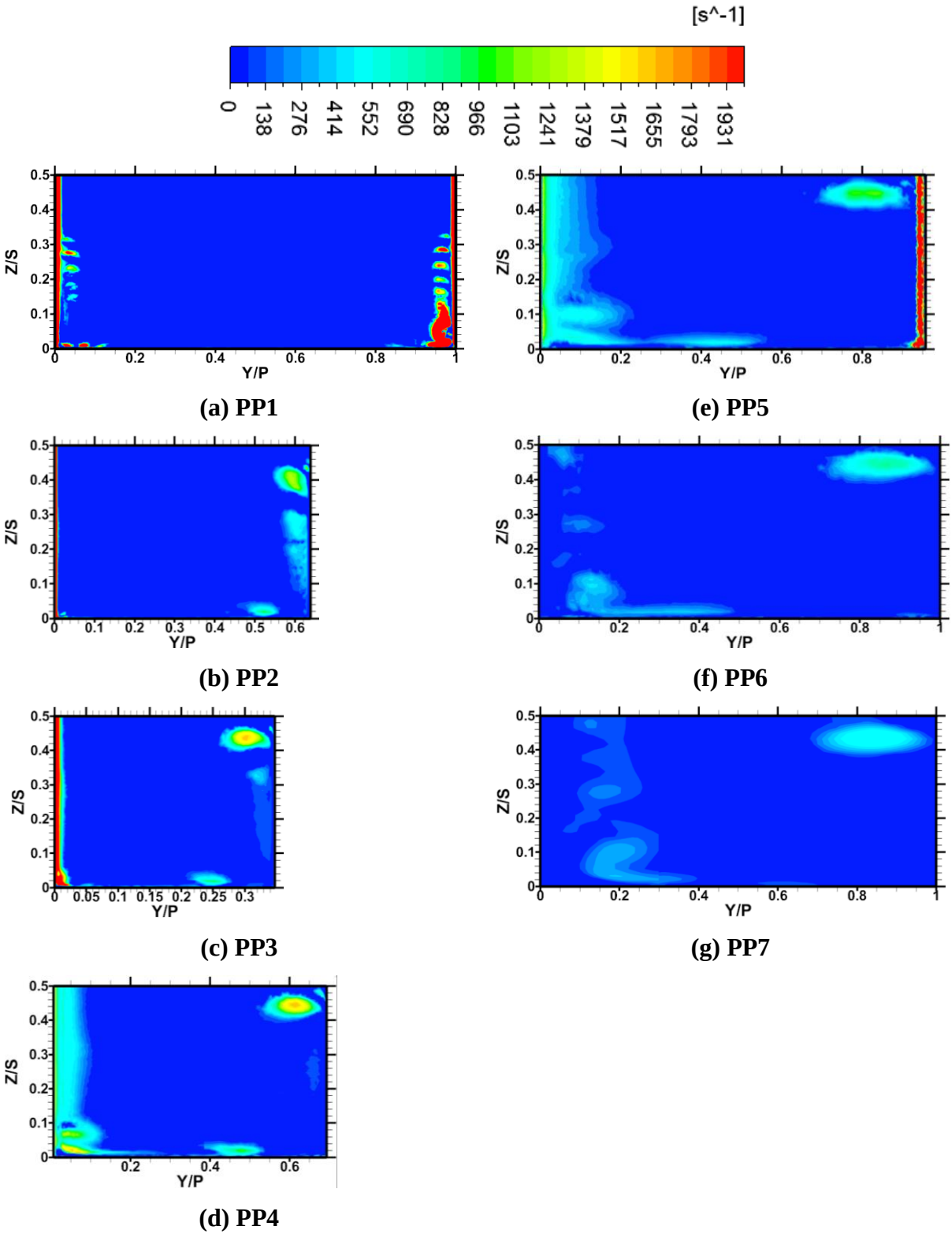

Figure 124: Swirling Strength Contours at various axial planes through the passage for the case X_h=2D, α=30°, β=30°, MFR=0.5%

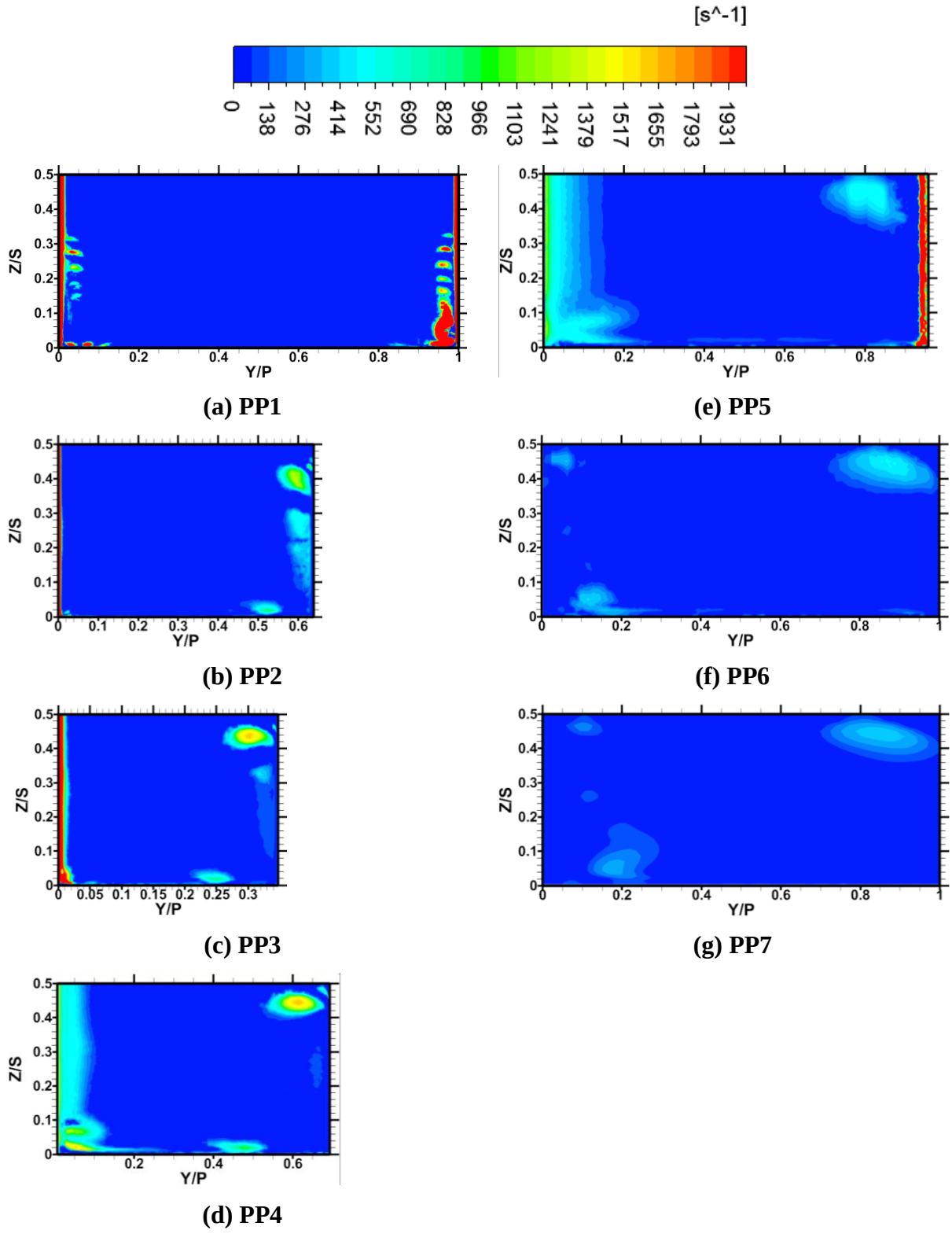

Figure 125: Swirling Strength Contours at various axial planes through the passage for the case X_h=2D, α=30°, β=45°, MFR=0.5%

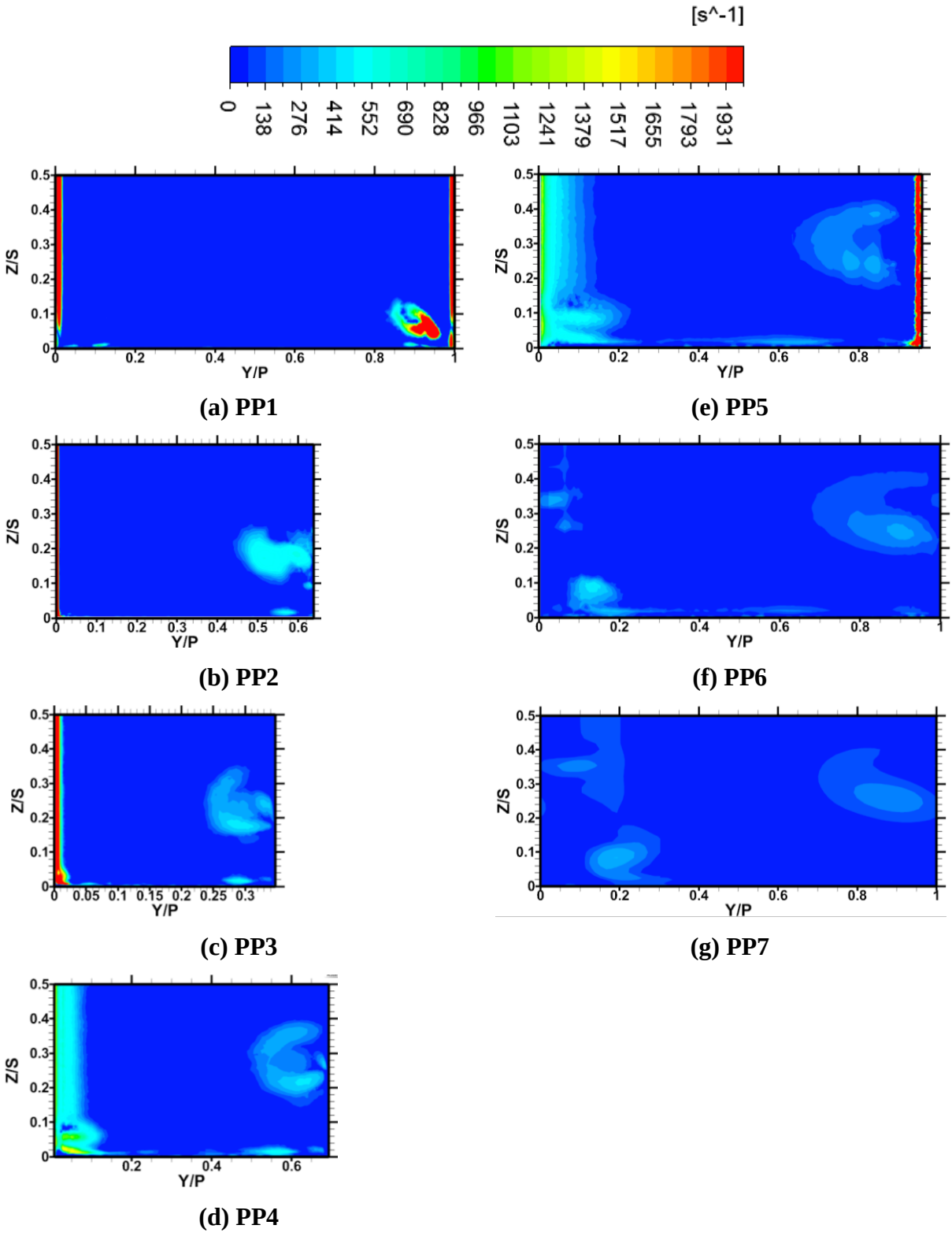

Figure 126: Swirling Strength Contours at various axial planes through the passage for the case X_h=2D, α=30°, β=60°, MFR=0.5%

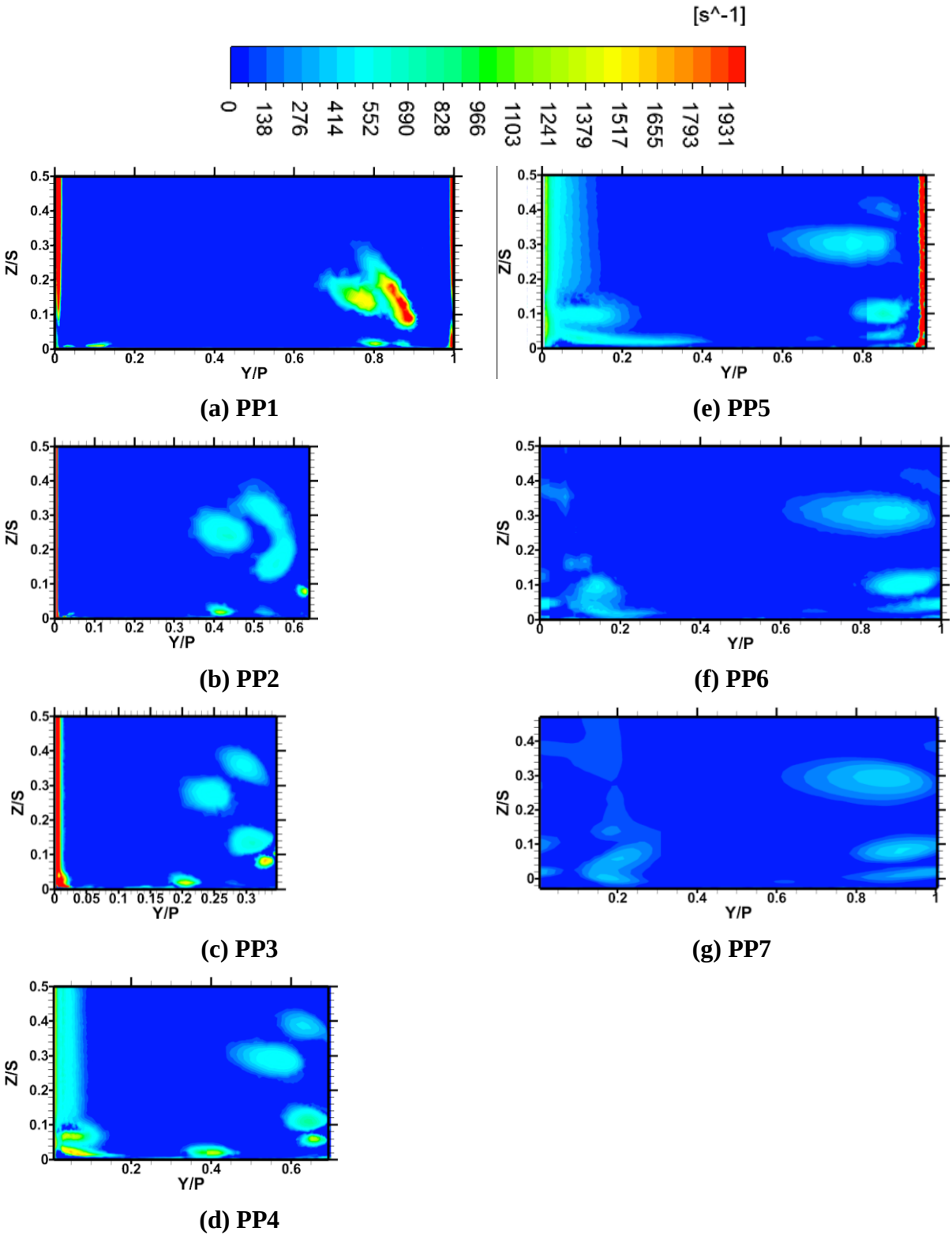

(a) PP1

(e) PP5

(b) PP2

(f) PP6

(c) PP3

(g) PP7

(d) PP4

Figure 127

: Swirling Strength Contours at various axial planes through the passage for the case X_h=2D, α=30°, β=90°, MFR=0.5%

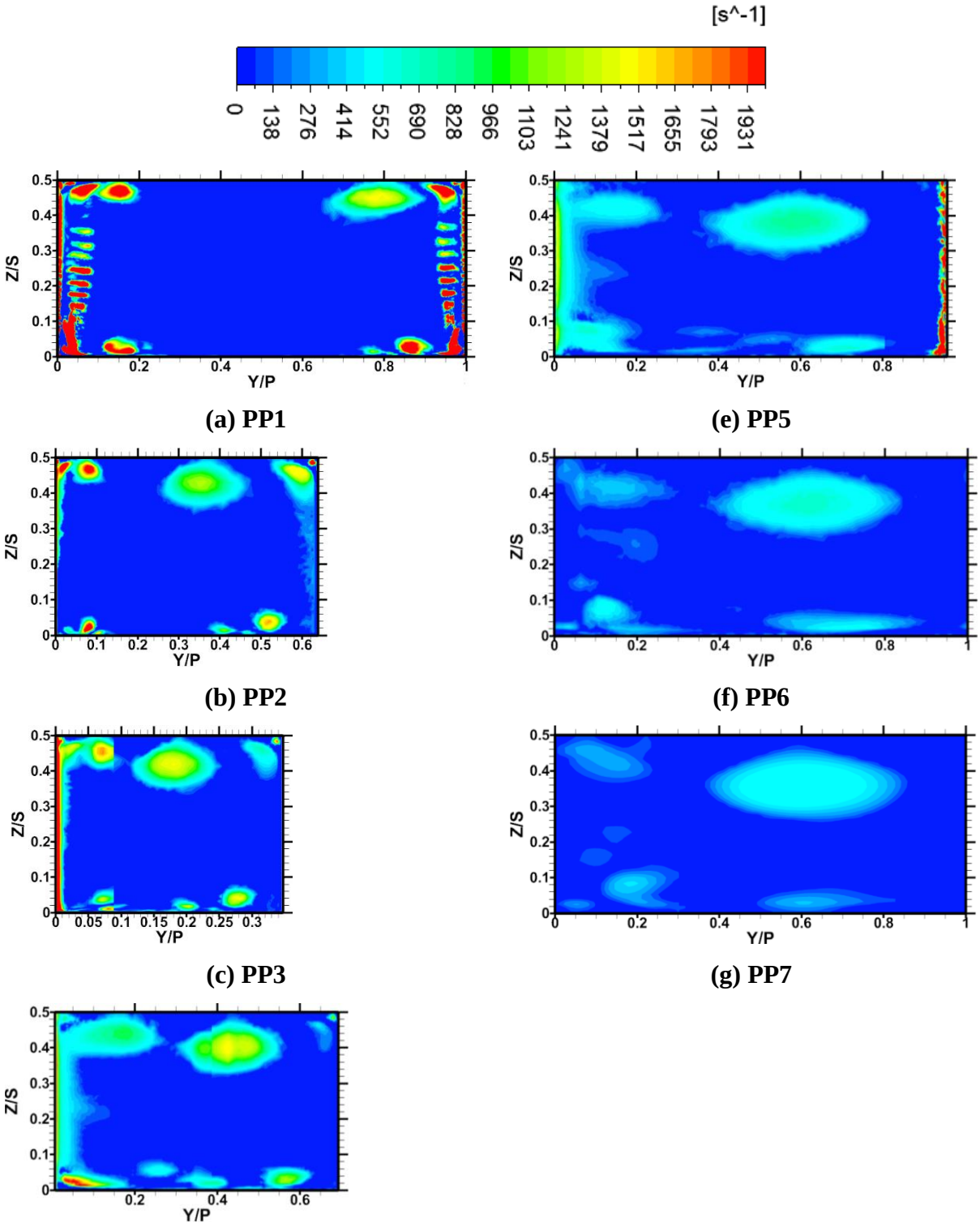

(a) PP1

(b) PP2

(c) PP3

(e) PP5

(f) PP6

(g) PP7

(d) PP4

Figure 128: Swirling Strength Contours at various axial planes through the passage for the case X_h=2D, α=30°, β=0°, MFR=1%

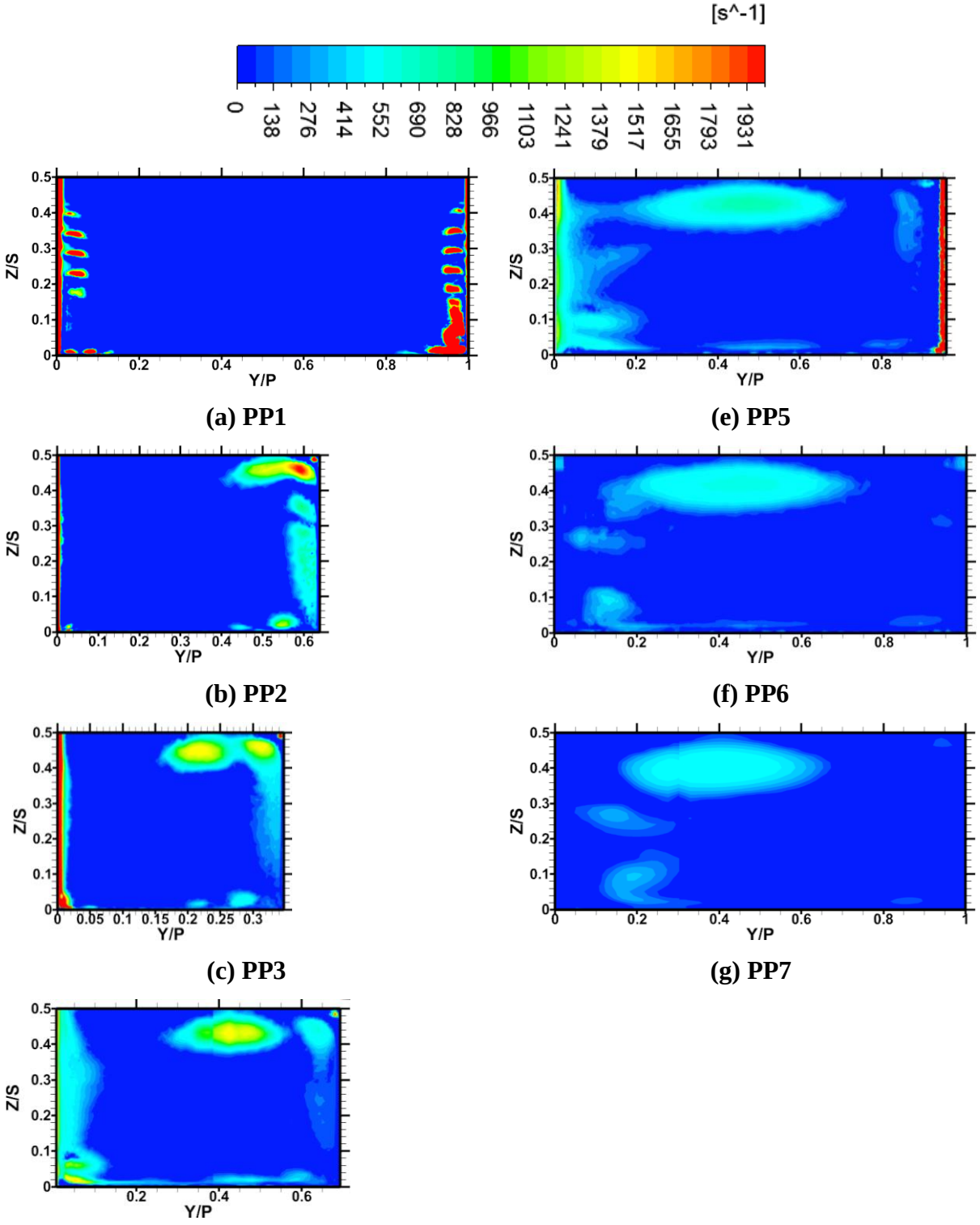

(a) PP1

(e) PP5

(b) PP2

(f) PP6

(c) PP3

(g) PP7

(d) PP4

Figure 129: Swirling Strength Contours at various axial planes through the passage for the case X_h=2D, α=30°, β=30°, MFR=1%

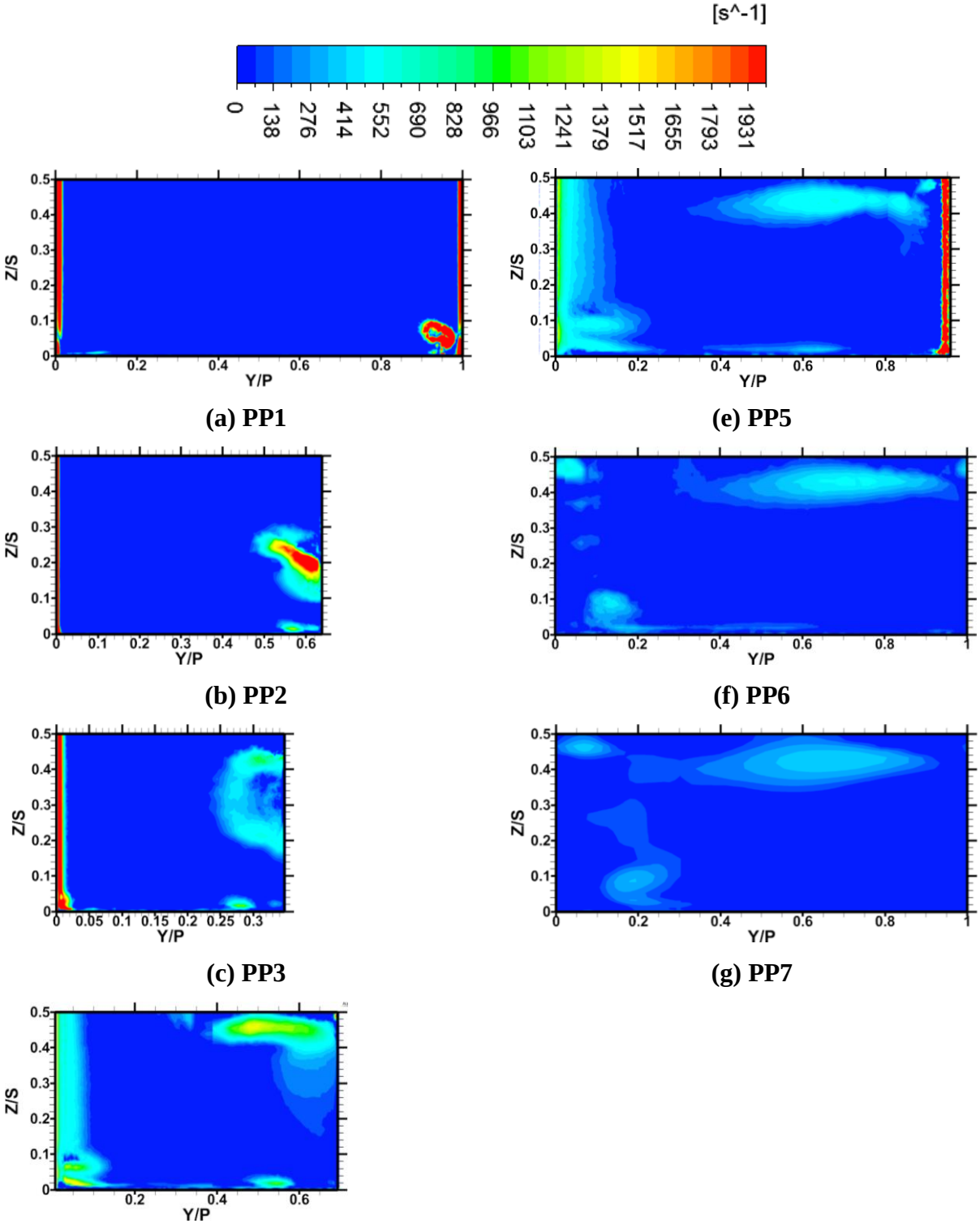

(a) PP1

(e) PP5

(b) PP2

(f) PP6

(c) PP3

(g) PP7

(d) PP4

Figure 130: Swirling Strength Contours at various axial planes through the passage for the case X_h=2D, α=30°, β=45°, MFR=1%

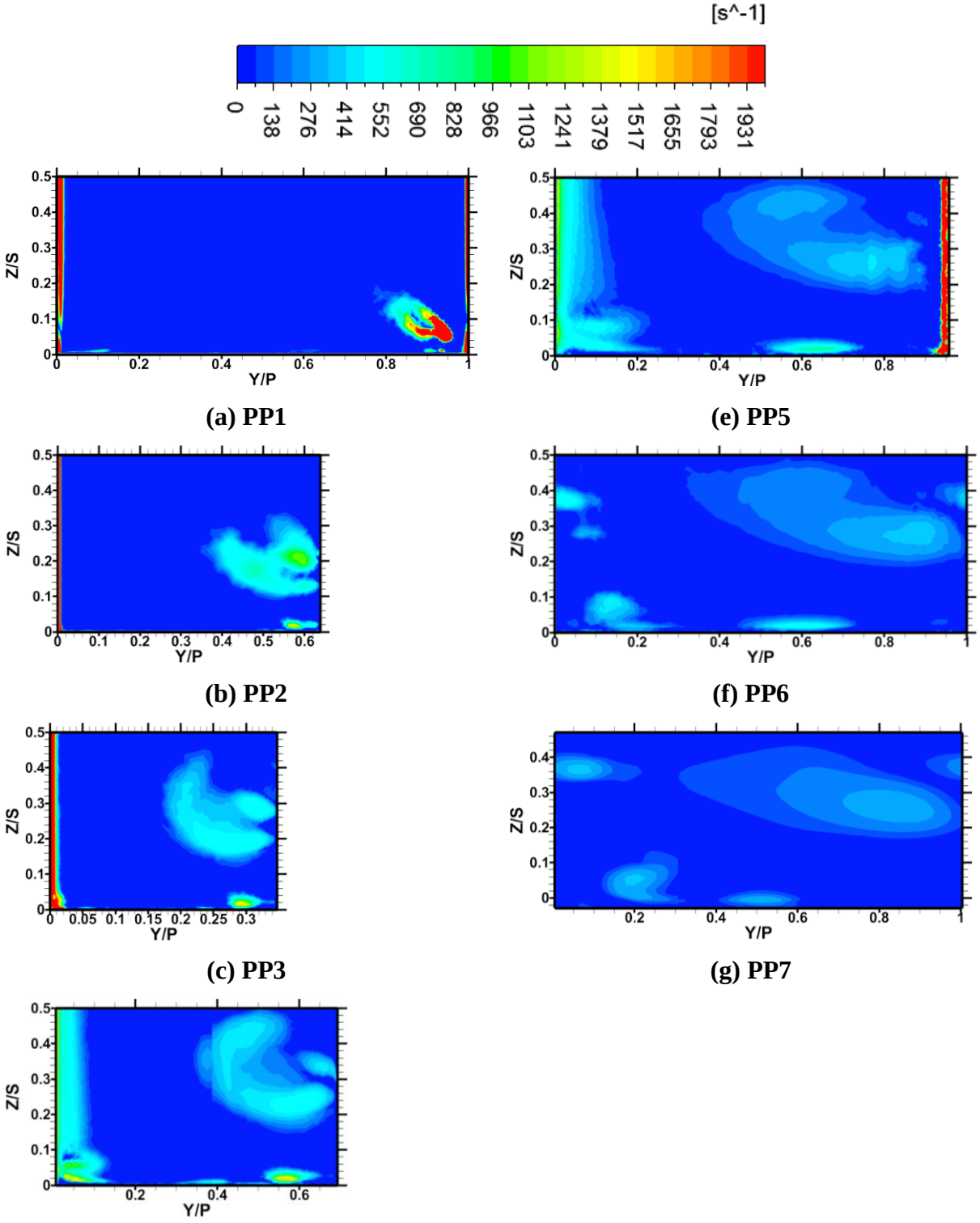

(a) PP1

(e) PP5

(b) PP2

(f) PP6

(c) PP3

(g) PP7

(d) PP4

Figure 131: Swirling Strength Contours at various axial planes through the passage for the case X_h=2D, α=30°, β=60°, MFR=1%

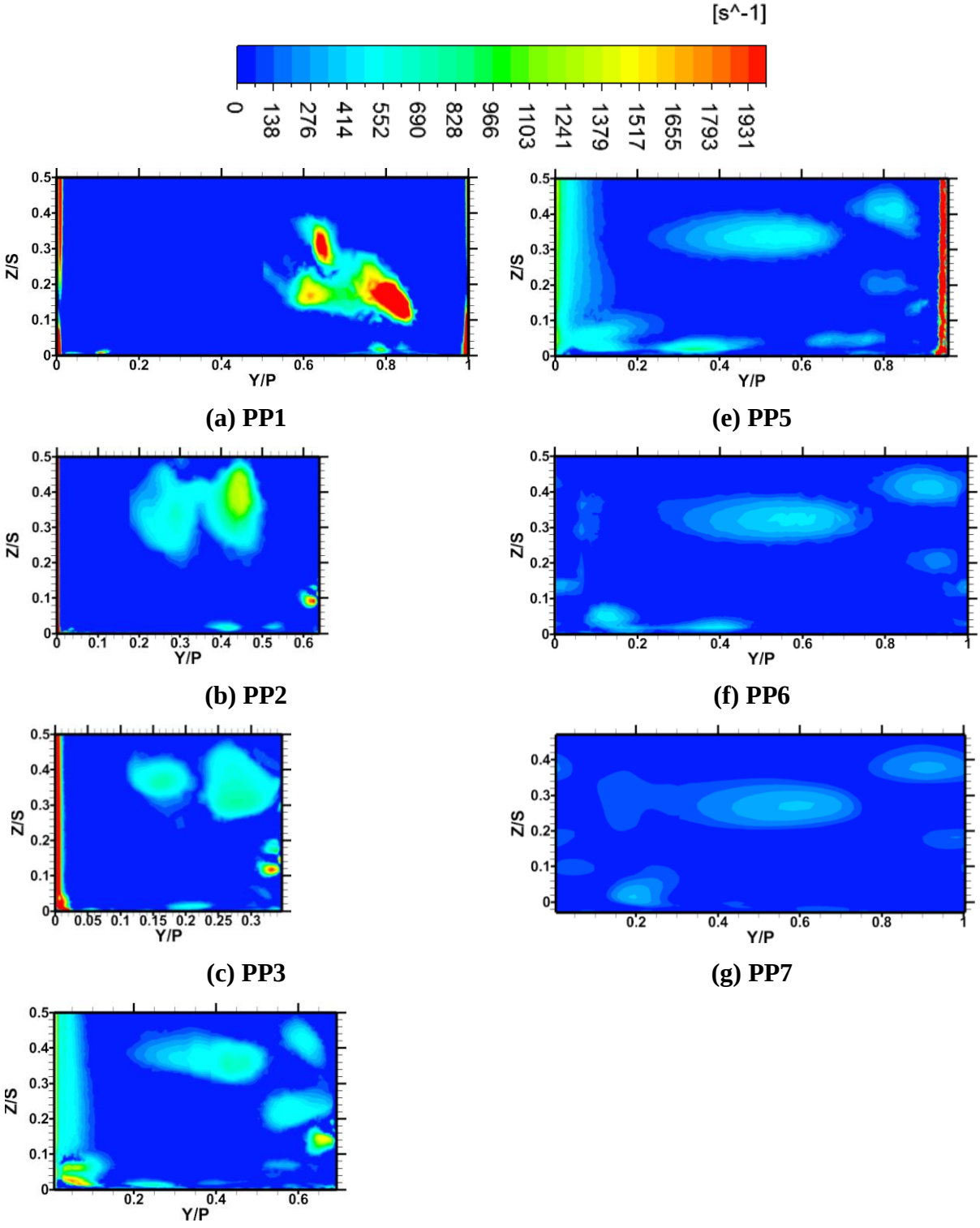

(a) PP1

(e) PP5

(b) PP2

(f) PP6

(c) PP3

(g) PP7

(d) PP4

Figure 132: Swirling Strength Contours at various axial planes through the passage for the case X_h=2D, α=30°, β=90°, MFR=1%

Exit Plane Total Pressure Loss Coefficient Plots

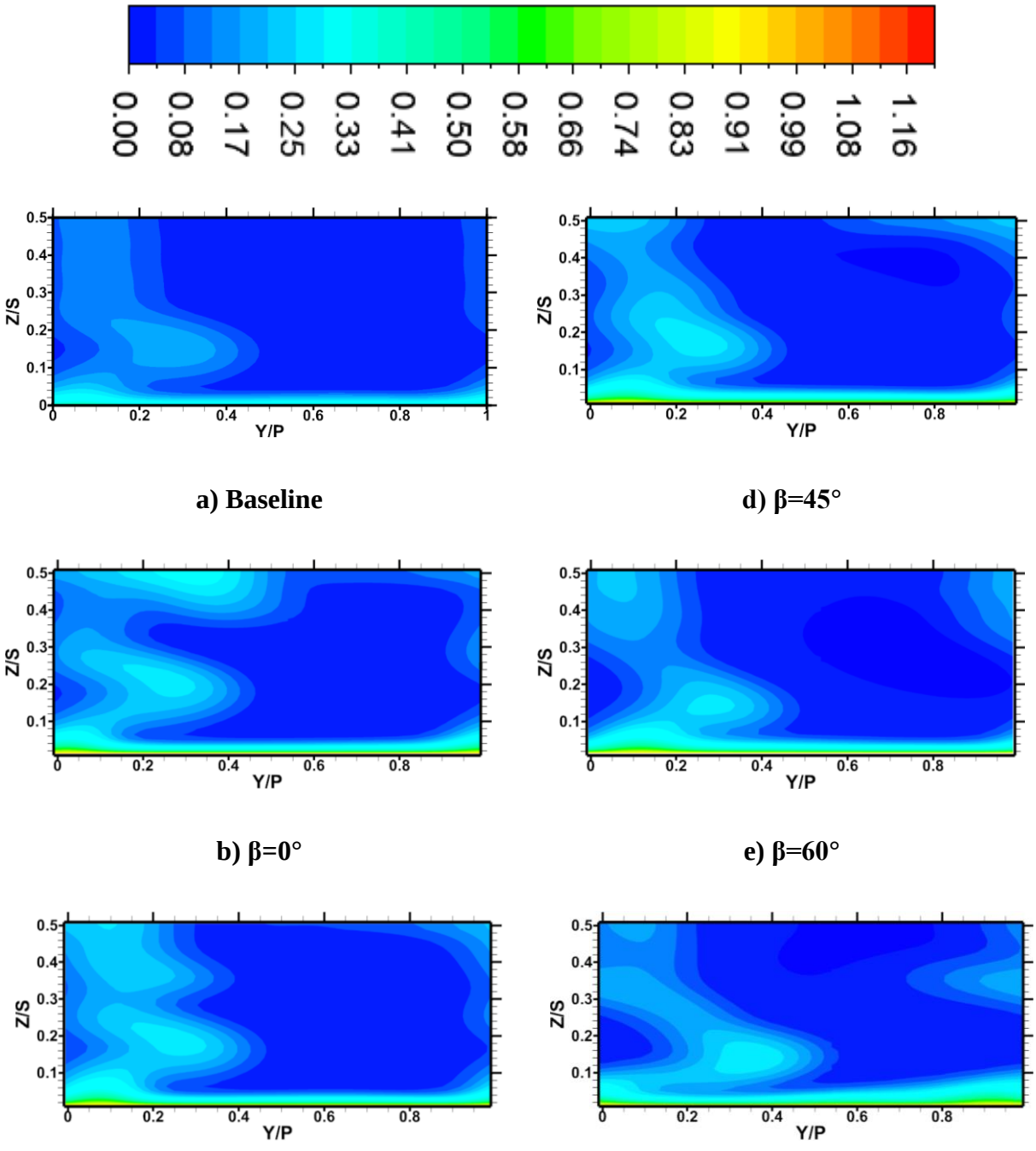

a) Baseline

d) β=45°

b) β=0°

e) β=60°

c) β=30°

f) β=90°

Figure 133: Exit plane total pressure loss coefficient contours for different β values at MFR=0.5% and X=D

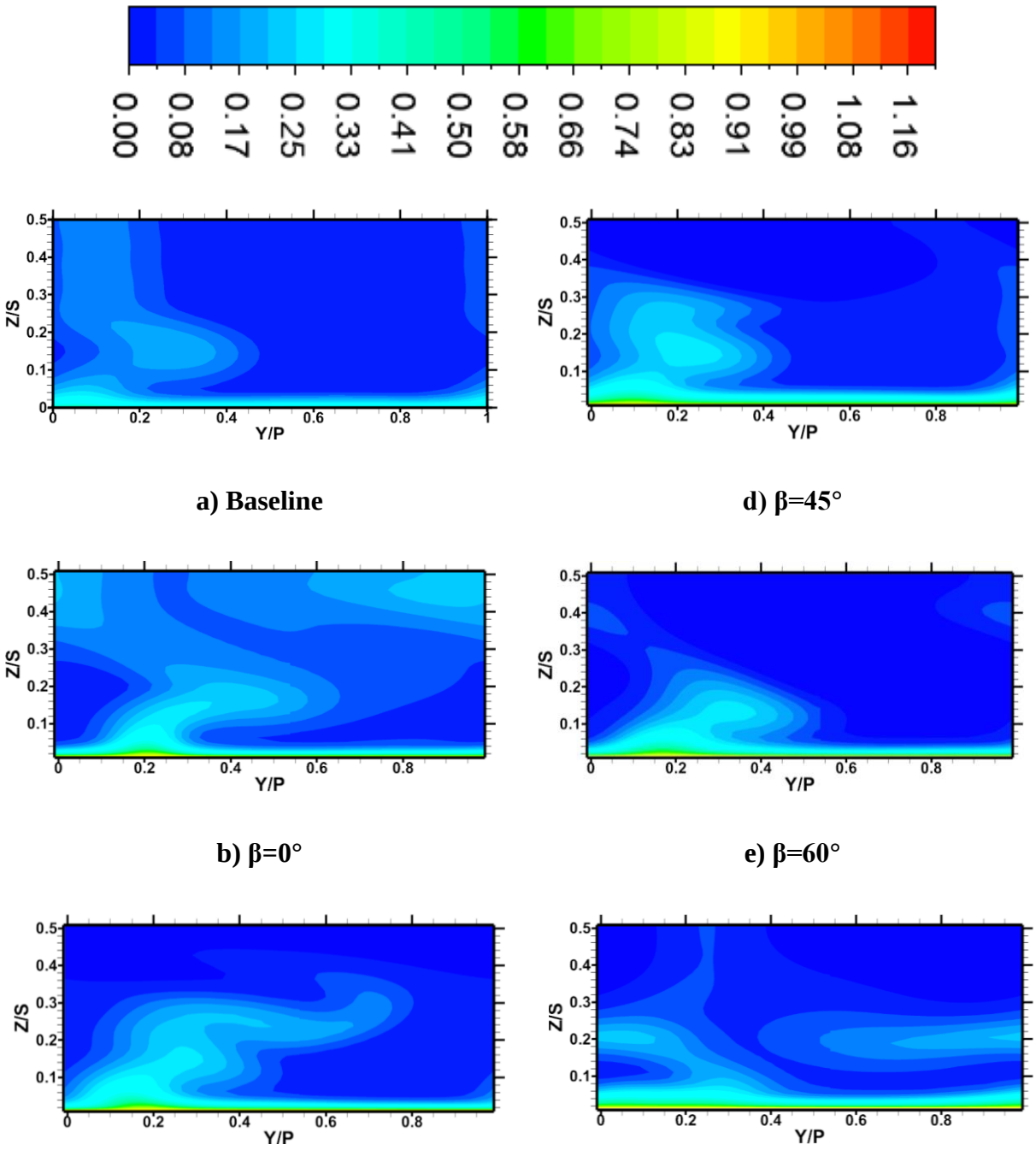

c) β=30° f) β=90°

Figure 134: Exit plane total pressure loss coefficient contours for different β values at MFR=1% and X=D

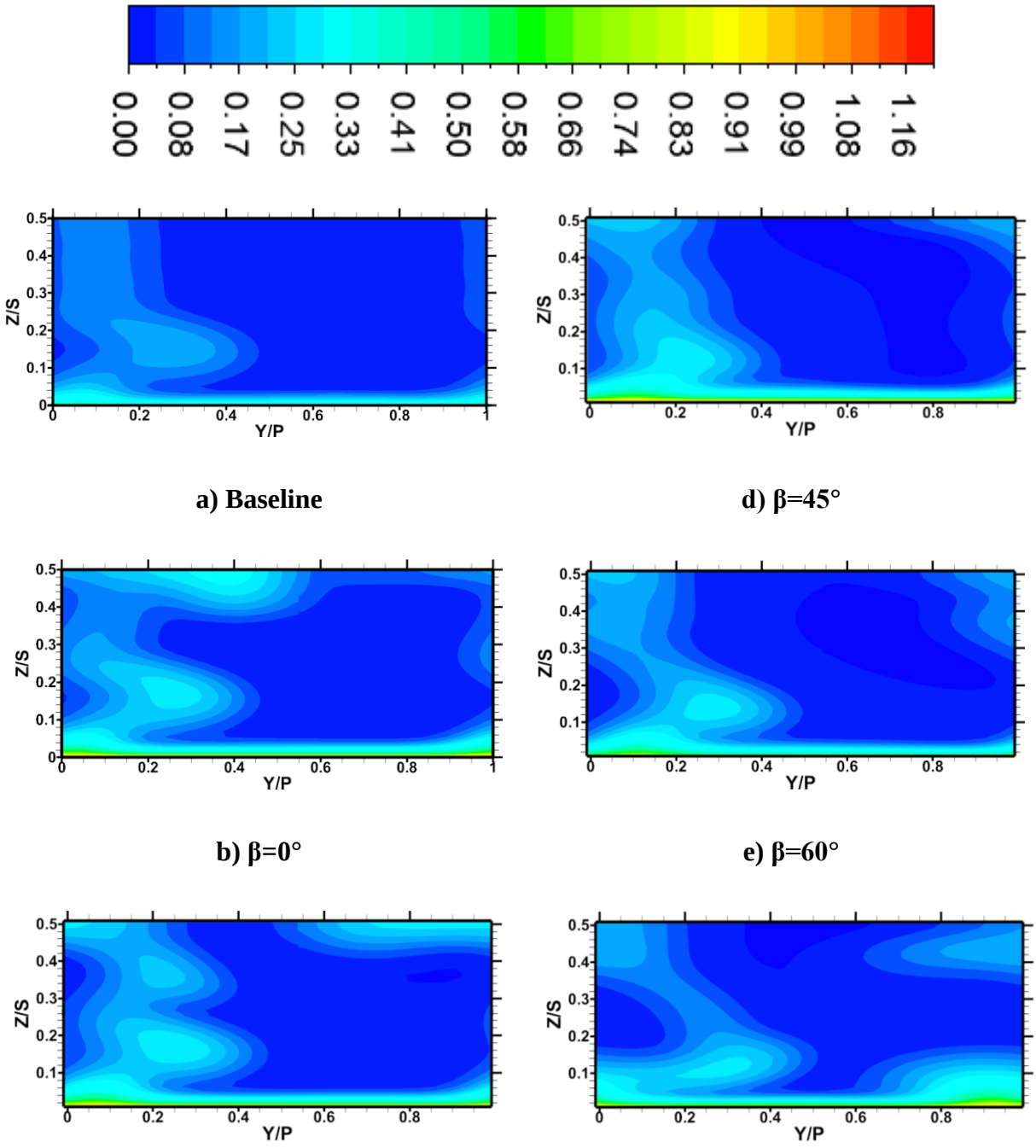

c) β=30° **f) β=90°**

Figure 135: Exit plane total pressure loss coefficient contours for different β values at MFR=0.5% and X=2D

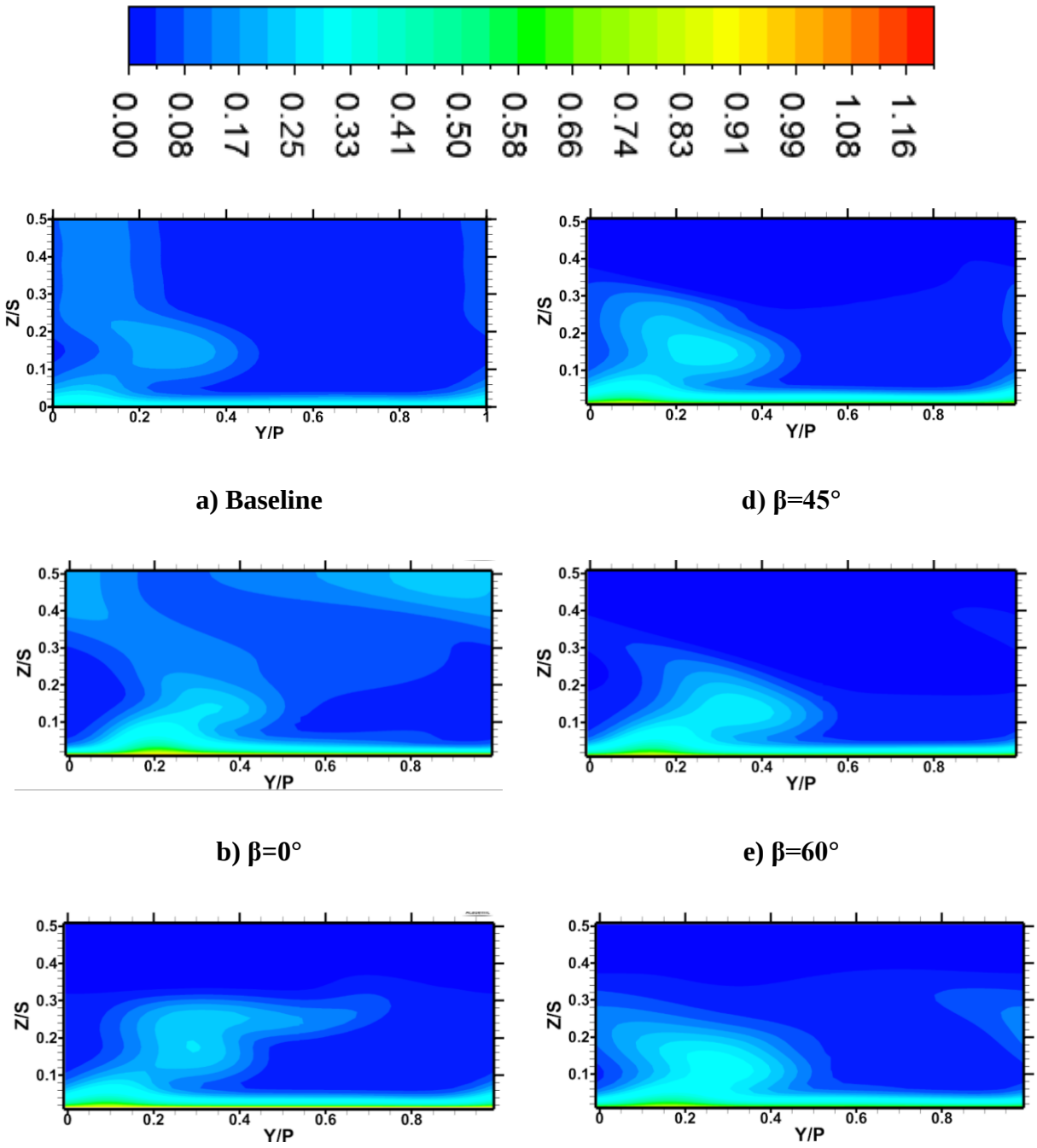

a) Baseline **d) β=45°**

b) β=0° **e) β=60°**

c) β=30° f) β=90°

Figure 136: Exit plane total pressure loss coefficient contours for different β values at MFR=1% and X=2D

Exit Plane Kinetic Energy Loss Coefficient Plots

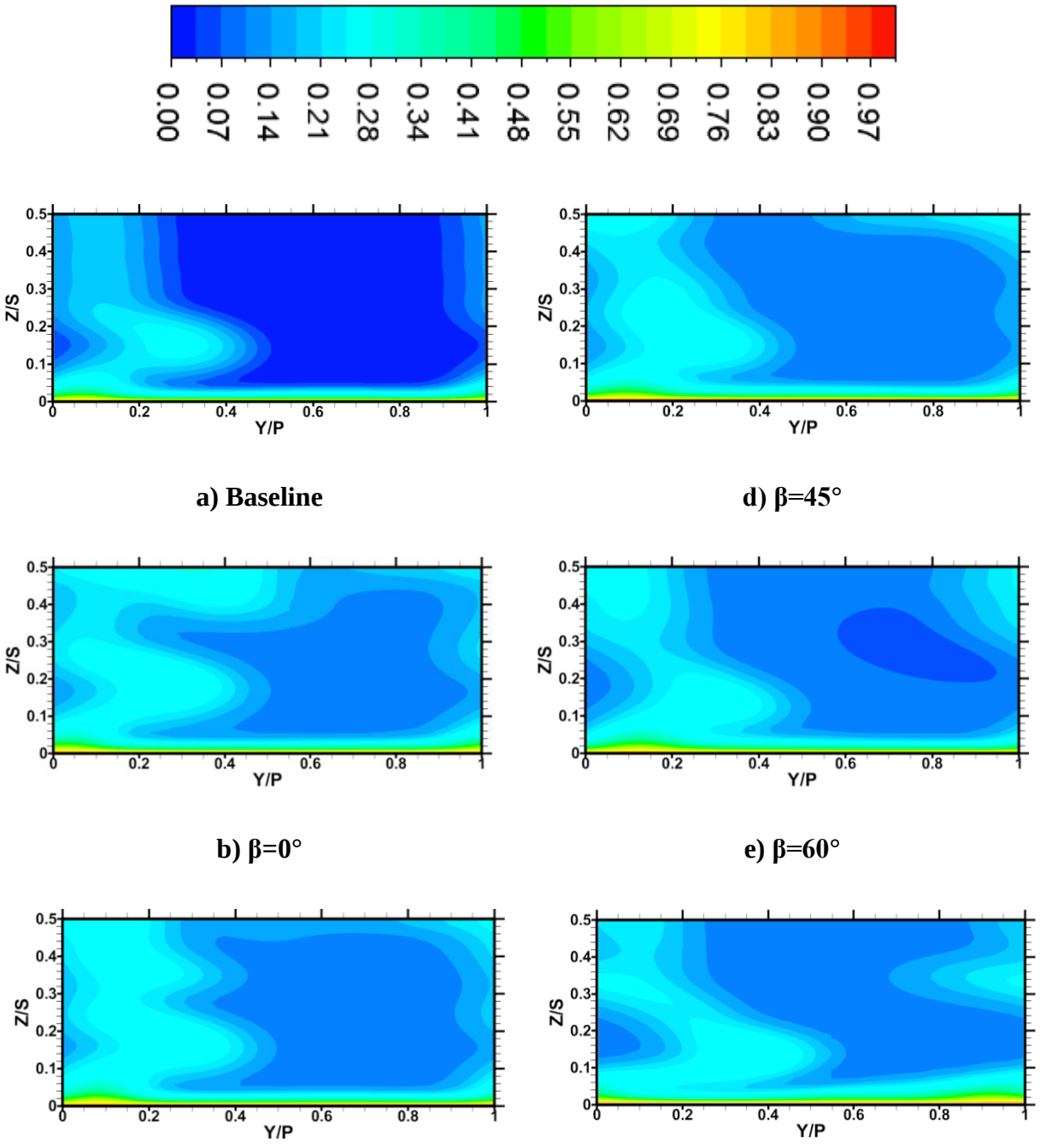

a) Baseline d) β=45°

b) β=0° e) β=60°

c) β=30° **f) β=90°**

Figure 137: Exit plane kinetic energy loss coefficient contours for different β values at MFR=0.5% and X=D

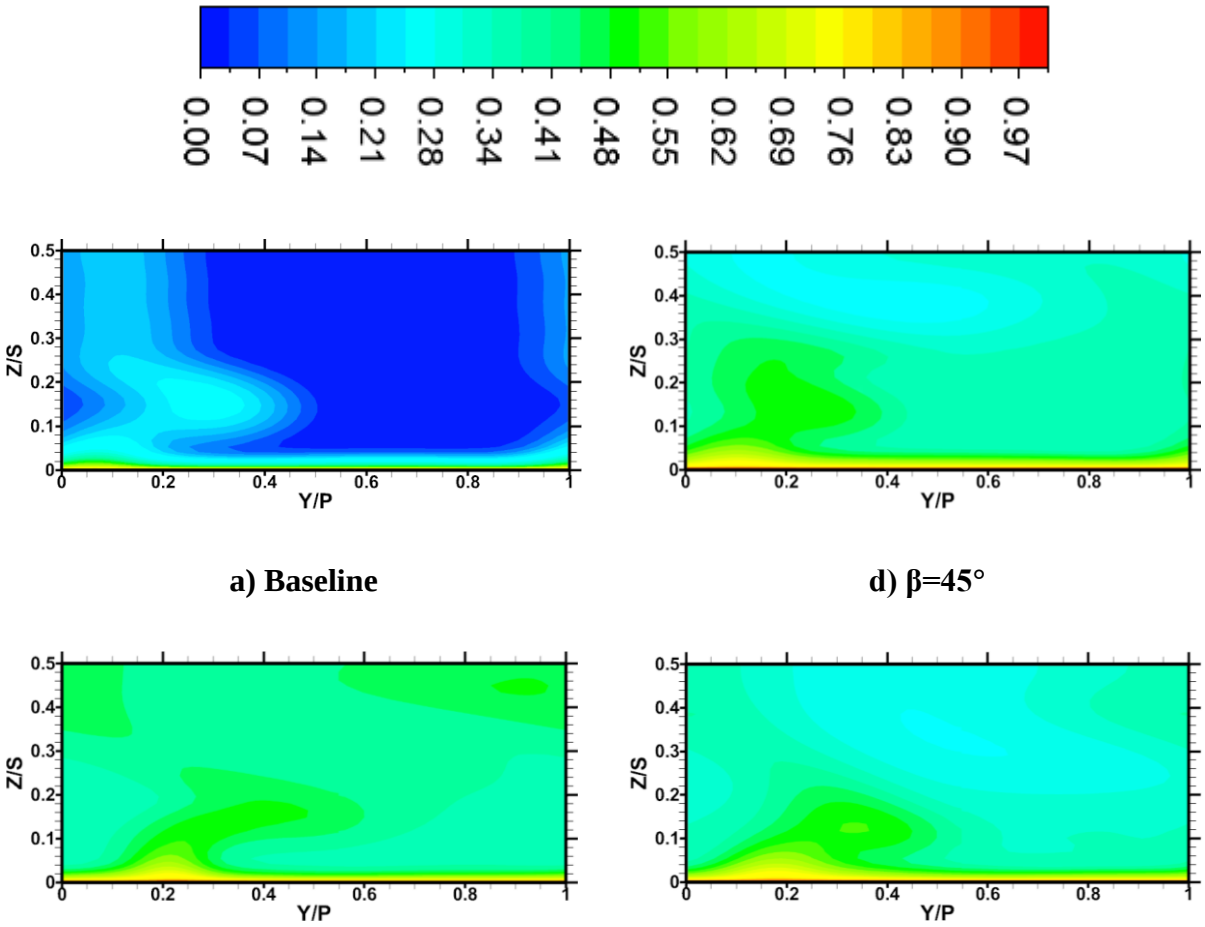

a) Baseline **d) β=45°**

b) β=0° **e) β=60°**

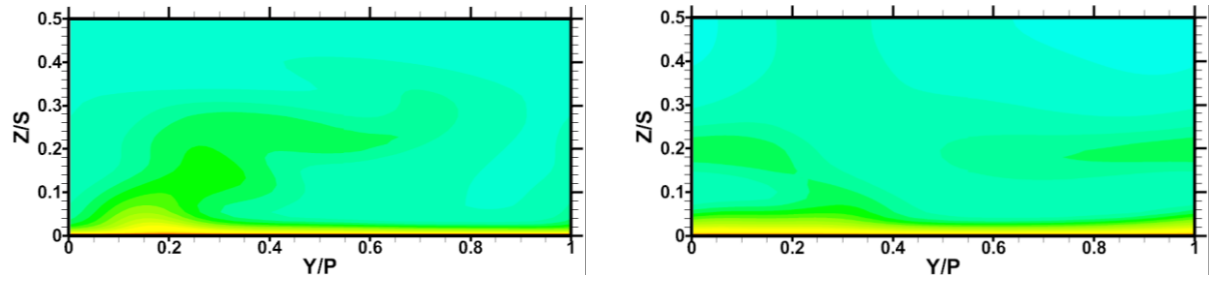

c) β=30° **f) β=90°**

Figure 138: Exit plane kinetic energy loss coefficient contours for different β values at MFR=1% and X=D

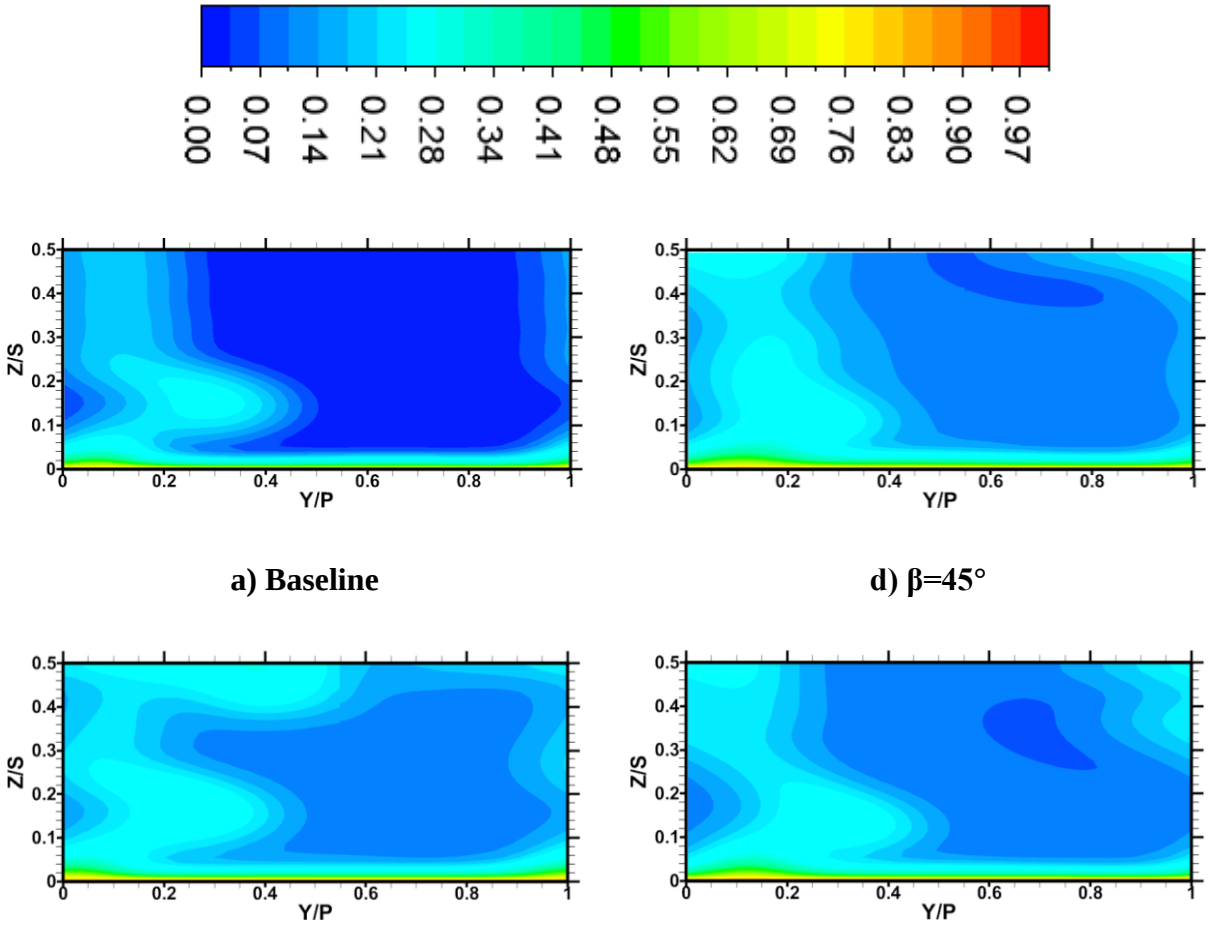

a) Baseline **d) β=45°**

b) β=0° **e) β=60°**

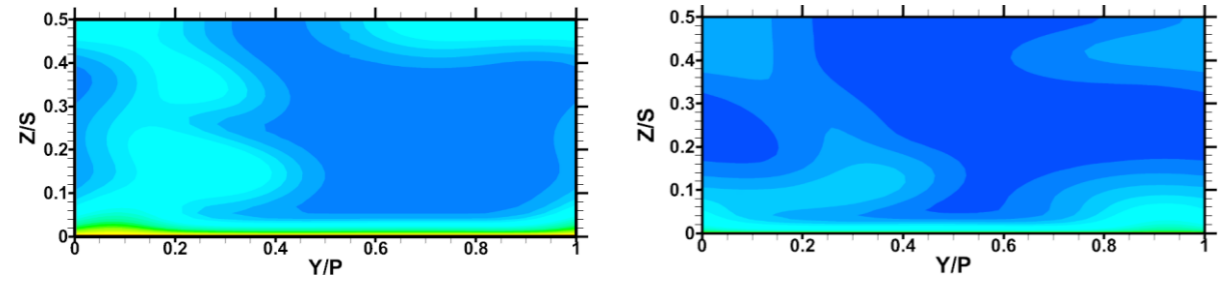

c) β=30° **f) β=90°**

Figure 139: Exit plane kinetic energy loss coefficient contours for different β values at MFR=0.5% and X=2D

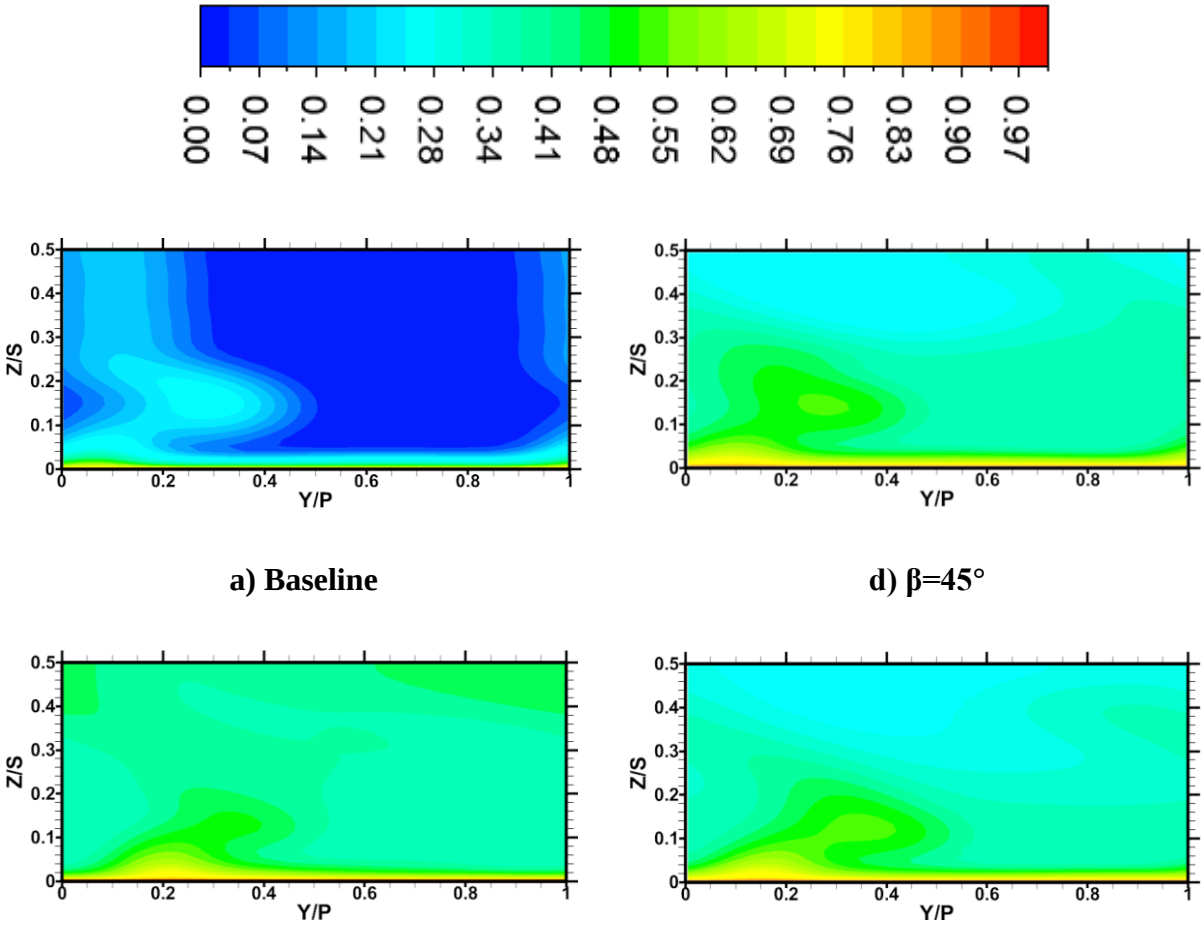

a) Baseline **d) β=45°**

b) β=0° **e) β=60°**

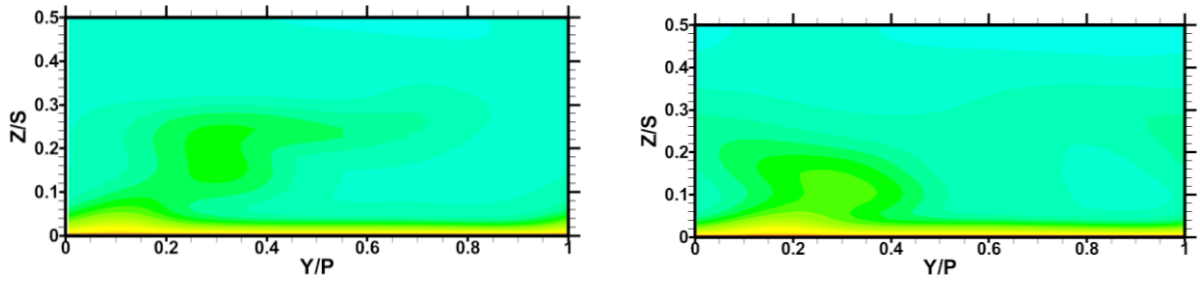

c) β=30° **f) β=90°**

Figure 140: Exit plane kinetic energy loss coefficient contours for different β values at MFR=1% and X=2D